

Winter 2010

# Development and Characterization of a Fast Neutron Imaging Telescope (FNIT) for 1--20 MeV Neutrons From the Sun and Nuclear Material

Richard S. Woolf

*University of New Hampshire, Durham*

Follow this and additional works at: <https://scholars.unh.edu/dissertation>

---

## Recommended Citation

Woolf, Richard S., "Development and Characterization of a Fast Neutron Imaging Telescope (FNIT) for 1--20 MeV Neutrons From the Sun and Nuclear Material" (2010). *Doctoral Dissertations*. 542.

<https://scholars.unh.edu/dissertation/542>

This Dissertation is brought to you for free and open access by the Student Scholarship at University of New Hampshire Scholars' Repository. It has been accepted for inclusion in Doctoral Dissertations by an authorized administrator of University of New Hampshire Scholars' Repository. For more information, please contact [nicole.hentz@unh.edu](mailto:nicole.hentz@unh.edu).

DEVELOPMENT AND CHARACTERIZATION OF A FAST NEUTRON IMAGING TELESCOPE  
(FNIT) FOR 1–20 MeV NEUTRONS FROM THE SUN AND NUCLEAR MATERIAL

BY

RICHARD S. WOOLF  
B.S. West Chester University, 2003

DISSERTATION

Submitted to the University of New Hampshire  
in Partial Fulfillment of  
the Requirements for the Degree of

Doctor of Philosophy

in

Physics

December, 2010

UMI Number: 3442537

All rights reserved

**INFORMATION TO ALL USERS**

The quality of this reproduction is dependent upon the quality of the copy submitted.

In the unlikely event that the author did not send a complete manuscript and there are missing pages, these will be noted. Also, if material had to be removed, a note will indicate the deletion.



UMI 3442537

Copyright 2011 by ProQuest LLC.

All rights reserved. This edition of the work is protected against unauthorized copying under Title 17, United States Code.



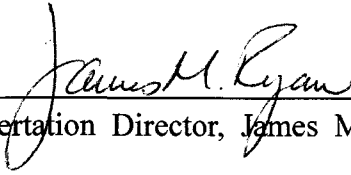
ProQuest LLC

789 East Eisenhower Parkway

P.O. Box 1346

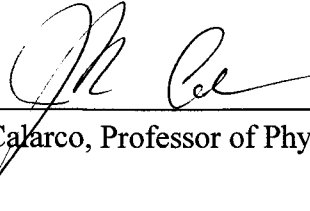
Ann Arbor, MI 48106-1346

This dissertation has been examined and approved.



---

Dissertation Director, James M. Ryan, Professor of Physics



---

John Calarco, Professor of Physics



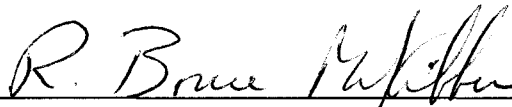
---

Benjamin D. G. Chandran, Associate Professor of Physics



---

Mark L. McConnell, Associate Professor of Physics



---

R. Bruce McKibben, Research Professor of Physics

11/3/10

---

Date

DEDICATION

*To my mother*

## ACKNOWLEDGMENTS

I express my deepest gratitude to my thesis advisor, Professor James Ryan. He provided challenging and informative problems to better my understanding of the Sun and instrumentation. He always had the patience and guidance to listen to any questions, no matter how numerous, that I had along the way. And a plethora of knowledge, always with an open door, to talk about research or life in general. It has been a sincere pleasure to have worked for him for the last five years. I would like to thank Professor Mark McConnell for also having an open door to discuss my research or any general concerns. His assistance and discussions were most appreciated. I would like to thank Professors John Calarco, Benjamin D. G. Chandran, and R. Bruce McKibben for serving on my thesis committee and providing valuable insight to this dissertation. Thank you to Dr. Silas Beane for serving on my thesis proposal committee. I would like to thank Dr. Peter Bloser for making the time for discussions regarding instrumentation and data analysis techniques. Thanks to Dr. Ulisse Bravar for all his help in the laboratory and during field campaigns to UC–Davis and PNNL. I would also like to thank Mr. Jason Legere for his help inside and outside the laboratory and Mr. John Macri for his guidance while getting my feet wet at the onset of laboratory work. Thanks to Katie Makem-Boucher, Michelle Waltz, and Robbin Williams for their assistance over the years.

Thanks to Dr. Alexander MacKinnon at the University of Glasgow for providing the insight into spectral de-convolution studies that aided in the completion of this work, and to Dr. Procheta Mallik, also at the University of Glasgow, who provided his

knowledge on spectral de-convolution and his work in developing the imaging algorithms used in this thesis. Thanks to Dr. Michael Moser for the simulation work completed while at the University of Bern and thanks to Dr. Benoît Pirard for his continuation of the simulation of neutron telescopes and spacecrafts for the inner heliosphere. His work was an integral part of my studies over the past two years. Thanks to Mr. Joshua Wood for his simulation efforts here at UNH and for running simulations on the fly quite often. Thanks to Dr. Carlos Castaneda and Tim Essert at UC–Davis for their help during neutron beam calibration work and after. Thanks to Dr. Mitchell Woodring at PNNL who went above and beyond in helping us complete our field work in Richland, WA. Thanks to Drs. Aaron Torok and Lorenzo Zana for many great conversations during our time both inside and outside of the classroom. And especially, thanks to Mr. Anthony Marcolongo whose advice was invaluable during my formative years of graduate school.

During my seven years at UNH I have had the fine pleasure of being associated with the campus observatory, serving as manager for five of those years. This role has brought me a great amount of joy and added so much to my UNH experience as a whole. I again would like to thank Professor James Ryan for appointing me to this role and serving as observatory committee chair for three of those five years. Professor Ryan served double duty during that time listening to both research and observatory problems. And again, thanks to Professor Mark McConnell who has served as observatory committee chair for the last two years. I would be remiss if I did not acknowledge Mr. John Gianforte and Mr. George Clark, for without your help, managing the observatory would not have been possible or such a pleasure.

To my family, I would like to begin by thanking my mother, Cynthia. It was her love, support and always making sure I had a supply of home-cooked meals when I returned from visits to Pennsylvania that kept me going during the last seven years. I cannot thank you enough for that. My dad, Richard, who was the one that sparked my initial interest in the skies above when I was six years old and fueling that fire with the purchase of my first telescope. My stepdad, Eugene, who has provided support and advice on all aspects of my life. And to Shirley, your love and support during the last two years has meant the world to me and I cannot imagine my life without you being a part of it.

This work was financially supported in part by grants from the National Nuclear Security Administration (NNSA), Office of Nonproliferation Research and Development (NA-22) Proliferation Detection Program, Contract No. DE-FG52-06NA27493 and the Nuclear and Radiological Security Program, Contract No. DE-FG52-04NA25687.



## CONTENTS

DEDICATION .....	iii
ACKNOWLEDGMENTS .....	iv
LIST OF TABLES .....	x
LIST OF FIGURES .....	xii
ABSTRACT .....	xxv
<b>1</b> INTRODUCTION .....	1
<b>2</b> SOLAR PHYSICS AND THE NUCLEAR MATERIAL PROBLEM .....	5
2.1 HIGH-ENERGY SOLAR PHYSICS .....	5
2.1.1 CORONAL HEATING .....	17
2.1.2 RELEVANCE TO INNER HELIOSPHERIC MISSIONS .....	20
2.2 NUCLEAR SECURITY .....	21
2.2.1 HISTORICAL AND MODERN PERSPECTIVE .....	21
2.2.2 NUCLEAR MATERIAL .....	23
<b>3</b> NEUTRON PHYSICS .....	29
3.1 NEUTRON INTERACTIONS .....	30
3.2 NEUTRON DETECTION .....	36
3.2.1 DETECTION PRINCIPLES FOR FNIT AND SIMILAR INSTRUMENTS .....	42

<b>4</b>	<b>FAST NEUTRON IMAGING TELESCOPE</b>	<b>50</b>
	4.1 SCIENCE MODEL I .....	50
	4.2 SCIENCE MODEL II .....	54
	4.3 PROTOTYPE CALIBRATION .....	57
	4.3.1 FNIT SM2: SYSTEM DIAGRAM .....	57
	4.3.2 TIME-OF-FLIGHT (ToF) .....	59
	4.3.3 INTERACTION LOCATION .....	63
	4.3.4 PULSE HEIGHT .....	66
	4.3.5 PULSE SHAPE DISCRIMINATION .....	72
	4.3.6 ANGULAR RESOLUTION MEASUREMENT .....	77
	4.4 NEUTRON BEAM CALIBRATION .....	80
	4.4.1 DATA ANALYSIS .....	89
	4.4.2 LIGHT OUTPUT FUNCTION FOR <1 MeV PROTONS .....	113
	4.5 BC-501 vs. BC-519 .....	116
	4.6 FISSIONABLE MATERIAL .....	120
	4.6.1 <sup>239</sup> Pu .....	120
	4.6.2 <sup>252</sup> Cf .....	121
<b>5</b>	<b>INSTRUMENT RESPONSE</b>	<b>127</b>
	5.1 GEANT4 SIMULATIONS .....	127
	5.1.1 SIMULATING FNIT SM2 .....	128
	5.2 RESPONSE ANALYSIS .....	131

	5.2.1 COMPARISON OF MEASURED AND SIMULATED DATA .....	132
	5.2.2 FLAT (1–10 MeV) INPUT SPECTRUM .....	134
	5.2.3 FIRST–ORDER EFFICIENCY CORRECTIONS .....	143
<b>6</b>	<b>SPECTRAL AND IMAGING DE-CONVOLUTION FOR DOUBLE SCATTER NEUTRON TELESCOPES</b>	<b>146</b>
	6.1 INVERSE AND ILL-POSED PROBLEMS .....	146
	6.2 SPECTRAL ANALYSIS .....	148
	6.3 IMPLEMENTATION .....	154
	6.3.1 FORWARD FOLDING .....	155
	6.3.2 TIKHONOV REGULARIZATION .....	162
	6.4 NEUTRON IMAGING .....	175
	6.4.1 MINIMAL NUMBER OF EVENT CIRCLES FOR LOCATION IDENTIFICATION .....	187
<b>7</b>	<b>PERFORMANCE MEASUREMENTS AND ESTIMATES FOR SOLAR AND TERRESTRIAL NEUTRON TELESCOPES</b>	<b>190</b>
	7.1 SOLAR NEUTRON TELESCOPE SENSITIVITY .....	194
	7.2 NEUTRON SPECTROSCOPE .....	210
<b>8</b>	<b>DISCUSSION AND CONCLUSIONS</b>	<b>219</b>
	REFERENCES	226

## LIST OF TABLES

4-1	CNL neutron beam energies and characteristics .....	83
4-2	Beam intensity at varying distances, normalized to collimator exit .....	87
4-3	Intensity of induced background at 6 m .....	88
4-4	Run time and number of triggers obtained for “low-energy” neutron beams at varying orientations .....	92
4-5	Run time and number of triggers obtained for “high-energy” neutron beams at 30° .....	108
4-6	Properties of organic liquid scintillators BC-501 (detectors A and C) and BC-519 (detector B) (Saint-Gobain Crystals n.d.) .....	117
5-1	List of output parameters from the simulation for each SM2 rod .....	130
6-1	Weighted mean and error for convolved data generated from the model and instrument response, $C$ ; laboratory measured data, $D$ ; chi-square value per bin with $\chi_v^2$ value for each energy and angle .....	159
6-2	Weighted mean and error for convolved data generated from the model and instrument response, $C$ ; laboratory measured data, $D$ ; chi-square value per bin with $\chi_v^2$ value for each energy and angle .....	162
6-3	Variation of the response matrix precision with respect to a constant number of 1.8–2.9 MeV neutron beam events to determine how the optimal value of the smoothing parameter varied .....	165

6-4	Variation of the response matrix precision with respect to a constant number of fission neutron events to determine how the optimal value of the smoothing parameter varied .....	165
6-5	Values of $\lambda$ and $\rho$ for (+/-) percent changes to the optimal value of $\lambda$ with 1.8-2.9 MeV neutron beam data at $30^\circ$ .....	168
6-6	Values of $\lambda$ and $\rho$ for (+/-) percent changes to the optimal value of $\lambda$ with fission neutron data at $30^\circ$ .....	171
7-1	The 1-20 MeV integrated neutron intensity for a $45^\circ$ cone centered on the sunward direction for each spacecraft position .....	202
7-2	Count rate for an effective area of $1.5 \times 10^{-2} \text{ cm}^2$ at each position on the spacecraft .....	203
7-3	Total number of neutrons for an integration time of 1000 s at each position on the spacecraft .....	203
7-4	The 1-20 MeV integrated neutron intensity for selections on spacecraft coordinates of $\Theta: (0^\circ, -30^\circ)$ , $\Phi: (-180^\circ, 180^\circ)$ .....	204
7-5	The 1-20 MeV integrated neutron intensity for selections on spacecraft coordinates of $\Theta: (-30^\circ, -60^\circ)$ , $\Phi: (-180^\circ, 180^\circ)$ .....	205
7-6	The 1-20 MeV integrated neutron intensity for selections on spacecraft coordinates of $\Theta: (-60^\circ, -90^\circ)$ , $\Phi: (-180^\circ, 180^\circ)$ .....	206

## LIST OF FIGURES

2-1	With neutron energy measurements, one can back propagate neutrons to the flare site seeing when they were produced with respect to other electromagnetic signatures .....	7
2-2	Relevant neutron and $\gamma$ -ray production cross-sections times a proton power law spectrum (Lockwood et al. 1997) .....	8
2-3	Cross-sections for important neutron producing reactions .....	14
2-4	Expected neutron fluence for varying heliocentric distance extrapolated from neutron measurements of the 15 June 1991 X12 flare .....	15
2-5	Neutron flux and energy distributions at 0.25, 0.33, 0.5 and 1 AU for neutron production dominated by heavy ions (CNO-Fe). Numbers are consistent with the 2.223-MeV line upper limit, for variations of the power-law index, $\delta$ , and the spectral hardness, $\alpha T$ (as defined on page 11) .....	18
3-1	Elastic neutron-proton scattering .....	43
3-2	Cross-section for elastic neutron-proton and neutron-carbon scattering .....	46
3-3	Cross-section for elastic neutron-proton scattering and the neutron capture reaction .....	47
3-4	Cross-section for elastic and inelastic neutron-carbon scattering .....	48
3-5	Differential elastic scattering cross-section as a function of scatter angle for	

	1–20 MeV incident neutrons .....	49
4–1	Single-layer of FNIT SM1 with MAPMT .....	51
4–2	Three-layer configuration of FNIT SM1 with MAPMT .....	52
4–3	Three-layer configuration of FNIT SM1 .....	53
4–4	FNIT SM2 rod shown without PMT. Liquid scintillator located within center cavity .....	54
4–5	SM2 rods shown with PMT (lower left) and front end electronics (lower right) .....	55
4–6	Three-rod configuration of FNIT SM2. Center-to-center rod separation: (A–C) 15 cm; (B–C) 17.6 cm .....	56
4–7	FNIT SM2 electronic block diagram for double scatter mode. The NIM module electronics for detector 2 are identical to that used for the detector 1 block .....	58
4–8	FNIT SM2 timing diagram in double scatter mode .....	59
4–9	ToF distributions for increasing energy stimuli. Coincident photons from: $^{22}\text{Na}$ (top), $^{60}\text{Co}$ (center); cosmic-ray muons (bottom) .....	62
4–10	ToF $\sigma$ -resolution as a function of electron equivalent energy deposited in separate SM2 rods .....	63
4–11	Spatial resolution along the length of rod: A (red), B (green), and C (blue) .....	64
4–12	Reconstructed positions for collimated source separated by 7 cm .....	65

4-13	Non-uniformity of pulse height for a SM2 rod .....	67
4-14	Three types of $\gamma$ -ray interactions given in terms of $Z$ of the material and incident photon energy (Evans 1955) .....	69
4-15	22-keV photopeak from $^{109}\text{Cd}$ as measured by a FNIT SM2 rod .....	70
4-16	90°-scatter peak from $^{137}\text{Cs}$ as measured by a FNIT SM2 rod .....	71
4-17	Energy resolution (FWHM) vs. energy for FNIT SM2 rods .....	72
4-18	Pulse shape vs. pulse height for detector A .....	75
4-19	PSD distributions for detector A (top), B (center), and C (bottom) .....	76
4-20	Angular Resolution Measurement (ARM) for a continuum neutron spectrum ....	78
4-21	Contribution to the error in the calculated scattering angle derived from errors in pulse height, ToF, and position .....	79
4-22	FNIT SM2 setup in the CNL beam line .....	84
4-23	Schematic display of CNL neutron beam simulation (top). Visualization of simulation conditions within the beam cave. Experiment location (red) and neutron beam (green) are shown (bottom) .....	85
4-24	Neutron beam profile at collimator exit (top), 6 m from exit (center), and the 10-MeV primary neutron angular distribution at 6 m (bottom) .....	86
4-25	Energy (left) and directional (right) distribution of induced background at 6 m ..	88
4-26	FNIT SM2 block diagram in double scatter mode .....	90
4-27	FNIT SM2 orientations with respect to the neutron beam .....	91
4-28	Beam ToF spectrum with no event selections applied .....	93



4-29	Instrument measured ToF for 1.0–2.9 MeV neutrons. $\gamma$ -ray events peak around 0 ns and neutron events are observed with ToF values $>5$ ns. Neutron back scatters can be observed with negative ToF values around $-15$ ns .....	94
4-30	ToF A–C vs. (a) detector A pulse height, (b) detector C pulse height; (c) pulse shape vs. pulse height in detector A, (d) pulse shape vs. pulse height in detector C .....	95
4-31	Beam ToF spectrum with instrumental ToF cuts for (a) neutrons, (b) $\gamma$ rays, (c) PSD <sub>1</sub> vs. PSD <sub>2</sub> with neutron ToF cuts applied, (d) PSD <sub>1</sub> vs. PSD <sub>2</sub> with $\gamma$ -ray ToF cuts applied .....	96
4-32	Beam ToF vs. PSD <sub>1</sub> with: instrumental neutron ToF cuts applied (top) and no instrumental ToF cuts applied (bottom) .....	97
4-33	1.0–2.9 MeV count spectrum and ARM for A–C orientations: $0^\circ$ (a) and (b), $15^\circ$ (c) and (d), $30^\circ$ (e) and (f) .....	100
4-34	1.0–2.9 MeV A–C count spectrum and ARM for A–C orientations: $45^\circ$ (a) and (b), $60^\circ$ (c) and (d), $-15^\circ$ (e) and (f) .....	101
4-35	1.0–2.9 MeV count spectrum and ARM for B–C orientations: $0^\circ$ (a) and (b), $15^\circ$ (c) and (d), $30^\circ$ (e) and (f) .....	102
4-36	1.0–2.9 MeV count spectrum and ARM for B–C orientations: $45^\circ$ (a) and (b), $60^\circ$ (c) and (d) .....	103
4-37	1.8–2.9 MeV count spectrum and ARM for A–C orientations: $0^\circ$ (a) and (b), $30^\circ$ (c) and (d), $60^\circ$ (e) and (f) .....	104

4-38	1.8–2.9 MeV count spectrum and ARM for B–C orientations: 15° (a) and (b), 45° (c) and (d) .....	105
4-39	<1.0–2.9 MeV count spectrum and ARM for A–C orientations: 0° (a) and (b), 30°(c) and (d), 60° (e) and (f) .....	106
4-40	<1.0–2.9 MeV count spectrum and ARM for B–C orientations: 15° (a) and (b), 45° (c) and (d) .....	107
4-41	Instrument measured ToF for 9.1–10.9 MeV neutrons .....	108
4-42	ToF A–C vs. detector A pulse height (left), detector C pulse height (right) .....	109
4-43	(a) Pulse shape vs. pulse height in detector A, (b) pulse shape vs. pulse height in detector C, (c) detector A pulse shape vs. detector C pulse shape .....	110
4-44	(Left) Instrument ToF A–C spectrum with detector A and C PSD cuts applied. (Right) Beam ToF spectrum with detector A and C PSD cuts applied .....	111
4-45	9.1–10.9 MeV count spectrum (left) and ARM (right) for A–C orientation 30° .....	111
4-46	9.1–10.9 MeV (a) count spectrum and (b) ARM for B–C orientation 45°. 17.6–18.9 MeV count spectrum and ARM for A–C orientation 30° (c) and (d), B–C orientation 45° (e) and (f) .....	112
4-47	BC–501 electron equivalent energy to proton equivalent energy conversion data (Mascarenhas 2007) .....	114
4-48	>1 MeV <sub>p.e.</sub> data (from Figure 4–47, blue) plotted with <1 MeV <sub>p.e.</sub> CNL data points and associated errors (red) .....	115

4-49	The ARM as a function of FNIT SM2 orientation with respect to varying energy neutron beams. Detector A (BC-501) with first scatter (black) and detector B (BC-519) with first scatter (red) .....	118
4-50	Single scatter counts in detectors A, B, and C normalized to the total single incident counts in detector A for 1.0-2.9 MeV CNL data .....	119
4-51	A-C (red) and B-C (black) double scatter counts normalized to the total number of double scatter counts recorded from 1.0-2.9 MeV CNL data. BC-501 is the scintillator in the first scatter for A-C and BC-519 is the scintillator in the first scatter for B-C .....	119
4-52	<sup>239</sup> Pu fission neutron spectrum with normalized theoretical distribution shown in red .....	121
4-53	<sup>252</sup> Cf fission spectrum combined from 38 different orientations. The normalized theoretical distribution is shown in red .....	122
4-54	<sup>252</sup> Cf fission neutron spectrum without shielding (red), and with 1-λ of shielding (blue) .....	124
4-55	<sup>252</sup> Cf γ-ray spectrum as measured by FNIT SM2 .....	125
5-1	90° cross-sectional cut out of the simulated FNIT SM2 rod. Liquid scintillator (yellow), borosilicate glass (blue), Teflon (white), aluminum (gray), and vacuum (black) .....	129
5-2	Scatter plot of the calculated scattering angle vs. reconstructed energy for measured (top) and simulated (bottom) neutrons .....	133

5-3	Calculated response for all double scatter events for an on-axis beam with a uniform energy spectrum .....	134
5-4	Calculated response for double scatter events with ToF cuts (top); additional constraints required one elastic n-p scatter in each rod (bottom) .....	135
5-5	The data of Fig. 5-4 with ToF cuts, one elastic n-p and zero n-C total scatters in each rod .....	136
5-6	Response for double scatter neutrons, incident from 30° .....	137
5-7	Response for double scatter neutrons, incident from 45° (top); 60° (bottom) ....	138
5-8	Dithered response for double scatter neutrons, incident from 0° A-C .....	139
5-9	Dithered response for double scatter neutrons, incident from 30° A-C (top), 45° A-C (bottom) .....	140
5-10	Dithered response for double scatter neutrons, incident from 60° A-C (center); 15° B-C (bottom) .....	141
5-11	Dithered response for double scatter neutrons, incident from 45° B-C (top); 60° B-C (bottom) .....	142
5-12	Dithered response for double scatter neutrons, incident from 75° B-C .....	143
5-13	<sup>252</sup> Cf spectra: input (black); uncorrected measured (red); simulated (blue) .....	144
5-14	Simulated data (black) corrected for efficiency (blue) to the input spectrum (red) .....	145
6-1	Neutron emissivity of the 15 June 1991 solar flare as a function of neutron energy, derived from COMPTEL data using a Maximum Entropy	

	de-convolution (lower points) compared to the earlier results obtained using only diagonal elements of the response matrix .....	152
6-2	The cumulative mid-latitude sea level neutron energy spectrum. Results obtained using Tikhonov regularization (circles) and iterative methods (squares) are shown .....	153
6-3	1.0-2.9 MeV neutron beam, A-C (a) 0°, (b) 30°, (c) 45°, (d) 60°; B-C (e) 15°, (f) 45°. Convolved data generated from the model and instrument response, <i>C</i> (red); laboratory measured data, <i>D</i> (black); chi-square value per bin (blue) .....	156
6-4	1.0-2.9 MeV neutron beam, B-C (a) 60°; 1.8-2.9 MeV neutron beam, A-C (b) 0°, (c) 30°, (d) 60°. Convolved data generated from the model and instrument response, <i>C</i> (red); laboratory measured data, <i>D</i> (black); chi-square value per bin (blue) .....	157
6-5	1.8-2.9 MeV neutron beam, B-C (a) 15°, (b) 45°. 9.1-10.9 MeV neutron beam, A-C (c) 30°; B-C (d) 45°. Convolved data generated from the model and instrument response, <i>C</i> (red); laboratory measured data, <i>D</i> (black); chi-square value per bin (blue) .....	158
6-6	<sup>252</sup> Cf count spectrum for A-C orientations: (a) 0°, (b) 30°, (c) 60°; B-C orientations: (d) 15°, (e) 45°, (f) 75°. Convolved data generated from the model and instrument response, <i>C</i> (red); laboratory measured data, <i>D</i> (black); chi-square value per bin (blue) .....	161
6-7	Response matrix singular values (blue), Fourier coefficients (green), and the ratio of the Fourier coefficients to the singular values (red) for response matrix	

at a 30° rotation with 200-keV linear bins (top) and lethargy bins (bottom).

	Plotting tools courtesy of P. C. Hansen .....	163
6–8	De-convolved 1.8–2.9 MeV neutron beam spectrum for (a) ~equal, (b) 2×, (c) 3.5×, (d) 4.5× the number of counts in the data set as is in the 200-keV linear binned response matrix at 30° .....	166
6–9	De-convolved fission neutron spectrum for (a) ~equal, (b) 2×, (c) 3.5×, (d) ~6× the number of counts in the data set as is in the lethargy binned response matrix at 30° .....	167
6–10	De-convolved 1.8–2.9 MeV neutron beam with optimal value of smoothing parameter (red). Variations of (a): 1% (green), 5% (blue), 10% (black); (b): 20% (green), 50% (blue), 100% (black); (c) 1% (green, with relative error in purple), 5% (blue, with relative error in gray); (d) 10% with relative error (blue); (e) 20% with relative error (blue); (f) 50% with relative error (blue) .....	169
6–11	De-convolved 1.8–2.9 MeV neutron beam with optimal value of smoothing parameter (red). Variations of (a) 100% with relative error (blue); (b) –1% (green, with relative error in light green), –5% (blue, with relative error in magenta); (c) –20% (green), –50% (blue), –99% (black); (d) –10% with relative error (blue); (e) –20% with relative error (blue); (f) –50% with relative error (blue) .....	170
6–12	De-convolved fission neutrons with optimal value of smoothing parameter (red). Variations of (left): 1% (green), 5% (blue), 10% (black); (right): 20% (green), 50% (blue), 100% (black) .....	171

6–13	De-convolved fission neutron spectrum with optimal value of smoothing parameter (red). Variations of (a) 1% with relative error in (blue); (b) 10% with relative error in (blue); (c) 20% with relative error in (blue); (d) 20% with relative error in (blue); (e) 20% with relative error in (blue); (f): –1% (green), –5% (blue), –10% (black) .....	172
6–14	De-convolved fission neutron spectrum with optimal value of smoothing parameter (red). Variations of (a): –20% (green), –50% (blue), –99% (black); (b) –1% with relative error in (blue); (c) –10% with relative error in (blue); (d) –20% with relative error in (blue); (e) –50% with relative error in (blue) ....	173
6–15	$\pm 1\text{-}\sigma$ error (black) in the optimal value of the smoothing parameter (red) for the de-convolved: 1.8–2.9 MeV neutron beam (left) and fission neutrons (right)....	174
6–16	Double scatter neutron event in FNIT SM2 producing an event cone .....	175
6–17	$\gamma$ -ray event circle imaging from GRB910503 measured with COMPTEL (Winkler et al.1993) .....	176
6–18	Image of the Sun in 15–80 MeV neutrons from 15 June 1991 X12 flare (McConnell 2010) .....	177
6–19	Event circle imaging (left) and corresponding intensity plots (right) for a 1.0–2.9 MeV neutron beam at 10 m away. For A–C scatters: viewing the source from one orientation of +30° (a) and (b); 0° (c) and (d); $\pm 15^\circ$ (e) and (f) .....	179
6–20	Event circle imaging (left) and corresponding intensity plots (right) for a 1.0–2.9 MeV neutron beam at 10 m away. For A–C scatters: $\pm 30^\circ$ (a) and (b); $\pm 45^\circ$ (c) and (d); $\pm 60^\circ$ (e) and (f) .....	180

6-21	Event circle imaging (left) and corresponding intensity plots (right) for a 1.0–2.9 MeV neutron beam at 10 m away. For B–C scatters: $\pm 0^\circ$ (a) and (b); $\pm 15^\circ$ (c) and (d); $\pm 30^\circ$ (e) and (f) .....	181
6-22	Event circle imaging (left) and corresponding intensity plots (right) for a 1.0–2.9 MeV neutron beam at 10 m away. For B–C scatters: $\pm 45^\circ$ (a) and (b); $\pm 60^\circ$ (c) and (d) .....	182
6-23	Composite image with 3-d view of the image plane for 1.0–2.9 MeV neutron beams from A–C angles varying between $\pm 60^\circ$ in increments of $15^\circ$ .....	183
6-24	Composite image with 3-d view of the image plane for 1.0–2.9 MeV neutron beams from B–C angles varying between $\pm 60^\circ$ in increments of $15^\circ$ .....	184
6-25	2-d view of the image plane for 1.0–2.9 MeV neutron beams from A–C (left) and B–C (right) angles varying between $\pm 60^\circ$ in increments of $15^\circ$ .....	184
6-26	3-d (left) and 2-d (right) views of the image plane for $^{239}\text{Pu}$ neutrons from A–C and B–C events summed together .....	185
6-27	Composite image with 3-d (top) and 2-d (bottom) view of the image plane for fission neutrons from A–C/B–C angles varying between $\pm 90^\circ$ in increments of $5^\circ$ .....	186
6-28	Imaging a source with: 100 event circles (top), 40 event circles (bottom) .....	188
6-29	Imaging a source with: 20 event circles (top), 10 event circles (bottom) .....	189
7-1	Effective $\gamma$ -ray discrimination with ToF cuts .....	191
7-2	Count spectra for fission neutrons with varying levels of selections on PSD ....	192
7-3	ARM for fission neutrons with varying levels of selections on PSD .....	193



7-4	Solar neutron fluence for the 15 June 1991 X12 flare at 10 (red), 20 (green) and 30 (blue) solar radii .....	196
7-5	Reconstructed solar neutron spectrum for the 15 June 1991 X12 flare at 10 (red), 20 (green) and 30 (blue) solar radii with original instrument design .....	197
7-6	Solar Probe Plus spacecraft mass model .....	198
7-7	Background fast neutron flux from primary GCRs for varying positions on the Solar Probe Plus spacecraft .....	199
7-8	Spacecraft mapped out in secondary 1-20 MeV neutrons from the vantage of position 1 .....	200
7-9	Spacecraft mapped out in secondary 1-20 MeV neutrons from the vantage of position 2 (top) and position 3 (bottom) .....	201
7-10	Secondary neutron intensity from a 45° half-angle cone centered on the sunward direction .....	202
7-11	Secondary neutron intensity with selections $\Theta$ : (0°, -30°), $\Phi$ : (-180°, 180°) .....	204
7-12	Secondary neutron intensity with selections $\Theta$ : (-30°, -60°), $\Phi$ : (-180°, 180°) .....	205
7-13	Secondary neutron intensity with selections $\Theta$ : (-60°, -90°), $\Phi$ : (-180°, 180°) .....	206
7-14	Secondary neutron intensity from a 20° half-angle cone centered on the sunward direction .....	208

7-15	Laboratory set up of the NSPECT prototype with three-cells per layer (left), prototype design schematic (right) .....	211
7-16	$^{60}\text{Co}$ ToF (top) and $^{241}\text{Am}$ pulse height (bottom) for a single cell of the NSPECT prototype .....	212
7-17	Count spectrum from fission neutrons measured by NSPECT .....	213
7-18	ARM (top) and image (bottom) for fission neutrons measured by the NSPECT prototype .....	214
7-19	Composite image of $^{252}\text{Cf}$ at four separate locations .....	216
7-20	$^{252}\text{Cf}$ 20° off-axis (top) without strong $\gamma$ -ray source present and (bottom) with strong $\gamma$ -ray source present .....	218

## ABSTRACT

### DEVELOPMENT AND CHARACTERIZATION OF A FAST NEUTRON IMAGING TELESCOPE (FNIT) FOR 1–20 MeV NEUTRONS FROM THE SUN AND NUCLEAR MATERIAL

by

Richard S. Woolf

University of New Hampshire, December 2010

We discuss the development and complete characterization of a double scatter telescope for 1–20 MeV neutrons intended for applications in solar physics and nuclear security. In high-energy solar physics, detecting the presence of low energy accelerated ions in the low corona is recognized as an important goal. The surest indication of the acceleration of these particles is the detection of low energy ( $<10$  MeV) neutrons. These measurements can only be made in the inner heliosphere due to the finite neutron lifetime and flux divergence as they leave the Sun. Additionally, the field of nuclear security has interest in an instrument that can detect, measure, and locate sources of ( $<10$  MeV) neutrons from nuclear material. Materials of interest, namely uranium and transuranics, emit neutrons via spontaneous or induced fission. Unlike other neutral emission from nuclear material, (e.g.  $\gamma$  rays), copious and penetrating neutron emission is unique to fissionable material.

The FNIT instrument was carefully tailored for both applications with a low energy threshold. A double scatter instrument allows for background rejection techniques to obtain increased sensitivity. A small, modular prototype instrument was constructed at

UNH with laboratory calibration completed to tune the pulse height and shape, threshold, and time-of-flight for neutron measurements. Quasi-monoenergetic neutron beams calibrated the prototype over the full energy range and fission neutrons were used to test the response and performance of the instrument.

Simulations characterized the instrument energy response and were used to generate response matrices for data inversion. We used zeroth-order Tikhonov regularization de-convolution algorithms to obtain the true neutron source spectrum for a given regularization (smoothing) parameter,  $\lambda$ . Independent of the binning strategy,  $\lambda$  is of order  $10^{-6}$ . We find that  $\lambda \pm \sigma$  results in a 2% error in total neutron counts; an error within  $\pm 5\text{-}\sigma$  results in a variation of  $\leq 30\%$  in total neutron counts. Double scatter imaging, adopted from  $\gamma$ -ray telescopes, demonstrate source location identification can be obtained. We apply laboratory and simulation information to obtain performance estimates of future instruments near the Sun and in the field.

## CHAPTER 1

### INTRODUCTION

The ability to detect and measure neutrons below 10 MeV is a goal shared by those in the solar physics and nuclear security communities. In solar physics, a lack of <10-MeV data is a problem of distance. The neutron, outside the nucleus, is unstable and subject to  $\beta^-$  decay via the weak nuclear force. The neutron is massive, and its propagation time from the Sun depends on its energy (velocity). Neutrons at low energies experience heavy decay losses. Neutron decay, coupled with divergence as the neutrons radiate from the Sun, results in <10 MeV neutrons being virtually impossible to observe at 1 AU. Understanding particle acceleration at the Sun can be achieved through the measurement of neutral radiation – neutrons and  $\gamma$  rays. Neutrons with an energy >15 MeV have been observed and measured at 1 AU with instruments in Earth orbit and up to several GeV with ground based instruments. These measurements, coupled with  $\gamma$ -ray data from flaring events, provide the information to constrain particle acceleration models, and the total number and composition of accelerated charged particles in the region near the Sun. However a full understanding of the acceleration mechanism for charged particles (protons and ions) requires full knowledge of the intensity, spectrum, and composition of the accelerated particles. The only way to make a direct measurement of low-energy (<15 MeV) neutron emission, and hence gain this full understanding, is to place neutron detection instrumentation close to the Sun.

In nuclear security, problematic quantities of nuclear material, namely uranium and transuranics, emit <10-MeV neutrons via spontaneous or induced fission with the bulk of neutron emission between 1–2 MeV, weakly dependent on the isotope. Unlike other forms of neutral emission from nuclear material (e.g.  $\gamma$  rays), copious and penetrating neutron emission is unique to manufactured nuclear material. Spectroscopic measurements from unknown neutron sources allow one to distinguish between fission and non-fission material, such as the manufactured  $^{241}\text{Am}/\text{Be}$  source – a strong neutron emitter from the mixture of the  $\alpha$  particle emitting actinide (Americium-241) and beryllium.

The instrument detailed in this work is the Fast Neutron Imaging Telescope (FNIT), designed to measure double scatter neutrons in the 1–20 MeV range. To achieve a level of sensitivity necessary to detect and analyze a weak neutron flux, one needs an instrument that measures the full energy of the neutron and rejects background. Full energy measurements are obtained by measuring the energy deposited to a recoil particle in the first scatter summed with the scattered neutron energy derived from time-of-flight measurements. To ensure a neutron's origin – either from the Sun or from nuclear material – an instrument with the capability to reduce background and isolate source location is necessary. A double-scatter neutron telescope is such an instrument. The primary source of neutron background is cosmic rays interacting with matter, producing secondaries. For a terrestrial instrument, cosmic rays bombard the top of the atmosphere and produce hadronic showers, a component of which are neutrons. In deep space, neutron background is produced locally by the interaction of cosmic rays and the

spacecraft material. The expected background flux will vary for space-based and terrestrial instruments depending on the amount and composition of matter (e.g. spacecraft material or atmosphere) in the vicinity of the instrument.

Reconstructed spectral (energy) measurements performed by FNIT are not the true form of the source spectrum one wishes to measure. The true spectrum is related to the measured spectrum by the energy response of the instrument. Through numerical simulations of how the instrument responds to stimulus of a given energy, one may obtain the true spectrum by untangling the instrumental and measurement effects. The problem at hand requires a de-convolution of the measured (count) spectrum using the instrument response. Spectral information is of utmost importance with FNIT and other like double scatter instruments. The methods outlined in this work apply in general to double scatter instruments and can be implemented with future incarnations, whatever form they may take.

In this thesis, we will discuss the characterization of the FNIT instrument and the data analysis algorithms developed for spectral measurements and imaging of neutrons from the Sun or nuclear material. In Chapter 2 we outline the importance of neutron measurements in high-energy solar physics and nuclear security. Chapter 3 reviews neutron interactions with matter and how these interactions are exploited in various detection systems and in FNIT. In Chapter 4 we discuss the complete characterization of the FNIT instrument – the basic underpinnings of the instrument design, the laboratory calibration and testing, neutron beam calibration, and field and laboratory testing with fissionable material measured by liquid scintillators with varying properties. In Chapter 5

we outline our simulation efforts that were undertaken to generate representative data from the FNIT prototype and subsequently used to build energy response matrices. In Chapter 6 we discuss the nature of FNIT data and how it is related to the broad class of inverse and ill-posed problems, the steps taken for spectral de-convolution, and how the precision of the response matrix and smoothing parameter affect the spectral sensitivity. This chapter concludes with a discussion and the results of neutron imaging algorithms applied to FNIT double scatter data. In Chapter 7 we discuss the application of FNIT laboratory results and simulation studies to estimate current and future instrument performance and sensitivity on-board the Solar Probe Plus mission and in an environment outside the laboratory.



## CHAPTER 2

### SOLAR PHYSICS AND THE NUCLEAR MATERIAL PROBLEM

#### **2.1 HIGH-ENERGY SOLAR PHYSICS**

Understanding particle acceleration (both electrons and ions) to high energies is important for solving the solar flare problem. The nature of the acceleration of energetic particles cannot be understood without understanding the large variability in the intensity, spectrum and composition of the accelerated particles. The closest we can come to an unbiased measurement of the energetic proton spectrum at the flare site comes from this secondary neutral radiation – neutrons and  $\gamma$  rays – the parent of which is the accelerated proton or ion spectrum at the flare site. Although substantial observational and theoretical progress has been made during the past few solar cycles, gaining a complete understanding of the acceleration and transport mechanisms for protons and/or ions remains one of the key goals of solar physics research.

Solar flares are the most energetic events in the solar system. The first observations of solar flares dates back to Carrington (1859) and Hodgson (1859). They independently observed an intense brightening in the continuum intensity over the background light of the Sun near a complex grouping of sunspots, known today as a “white-light” flare. While events of this nature are rare, all flares exhibit emission of the hydrogen-alpha ( $H\alpha$ ) (Balmer alpha) line in the optical waveband (Longair 1992). More

detailed observations of solar activity in wavelengths other than optical reveal that these events are transient in nature and exhibit several identifiable phases and strengths, often marked by their X-ray emission that arise from electron bremsstrahlung in the hot, coronal plasma. The characterization of solar flares in terms of H $\alpha$  brightening, resulting from de-excitation of ionized hydrogen in the chromosphere from the third to the second excited state, is divided into the following phases: pre-flare, flash and main phase (Priest 1981). However, an examination at other wavelengths shows an impulsive period at the start of the flash phase during which high-energy radiation is being released “impulsively,” on time scales of seconds or less (Dennis and Schwarz 1989). This impulsive phase is characterized by hard X-ray and  $\gamma$ -ray emission and type III radio bursts, indicating ion and electron acceleration. The impulsive phase is followed by the gradual phase where the high-energy emission decays away exponentially. However, it has been observed in some flares that secondary phases of particle acceleration can extend for many hours, indicating an additional acceleration mechanism (Ryan 2000).

Biermann et al. (1951) and Morrison (1958) first proposed that neutral emission could be produced by the nuclear interactions that take place between accelerated charged particles and the ambient solar atmosphere. The details leading to the nature of the production of neutral emission were later examined by Lingenfelter et al. (1965a; 1965b) and Lingenfelter and Ramaty (1967). Solar neutrons were first inferred from the measurement of the 2.223-MeV neutron capture  $\gamma$ -ray line observed by the NaI scintillator aboard the Seventh Orbiting Solar Observatory (OSO-7) (Chupp et al. 1973; Ramaty et al. 1975). Direct measurement of solar neutrons followed with the Gamma-

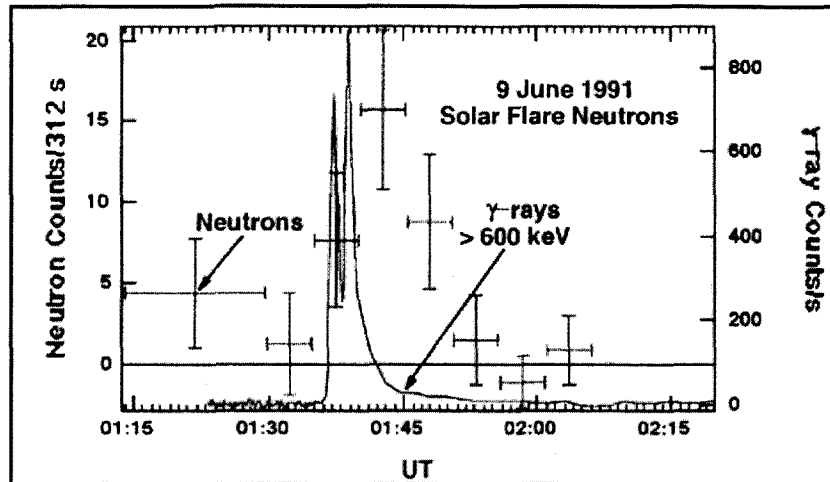


Figure 2–1: With neutron energy measurements, one can back propagate neutrons to the flare site seeing when they were produced with respect to other electromagnetic signatures.

Ray Spectrometer (GRS) aboard the Solar Maximum Mission (SMM) for flares occurring on 21 June 1980 and 3 June 1982 (Chupp et al. 1982; 1987).

Protons and electrons resulting from the decay of solar neutrons (see below) were first predicted by Roelof (1966) and subsequently observed by Evenson et al. (1983); Ruffolo (1991); Dröge et al. (1996). Decay protons provide an additional handle on the neutron spectrum in the 20–200 MeV range and the level of pitch angle scattering occurring in the solar plasma because they are produced with the same direction and velocity as the parent neutron. The intensity of decay electrons provides a measure of the total number of interplanetary neutrons since solar neutrons of all energies yield a similar spectrum of decay electrons (Daibog and Stolpovskii 1987). More recent measurements of solar neutrons have been conducted with the COMPTon TELscope (COMPTEL) (Ryan et al. 1994) and Oriented Scintillator Spectrometer Experiment (OSSE) (Murphy et al. 1999) instruments onboard the space-based Compton Gamma Ray Observatory

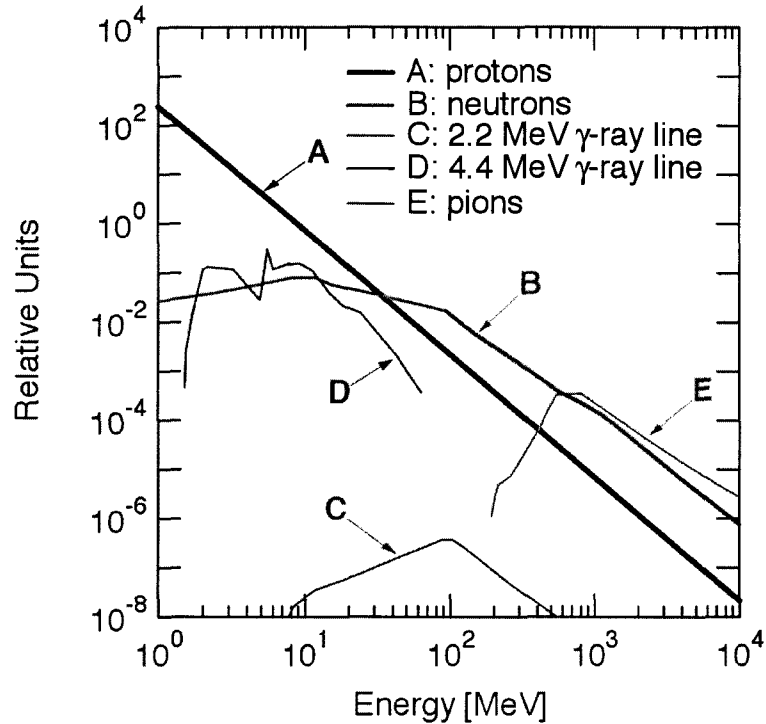


Figure 2-2: Relevant neutron and  $\gamma$ -ray production cross-sections times a proton power law spectrum (Lockwood et al. 1997).

(CGRO) and with ground-based neutron monitors (Debrunner et al. 1983; Efimov et al. 1983; Iucci et al. 1984). These measurements provide insight to the neutron energy spectrum covering  $>15$  MeV from the space-based measurements up to  $\sim$ GeV energies from the ground measurements. Neutrons carry unambiguous temporal and spectral information on the interacting particles at low altitudes. The temporal neutron information must come from the measured arrival time and energy of the detected neutrons, requiring neutron-by-neutron energy measurements to deduce the release time at the Sun. Ryan et al. (1993) showed after removing velocity dispersions, the time-intensity profile of neutron production started at the same time as  $\gamma$ -ray production but

extended for a longer period of time, indicating an additional acceleration mechanism or storage of protons that interact to produce the neutrons (Figure 2–1).

Ultimately the best spectral information is obtained from the joint interpretation and measurement of solar flare  $\gamma$  rays. Neutron and  $\gamma$ -ray measurements are sensitive to different cross-section reactions and spectral regions. Figure 2–2 (Lockwood et al. 1997) shows a falling power law ion spectrum (curve A) of the form  $dJ/dE \sim E^{-2.5}$  and the relevant energies where neutron and  $\gamma$ -ray producing reactions occur. These curves were produced by weighting the average composition of the target material and energetic flare particles (Ramaty 1979) and then folding the total cross-section into the proton spectrum.  $\gamma$ -ray production is sensitive to relatively narrow energy bands, whereas neutron production samples a much larger energy range (Curve B). Curve C is the neutron capture  $\gamma$ -ray line produced from thermal neutron capture by hydrogen to form deuterium and release a 2.223-MeV  $\gamma$  ray in the process. This reaction takes place deep in the chromosphere where the neutron becomes thermalized on timescales in the order of 100 s. Curve D corresponds to nuclear lines from the de-excitation of accelerated heavy ions interacting with ambient solar hydrogen. Curve E samples the high-energy proton spectrum ( $>300$  MeV) from the production of charged and neutral pions. Decaying neutral  $\pi$  mesons produce two 67.6-MeV  $\gamma$  rays, while a continuum spectrum  $>10$  MeV is formed by bremsstrahlung from the charged pions (Murphy et al. 2007). Measuring neutrons and  $\gamma$  rays over a wide energy range can provide information on the bulk metallicity of the energetic ions and the target isotopic composition. As an example, the  $\gamma$ -ray emission from excited nuclei such as Mg can be caused by either protons or  $\alpha$

particles, but heavy nuclei excitation by  $\alpha$  particles will be accompanied by enhanced neutron emission (Moser et al. 2007). Thus, an ion population enhanced in heavy ions will be more prolific in neutron production than for the same  $\gamma$ -ray emission (Chupp and Ryan 2009).

Measurements of the neutron energy spectra and  $\gamma$ -ray line fluences from flares can be compared to calculations and used to help determine or constrain the acceleration mechanism, composition of the ion spectrum and ambient medium and spectral shape. Particle acceleration requires a sufficiently low ambient density so that the acceleration rate exceeds the energy loss (Ramaty et al. 1983). Such conditions can be found in the corona or interplanetary space. It is believed that particles are accelerated when strained coronal magnetic loops dissipate their energy via reconnection. Two main processes have been applied to explain particle acceleration – shock and stochastic acceleration. Charged particle acceleration by DC electric fields has also been investigated. The process of stochastic or second order Fermi acceleration was first proposed (Fermi 1949) as a mechanism for the acceleration of high-energy cosmic rays. In stochastic acceleration the particles randomly gain and lose energy via interactions between uncorrelated magnetic disturbances. The random walk process results in an overall gain in energy and proceeds on rapid time scales, appropriate for the acceleration of ions (Lee 1994). For steady state stochastic acceleration in a region where the diffusion mean free path and escape time are independent of particle energy and species, the accelerated ion spectrum can be described by a Bessel function of second kind in momentum space given as

$$N_i(E) \propto C_i K_2 \left( \sqrt{\frac{12p}{m_p c \alpha T}} \right), \quad (2.1)$$

where  $N_i(E)$  is the number of particles of species  $i$  per unit kinetic energy per nucleon  $E$  with abundance  $C_i$ ,  $p$  is the momentum per nucleon,  $m_p$  is the mass of the proton,  $\alpha$  is the acceleration efficiency proportional to the ratio of the square of the velocity of the scattering centers to the diffusion mean free path,  $T$  is the escape time from the acceleration region, and  $K_2$  is a modified Bessel function. The parameter  $\alpha T$  characterizes the hardness of the spectrum (Ramaty 1979; Murphy et al. 1987). Both the observed and inferred – from neutral emission measurements – non-relativistic proton spectrum can be described by varying the parameter  $\alpha T$  in equation 2.1. Although this mechanism was derived for protons and nuclei in the non-relativistic regime, it can be extended into the region of accelerated charged particles with relativistic energies. To account for the observed ultra-relativistic electron spectrum, as well as the proton and ion spectra, the mechanism of shock acceleration has been implemented.

The process of diffusive shock acceleration (also known as first order Fermi) is where particles gain energy by scattering many times back and forth across a shock front and experience a cumulative acceleration effect during multiple shock encounters (Axford 1981). This phenomena is known to occur in our solar system (planetary magnetospheres) and in the universe (supernovae remnants). In this mechanism with no losses, particles gain energy by scattering freely between converging upstream and downstream plasmas without influencing the shock structure. The accelerated particle spectrum for the case of an infinite and planar shock front and stationary conditions is

described in terms of momentum by a power law of the form of (Ellison and Ramaty 1985)

$$f(p) \propto p^{-\sigma}, \quad (2.2)$$

where  $f(p)$  is the number of particles per volume of momentum space. The quantity  $\sigma$  is the compression ratio,  $3r/(r-1)$ , where  $r$  is the ratio of the upstream ( $u_1$ ) to downstream ( $u_2$ ) bulk plasma flow velocity. Any acceptable acceleration mechanism must account for the accelerated particle energy spectra, total numbers and the observed electron-to-proton ratios (Ramaty and Murphy 1987). Measurements from interplanetary space suggest that both stochastic and diffusive shock acceleration mechanisms are at work, with different data sets showing evidence for either one or the other. Schlickeiser et al. (1993), and references therein, point out that adding momentum diffusion (second order Fermi) with shock acceleration can account for the discrepancies observed in ongoing particle shock acceleration in several astrophysical environments, including: solar flare particle spectra, in-situ particle spectra from cometary bow shocks, synchrotron spectra from shell-type supernova remnants, and synchrotron spectra from extragalactic radio jets. For the scenario when both processes are at work, the stochastic acceleration is taking place downstream of the shock front.

Flare events are generally divided up into two classes, impulsive and gradual, each displaying properties of the different acceleration mechanisms (Reames 1990). Impulsive events are thought to be explained by small flare events where accelerated particles escape from the flare-heated plasma and display a composition rich in heavy ions and have an enhancement of electrons and  $^3\text{He}$  (Reames et al. 1994). Gradual events,



on the other hand, are associated with large flare events that produce coronal mass ejections. Acceleration from the CME shock produces particles that overwhelm the original flux accelerated by the flare (Cliver 1996) and are composed of a low  $^3\text{He}/^4\text{He}$  ratio and small relative abundance of electrons (Kahler 1992). Energetic neutrons produced by flare accelerated ions are not produced isotropically, but tend to be produced predominantly in the direction of motion of the incident ions, so measurement of the neutron flux from solar flares can also provide unique information on the angular distribution of the accelerated ions in flares (Lingenfelter 1994).

Charged particles are accelerated both up (into interplanetary space which may later serve as seed particles in gradual events) and down (to the chromosphere and photosphere) from the top of a flare loop. Protons and ions escape into interplanetary space and encounter low densities that are not efficient for the production of neutrals. This can be described by the so-called thin target model where neutron and  $\gamma$ -ray yields are proportional to the total number of escaping accelerated particles and the amount of matter traversed (Ramaty and Forman 1986). Efficient production of neutrals occurs when the ambient density of the solar atmosphere is high enough to stop particles and nuclear reactions can occur in the so-called thick target model. In the standard solar flare loop model, neutron and  $\gamma$ -ray production occurs deep within the chromosphere at the footpoints of the flare loops. The emission is viewed for events that either take place on the solar disk or the limb. When events are near or over the limb of the Sun, the 2.223-MeV  $\gamma$  rays exhibit limb darkening as a result of Compton scattering in the photosphere (Wang and Ramaty 1974; Kanbach et al. 1975).

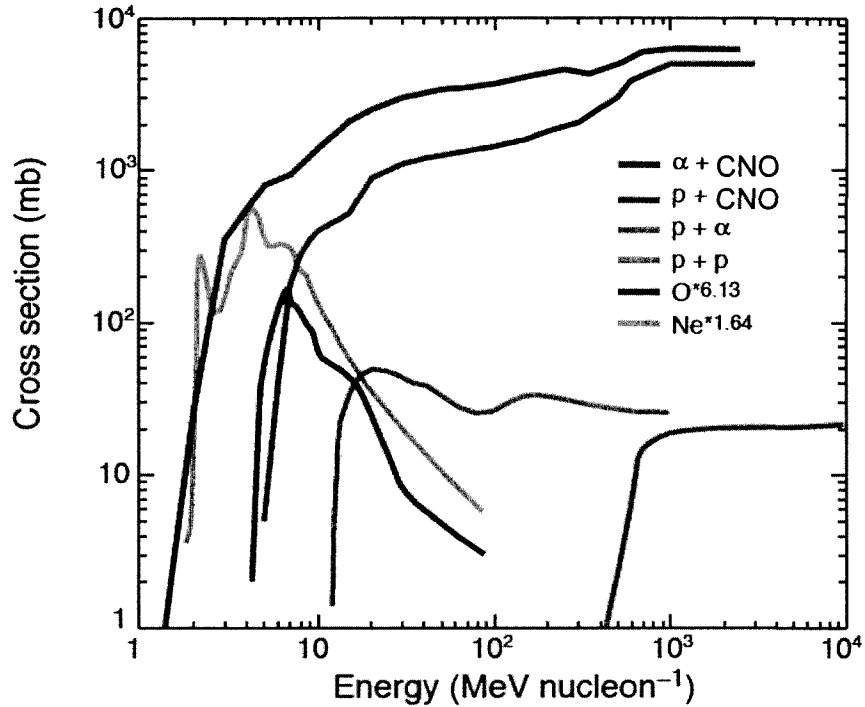


Figure 2-3: Cross-sections for important neutron producing reactions.

Line fluxes from flares give an additional measure of the accelerated ion spectrum and numbers. The neutron capture line at 2.223 MeV not only tells us that neutrons are present, but also yields a measure of the photospheric  $^3\text{He}$  abundance. The capture of a neutron on  $^3\text{He}$  is a radiation-less process; the abundance is deduced by measuring the time-dependent 2.223-MeV  $\gamma$ -ray line flux and calculating the number of neutrons present (Kanbach et al. 1981). Positron emitters decay and react with electrons in the ambient medium to form the  $\gamma$ -ray line at 0.511 MeV. Important  $\gamma$ -ray lines are the nuclear de-excitation lines produced by  $^{12}\text{C}$  and  $^{16}\text{O}$  at 4.438 MeV and 6.129 MeV, respectively. These lines constitute the bulk of the emission in the 4–7 MeV region. Other less intense lines from nuclear de-excitation are from  $^8\text{Si}$  (1.779 MeV),  $^{20}\text{Ne}$  (1.634 MeV)

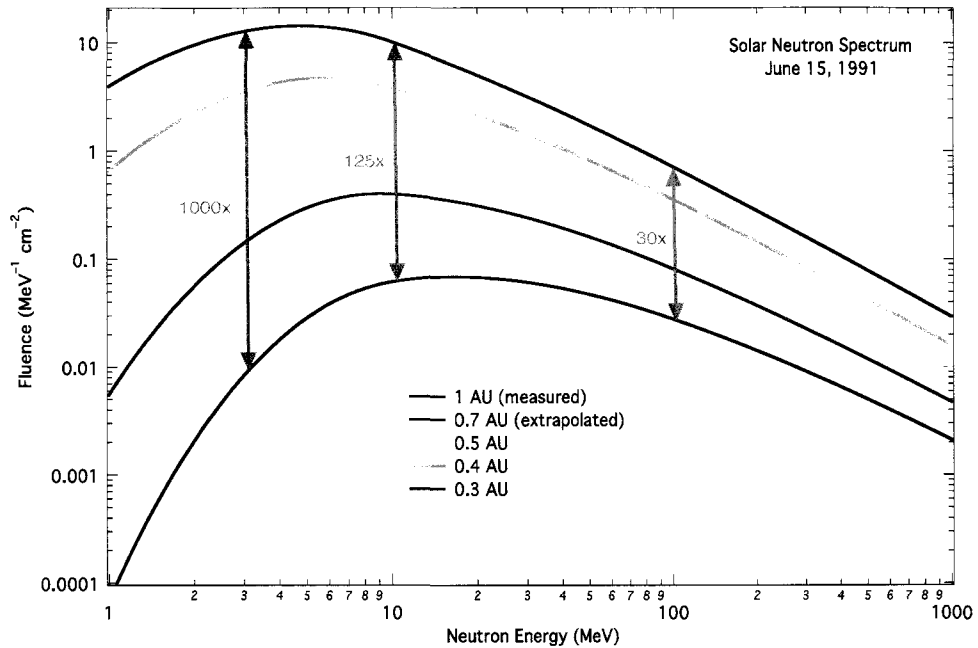


Figure 2-4: Expected neutron fluence for varying heliocentric distance extrapolated from neutron measurements of the 15 June 1991 X12 flare.

,  $^{24}\text{Mg}$  (1.369 MeV),  $^{56}\text{Fe}$  (0.847 MeV),  $^7\text{Li}$  (0.478 MeV), and  $^7\text{Be}$  (0.429 MeV) (Murphy et al. 1991). Line features are superimposed on the solar flare  $\gamma$ -ray continuum caused by electron bremsstrahlung and gyrosynchrotron radiation. Decay of  $\pi$ -mesons form the continuum in the high-energy part of the solar  $\gamma$ -ray spectrum. A sensitive measure to different parts of the accelerated ion spectrum can be determined by taking the fluence ratio of specific energy bands. The ratio of the 2.223 MeV to 4–7 MeV fluence is sensitive to the 10–100 MeV range, whereas the fluence of  $\gamma$  rays from pion production and decay is sensitive to the proton spectrum above 300 MeV (Lockwood et al. 1997).

Neutrons are produced in proton-proton,  $\alpha$ - $\alpha$ , proton- $\alpha$ , and  $\alpha$ -proton reactions and reactions of protons and  $\alpha$  particles with heavier ambient nuclei in their inverse

reactions (Murphy et al. 2007). All of the reactions listed depend on the accelerated ion spectrum and the ambient and accelerated ion composition. The threshold energies for neutron production turns on at a few MeV nucleon<sup>-1</sup> for interactions between  $\alpha$  particles and heavy nuclei (CNO), 5–10 MeV nucleon<sup>-1</sup> for proton and heavy nuclei, 30 MeV nucleon<sup>-1</sup> for proton and  $\alpha$  particles, 10 MeV nucleon<sup>-1</sup> for  $\alpha$ - $\alpha$  and  $\sim 300$  MeV for proton-proton reactions. Simulations show that a soft ion energy spectrum interacting with a target with heavy ion abundance would produce copious neutron emission (Hua et al. 2002).

Neutrons that are produced retain a significant fraction of the incident proton or ion energy and leave the corona unaffected by transient magnetic fields. The free neutron outside the nucleus is unstable and subject to decay via the weak nuclear force. The neutron undergoes  $\beta^-$  decay into a proton, electron, and anti-electron neutrino,



with a finite lifetime of the neutron (at rest) of  $\tau = 885.7 \pm 0.8$  s (Pokotilovski 2010). The probability of a neutron produced at the Sun surviving to a distance,  $r$ , is given by the energy-dependent expression

$$P(E) = \exp\left(-\frac{t}{\gamma\tau}\right), \quad (2.4)$$

where  $t = r(c\beta)^{-1}$ ,  $\gamma\tau$  is the dilated lifetime of the neutron,  $\gamma = 1 + E/m_n c^2$  is the Lorentz factor with  $m_n$  the rest mass of the neutron,  $r$  is the distance traveled,  $\beta = (1 - \gamma^{-2})^{1/2}$ , and

$c$  is the speed of light ( $3 \times 10^8 \text{ m s}^{-1}$ ). Another competing factor to reduce the number of solar neutrons is flux divergence, or  $r^{-2}$  effects, which will heavily reduce the low-energy neutron density at 1 AU. It is for these reasons that low-energy ( $<10 \text{ MeV}$ ) neutrons have yet to be measured. The solution is to have neutron detection capabilities near the Sun. Measurements of this nature would shed light on the “invisible” energetic proton spectrum below a few MeV and the composition of the particles producing the neutrons. It will also help to answer the question regarding which phase of the flare the low-energy neutrons are emitted by making good energy measurements of individual neutrons to remove the effect of velocity dispersion (Chupp and Ryan 2009).

### 2.1.1 CORONAL HEATING

One of the most perplexing and still unanswered questions in solar physics is: what is the cause of the million degree corona? The original X-ray observations of the corona revealed a plasma temperature of  $\sim 1 \times 10^6 \text{ K}$  – a sharp temperature gradient from just above and at the solar surface. Theories as to what contributes to the heating could be, but are not exclusive to: small-scale reconnection flaring events (Parker 1988), dissipation of MHD waves (Jess et al. 2009), or dissipation of magnetic turbulence (Leamon et al. 2000). The small reconnection events, nano- and micro-flaring, like larger flares, are thought to be powered by the relaxation of tangled magnetic fields into a relaxed equilibrium state. Such small flares could accelerate short bursts of MeV ions that range out in the corona or escape into space. As such, they would serve to heat the corona

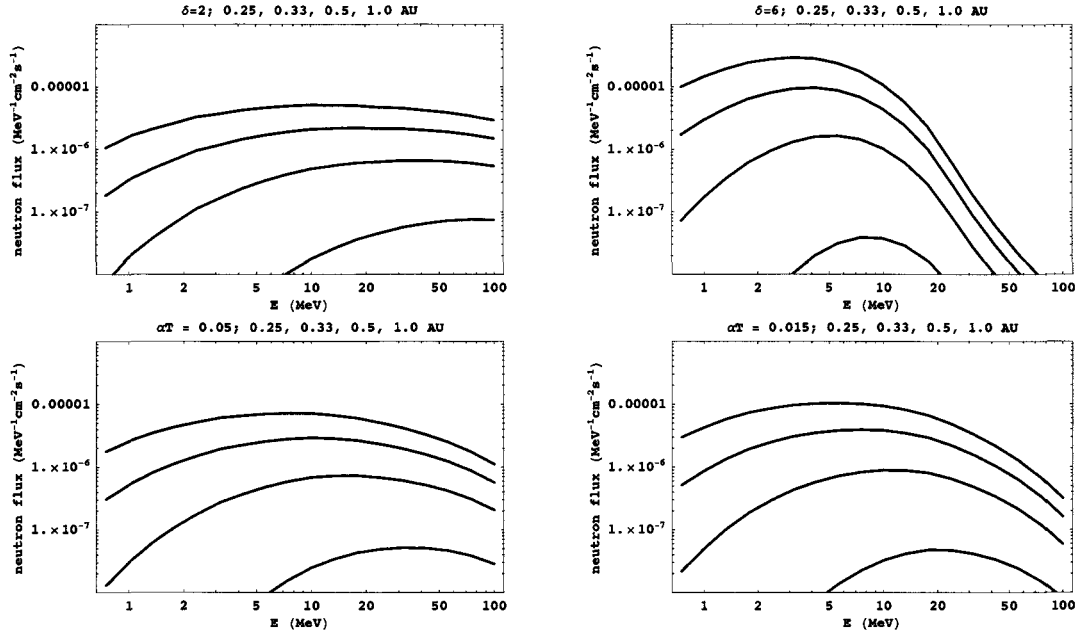


Figure 2–5: Neutron flux and energy distributions at 0.25, 0.33, 0.5 and 1 AU for neutron production dominated by heavy ions (CNO–Fe). Numbers are consistent with the 2.223-MeV line upper limit, for variations of the power law index,  $\delta$ , and the spectral hardness,  $\alpha T$  (as defined on page 11).

via Coulomb collisions and provide a steady stream of seed particles into the interplanetary medium. Their presence could be detectable through quasi-steady low-energy neutron emission, where  $\alpha$  particles and heavier accelerated ions would release neutrons after collisions in the low corona or photosphere (see section 7.1). Impulsive-flare compositions are known to be rich in heavier nuclei. The neutron spectra measured during quiescent periods and from numerous unresolved flares would provide a measure of the number of low and medium energy ions interacting during a solar flare. Combined with the  $\gamma$ -ray data, an energy spectrum and composition profile of the energetic particles would be obtained.

Coronal heating models cannot be supported or refuted by current measurements. There is evidence of micro-flaring in the hard X-ray data; Lin et al. (1984) found that the peak luminosity distribution of flares and micro-flares follows a decaying power law with index of  $-1.8$ . A spectrum with index less than  $-2$  is required for heating from flaring to be significant. Current X-ray observations from the Reuven Ramaty High Energy Solar Spectroscopic Imager (RHESSI) catalog of micro-flaring events (Hannah et al. 2008) supports previous work. However, micro-flaring events cover the range down to  $\sim 10^{26}$  ergs and current observational limits are not sensitive to the supposed, undetectable nano-flaring events. No such evidence has been measured in neutrons or  $\gamma$  rays. McConnell et al. (1997) used data from quiet Sun observations by COMPTEL over a 24-day period to search for the 1–10 MeV  $\gamma$ -ray nuclear line emission. The results placed a  $2\text{-}\sigma$  upper limit on the quiescent  $\gamma$ -ray flux of  $2.1 \times 10^{-5} \text{ } \gamma \text{ s}^{-1} \text{ MeV}^{-1}$ . Similar tests finding consistent numbers were also conducted to place limits on the quiescent Sun flux with data from SMM/GRS (Harris et al. 1992) and the High REsolution Gamma-ray and hard X-ray Spectrometer (HIREGS) balloon instrument (Feffer et al. 1997). Based on this number MacKinnon and Ryan (2010) derived the upper limit quiet time neutron flux constrained by the upper limit found by McConnell et al. (1997). The shape and spectral characteristics for accelerated ions is unknown for small flaring events. If one assumes scaling from larger flares, then Figure 2–5 shows the anticipated neutron flux for varying distances from the Sun and the parameters of the accelerated ion spectra. An instrument with detection capabilities below 10 MeV could lead to the discovery of neutrons during periods of little or no apparent solar activity.

### 2.1.2 RELEVANCE TO INNER HELIOSPHERIC MISSIONS

A mission to the inner heliosphere to make in situ measurements in the low corona are needed to help address some of the issues previously mentioned. These measurements are paramount for a complete understanding of energetic ions in the corona. Our current knowledge is limited by the sensitivity and threshold to  $\gamma$ -ray lines that have been measured from 1 AU; a neutron spectrometer with  $\gamma$ -ray detection capabilities would achieve a lower threshold and a gain in the sensitivity. Currently, only a fraction of the full picture of the Sun is understood from neutron and  $\gamma$ -ray measurements made by previous instruments from large (bright) events. More sensitive measurements will allow for a greater observational database, and would enhance the current understanding of the processes in the low corona. Several near Sun missions have been outlined, including NASA's Solar Sentinels and the European Space Agency's (ESA's) Solar Orbiter. While the Solar Sentinels and Solar Orbiter missions have a planned perihelion of approximately 0.2–0.3 AU, a mission with a perihelion of a few solar radii was envisioned as early as the 1950s. Although ambitious, a mission this close to the Sun is difficult given the harsh environment and the consequent cost and technology needed. The original mission concept – NASA's Solar Probe – was to pass within four solar radii on a single shot flyby. This idea was reworked in 2008 into a new concept – Solar Probe Plus. The new mission and orbital plan would take the spacecraft to within ten solar radii at perihelion and make multiple solar passes for more observation time within 30 solar radii. At the time of completion of this work, the Solar Probe Plus mission is slated for



launch between 2015–2018 and reach perihelion 6.9–7.7 years after launch depending on the number of Venus gravity assists needed to achieve its final orbit (The Johns Hopkins University Applied Physics Laboratory 2008). The announcement of opportunity for inner heliospheric missions outlines a neutron/ $\gamma$ -ray spectrometer as one of the instruments in the strawman payload design. The mass and power for a mission instrument will be stringent, but an instrument designed to limit the background and provide a good energy measure would be able to achieve sensitivity to low energy neutrons. This would allow for the measurement of more neutron events  $\leq 10$  MeV, investigate ion acceleration and energy content  $\sim 10$  MeV for smaller magnitude flares, test whether ion acceleration in most flares occurs down to much lower thresholds, and connect low-energy neutron measurements and energetic particle information to study the link between interacting and escaping particles and ridding the transport effects encountered in the solar atmosphere (Vilmer and Maksimovic 2001). Proximity to the Sun will also aid in  $\gamma$ -ray detection sensitivity of weak flares and the  $\gamma$ -ray flare emission that could present itself during quiet times. Extended observation time near the Sun would allow for observation over a large fraction of the total solar cycle and the variation of the neutron emission.

## **2.2 NUCLEAR SECURITY**

### **2.2.1 HISTORICAL AND MODERN PERSPECTIVE**

The first experiments to understand the reactions involving the atomic nucleus date

back to the early part of the twentieth century. Work at the Cavendish laboratory by Ernest Rutherford demonstrated the transmutation of light elements and work by John Cockcroft and Ernest Walton demonstrated the splitting of the atom was possible. Later work by Enrico Fermi suggested that heavy elements could be split into lighter elements when struck by the then recently discovered neutron (see Chapter 3). Radiochemists Otto Hahn and Fritz Strassmann experimented with neutron bombardment of uranium that led to the splitting of the heavy nucleus into lighter nuclei with an accompanied release of energy explained by Einstein's relation of mass-energy equivalence. Lise Meitner and Otto Frisch surmised that these results could be explained by the liquid drop model of the nucleus proposed by Niels Bohr. In this model, a heavy nucleus would absorb a free neutron causing it to oscillate and divide. Frisch experimentally confirmed that a large amount of energy is released upon each fission corresponding to  $\sim 200$  MeV/atom, far exceeding the free energy released in chemical reactions ( $\sim 1$  eV) (Serber 1992).

Using this new found technology for the purpose of a weapon followed shortly thereafter during World War II. On 16 July 1945 the US performed the first nuclear weapon test called Trinity, followed by war time use less than three weeks later. Each weapon detonated had an explosive yield of  $\sim 20$  kilotons (the explosive yield of one ton of TNT equivalent is 4.2 gigajoules). After the war ended, it was believed that atomic energy could be used for the non-destructive purpose of energy generation. As nuclear power plants began to emerge in the mid-1950s, the United Nations established the International Atomic Energy Association (IAEA) to regulate the development and use of nuclear material in 1957. The United Nations established the Nuclear Non-Proliferation

Treaty (NPT) in 1968, thereby assigning the IAEA to place safeguards on nuclear material to be used only for peaceful purposes. A potential source of risk that the IAEA regulates is the by-product spent nuclear fuel from reactors. A serious risk is posed with the improper storage or safeguarding of the nuclear waste material. The ability to efficiently detect and identify problematic quantities of nuclear material is needed to close the critical gap in the nuclear security infrastructure. In the next section we discuss why neutron detection is of particular importance for nuclear material detection and monitoring.

### 2.2.2 NUCLEAR MATERIAL

Nuclear fission is the process by which a heavy nucleus splits either via induced or spontaneous fission. A heavy nucleus that can split into two lighter elements when struck by a fast neutron is said to be fissionable, e.g.,  $^{232}\text{Th}$  and  $^{238}\text{U}$ . Nuclei that fission when struck by a slow or thermal neutron are fissile, these are:  $^{233}\text{U}$ ,  $^{235}\text{U}$ , and  $^{239}\text{Pu}$ . Uranium (U) is a naturally occurring element on Earth, but the majority of U found on Earth is in the form of  $^{238}\text{U}$  with 0.7%  $^{235}\text{U}$ .  $^{233}\text{U}$  is formed by neutron bombardment of  $^{232}\text{Th}$ . Plutonium (Pu) is not found in nature due to its comparatively short half-life with respect to the age of the Earth. Pu was first produced inside the University of California – Berkeley reactor by Edwin McMillan and Glenn Seaborg in 1940 through the process of neutron capture by  $^{238}\text{U}$  during neutron bombardment. A slow neutron is captured by  $^{238}\text{U}$  to form  $^{239}\text{U}$  which then  $\beta^-$  decays in the nucleus to form  $^{239}\text{Np}$ . With a half life of 2.4

days,  $^{239}\text{Np}$  then decays into  $^{239}\text{Pu}$ , an electron and an anti-electron neutrino. In spontaneous fission the nucleus splits on its own without the assistance of another neutron. The lightest nuclei where the probability of spontaneous fission becomes significant – the point at which the mutual Coulomb repulsion of the protons exceeds the attractive nuclear force – occurs in certain uranium isotopes (Povh, et al. 2004). Nuclei that decay via spontaneous fission are strong emitters of neutrons through an evaporation process. Nuclear evaporation can be thought of statistically as the emission of a neutron from an ensemble of excited particles held in a potential well with a binding energy of  $\sim 8$  MeV. For nuclei with many particles, a statistical approach can be used to analytically describe the energy spectrum of emitted neutrons as a Maxwellian distribution with an exponential fall-off characterized by the nuclear temperature,  $T$ . Each escaping neutron carries away an average energy of  $\sim 2kT$  where  $k$  is Boltzmann's constant. The nucleus continues to emit neutrons while the excitation energy is above the neutron binding energy within the nucleus. Once below the threshold for neutron emission, the nucleus decays by  $\gamma$ -ray emission (Fermi 1950). The numbers released upon each fission is, on average,  $\sim 2\text{--}3$  neutrons and  $\sim 7$   $\gamma$  rays. The exact numbers will vary depending on the isotope (Povh, et al. 2004). These are prompt neutrons and  $\gamma$  rays and are released  $\sim 10^{-14}$  s after fission.

Liberated neutrons that are not captured or escape are likely to interact with other nuclei and induce fission. This process repeats and a chain reaction can be maintained if a *critical* amount of mass is present. Nuclear power generators rely on a steady, controlled chain reaction by maintaining a critical mass of fissile material as opposed to an

explosive device, i.e., an uncontrolled, exponentially growing chain reaction.

Nuclear fuels are categorized according to the percentage of fissile isotope in a given substance. Uranium is classified into three categories: natural ( $^{238}\text{U}$ : 99.3%,  $^{235}\text{U}$ : 0.7%), reactor-grade or low-enriched ( $^{235}\text{U}$ : ~3–5%), and weapons-grade or highly-enriched ( $^{235}\text{U}$ : ~90%). The uranium that is left over after enrichment is referred to as depleted uranium and can be used as a tamper (neutron reflector). The main constituent isotopes of the plutonium produced in reactors are:  $^{239}\text{Pu}$  and  $^{240}\text{Pu}$ . Other isotopes are also present in trace amounts, i.e.,  $^{238}\text{Pu}$ ,  $^{241}\text{Pu}$ , and  $^{242}\text{Pu}$ . Plutonium classification system is given as: super-grade ( $^{239}\text{Pu}$ : 98%,  $^{240}\text{Pu}$ : 2%), weapons-grade ( $^{238}\text{Pu}$ : 0.012%,  $^{239}\text{Pu}$ : 93.8%,  $^{240}\text{Pu}$ : 5.8%,  $^{241}\text{Pu}$ : 0.35%,  $^{242}\text{Pu}$ : 0.022%), and reactor-grade ( $^{238}\text{Pu}$ : 1.3%,  $^{239}\text{Pu}$ : 60.3%,  $^{240}\text{Pu}$ : 24.3%,  $^{241}\text{Pu}$ : 9.1%,  $^{242}\text{Pu}$ : 5%) (Mark 1993). The highly processed fuel is obtained by isotopic separation, usually accomplished by diffusion, or through the use of a centrifuge or lasers. Nuclear material separated such that the main constituent of the fuel is weapons- or reactor-grade poses a risk if proliferated through protective security points and used in the configuration of an explosive device.

Possible entrance points of illicit nuclear material are: shipping ports, railways, and vehicle border crossings. Ports pose a risk considering that 90% of US imports are in containers and arrive by sea at the rate of nearly 10 million per year (Slaughter et al. 2007). Effective and efficient interdiction of this material is necessary with an instrument that can make spectroscopic measurements of neutrons with  $\gamma$ -ray detection capabilities to differentiate between source and natural background. Imaging capabilities can be used to locate the source inside the transport vehicle. The two main methods for the detection

of nuclear material are: passive detection and induced fission with an active interrogation.

In passive detection, a detector is located at a given distance away and monitors for a specific radiation signature. This method is more advantageous for Pu detection since isotopes of Pu undergo spontaneous fission far more readily than isotopes of U, leading to much higher rates of neutron emission. Therefore reactor-grade Pu (with higher concentration of  $^{240}\text{Pu}$ ) can be detected passively from a greater standoff distance. Current detection systems in the field have not changed significantly in the last few decades. Bonner spheres (Bramblett et al. 1960) have been used to detect neutrons only after moderating them, destroying information on the neutron energy spectrum and the incident direction (see section 3.2).

Induced fission not only produces prompt fission events, but delayed radiation emission. An active interrogator can be used to induce fission in nuclear material yielding a flux of neutrons and  $\gamma$  rays that depends on the neutron flux from the interrogator and the time of interrogation. In a reactor, delayed neutrons are integral to the operation as they increase the reactor period and allow for easier control of the reactions. The radioactive decay of fission products occurs in a characteristic time of a few seconds to minutes. The delayed neutron emission per fission is: 0.008 for  $^{239}\text{Pu}$  and 0.017 for  $^{235}\text{U}$  (Slaughter et al. 2005). An interrogator can induce fission with fast neutrons (14-MeV neutron generator from a deuterium–tritium (D–T) fusion reaction) or thermal neutrons (in tandem with a moderating material or through a (p, n) reaction). Photon-induced fission (photo-fission) has been used in the past for active methods but the flux created is typically less than that from neutron interrogation.

A neutron interrogator is a pulsed beam of neutrons that can operate with duty cycles of nanoseconds to seconds. After pulsing the area of interest, the signature of the delayed emission is sought out with passive neutron and/or  $\gamma$ -ray detectors.

In both passive and active interrogation, a competing factor in the detection window is the natural background. For distances of  $<100$  m – after which attenuation in air becomes significant – the distance,  $r$ , at which the source signal and the background signal are equal can be expressed as

$$r = \sqrt{\left( \frac{A_s \varepsilon_s S}{4\pi A_b \varepsilon_b b} \right)}, \quad (2.5)$$

where  $A_s$  and  $A_b$  are the areas of the detector for detecting the signal and the background [ $\text{m}^2$ ],  $\varepsilon_s$  and  $\varepsilon_b$  are the efficiencies for detecting the signal and background,  $r$  is the detector–source distance,  $S$  is the source strength [particles  $\text{s}^{-1}$ ], and  $b$  is the average background rate [particles  $\text{m}^{-2} \text{s}^{-1}$ ]. The background rate near the detector can be reduced if shielded, however, one can wait until the signal from the source is greater than the statistical fluctuations in the background. The size of the fluctuation in background grows as  $t^{1/2}$ , while the source signal grows linearly (Fetter et al. 1990).

Because free neutrons are rare in nature, the main source of neutron background is caused by the interaction of cosmic rays with atmospheric nuclei. Omni-directional background neutron flux calculations show that on average, one should expect  $5 \times 10^{-3}$  n  $\text{s}^{-1} \text{cm}^{-2}$  at sea level with slow excursions due to solar activity and a dependency on both latitude and altitude (Moser et al. 2005). Depending on the site, a competing neutron

background could be the so-called ship effect (Kouzes et al. 2007) due to cosmic-ray interactions in surrounding vehicles and environment. This effect enhances the background neutron rate as a result of cosmic rays interacting with high- $Z$  material near the detector. It is therefore important to have the ability to reduce the overall neutron background rate to limit these events. The  $\gamma$ -ray background flux is over 1000 times greater than the neutron background (Fetter et al. 1990) with contributions from natural radioactivity and an effect called skyshine (Kouzes et al. 2008). Line features in the background spectrum are caused by the radioactive decay of elements naturally found within the Earth's crust, such as  $^{40}\text{K}$  and  $^{238}\text{U}$ . In the absence of  $\gamma$ -ray lines the presence of background counts can be enhanced by the effect of skyshine where radiation above the detector system is scattered by air and redirected downward. Skyshine can have an effect from several hundreds meters away by locally increasing the count rate in radiation detectors.

The Fast Neutron Imaging Telescope outlined in this work has the ability to measure individual neutron energies on an event-by-event basis and construct a spectrum below 10 MeV. Fast and reliable neutron detection rests on the instrument ability to achieve directionality for rejecting background, thereby increasing sensitivity. In the next chapter we will discuss the type of instrument for performing the aforementioned tasks to contribute to solving the solar physics and nuclear material problems.



## CHAPTER 3

### NEUTRON PHYSICS

The existence of the neutron was experimentally confirmed in 1932 by James Chadwick. When beryllium is bombarded by  $\alpha$  particles (produced by the decay of a heavy radioactive element), it was observed that a quantum of neutral emission was released in the process. Initially Joliot-Curie suggested that the emission was  $\gamma$  radiation with an energy of  $\sim 50$  MeV. Invoking conservation of energy, Chadwick realized that this singular quantum – the neutron – had an energy of  $\sim 5-7$  MeV, a mass nearly equal to that of a proton and no net charge (Chadwick 1932).

It is now well-known that the neutron has a mass, measured in mass-energy equivalent units, of:  $939.565346 \pm 0.000023$  MeV  $c^{-2}$  or  $1.00866491597 \pm 0.00000000043$  atomic mass units (u) where  $1 \text{ kg} = (6.02214179 \pm 0.000000030) \times 10^{26}$  u. The neutron has a greater mass than that of the proton with a difference ( $\Delta m = m_n - m_p$ ) of:  $1.29333214 \pm 0.00000043$  MeV (Amsler et al. 2008). The neutron is baryonic matter consisting of three quarks (up, down, down) with a spin =  $1/2$ ; it is a fermion and subject to Fermi-Dirac statistics and thus the Pauli exclusion principle. Because the neutron is composed of constituent quarks it has a magnetic moment with the value of:  $-1.9130427 \pm 0.0000005$   $\mu_N$ , where  $\mu_N$  is the nuclear magneton with a value of:  $(5.05078324 \pm 0.00000013) \times 10^{-27}$  J  $T^{-1}$ . The value of the magnetic moment of a particle determines

how it interacts with a magnetic field and the sign determines how its spin axis aligns with the magnetic field. Neutron energy regimes are classified as: cold ( $<1$  meV), thermal ( $\sim 0.025$  eV), epithermal ( $\sim 1$  eV), slow ( $\sim 1$  keV), and fast (100 keV – 10 MeV). The design of an instrument for the detection of neutrons relies on the physics of how neutrons interact with matter over a wide range of energies. Throughout this chapter we investigate the main modes of interaction of neutrons with matter, detection methods, and the principles of the FNIT.

### **3.1 NEUTRON INTERACTIONS**

Neutron interactions with the nucleus occur via the strong nuclear force. The short range of the strong nuclear force implies that a neutron must come within  $10^{-15}$  m of the nucleus to undergo an interaction – the de Broglie wavelength of a fast neutron. Neutron-nucleus interactions occur through either scattering or absorption. Scattering can proceed through either a direct reaction – elastic scattering with the nuclear potential – or through a resonance reaction – elastic and inelastic – characterized by the formation of a compound nucleus. Absorption of a neutron by the nucleus is a resonance reaction that can occur through either: capture (radiative or charge particle) or cascade reactions.

The probability of an interaction occurring between a neutron and a target nucleus depends on the effective cross-sectional area of the target, determined by the strength, shape and range of the interaction potential. The physical quantity used to describe the probability of a reaction is the cross-section. The cross-section has units of area,

represented by the barn, defined as: 1 barn =  $10^{-24}$  cm<sup>2</sup> (Povh, et al. 2004). The cross-section is expressed as either microscopic ( $\sigma$ , interaction of neutrons with a nucleus or particle) or macroscopic ( $\Sigma$ , interaction of neutrons with bulk matter). The total microscopic cross-section,  $\sigma_t$ , is the sum total of the interaction modes with the probability dependent on the target and energy of the incident neutron. The concept of the macroscopic cross-section can be used to experimentally determine the value of the total microscopic cross-section. By comparing the intensity of incident neutrons to the intensity of neutrons that pass through a material of thickness  $x$

$$I = I_0 \exp\left(-\frac{x}{\lambda}\right), \quad (3.1)$$

for a number density of atoms per cm<sup>3</sup>,  $N$ , the total macroscopic cross-section is given as  $\Sigma_t = N\sigma_t$  and  $\lambda = 1/\Sigma_t$  is the neutron mean free path through the material (Rinard 1991) .

Direct neutron-nucleus interactions occur when the neutron is in the vicinity of the nucleus – of order  $10^{-22}$  s – such that the formation of a compound nucleus does not occur. We first consider the neutron elastically scattering from a nuclear potential,  $V(r)$ . The incoming neutron and outgoing neutron after scattering from the potential is represented by the sum of the total wave function as:  $\psi(r, \theta) = e^{ikz} + f(\theta)e^{ikr}$  where the wave representation of the neutron is given by  $e^{ikz}$  for an incoming plane wave and  $e^{ikr}$  for an outgoing spherical wave. In scattering theory the differential cross-section – the probability of a neutron to scatter through a given solid angle – is given by the square of

the scattering amplitude,  $f(\theta)$ . It is expressed via a partial wave analysis for elastic scattering in the center-of-mass frame by

$$\frac{d\sigma}{d\Omega} = |f(\theta)|^2 = \left| \frac{1}{2ik} \sum_{l=0}^{\infty} (2l+1) P_l(\cos\theta) (1 - e^{2i\delta_l}) \right|^2, \quad (3.2)$$

where  $P_l(\cos\theta)$  are the Legendre polynomials,  $l$  is the angular momentum number,  $k$  is the wave number, and  $\delta$  is the phase shift. For a spherically symmetric potential,  $l = 0$ , integrating over the spherical volume yields the total cross-section,  $\sigma = 4\pi|f(\theta)|^2$ . By matching the boundary conditions at the nuclear surface and re-expressing equation 3.2 in terms of the scattering length,  $a$  – related to the negative reciprocal of  $k \cot(\delta)$  in the limit that  $k \rightarrow 0$ , the elastic  $S$ -wave (low-energy) scattering cross-section takes the form

$$\sigma_{elastic} = 4\pi \left| \frac{e^{ikR} \sin(kR)}{k} + \frac{1}{ik + 1/a} \right|^2, \quad (3.3)$$

where  $R$  is nuclear radius, proportional to the cube root of the atomic mass number,  $A = Z + N$ . For pure elastic potential scattering, equation 3.3 reduces to the case of hard-sphere scattering – four times the geometrical area ( $4\pi R^2$ ) – equivalent to classical particles bouncing off a hard sphere each with equal radii,  $R$ . For elastic neutron-proton scattering, the values for the cross-section monotonically decrease from 20 barns at 1 keV to 0.5 barns at 20 MeV. This is the case for which the scattering is purely potential and the neutron does not enter the nucleus. Reactions for potentials with the angular momentum,

$l, \neq 0$  require a multiplicative correcting term in the cross-section to account for spin of the incident neutron and angular momentum of the target nucleus.

In resonance scattering, the internal structure of the nucleus plays an important role in the scattering process. Resonance scattering occurs through the formation of a compound nucleus that forms when a neutron interacts with the nucleus and forms an excited state that is (relatively) long-lived,  $\sim 10^{-17}$  s. While direct elastic scattering can always occur, the compound nucleus can form only if the sum of the kinetic energy of the incident neutron and the binding energy are equal to or greater than the lowest excitation level (Beckurts and Wirtz 1964). Resonance results in sharp maxima in the cross-section for an incident neutron with the precise energy to promote the nucleus into an excited state. The energy-dependent cross-section for the formation of a compound nucleus, through a single-level resonance, is described by the Breit-Wigner formula as

$$\sigma(a,b) = \frac{\lambda^2}{4\pi} (2l+1) \left( \frac{\Gamma_a \Gamma_b}{\Gamma^2/4 + (E - E_0)^2} \right) \left( \frac{\Gamma_b}{\Gamma} \right), \quad (3.4)$$

where  $a$  is the incident particle,  $b$  is the outgoing particle, and  $\lambda$  is the deBroglie wavelength in the center-of-mass frame. The finite lifetime of a compound state, before it decays, depends on its total width due to energy uncertainty,  $\Gamma (= h/2\pi\tau)$ , given in units of electron-volts (Bethe and Morrison 1956). The total width is a sum of the partial widths for all possible decays modes of the compound nucleus. Decay from excited energy levels occurs in a variety of ways and is used to explain the associated emission observed from scattering and absorption reactions. The ratio of the partial width for a particular

reaction to the total width gives the probability that the compound nucleus will decay by that process. This expression does not apply to elastic scattering due to interference and coherence between the phase shifts of the incoming and outgoing wave representations of the neutron. In elastic resonance scattering the ratio of the partial to the total width ( $\Gamma_a/\Gamma$ ) results in  $\Gamma^2$ , but this requires that there is no contribution from potential scattering (Evans 1955). In the case where there is a contribution, the effects reduce to equation 3.3 and the results that follow.

The non-relativistic neutron energy varies as the square of the neutron velocity,  $v$ . Cross-section data as a function of energy shows a  $1/v$  behavior in the cross-section for increasing energy. Isolated resonances corresponding to excited virtual energy levels of the compound nucleus are superimposed on the  $1/v$  dependence. Depending on the atomic number of the nucleus, the shape of the cross-section varies as expected from a  $1/v$  law cross-section at low energy with resonance reactions occurring at higher energy. Heavy nuclei exhibit resonances at lower energy than lighter nuclei. When energy levels are spaced out such that the width of the resonances ( $\Gamma$ ) are well separated, the cross-section exhibits behavior with sharp, separated peaks. A continuum is observed in the cross-section data when closely spaced resonance widths overlap.

Inelastic scattering is when the target nucleus intercepts an incident neutron and excites the target into a higher energy state. The nucleus decays by emission of a neutron – with less energy than the incident – and  $\gamma$  rays or charged particles. Inelastic scattering is a threshold reaction that requires the incident neutron to have enough energy to excite

the nucleus into a higher energy level. Elastic scattering is the limiting case of neutron-nucleus scattering for the product nucleus remaining in the ground state.

Absorption reactions occur by the formation of a compound nucleus that decays by either  $\gamma$ -ray, charged particle or neutron emission. The nucleus can absorb a thermal neutron with no threshold for this reaction to occur and emit a  $\gamma$  ray with an energy corresponding to the binding energy in the nucleus. This is observed as a neutron capture line. The number of  $\gamma$  rays emitted and whether or not line structures in the spectrum are present depends on the target nucleus in the reaction. Charged particle emission from the compound nucleus occurs most commonly via the release of a proton or an  $\alpha$  particle, or in some cases, a deuteron. The charged particle is held within the nucleus by the attractive potential of the strong nuclear force with a probability of escape from the potential depending on the probability that the particle will penetrate the Coulomb barrier. These reactions have large reaction cross-sections at low energies.

Cascade reactions as a result of absorption are classified as multiplication and fission reactions. In cascade reactions a neutron strikes a heavy nucleus and causes the emission of several neutrons or neutrons and charged particles. Reactions of the form  $(n, 2n)$  are most probable for incident neutrons with energies  $<20$  MeV and can occur with the elements of  $^{12}\text{C}$ ,  $^9\text{Be}$ ,  $^4\text{He}$ , and  $^2\text{H}$ . Other notable multiplication reactions can occur via  $(n, np)$  or  $(n, nt)$ . The details of fission reactions were given in section 2.2.2 as they related to nuclear material. As with other absorption reactions, the fission reaction results from the formation and decay of a compound nucleus. The binding energy per nucleon in the range of uranium and plutonium is  $\sim 7.5$  MeV/nucleon, or  $\sim 0.9$  MeV/nucleon greater

than the compound nucleus in the range of mass numbers from 40 to 150. Fissionable elements contain upwards of 230 nucleons, resulting in an energy release of  $\sim 200$  MeV. The fission cross-section in the low-energy regime deviates from an expected  $1/v$  law and cannot be reproduced by simply summing the resonances in the Breit-Wigner formula (Foderaro 1971). In the next section, we will examine how the scattering and absorption processes are implemented in neutron detection technology.

### **3.2 NEUTRON DETECTION**

Neutrons are neutral particles and therefore not subject to interactions via the electromagnetic (Coulomb) force. Unlike charged particles, neutrons do not produce ionization in a medium as they pass through it. Thus, they can traverse the medium relatively unimpeded. Consequently, neutrons must be detected by indirect means, namely by interacting with a medium such that a measurable quantity is produced and can be detected with an appropriate apparatus. The instrument used should be dictated by the neutron energy range to be detected because some instruments are optimized for slow neutrons, some for fast neutrons and some overlap to cover the full energy range. One must also consider the detector size and application for desired efficiency. Neutron measurements are often associated with a high  $\gamma$ -ray background, so the ability to discriminate between the two is important for achieving a sensitive measurement. Several types of detector materials have been used for measurements of slow and fast neutrons in the past and are in current use today. These include ionization chambers, proportional



counters, and scintillators. Neutron detection techniques rely on either the scattering or absorption reactions discussed in the previous section.

Proton recoil gaseous proportional counters are often composed of either hydrogen or methane (Pinchenot et al. 2002). An incident neutron scatters from a proton and the proton energy loss is measured to determine the neutron energy (Takeda et al. 1999) assuming a full energy transfer to the proton. The electrons – produced as a result of proton ionization – drift in an applied electric field and can cause further ionization if they have enough energy to cause an amplification in the gas. For typical fill gases at atmospheric pressure, the nominal electric field strength in proportional counters is of the order of  $10^6$  V/m (Knoll 2000). Proportional counters based on tubes filled with a gaseous medium are subject to wall effects where the recoil particle(s) interact with the inner wall of the detector and lose energy, resulting in a overall lower pulse height, or altogether escape from the detection volume. These effects play an important role when the detector volume is small compared to the range of the recoil particles.

Scintillating material detects incident radiation from the ionization produced by recoil particles. The process – common to organic and inorganic scintillation material – is governed by the de-excitation of electrons with the emission of light, known as luminescence. Light emission can occur immediately after de-excitation (fluorescence), at a later time characterized by the scintillator (delayed fluorescence), or at a wavelength longer than that emitted during fluorescence (phosphorescence). The intensity of the light in each process is exponentially decaying with a characteristic time of a few ns (fast scintillators) to several microseconds (slow scintillators). Certain scintillation materials

are sensitive to ionizing radiation with varying  $dE/dx$  (energy loss per unit path length) and can be used to provide a measure of the specific type of the incident radiation via the use of pulse shape discrimination (see section 4.3.5). The light produced in the scintillator can be transformed into an electrical current when coupled to a photomultiplier (PM) tube for measurement.

A high-density, high- $Z$  inorganic scintillator material, such as NaI(Tl) or CsI(Tl), is effective for  $\gamma$  ray detection via the three basic interactions mechanisms: the photoelectric effect, Compton scattering, and pair production (Evans 1955). Effective neutron detection is accomplished by providing a hydrogen-rich (low- $Z$ ) organic scintillation material as a target (see section 3.2.1). Organic material comes as a pure crystal (anthracene or trans-stilbene), or p-terphenyl is mixed with an aromatic hydrocarbon toluene (liquid) or polystyrene (plastic). The 2,2'-p-phenylene-bis-(5-phenyloxazole) benzene (POPOP) molecule can be used in the solution to shift the wavelength of scintillation light to better match the PM tube response. Aromatic molecules in scintillators contain free valence electrons in  $\pi$ -orbitals ( $\pi$ -electrons) that are responsible for luminescence upon de-excitation. The hydrogen rich material used for neutron detection exploits the large and well-established cross-section for elastic neutron-proton scattering. Scintillation detectors can vary in size based on desired efficiency and light read out; the effective area (geometrical area  $\times$  efficiency) increases proportional to the number of protons in the detector volume, except in very thick targets. However, scintillation detectors suffer from non-linear light output for high  $dE/dx$  particles (protons

and  $\alpha$  particles), and the effects associated with multiple neutron-proton scatters or carbon scatters.

Recoil detectors rely on the scattering and detection of a recoil particle within a gaseous, liquid, or solid detection medium. Detectors of this type are divided into recoil telescopes and recoil proportional counters. Recoil proportional counters can operate in the energy range of 50 keV to 5 MeV before wall effects start to become a dominant problem. Wu et al. (1999) found good agreement between the measured and calculated response function for H<sub>2</sub> and CH<sub>4</sub> recoil proportional counters (active length = 17.8 cm, effective diameter = 36.3 mm) sensitive to neutrons with an energy of 0.565 MeV.

Recoil telescopes rely on the measurement of either a scattered proton or neutron. Proton Recoil Telescopes (PRTs) operate in coincidence for the detection of a recoil proton produced by an incident neutron from a thin, hydrogen-rich target scattered into a separate  $\Delta E$ - $E$  telescope a given distance away subtending some solid angle. PRTs have a working energy range of 1–250 MeV depending on the geometry. Baba et al. (1999) found a 4% pulse height resolution at 60 MeV with a polyethylene radiator and a 5-cm diameter by 3-cm thick NaI(Tl) and Passivated Implanted Planar Silicon (PIPS) coupled to a PM tube for the  $\Delta E$ - $E$  telescope. Neutron time-of-flight techniques can be used to determine the total energy of a scattered neutron. The recoil neutron is detected in a separate layer with an energy computed from the known distance between each layer and the measured time difference. This method is employed in the 1–15 MeV neutron energy range and used by FNIT (discussed in further detail in Chapter 4).

Neutron detection methods that rely on absorption measure the charged particle products and energy released from nuclear reactions within the detector volume to determine the total neutron energy. Common nuclear reactions used for neutron detection are:  ${}^3\text{He}(n, p){}^3\text{H}$  ( $Q$ -value: 764 keV),  ${}^{10}\text{B}(n, \alpha){}^7\text{Li}$  ( $Q$ -value: 2.972 MeV, ground state; 2.310 MeV, first excited state of  ${}^7\text{Li}$ ), and  ${}^6\text{Li}(n, \alpha){}^3\text{H}$  ( $Q$ -value: 4.78 MeV) (Brooks and Klein 2002). As discussed in section 3.1, the neutron capture reaction cross-section is large at low energy and decreases steadily for increasing energy. Fast and slow neutrons can be detected via nuclear reactions in a solid (crystal or glass detectors with  ${}^6\text{Li}$ ) or a gaseous medium ( ${}^3\text{He}$  and  ${}^{10}\text{B}$  in gaseous form are used as proportional counters and ionization chambers).

The  ${}^3\text{He}(n, p){}^3\text{H}$  reaction has been implemented in both ionization chambers and proportional counters.  ${}^3\text{He}$  ionization chambers operate in the nominal energy range of 0.5–10 MeV with a pulse height resolution (FWHM) of 2% at 3 MeV (Iguchi et al. 1994). deNolfo et al. (2009) coupled an ionization chamber filled with gaseous  ${}^3\text{He}$  to a 2-d array of gas micro-well detectors for charge collection from the ionization tracks produced by the energy loss of the proton and triton in the detector volume. This setup allows for measurement of both the energy and direction of the incident neutron, reconstructed from the ionization tracks. Detectors of this nature have associated large volume to achieve a high detection efficiency.

The reaction between a neutron and  ${}^{10}\text{B}$  is effective for the detection of both fast and slow neutrons.  ${}^{10}\text{B}$  has a large cross-section in the thermal neutron range, making it a popular choice for the direct detection of low-energy neutrons and thermal neutron

shielding. As a proportional counter the gas boron trifluoride ( $\text{BF}_3$ ) is employed in neutron monitors and long counters. The gas is surrounded by a moderating, low-Z material such that the neutron can enter the moderator, thermalize and be detected (neutron monitor) or scatter out before reaching the gas, making the instrument direction sensitive (long counter). The reaction products ( ${}^7\text{Li}$  and  $\alpha$ ) produced are detected by their ionization in the gas as described for proportional counters.

Combining differing scintillators has proved advantageous for detecting neutrons. Solid  ${}^6\text{Li}$  detectors employ the reaction involving  ${}^6\text{Li}(\text{n}, \alpha){}^3\text{H}$  and can be used over a wide neutron energy range.  $\text{LiI}(\text{Eu})$  crystal has a large neutron capture cross-section at low energy and is used to directly detect slow neutrons; fast neutron detection is achieved by coupling with a neutron moderator. Bonner spheres, which operate over an energy range from thermal to fast neutrons, is a detector that combines a set of nested polyethylene spheres to moderate fast neutrons to an energy where detection by a  $\text{LiI}(\text{Eu})$  crystal, located in the center, can take place. Information on the incident neutron direction is lost and an estimate of the source spectrum can be obtained through modeling of the complex neutron transport through the moderating layers. Solid  ${}^6\text{Li}$  or pressurized  ${}^3\text{He}$  gas positioned between two semiconductors can be used for fast neutron detectors in a so-called sandwich detector. The charged particle created in either the  ${}^3\text{He}(\text{n}, \text{p}){}^3\text{H}$  or  ${}^6\text{Li}(\text{n}, \alpha){}^3\text{H}$  reaction passes through a solid state detector creating electron-hole pairs where the electrons are subject to drift by an applied electric-field. Semiconductors provide excellent energy resolution as the number of charge carrier pairs created by ionization is substantially larger than scintillator detectors, and hence subject to lower percentage

statistical fluctuations. An energy resolution of 50 keV at 1 MeV can be achieved with a  $^3\text{He}$  sandwich spectrometer (Kluge and Weise 1982). However, solid state and hence sandwich spectrometers are often quite small in size providing a small amount of effective detection area. Another type of sandwich detector is the phosphor sandwich, or phoswich. A phoswich detector combines two scintillators with differing decay times dependent on the recoil particle. McKibben et al. (2005) showed that organic scintillator surrounded by inorganic scintillator can provide a small and effective device to measure fast neutrons and provide discrimination of neutrons and  $\gamma$  rays.

A capture-gated neutron spectrometer is the combination of a neutron moderator material (organic scintillator) with a separate scintillator with a large thermal neutron cross-section for capture. The scintillator used for neutron capture incorporates a small concentration of a nuclide, such as  $^6\text{Li}$  or  $^{10}\text{B}$ , due to the large thermal neutron cross-section. The integrated signal from the fully moderated neutrons can be separated from all other events by tagging with the considerably delayed capture signal identified by time correlation or pulse shape (Brooks and Klein 2006).

### 3.2.1 DETECTION PRINCIPLES FOR FNIT AND SIMILAR INSTRUMENTS

The method employed for the fast neutron imaging telescope (FNIT) and similar double scatter instruments is the detection of elastically scattered protons produced by fast neutrons in the 1–20 MeV energy range. The ideal material, acting both as neutron scatterer and recoil proton detector, is an organic scintillator. This material consists of

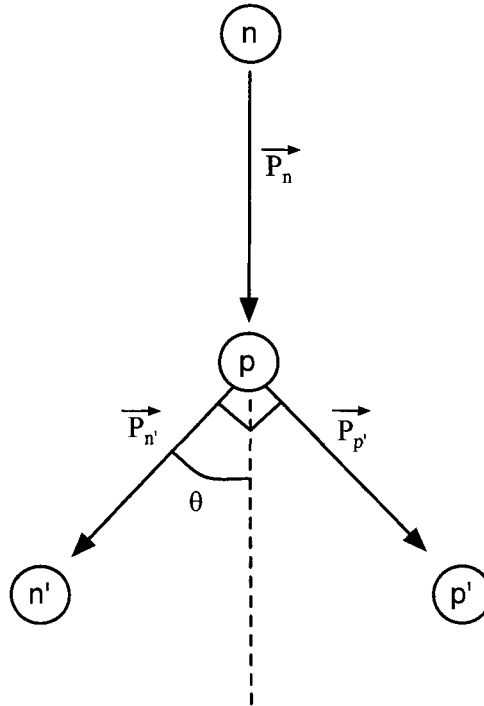


Figure 3–1: Elastic neutron-proton scattering.

mainly hydrogen and carbon with trace amounts of oxygen; the amount of hydrogen – number of potential scattering centers – varies with scintillator choice. There are instrumental trade-offs that warrant consideration when choosing a scintillator, such as the desire to have high hydrogen content for increased efficiency, but at the price of decreased light output as a result, ultimately affecting the overall performance (see section 4.5 for scintillator comparison).

In low-energy elastic scattering the particle kinematics obey hard sphere scattering with the conservation of energy and linear momentum. In the laboratory frame of reference the collision between the incident neutron and the target proton proceeds as shown in Figure 3–1. The conservation of linear momentum states

$$\vec{p}_n = \vec{p}_{p'} + \vec{p}_{n'}. \quad (3.5)$$

Simple geometry shows that the relationship between the neutron scattering angle and the momentum of the scattered particles can be expressed as

$$\tan \theta = \frac{\vec{p}_{p'}}{\vec{p}_{n'}}. \quad (3.6)$$

Given that the  $m_n \sim m_p$ , the energy ( $E = p^2/2m$ ) can thus be expressed as

$$E_n = E_{p'} + E_{n'} + Q. \quad (3.7)$$

$Q = 0$  for elastic scattering (no excited states for the neutron or proton) and equating conservation of energy and momentum relations shows that the recoil neutron and proton always scatter at right angles to each other. Using conservation of energy and momentum, the relationship between the scattering angle and the energy of the scattered particles is

$$\sin^2 \theta = \frac{E_{p'}}{E_n}. \quad (3.8)$$

The energy imparted to a recoil nucleus depends on the scattering angle and the mass number of the scattering nucleus, given by

$$E_{recoil} = \frac{4A}{(A+1)^2} E_n (\cos^2 \theta), \quad (3.9)$$

where  $A$  is the atomic mass number of the heavy nucleus. Therefore a maximum in the energy transfer of the neutron to the scattered nucleus occurs for a head-on collision ( $\theta \cong 0^\circ$ ) with a light nucleus, specifically  $A = 1$ . In the case of the constituents of organic



scintillator, a neutron can deposit between zero to 100% of its initial energy with a single scatter off a hydrogen nucleus ( $A = 1$ ) depending on the scattering angle, whereas the neutron can only deposit 28% to carbon ( $A = 12$ ) and 21% to oxygen ( $A = 16$ ). Neutrons undergoing multiple interactions slow down in logarithmic steps of energy per collision. The parameter of lethargy,  $u$ , is mathematically represented as

$$u = \ln\left(\frac{E_q}{E}\right), \quad (3.10)$$

where  $E_q$  is an arbitrary reference energy; in most practical applications,  $E_q$  is taken to be the highest energy appearing in the source spectrum.  $u = 0$  at the beginning of the slowing down process and during the moderation increases continuously. We use this quantity to logarithmically bin our simulated response matrix data (Chapter 5) for deconvolution studies of fission neutron data (Chapter 6).

Neutron cross-section data relevant for organic scintillators are shown in Figures 3–2 through 3–4 (Chadwick et al. 2006). The cross-section for elastic neutron-proton scattering is larger than that of the competing carbon reaction for an incident neutron with energy  $<12$  MeV. Resonance reactions peak at specific energies, but these reactions remain undetectable given that the carbon nucleus receives a small energy transfer and produces a low-light output in organic scintillators. The light output equivalent of a 1-MeV proton is equivalent to that of a  $\sim 30$ -MeV carbon and equivalent to a  $\sim 0.3$ -MeV electron. However, carbon scattering, as well as multiple hydrogen scattering, can affect the overall response and imaging capabilities of a detector. An intervening carbon scatter between successive neutron-proton scatters will not result in much energy transfer, but

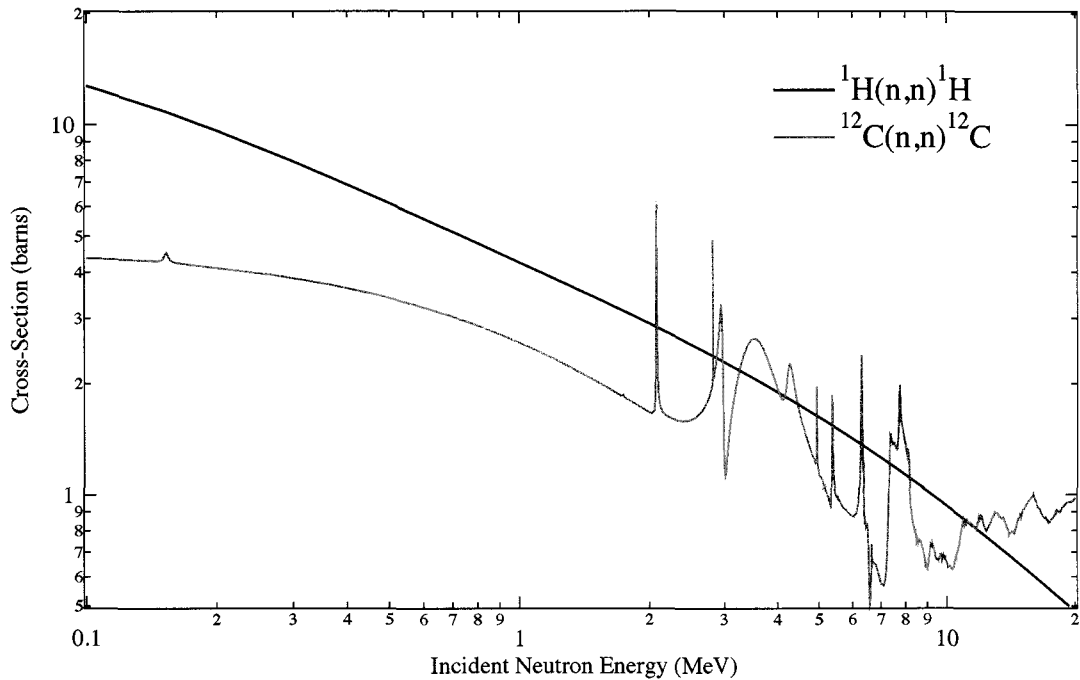


Figure 3–2: Cross-section for elastic neutron-proton and neutron-carbon scattering.

will alter the scatter direction of the neutron. Multiple hydrogen scatters will result in larger pulse height measurements where the scintillation light from each scatter is recorded within the same time window as one cumulative pulse. The cross-section for the neutron capture reaction to occur is orders of magnitude lower than that of elastic neutron-proton scattering (Figure 3–3).

Additional effects on the instrument response occurs at higher neutron energies where competing reactions turn on and the particle range and detector size become increasingly important. With a reaction threshold of  $\sim 6$  MeV, inelastic scattering between high-energy neutrons and carbon nuclei becomes energetically possible. One reaction in particular,  $^{12}\text{C}(n, n')^3\alpha$ , has a reaction threshold of 8 MeV and can affect the counting

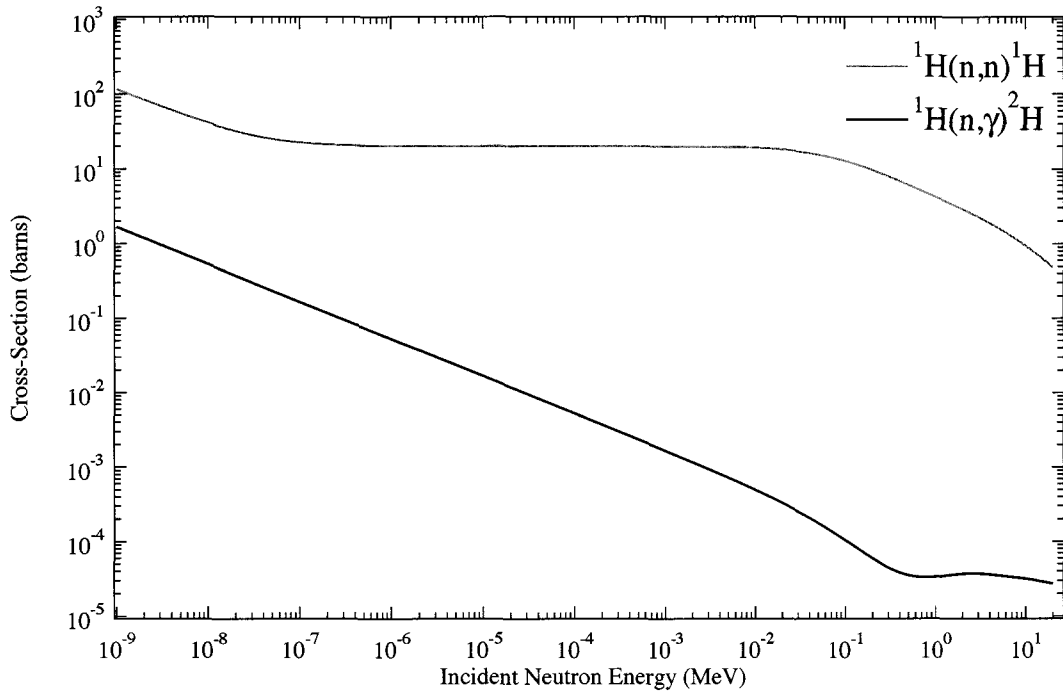


Figure 3–3: Cross-section for elastic neutron-proton scattering and the neutron capture reaction.

efficiency of the instrument. Edge effects from the loss of a recoil proton out of the detector volume results in an overall reduction in pulse height, leading to a lower recoil proton energy, and hence lower total neutron energy.

For monoenergetic neutrons the ideal response of the proton recoil energy distribution is rectangular – uniform from  $E_p = 0$  to  $E_p = E_n$  – given that, on average, the neutron will deposit half of its energy to the proton through one scatter. For neutron-proton collisions below an incident neutron energy ( $E_n$ ) of 10 MeV, the scattering is isotropic, that is all angles of recoil are equally probable in the center-of-mass system (Barschall and Kanner 1940).

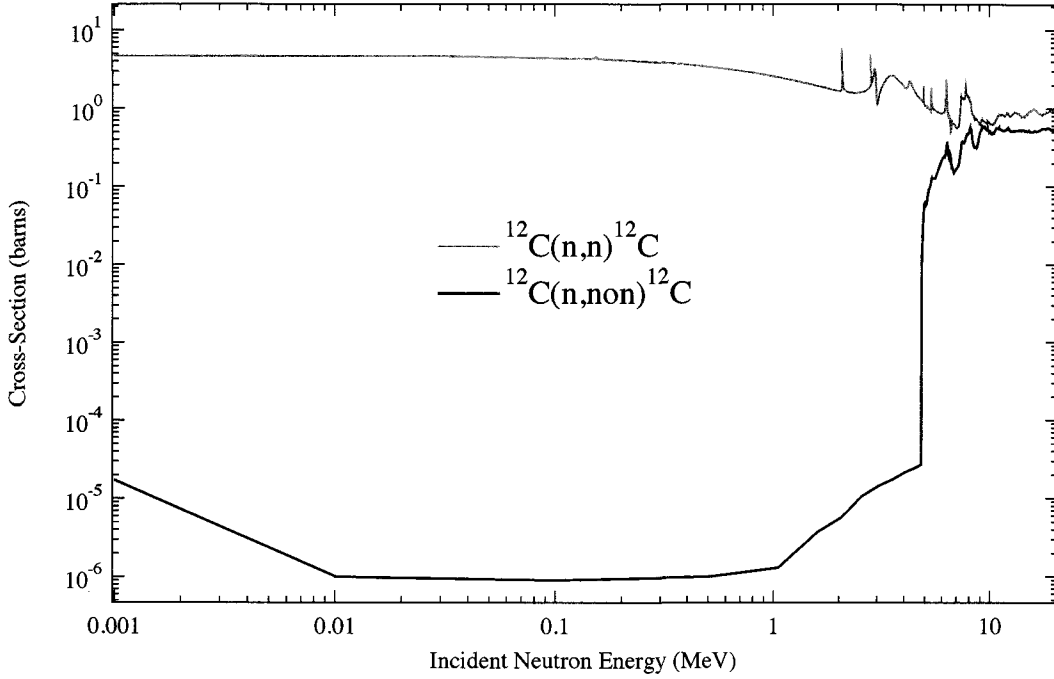


Figure 3-4: Cross-section for elastic and inelastic neutron-carbon scattering.

The efficiency in  $\text{cm}^2$  of a double scatter detector is outlined by Moon et al. (1976) as:

$$\varepsilon(E_n, \theta) = N_H \left[ \frac{d\sigma(E_n, \theta')}{d\Omega} \right]_{np} \times [N_H \sigma_{np}(E_{n1}) + N_C \sigma_{nC}(E_{n1})] \times f_1(E_{n1}) \frac{V^2}{r^2} \quad (3.11)$$

where  $\theta$  is the incident scattering angle,  $\theta'$  is the scattering angle of the neutron-proton interaction in  $D_1$ ,  $N_H$  is the density of hydrogen atoms per  $\text{cm}^3$ ,  $N_C$  is the density of carbon atoms per  $\text{cm}^3$ ,  $d\sigma(E_n, \theta')/d\Omega$  is the differential elastic cross-section for neutron-proton scattering,  $\sigma_{np}(E_{n1})$  is the total elastic cross-section for neutron-proton scattering into  $D_2$  evaluated at  $E_{n1}$  that gives a signal above threshold,  $\sigma_{nC}(E_{n1})$  is the inelastic cross-section for neutron-carbon scattering into  $D_2$  evaluated at  $E_{n1}$  that gives a signal above threshold,  $f_1(E_{n1})$  is the fraction of neutrons that scatter in  $D_1$  and survive to  $D_2$ ,  $V$  is the

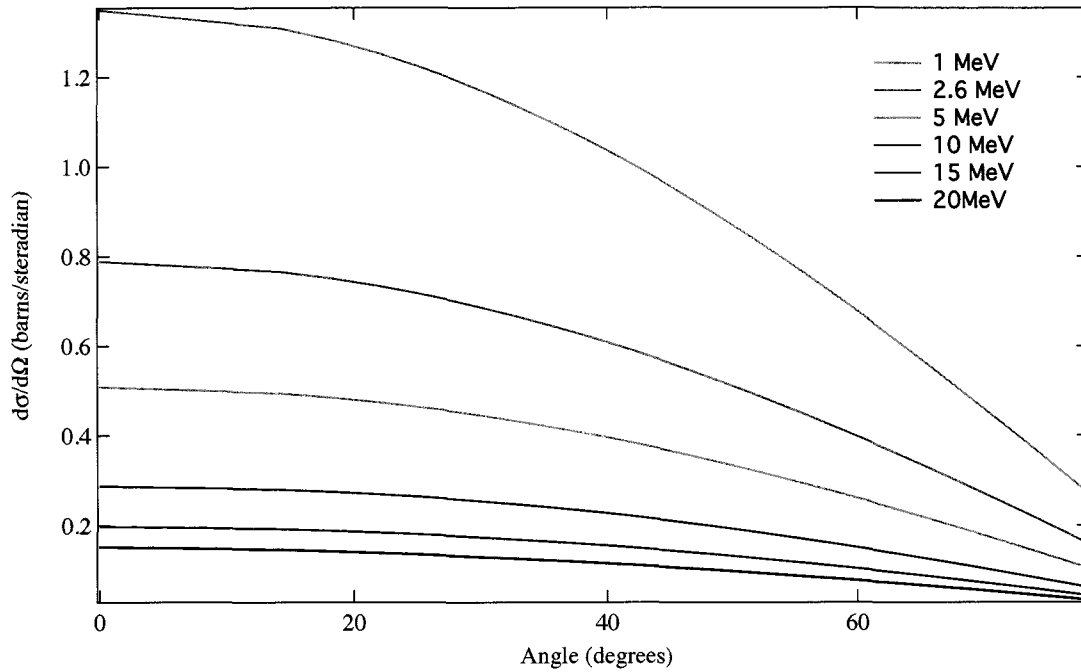


Figure 3-5: Differential elastic scattering cross-section as a function of scatter angle for 1–20 MeV incident neutrons.

volume of active scintillator, and  $r$  is the separation between  $D_1$  and  $D_2$ . The  $d\sigma(E_n, \theta')/d\Omega$  data for the elastic scattering of protons by 1, 2.6, 5, 10, 15, and 20 MeV neutrons is given in Figure 3-5. The information shown here is to serve as a guide for instruments of a similar nature with a larger effective area better suited outside the laboratory.

## CHAPTER 4

### FAST NEUTRON IMAGING TELESCOPE

#### **4.1 SCIENCE MODEL I**

Initial testing of prototypes for a neutron telescope was conducted to determine the material, geometry, and light collection methods that would optimize the design. The design chosen for Science Model 1 (SM1) consisted of three monolithic slabs ( $12\text{ cm} \times 12\text{ cm} \times 1.5\text{ cm}$ ) of plastic scintillator, vertically separated by 9 cm. Sixty-four (32  $x$ -fibers, 32  $y$ -fibers) wavelength shifting (WLS) plastic fibers were bonded into orthogonally oriented machined grooves on each side of the slab. Each fiber had a thickness of 1 mm, including cladding. Scintillation emission (blue) light, produced at the point of ionization in the scintillator, is absorbed by the WLS and re-emitted as green light; some of which is piped along the light guide to a Hamamatsu (H8711–10) multi-anode photomultiplier tube (MAPMT). The 8711–10 is a metal channel dynode type MAPMT with a focusing mesh between the photocathode and each of the 16 anodes, limiting crosstalk during electron multiplication. The original test design of the fiber pitch was approximately the same as the scintillator thickness, 1.5 cm. To increase efficiency and decrease the effects of light loss, the fiber spacing was decreased to 3.75

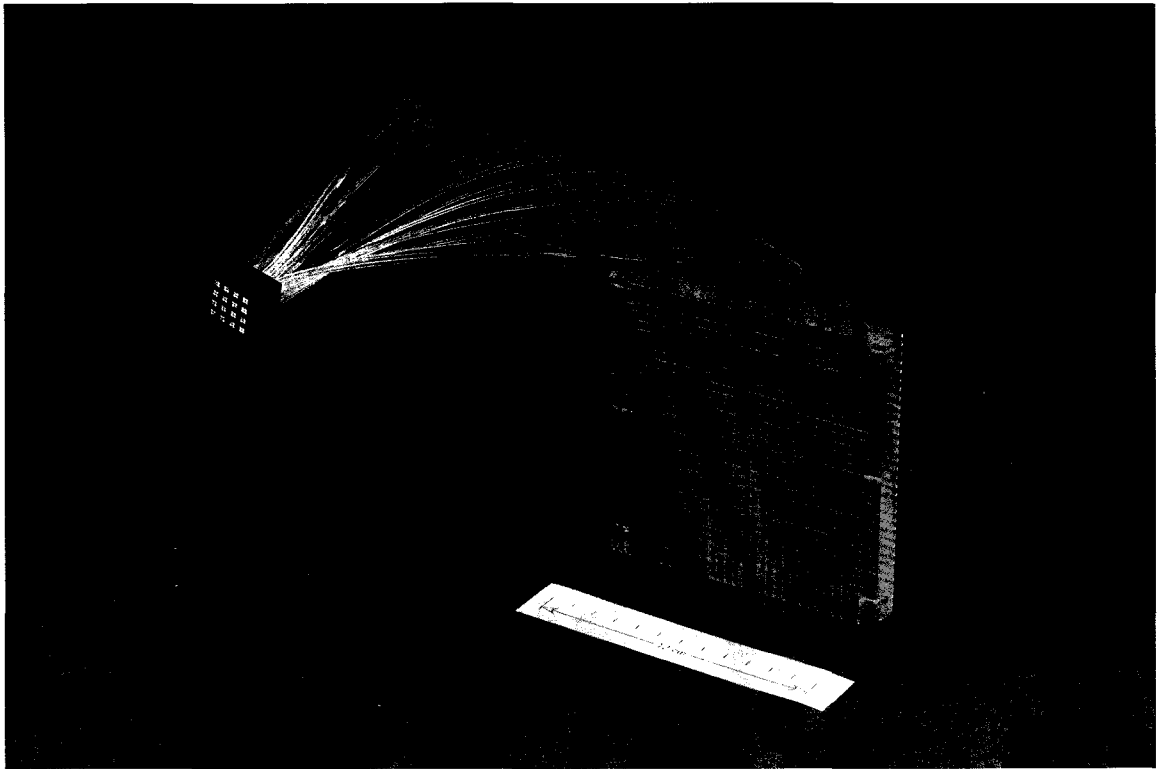


Figure 4–1: Single-layer of FNIT SM1 with MAPMT.

mm. Polished mirrors were affixed to the end of unterminated fibers to collect more light. A thin sheet of aluminized mylar cut to the size of each scintillator plate was adhered to the top and bottom surfaces to minimize light loss. The length of each WLS is such that the scintillation light travels an equal distance of  $\sim 20$  cm and terminates at the face of a MAPMT. Each anode signal of the MAPMT was used to measure the amount of scintillation light from a bundle of four fibers. The interaction location was reconstructed from the amount of scintillation light recorded by a fiber bundle using a center-of-gravity algorithm (Landi 2003) to find the fiber (and its neighbors) with the largest pulse height, statistically determining the location of the point of ionization. The total amount of scintillation light (pulse height) used to obtain a measure of the total energy deposit was



Figure 4–2: Three-layer configuration of FNIT SM1 with MAPMT.

derived from the dynode signal of the MAPMT. The dynode signal is simply the summed contribution of each individual fiber.

The system trigger was a coincident dynode pulse above threshold in two or more layers. The SM1 prototype was tested with  $\gamma$ -ray emitting isotopes and an  $^{241}\text{Am}/\text{Be}$  neutron/ $\gamma$ -ray source. The spatial, energy, timing, and angular resolution measurements tested the performance of this setup (details on each of these parameters are described below). Horizontal spatial resolutions of  $\sigma_x = 1.3$  cm and  $\sigma_y = 0.5$  cm was achieved for 2-MeV deposits ( $^{90}\text{Sr}$   $\beta^-$  source). The discrepancy in  $x$  and  $y$  resolutions is due to the fiber's location on each plate. Scintillation photons that reach the bottom side of the plate –  $x$  dimension – experience a longer and more indirect path to the fibers due to multiple



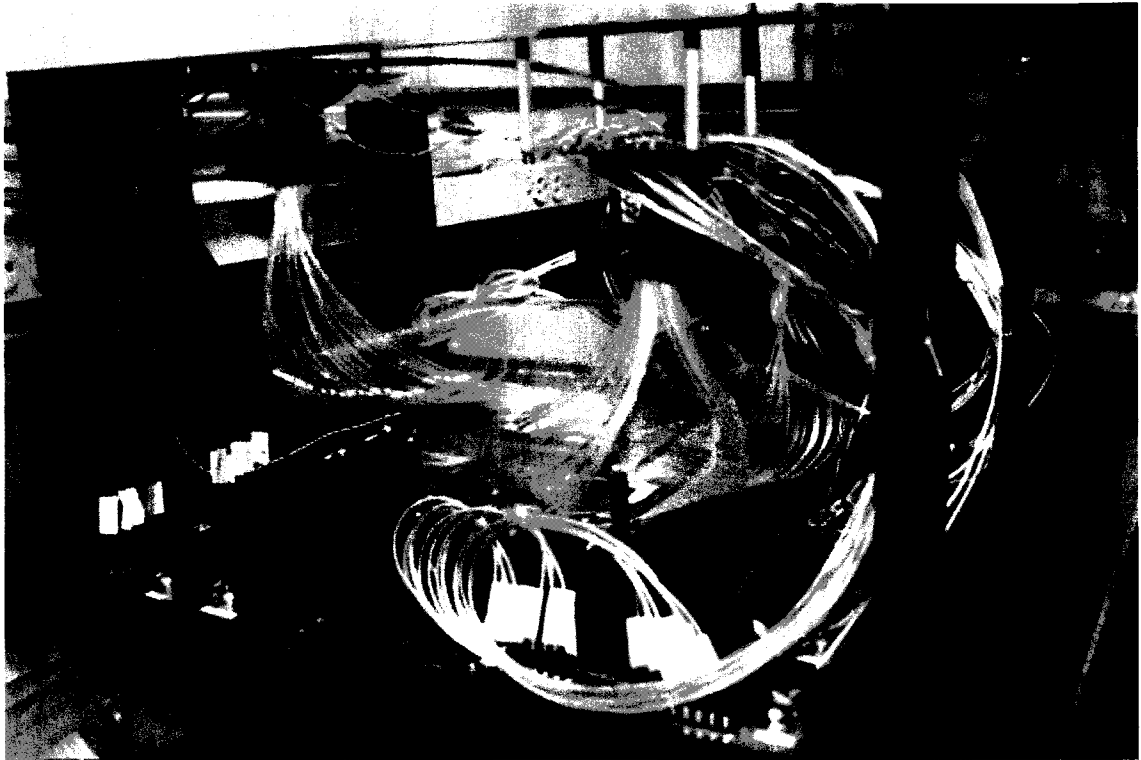


Figure 4–3: Three-layer configuration of FNIT SM1.

reflections off the plate surfaces, resulting in a broader spatial resolution distribution. A larger fraction of photons collected by the  $y$ -dimension fibers are likely to have undergone no reflections, leading to a narrower spatial resolution distribution. The combination of pulse height and time-of-flight measurements yielded an energy resolution ( $\sigma_E/E$ ) of 16% at 2.6 MeV $_{ee}$  (Bravar et al. 2006) and an angular resolution ( $\sigma_\theta$ ) of 10°. However, the threshold obtained with this configuration was  $\sim 2$  MeV for doubly scattered neutrons, higher than originally intended for solar and SNM neutrons ( $< 1$  MeV).

In addition to the high threshold, the large volume that SM1 occupies (due to fiber connections) was not favorable for a deep space instrument. The bi-directional SM1 design was subsequently rejected in favor of a design consisting of a more compact,

radially symmetric configuration of cylindrical rods suitable for a rotating spacecraft. A second science model (SM2) was designed, built and tested and is discussed below.

#### **4.2 SCIENCE MODEL II**

The Science Model II (SM2) of the FNIT prototype consisted of three hollowed-out cylindrical aluminum (Al) rods, each with a length of 15 cm and an inner diameter 1.5 cm. The thickness of the Al wall is 0.05 cm. Al cups with a length of 4.8 cm and a diameter of 8 cm were used to house the PMTs and front-end electronics. The three detectors in the prototype were assigned the labels of A, B, and C, as shown in Figure 4-6. Each rod was filled with an organic liquid scintillator. The scintillators chosen were BC-501 (by Bicorn Radiation Measurement Products, equivalent to Nuclear Enterprise Ltd. 213A) and BC-519 (Nuclear Enterprise Ltd. 228 equivalent).

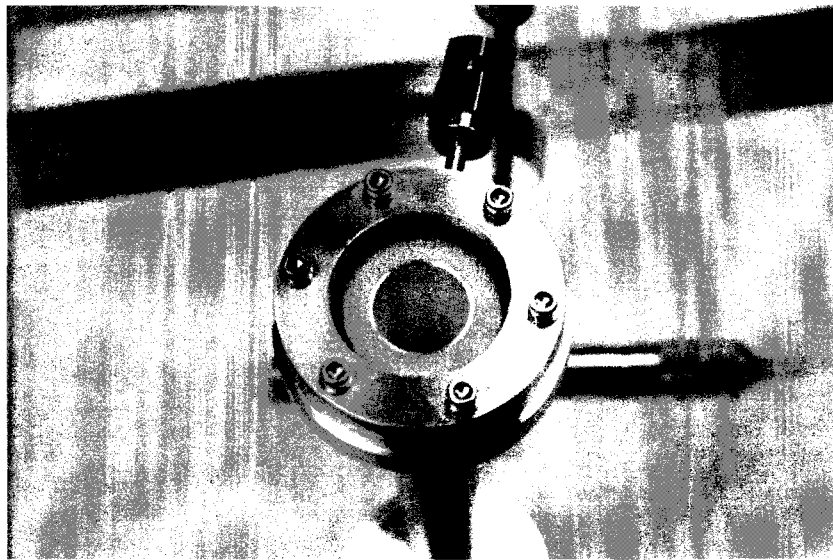


Figure 4-4: FNIT SM2 rod shown without PMT. Liquid scintillator located within center cavity.

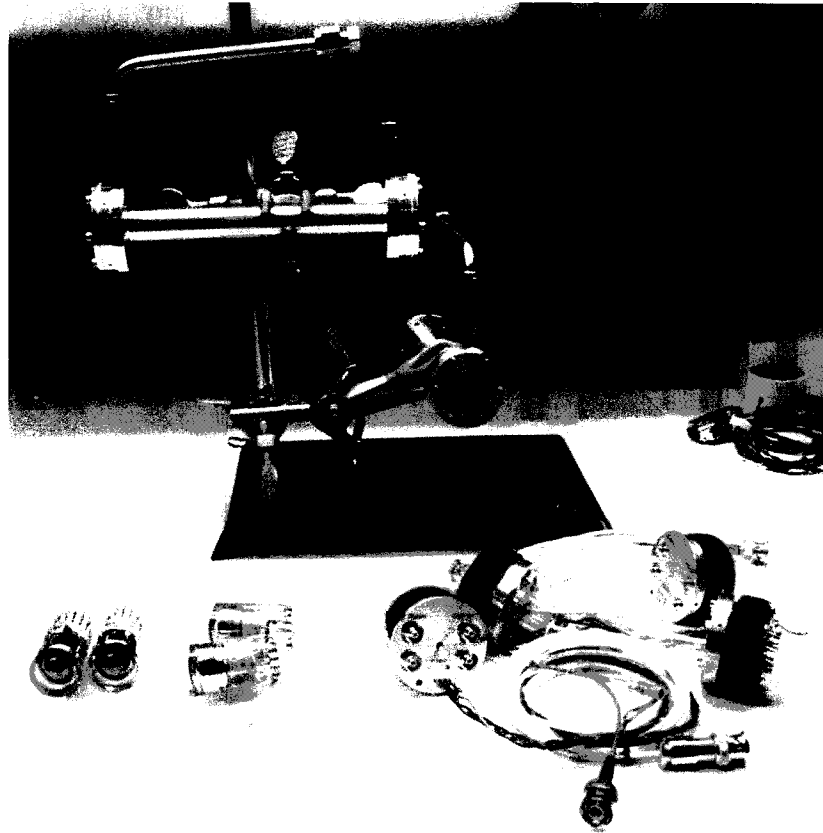


Figure 4–5: SM2 rods shown with PMT (lower left) and front end electronics (lower right).

BC–501 was used in front detector A and rear detector C, BC–519 was used in the second front detector B. This setup allowed for the testing of scintillators with differing efficiency and light output. The results of the performance testing and the scintillator properties are discussed in section 4.5.

The rods were hermetically sealed and purged with  $N_2$  gas to remove impurities (e.g. oxygen) that can degrade total light output. Each end of a rod has a Pyrex glass face (Figure 4–4) to which a Hamamatsu R–1924A PMT was directly coupled with a thin

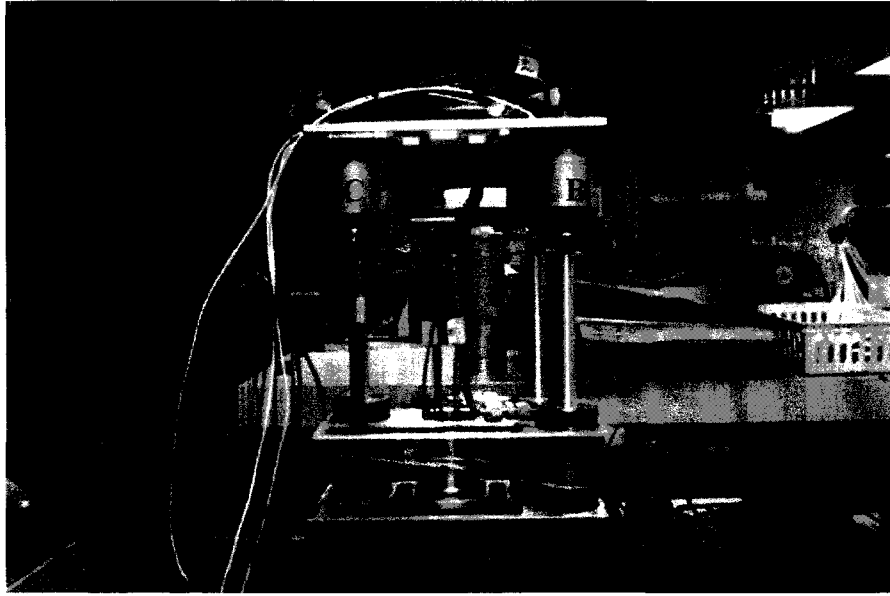


Figure 4–6: Three-rod configuration of FNIT SM2. Center-to-center rod separation: (A–C) 15 cm; (B–C) 17.6 cm.

layer of optical grease. The PMT was sealed inside the Al cup forming a light tight fixture. A fast pulse (rise time of  $\sim 10$  ns) from the PMT anode was used for coincidence gating, time-of-flight triggering and pulse-shape information. Within the event integration time, a second, slow pulse (rise time of  $\sim 1$   $\mu$ s) was obtained from the last dynode of the PMT. This signal was pulse height analyzed.

A reflective surface on the inner aluminum walls was required to achieve satisfactory light collection based on initial pulse height tests. Two potential solutions were tested in separate rods: a white, highly reflective paint (Bicron BC–620) and reflective Teflon™ lining (thickness = 0.254 mm) on the inner wall of the rod, both of which had to be compatible with the scintillator. Comparing the pulse height output for equal inputs showed that the reflective material yielded a larger gain increase compared to the reflective paint. However, it was ultimately found that the reflective paint in

combination with the translucent lining achieved the best results. The next sections discuss the complete calibration of the SM2 prototype; the interested reader will find a condensed version in Bravar et al. (2009) and Woolf et al. (2009).

### **4.3 PROTOTYPE CALIBRATION**

#### **4.3.1 FNIT SM2: SYSTEM DIAGRAM**

Figure 4–7 shows the block diagram for FNIT SM2 in a double scatter configuration. The front-end electronics associated with each PMT produces two separate voltage signals, one fast and one slow. The individual slow signals (‘C’ in Figures 4–7 and 4–8) from each PMT are read into a spectroscopy amplifier, processed, and read out directly to the Analog-to-Digital Converter (ADC). The fast signal from each PMT was analog summed and fed into a 4 channel particle discriminator Mesytec (Mesytec MPD–4 n.d.) NIM unit designed specifically for neutron and  $\gamma$ -ray measurements (‘A’ in Figures 4–7 and 4–8). The MPD–4 (Ruben et al. 2007) provided logic and time-of-flight gates as well as providing a measurement of the pulse shape and summed pulse height (‘B’ and ‘D’ in Figures 4–7 and 4–8). Coincidence between two SM2 rods occurred when input gates were received within a 64-ns timing window (‘E’ in Figures 4–7 and 4–8). A four-fold logic unit initiates a logic signal which then relays a 3- $\mu$ s wide square pulse to gate the 32-channel peak sensing CAEN 12-bit ADC unit (‘F’ and ‘G’ in Figures 4–7 and 4–8).

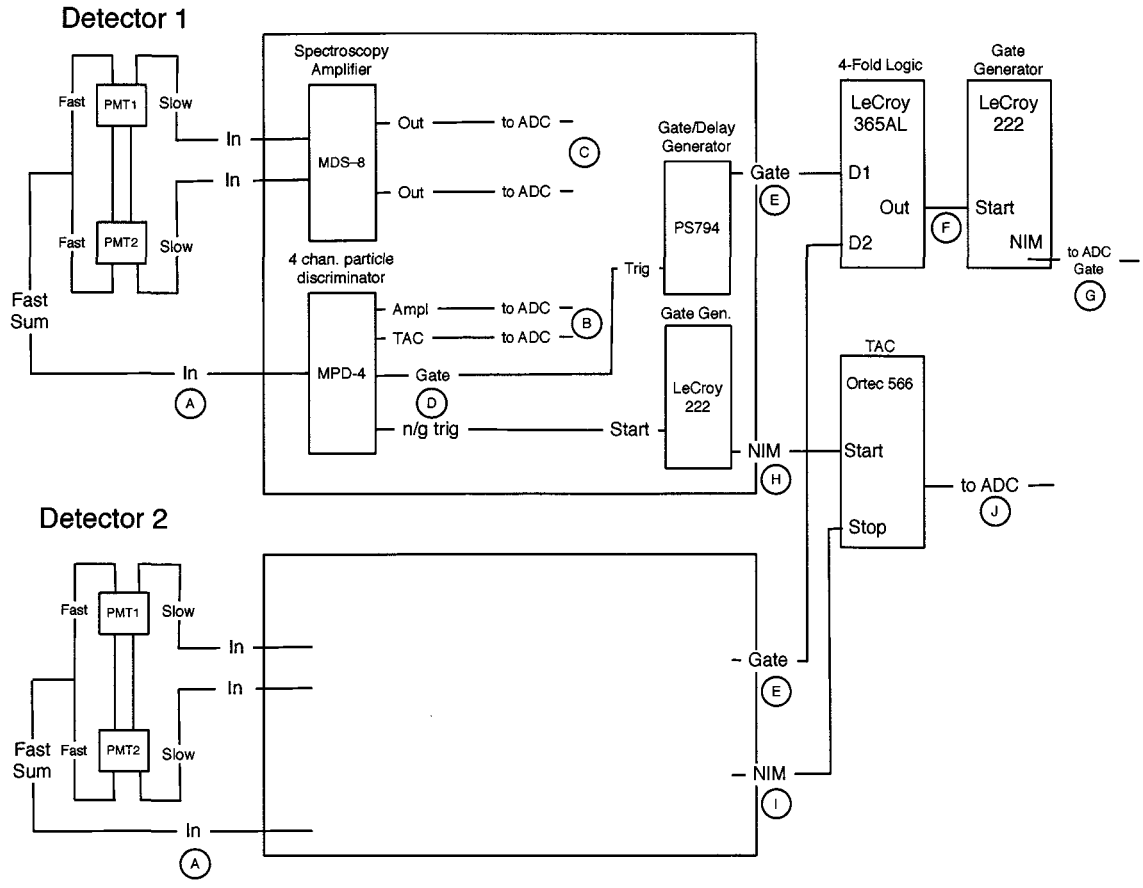


Figure 4-7: FNIT SM2 electronic block diagram for double scatter mode. The NIM module electronics for detector 2 are identical to that used for the detector 1 block.

Buffer reads are performed via USB transfer to a data acquisition computer for a LabVIEW™-based virtual instrument.

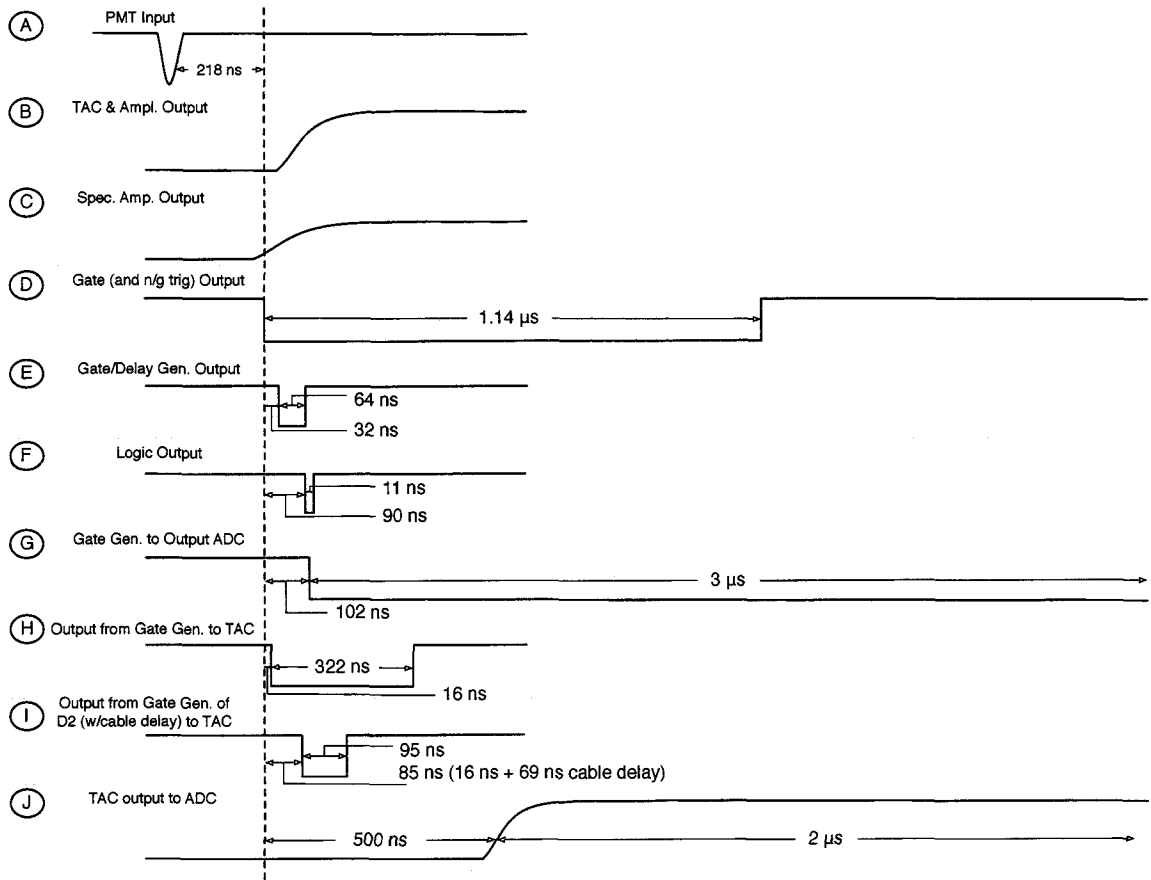


Figure 4–8: FNIT SM2 timing diagram in double scatter mode.

#### 4.3.2 TIME-OF-FLIGHT (ToF)

Time pickoff methods in fast, scintillating detectors can be accomplished by three methods: 1) Leading-edge triggering, 2) Cross-over timing, and 3) Constant Fraction Discrimination. Other methods also exist for performing time pickoff (Lynch 1966). Methods 1) and 2) generally lead to undesirable timing resolution due to time jitter and amplitude walk (time slewing) because each depends on the input pulse height used as

the trigger. The method of Constant Fraction Discrimination (CFD) triggers the timing signal by producing an output pulse a fixed amount of time after the input has reached a constant fraction of the peak amplitude (Knoll 2000), empirically found to be between 10–20% (Gedcke and McDonald 1968). CFD timing was used for the FNIT SM2 prototype given the expected range of input signals.

To perform the measurement of the ToF a Time-to-Amplitude Converter (TAC) was used. Two common types of TACs in use today are overlap and START–STOP. The overlap principle converts the rectangular area of two overlapping pulses and carries out a time-to-amplitude conversion. However this method lacks a linear response over a large dynamic range (Knoll 2000). A TAC operating on the START–STOP generates an output pulse based on the amount of charge a capacitor acquires over an integration time given the difference between input signals ('H', 'I', and 'J' in Figures 4–7 and 4–8). The STOP is delayed by a fixed amount (69 ns for FNIT SM2). ToF calibration and performance were assessed using radioactive isotopes that produce multiple simultaneous photons. Path-length-difference effects were eliminated by placing the sources halfway between detector modules. Due to the 15-cm spacing of two detector modules and the resolution of the processing electronics, the arrival of START and STOP signals are seen as instantaneous and provide simultaneous signals. This “zero-ToF” was tuned such that ToF measurements could be made for both forward and backward traveling neutrons. Known cable delays were inserted into the STOP signal causing the ToF values obtained without delay to be shifted by a fixed value. The calibration of measured ADC channel to ToF is accomplished by inserting delays of different amounts. The resulting ToF distribution



arises from measurement uncertainties and fit with a Gaussian function to obtain the mean and width. The ToF resolution, in terms of the standard deviation ( $\sigma$ ) width of the Gaussian, is a function of the number of photoelectrons, and hence the pulse height.  $\gamma$ -ray photons from  $^{22}\text{Na}$  and  $^{60}\text{Co}$ , and cosmic-ray muons were used to determine the ToF resolution as a function of increasing pulse height in each rod.  $^{22}\text{Na}$  emits simultaneous 511 keV photons from the electron–positron annihilation at a  $180^\circ$  angle;  $^{60}\text{Co}$  emits simultaneous photon pairs with energies of 1170 and 1330 keV in random directions. Muons, produced by the electromagnetic cascade from cosmic-ray particles hitting the atmosphere, were used (with luminal ToF) for larger pulse height measurements. These particles are more massive than electrons, but move at relativistic velocities and are minimum ionizing particles, like fast electrons, based on the Bethe formula (Bethe and Ashkin 1953). Pulse height selected spectra in each rod yields the ToF distributions shown in Figure 4–9 for coincident  $^{22}\text{Na}$  and  $^{60}\text{Co}$   $\gamma$ -ray photons and cosmic-ray muons. To determine the ToF resolution as a function of energy, we plot (Figure 4–10) the  $\sigma$ -width of each ToF distribution vs. the corresponding sum of the electron equivalent energy from each rod ( $E_{ee,1}$  and  $E_{ee,2}$ ) and fit the data with a function of the form

$$\sigma_t(E_{tot}) = a + b \times \exp\left(\frac{-(E_{ee,1} + E_{ee,2}) - c}{d}\right), \quad (4.1)$$

where  $a = 0.29$ ,  $b = 0.40$ ,  $c = 0.68$ , and  $d = 1.11$  for FNIT SM2 rods.

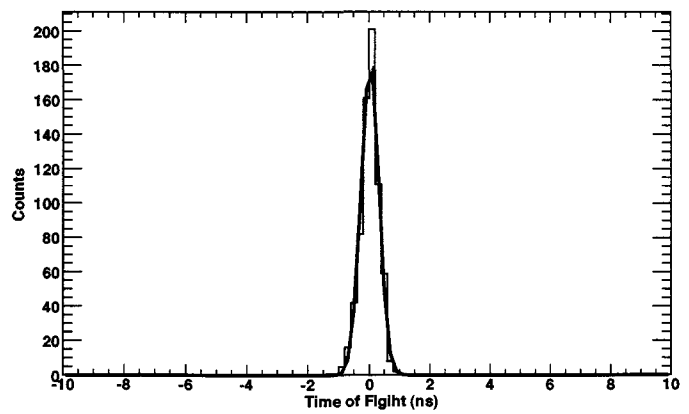
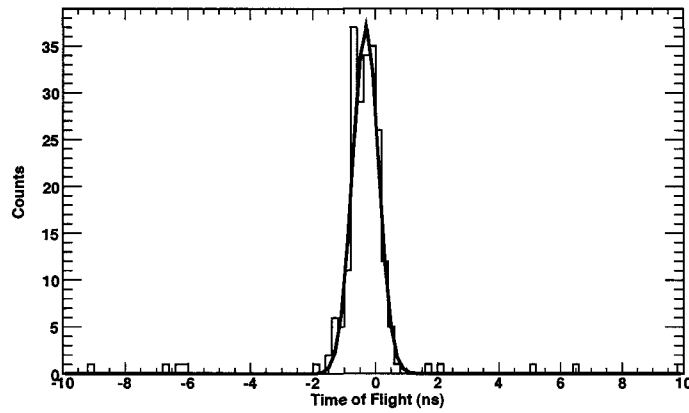
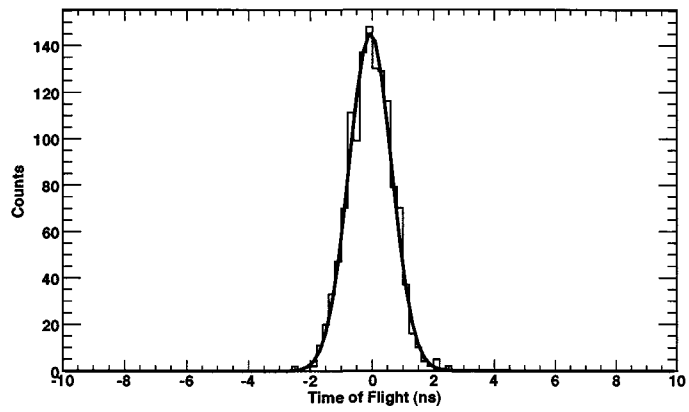


Figure 4–9: ToF distributions for increasing energy stimuli. Coincident photons from:  $^{22}\text{Na}$  (top),  $^{60}\text{Co}$  (center); cosmic-ray muons (bottom).

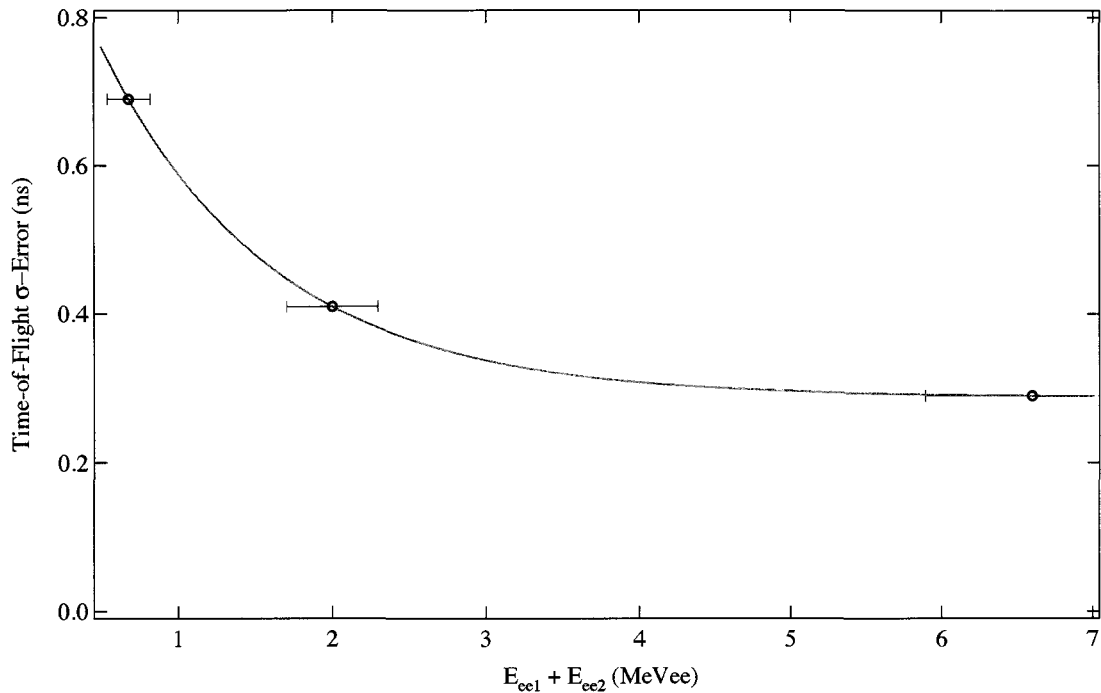


Figure 4-10: ToF  $\sigma$ -resolution as a function of electron equivalent energy deposited in separate SM2 rods.

#### 4.3.3 INTERACTION LOCATION

The longitudinal ( $z$ ) component is determined by the pulse height measurement from the PMTs at the end of the rod. The transverse ( $x$  and  $y$ ) components are defined orthogonally to the  $z$  axis – and to each other – for each SM2 rod. Scintillation light exhibits an exponential decay away from the point of ionization, so that the simple ratio of the two pulse heights is a non-linear function of the interaction point. However, the natural logarithm of the ratio of the two pulse heights responds linearly along the length of the rod,

$$z = \frac{1}{2\alpha} \ln\left(\frac{P_2}{P_1}\right) \quad (4.2)$$

where  $\alpha$  is the measured light attenuation coefficient of the rod and  $P_1$  and  $P_2$  are the relative pulse heights from each PMT. The quantity  $\alpha$  was determined by mapping each rod with a source of collimated  $^{137}\text{Cs}$  662-keV  $\gamma$  rays at nine positions along the 15 cm length of the rod, or every 1.75 cm, yielding values for  $\alpha$  of: 0.196  $\text{cm}^{-1}$ , 0.235  $\text{cm}^{-1}$ , and 0.223  $\text{cm}^{-1}$  for A, B, and C respectively. The longitudinal RMS resolution ( $\sigma_z$ ) of 0.7 cm was observed for center interactions and degraded to  $\sim 1$  cm at the extremities. Figure 4–11 shows the position-dependent  $\sigma$ -resolutions for detectors A, B, and C. The difference between A and C is due to the combination of reflective paint and reflecting material in A, while C only contains reflective material. The poorer performance of detector B,

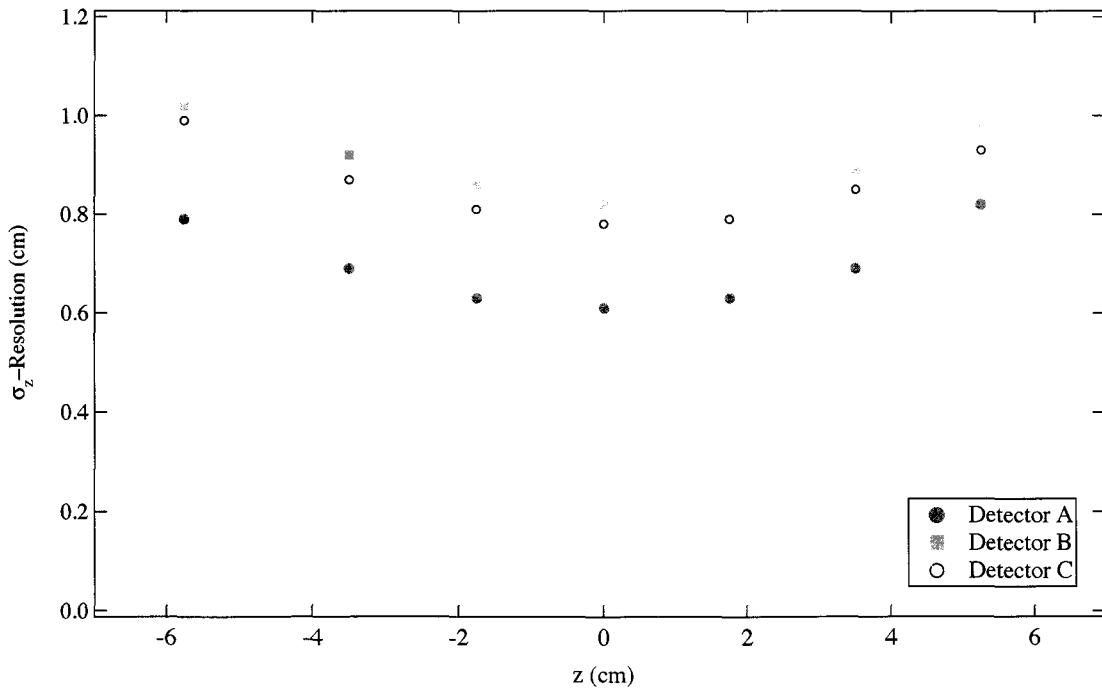


Figure 4–11: Spatial resolution along the length of rod: A (red), B (green), and C (blue).

compared to detector C, is due to the lower light output of the BC-519 scintillator.

The  $\sigma$ -resolutions in the transverse direction ( $x$  and  $y$ ), given by the square root of the expectation value of  $r^2$ , are:  $\sigma_x = \sigma_y = 0.53$  cm. Fixed transverse location and resolution information were assumed because these parameters cannot be easily measured, but should be uniformly distributed in any rod.

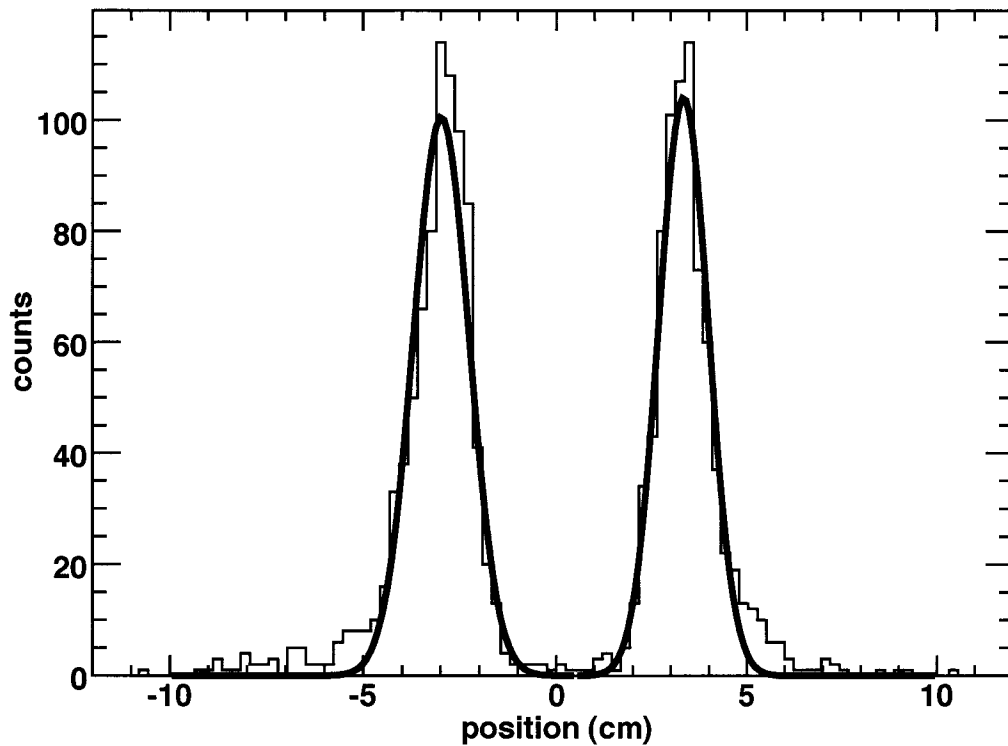


Figure 4-12: Reconstructed positions for collimated source separated by 7 cm.

#### 4.3.4 PULSE HEIGHT

Relating pulse height information to the energy loss is given as the light output function of the scintillating material for various stimuli, described as (Birks 1964)

$$\frac{dL}{dx} = \frac{S \frac{dE}{dx}}{1 + kB \frac{dE}{dx}}, \quad (4.3)$$

where  $S$  is the absolute scintillation efficiency,  $k$  is the quenching parameter, and  $B$  is a scintillator dependent constant. In scintillators quenching refers to de-excitation of excited molecules through a radiation-less process (the excitation is degraded mainly to heat), resulting in a lower light output (Knoll 2000). The constant  $kB$  depends on radiation type and increases with particle mass. Equation 4.3 relates the amount of fluorescence emitted per unit path length to the specific energy loss of the incident stimuli within the scintillating material. In the limit that  $dE/dx$  is small, the quenching effects are negligible and the light output is directly proportional to the energy loss. Such is the case for  $\gamma$  rays interacting with scintillator, producing fast electrons and small  $dE/dx$ . Monoenergetic  $\gamma$ -ray emission from unstable nuclear decay can be used to relate the scintillator pulse height to an electron equivalent energy whose response is linear in energy over many orders of magnitude. Neutron measurements require the light output information from the ionization produced by recoil protons interacting in the scintillator material. Proton recoils are subject to larger quenching effects and a larger  $dE/dx$ , resulting in a smaller light output with non-linearity across a broad energy range.

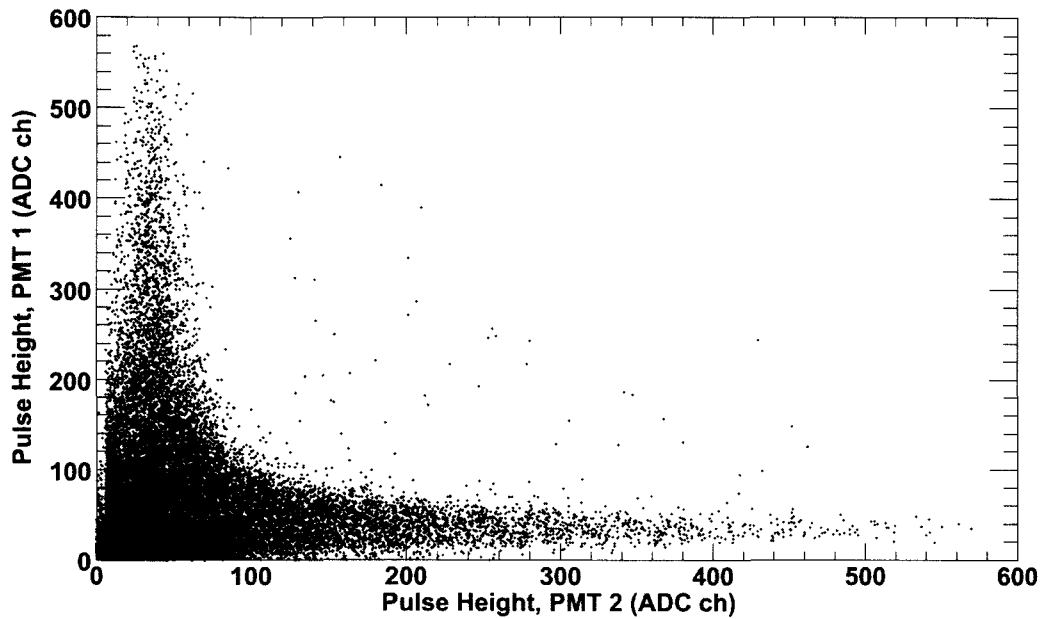


Figure 4–13: Non-uniformity of pulse height for a SM2 rod.

Conversion between electron equivalent and proton equivalent energies are available for many standard scintillators in the literature (Cecil et al. 1979) and can be verified with a suitable measurement (see section 4.4.2).

The system trigger is derived from the analog sum of both PMTs. The trigger threshold was optimized by maximizing the MPD–4 amplifier gain and raising an internal CFD threshold so that random noise triggers would not affect the measurement. The total pulse height (energy) is derived from the integrated slow charge signal acquired by the PMTs at each end as measured by a Mesytec NIM unit (Mesytec MDS–8 n.d.). The MDS–8 is an 8 channel spectroscopy amplifier with an integrated-timing filter amplifier. Positive, slow signals with long ( $\sim\mu\text{s}$ ) rise times are shaped and gain adjusted with an external potentiometer. Triggering the system on the sum of the PMT signals leads to a

non-uniform threshold along the length of the rod, as shown in Figure 4–13. A uniform trigger threshold should produce a  $y = -x + (\text{constant})$  relationship for equal input pulses. In the same vein as obtaining location information, simply adding the pulse height from each PMT results in an overall lower total energy. The geometric mean of the pulse heights produces a near constant trigger response across the length of the rod, given as

$$I_{total} = \sqrt{I_1 I_2}. \quad (4.4)$$

The pulse height to electron equivalent energy conversion was determined from photopeaks, a 90°-scatter peak and Compton edges from the interaction of  $\gamma$  rays with atomic electrons in the scintillator (Diehl and Graser 1981).  $\gamma$  rays interact primarily through three energy-dependent modes: photoelectric absorption, Compton scattering and pair production. For organic scintillator consisting of mainly hydrogen ( $Z = 1$ ) and carbon ( $Z = 6$ ), Compton scattering is the dominant mode of interaction (Figure 4–14). The photoelectric effect, which produces a “photopeak” in a pulse height spectrum from the full absorption of the incident  $\gamma$  ray and ejection of an electron, can be achieved in the energy range where this mode dominates ( $\leq 100$  keV). Triggers from 22-keV  $^{109}\text{Cd}$   $\gamma$  rays were achieved in each rod. The RMS energy resolution near threshold ( $\sigma_E/E$ ) was found to be ~23% (FWHM: 67%) (Figure 4–15). Using Poisson statistics, the lower limit on the number of photoelectrons,  $n$ , in the peak was of order 20 from the relation (Barton 1976)

$$\frac{1}{\sqrt{n}} = 23\%. \quad (4.5)$$



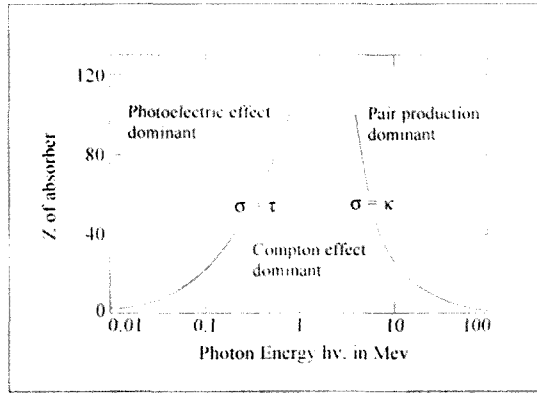


Figure 4–14: Three types of  $\gamma$ -ray interactions given in terms of  $Z$  of the material and incident photon energy (Evans 1955).

60-keV photons from  $^{241}\text{Am}$  produced a photopeak with a resolution of 48% (FWHM). Calibration points with the Compton edge from  $^{133}\text{Ba}$  (207 keV),  $^{137}\text{Cs}$  (477 keV), and  $^{60}\text{Co}$  ( $\sim 1$  MeV) were also used. An additional calibration point was obtained by exploiting the geometrical setup of the detector rods. Triggering the system in coincidence mode and requiring that the photon scatter at a fixed angle gives a known energy deposit in the first scatter. 662-keV photons from  $^{137}\text{Cs}$  entering the scattering rod deposits 374 keV<sub>ee</sub> for a 90°-scatter with a resolution of 29% (FWHM) (Figure 4–16). Figure 4–17 shows that the energy resolution,  $R$ , takes a functional form of

$$R(\text{FWHM}) = \sqrt{a + \frac{b}{E}}, \quad (4.6)$$

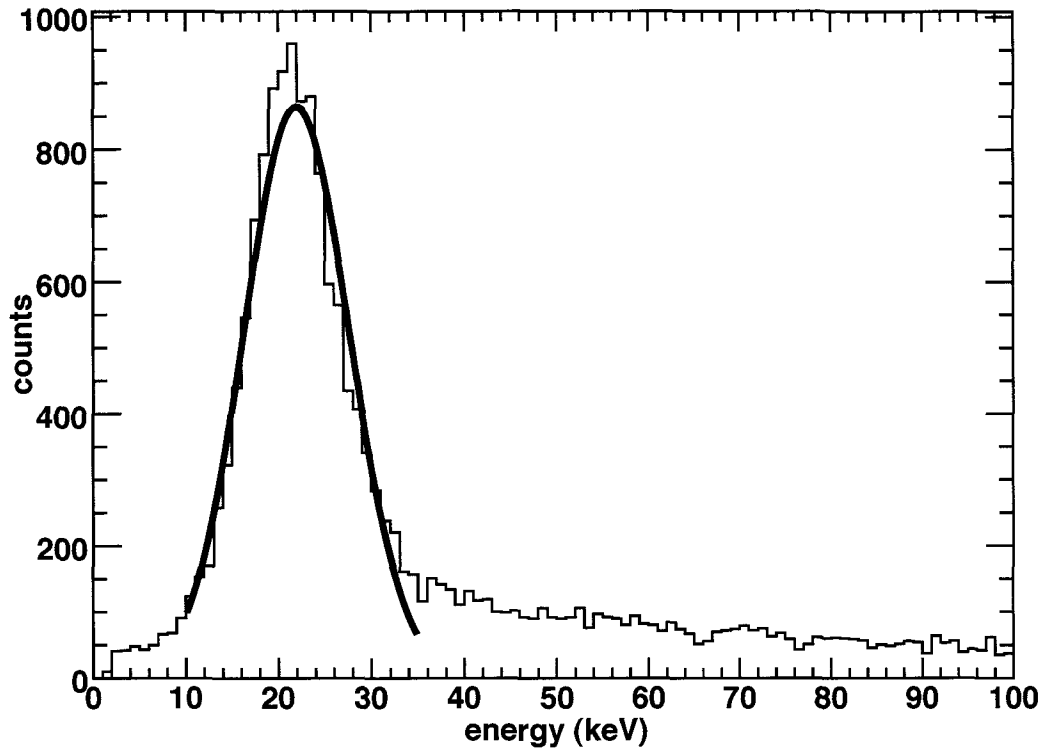


Figure 4–15: 22-keV photopeak from  $^{109}\text{Cd}$  as measured by a FNIT SM2 rod.

where  $a$  and  $b$  are the coefficients for a given scintillator (Bravar et al. 2006). For the rods with BC-501 (A and C), the values of  $a$  and  $b$  were determined from three calibration points of the  $^{109}\text{Cd}$  and  $^{241}\text{Am}$  photopeaks and the  $^{137}\text{Cs}$  90°-scatter peak. The coefficients were determined to be:  $a = (6.4 \pm 1.2) \times 10^{-2}$  and  $b = 8.9 \pm 0.7$  keV (detector A);  $a = (0.37 \pm 1.5) \times 10^{-1}$  and  $b = 38 \pm 11$  keV (detector C). Detector B could not resolve a 60-keV photopeak from  $^{241}\text{Am}$  and hence only yields two data points from the  $^{109}\text{Cd}$  photopeak and  $^{137}\text{Cs}$  90°-scatter peak. One can observe from the two data points that the resolution is worse, as expected, in detector B, but follows a similar trend as detectors A

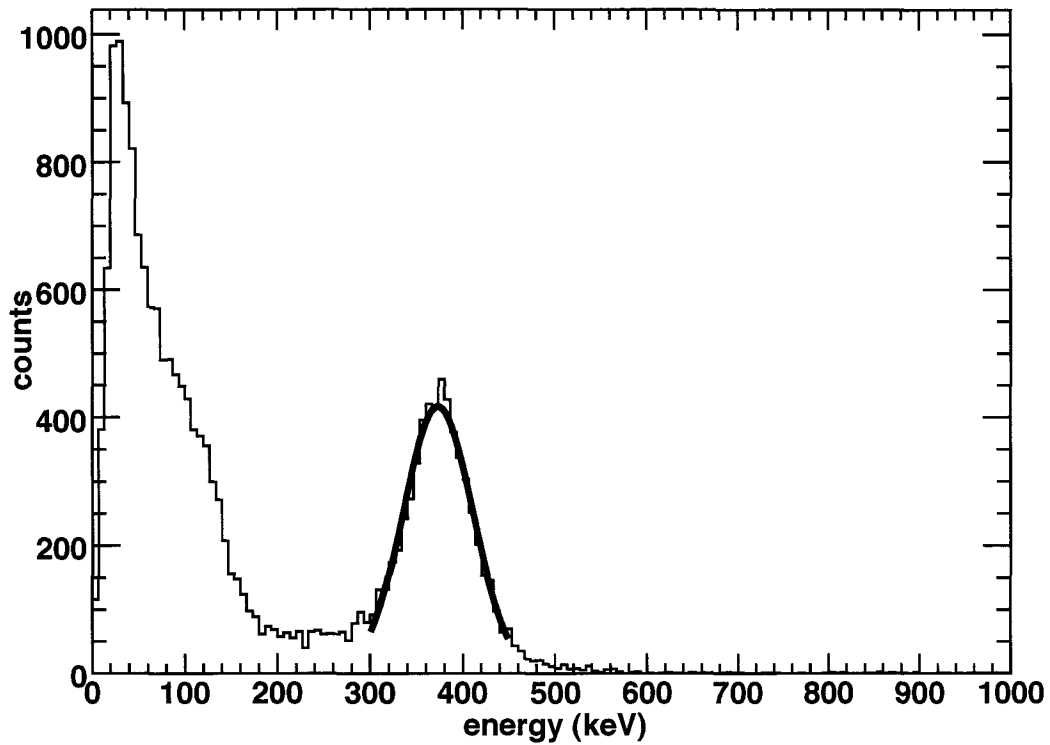


Figure 4–16: 90°-scatter peak from  $^{137}\text{Cs}$  as measured by a FNIT SM2 rod.

and C. Using the functional form given by equation 4.6, the coefficients for detector B were determined to be:  $a = 0.2$  and  $b = 30$  keV. An extrapolation would yield an expected resolution for  $^{241}\text{Am}$  of  $\sim 80\%$  (FWHM).

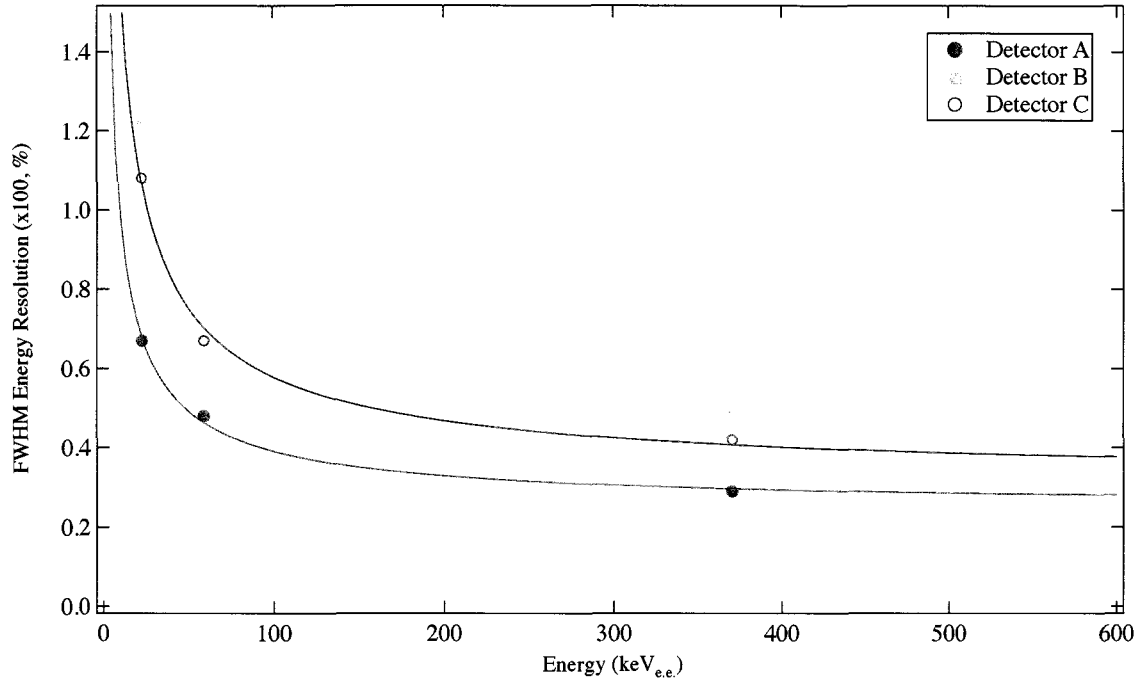


Figure 4-17: Energy resolution (FWHM) vs. energy for FNIT SM2 rods.

#### 4.3.5 PULSE SHAPE DISCRIMINATION

Certain materials exhibit the properties that scintillation light contains both a fast, decaying component ( $\sim$ few ns) and a slow, decaying component ( $\leq \mu$ s). This behavior is analytically represented by the number of photons  $N$  emitted at time  $t$ , given as the sum of two exponentials

$$N = A \exp\left(\frac{-t}{\tau_f}\right) + B \exp\left(\frac{-t}{\tau_s}\right), \quad (4.8)$$

where  $\tau_f$  is the decay constant of the fast component,  $\tau_s$  is the decay constant of the slow component, and the values of  $A$  and  $B$  are material dependent constants. Scintillator material produces light via fluorescence or phosphorescence, both of which result from the absorption and reemission of energy. Prompt fluorescence occurs when incident radiation with small  $dE/dx$  excites free valence electrons in a spin singlet state and subsequently decays to the ground state via the emission of a photon. Large  $dE/dx$  radiation results in larger quenching effects and gives rise to the population of spin triplet state, which decays down to the singlet state after a given amount of time, resulting in the slow component (Leo 1994). Scintillators, such as organic liquids and stilbene crystals, produce a significant portion of the light in the slow component for high  $dE/dx$  particles, ~10–30% as opposed to <3% found in plastics (Brooks and Klein 2006). It has been shown that pulse-shape information can be extracted from certain plastics (Normand et al. 2002; Brooks et al. 1958). The property that the decay of the long, slow component depends upon the radiation type is useful for separating neutrons and  $\gamma$  rays. Several methods exist to discriminate between  $\gamma$  rays, neutrons, and  $\alpha$  particles. Charge integration and zero-crossing methods have been successfully used in previous experiments (Flaska 2007; Verbinski et al. 1968). Charge integration relies on isolating part of the light pulse and comparing it to the total light output while zero-crossing branches the original pulse into two components, one of which depends on the decay time of the integrated pulse (Bell 1981).

The Mesytec MPD–4 unit provides PSD via a single channel time-to-amplitude converter (TAC) output that is read directly to the ADC. MPD–4 PSD is performed with a

zero-crossing type method. A fast, gain-amplified, linear pulse is used as input and split into two branches. One branch triggers a CFD on the leading edge for the START signal of the internal TAC. The second part of the signal is fed into a higher order trapezoidal filter, mainly used to reduce noise from low amplitude signals. The STOP for the timing measurement is provided by the zero-crossing of the subtracted portion of the integrated fast signal from the shaped signal. The STOP signal therefore does not depend on pulse height and is proportional to the trailing edge of the signal, which indicates the particle type (Ruben et al. 2007). PSD is optimized by adjusting the *ndis* and *walk* parameters via a computer connected to the MPD-4 via a USB-2 interface. The *ndis* adjusts an internal discrimination threshold to obtain the correct cut between neutrons and  $\gamma$  rays; the *walk* setting is used to obtain maximum discrimination resolution affected by varying amplitude (Mesytec MPD-4 n.d.). A scatter plot of the amplitude vs. PSD is necessary to determine whether the walk setting needs adjustment, such that the  $\gamma$ -ray pulse shape values follow a linear trend (Figure 4-18) and allows for the simplest demarcation to be implemented in post-processing. PSD performance is assessed via the energy-dependent figure-of-merit  $M(E)$  parameter, given as

$$M(E) = \frac{X}{W_n + W_\gamma}, \quad (4.9)$$

where  $X$  is the peak separation and  $W$  is the FWHM of the neutron and  $\gamma$ -ray peaks. The PSD performance was tested with an  $^{241}\text{Am}/\text{Be}$  neutron/ $\gamma$ -ray source shielded by a thin layer of Pb to reduce the flux of 60-keV  $\gamma$  rays. BC-501 achieved a spectrum-averaged  $M(E)$  of 0.7 and 0.8 for detectors A and C, respectively.

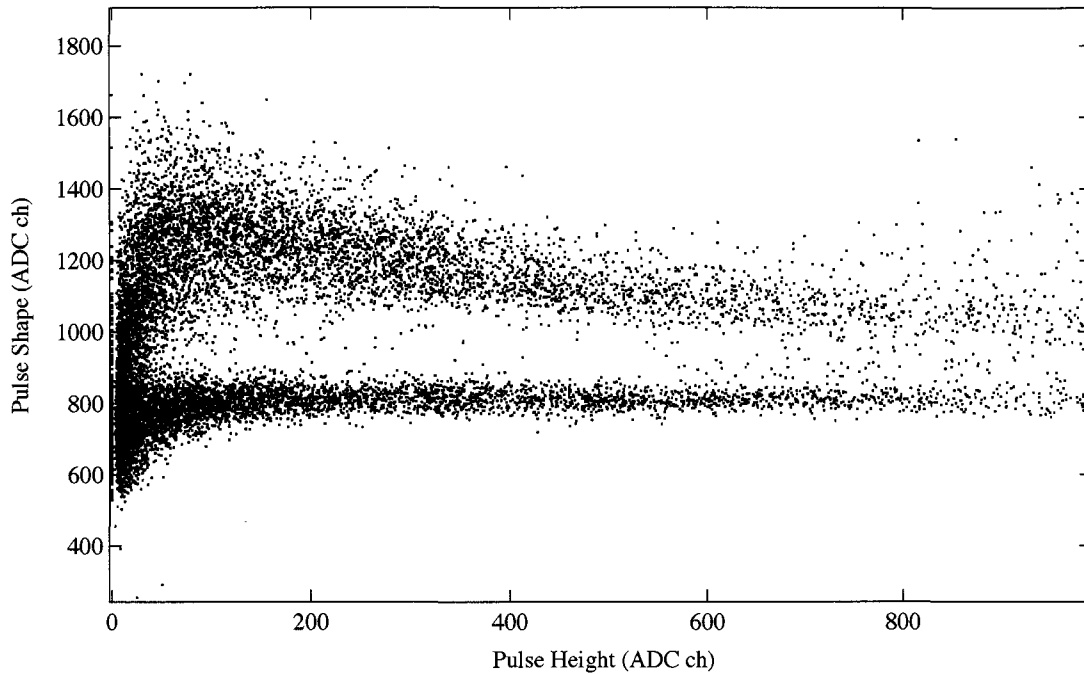


Figure 4–18: Pulse shape vs. pulse height for detector A.

As shown in Figure 4–18, the neutron/ $\gamma$ -ray separation becomes more distinct as a function of increasing pulse height. The BC–519 PSD performance did not produce clearly separated peaks. Although it has been shown (Horvath et al. 2000; Saxena 1990) that BC–519 can achieve separation comparable to BC–501, poor light collection resulted in the PSD shown in Figure 4–19 (center). PSD cuts for BC–519 are gauged from the distribution observed with only a  $\gamma$ -ray source present (red curve in Figure 4–19, center); ToF cuts and the PSD selections in detector C in double scatter mode account for the additional restrictions made on neutron events.

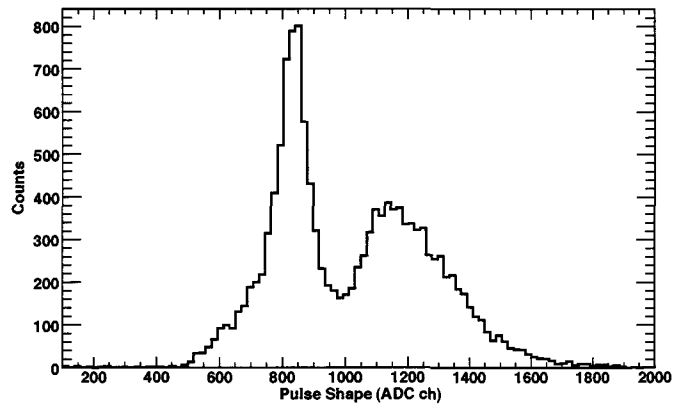
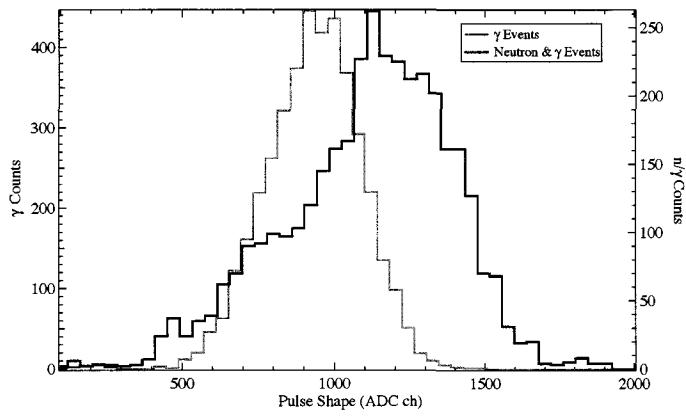
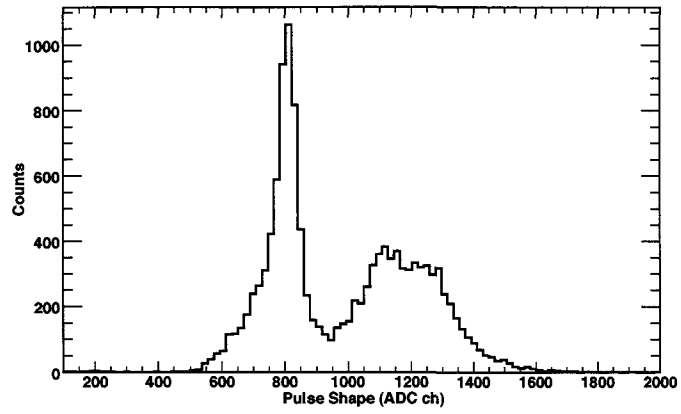


Figure 4–19: PSD distributions for detector A (top), B (center), and C (bottom).



#### 4.3.6 ANGULAR RESOLUTION MEASUREMENT

The angular resolution of the prototype instrument is determined from pulse height (energy) measurements and from spatial information of the source and detector. As discussed in Chapter 3 the incident neutron scattering angle is determined from the recoil proton energy and scattered neutron energy, a function of the neutron path length and ToF. The error in the scattering angle thus depends upon the pulse height conversion and resolution, ToF resolution, and reconstructed longitudinal spatial resolution. Neutrons from an continuum source at a known location within the detector coordinate system defines the true scattering angle. The difference between the calculated scattering angle and the true scattering angle is the ARM (Angular Resolution Measurement) (Van Dijk 1996), defined as

$$\Theta_{error} = \Theta_{calculated} - \Theta_{geometrical} \quad (4.10)$$

For properly reconstructed full energy measurements, the ARM distribution peaks near 0°; events that are incorrectly reconstructed are offset from 0°. A 1- $\sigma$  width corresponds to the intrinsic angular resolution of the instrument. Laboratory measurements determined the mean of the ARM distribution to be skewed by <1° from 0° with a resolution of 5.6° ( $\sigma$ ) at 30° (Figure 4–20).

$$(\Delta\Theta_{error})^2 = (\Delta\Theta_{calculated})^2 + (\Delta\Theta_{geometrical})^2 \quad (4.11)$$

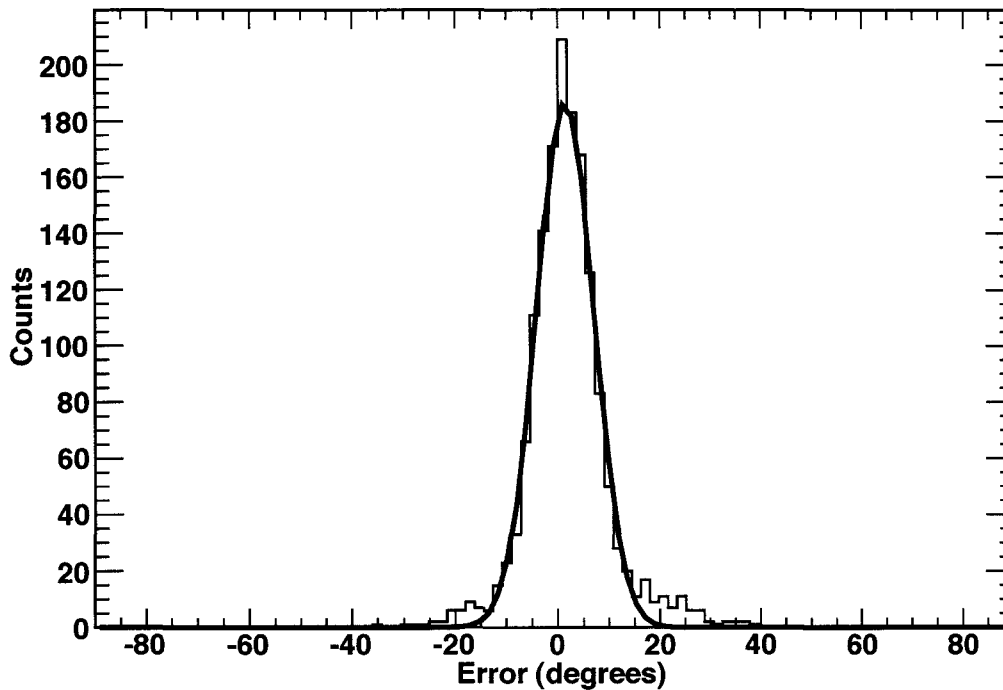


Figure 4–20: Angular Resolution Measurement (ARM) for a continuum neutron spectrum.

The sum of the square of the errors, as given in equation 4.11, in the calculated and geometrical scattering angle account for the total width of the distribution. The geometric scattering angle error is driven by the pulse height information used to determine the location of interaction in the  $z$  dimension;  $x$  and  $y$  do not depend on this quantity. The main contribution to the error is from the pulse height, ToF, and path length measurements used to determine the calculated scattering angle as shown in Figure 4–21.

The distribution in Figure 4–20 shows outlying ARM events in the region  $>15^\circ$  and  $<-15^\circ$ . Simulation studies (more detailed discussion in Chapter 5) show that these events result from scatters in the rear detector (C) with  $<1$  MeV energy deposit and are

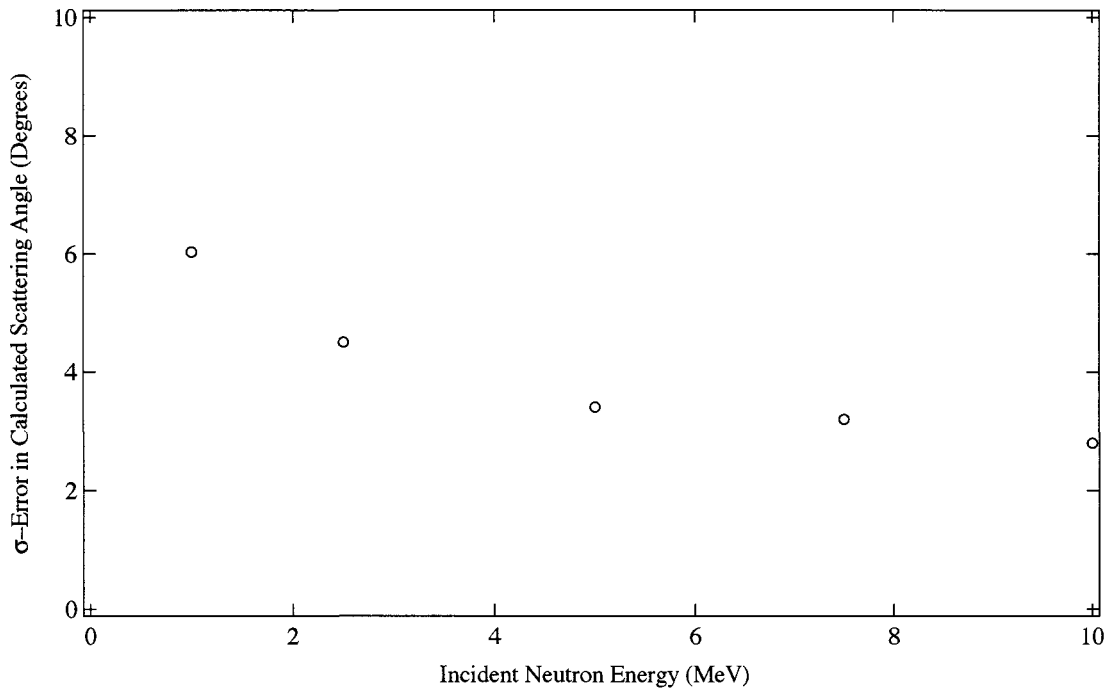


Figure 4–21: Contribution to the error in the calculated scattering angle derived from errors in pulse height, ToF, and position.

not present above this energy. The low-energy transfer to the recoil proton in the rear (second) detector results in low pulse height, leading to greater error in the ToF. Error in the ToF drives the error in the total energy and results in the calculated scattering angle to have either artificially large or small values, producing the outliers.

#### **4.4 NEUTRON BEAM CALIBRATION**

The FNIT SM2 prototype was irradiated for calibration and response with quasi-monoenergetic neutron beams at the Crocker Nuclear Laboratory (CNL) on the University of California–Davis campus located in Davis, CA. The CNL facility is designed to provide a charged particle radiation source for government and space applications and for the radiation therapy for cancer treatment (Castaneda 2001).

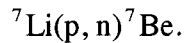
In traditional linear accelerators, charged particle acceleration is done by applying an electric field between two electrodes with the energy gain proportional to the potential difference. In order to achieve greater energization in a workable volume, the cyclotron was developed by Ernest O. Lawrence at the University of California at Berkeley in 1930 (Chu 2005). Cyclotrons occupy smaller volumes and achieve energization by accelerating charged particles through a gap between two semi-circular objects known as “dees” due to their resemblance to a capital letter ‘D.’ A potential difference exists in the gap and the charged particle is accelerated into the hollowed out region of the dee. An axial magnetic field is applied that causes the particles to accelerate with a circular trajectory. Upon exiting the dee, the polarity of the field is reversed and the charged particle is once again accelerated across the gap. The process continues and the orbit increases until it becomes less circular due to relativistic mass increase of the charged particle as it gains energy, at which point the cyclotron frequency is no longer constant. This is the main hinderance of the classical cyclotron. The solution to correct for the nature of this problem is to increase the magnetic induction as a function of increasing radius, which is not possible in the classical cyclotron due to orbital instability (Strijckmans 2001). Isochronous cyclotrons

provide an azimuthally varying field (AVF) that allows the ions to have a constant orbital frequency by increasing the magnetic induction to compensate for the relativistic effects (Chao and Tigner 1999). The AVF also provides beam focusing to minimize losses and efficiently extract the particles.

CNL houses a 76" isochronous cyclotron to accelerate protons, deuterons, and  $\alpha$  particles (Murray et al. 1989). A gas is exposed to high voltage arcing, producing ions that are then removed by an electrode coupled to the radio frequency (RF) of the beam. An alternating current produces an electric field that accelerates the charged particles through each passing of the gap in the  $180^\circ$  dees. Higher harmonics of the electromagnetic field are used to accelerate the heavier deuterons and  $\alpha$  particles without varying nominal beam settings for protons. Axial focusing forces that correct the axial instability are obtained by varying the shape of the magnet surface into a series of "hills" and "valleys." This type of magnetic topography compensates for the relativistic mass increase and allows for higher energies to be achieved.

A quadrupole magnet intercepts the proton beam and focuses it upon a  $^7\text{Li}$  target. A steering magnet adjusts the horizontal and vertical directions to center the beam onto the target. A cylindrical beam pick-off (length = 20 cm, inner diameter = 2.5 cm) provides the zero time signal on the beam ToF scale for ToF measurements of the neutrons traveling between the pick-off and FNIT SM2. The protons then encounter a four jaw carbon collimator to adjust the beam size to be slightly larger than the beam spot on the  $^7\text{Li}$  target so that the transverse location of the neutron source is fixed (Jungerman et al.

1970). Monoenergetic protons interacting with the target produce monoenergetic neutrons of similar energy in the forward direction from the charge exchange reaction



The threshold proton energy for emission of 120-keV neutrons is 1.92 MeV (Beckurts and Wirtz 1964). For protons with energy  $\geq 478$  keV above this threshold, a reaction that results in the  ${}^7\text{Be}$  nucleus left in an excited state becomes energetically possible and produces additional neutrons and de-excitation  $\gamma$  rays. A clearing magnet deflects additional beam protons into a carbon Faraday cup surrounded by a magnet to further reduce the background. A steel collimator (length = 1.55 m) forms an on-axis beam of neutrons that exits from an aluminum window 2.85 m away from the target.

Neutron beams of differing energies can be produced by varying the RF of the cyclotron; there is an inherent spread in the “monoenergetic” neutron beam due to the ionization energy loss in the  ${}^7\text{Li}$  target, which is a function of the particle range through the target (i.e. the target thickness). Five beam energies were provided based on the reactions near resonance of the differential elastic cross-section of  ${}^7\text{Li}(p, n){}^7\text{Be}$  (Liskien and Paulsen 1975). The energies we requested were: 1, 2, 5, 10, and 18 MeV; resonance reactions and the ionization energy losses in the target led to quasi-monoenergetic neutron beams of: <1.0–2.9 MeV, 1.0–2.9 MeV, 1.8–2.9 MeV, 3.6–4.7 MeV, 9.1–10.9 MeV, and 17.6–18.9 MeV. We chose the neutron beam energy range to test the full dynamic range of the prototype instrument to double scatter neutrons. The beam neutron energy is calculated by subtracting the reaction energy (the “ $Q$ -value”) from the incident charged particle energy. The reaction is endothermic and has a  $Q$ -value of  $-1.64$  MeV.

Neutron Energy (MeV)	Target Thickness (mm)	Primary Beam Energy (MeV)	Particle Type	Beam Current ( $\mu\text{A}$ )
3.6 – 4.7	0.39	12.7	$\text{H}_2^+$	4
1 – 2.9	0.39	9	$\text{H}_2^+$	1.5
1.8 – 2.9	0.25	9	$\text{H}_2^+$	0.9
1	0.75, 0.25	5	$\text{H}_2^+$	4, 6
<1 – 2.9	0.89	9	$\text{H}_2^+$	2
9.1 – 10.9	0.89	12.5	$\text{H}^+$	1.6, 2
17.6 – 18.9	0.89	20.4	$\text{H}^+$	0.05 – 0.25

Table 4–1: CNL neutron beam energies and characteristics.

The charged particle and neutron beam energy along with the target thickness and beam current are outlined in Table 4–1. The number of neutrons liberated per RF pulse is Poisson distributed and produces <1 neutron per pulse. A pulsed beam with a 100-ns period produces of order  $1 \times 10^{-3}$  neutrons per pulse.

Varying the orientation of FNIT SM2 with respect to the beam allowed for the determination of the prototype response as a function of incident angle. Instrument rotations in  $15^\circ$  increments between on-axis and  $90^\circ$  were performed for most energies, but limited to the most efficient angles in some cases. The beam size formed by the collimator exit is  $2 \text{ cm} \times 2 \text{ cm}$ . FNIT SM2 was set up on a  $x$ - $y$  rotation and translation table at a distance of 7 m from the collimator exit, a total of 9.85 m away from the target to allow beam divergence to fully cover the largest cross section of the instrument. The

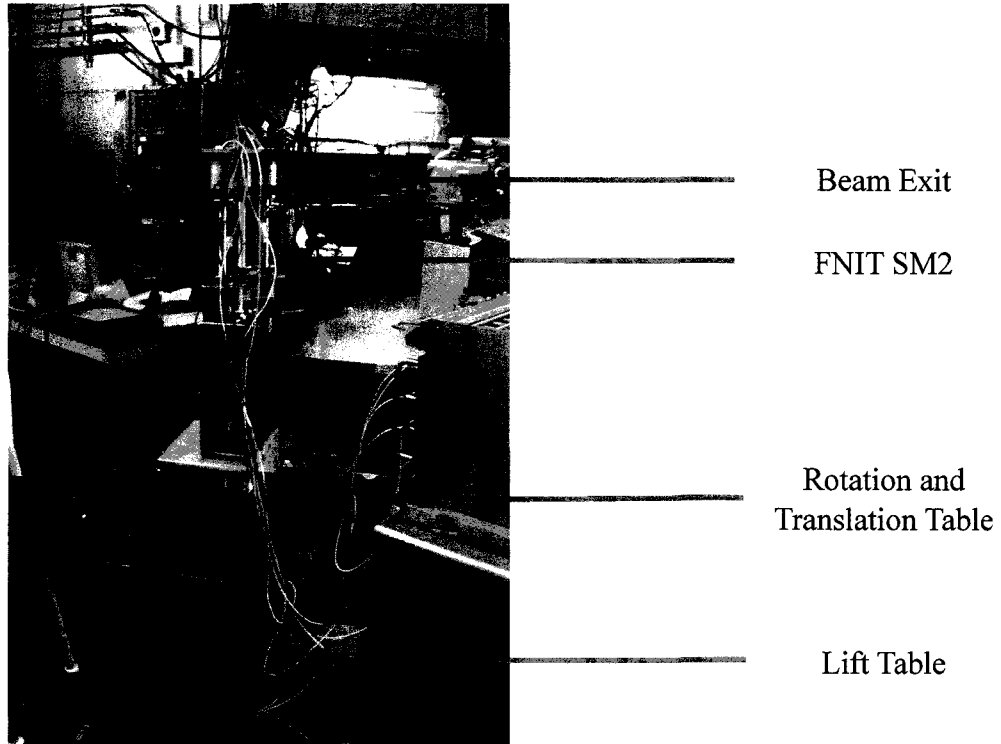


Figure 4–22: FNIT SM2 setup in the CNL beam line.

height of the center of SM2 above the floor was 1.4 m, providing co-alignment with the center of the beam exit (verified by a laser level). The FNIT SM2 location placed it 6 m from the concrete wall located directly behind the prototype.

Dr. Benoît Pirard of the University of Bern (a UNH collaborator) simulated the beam profile, intensity, and background produced by secondary neutrons and  $\gamma$  rays. The simulation consisted of neutrons emitted from a 1.9-cm disk and exiting through a steel collimator (the charge exchange reaction was not simulated). The ambient medium through which the neutrons propagated was modeled as one atmosphere of air. A total of ten sensitive detectors in the simulation monitored the beam as it propagated from the emission disk, interacted with the prototype and the surrounding medium, i.e., concrete



walls near the beam exit and 7 m behind the prototype location. Eight of the ten sensitive detectors were spaced every 2 m between the beam exit and the back wall; the ninth detector was located 1.5 m behind the beam exit and a spherical tenth detector encapsulated the beam emission disk. Neutrons at the experiment location were monitored with an additional spherical sensitive detector for beam profile, intensity and secondaries.

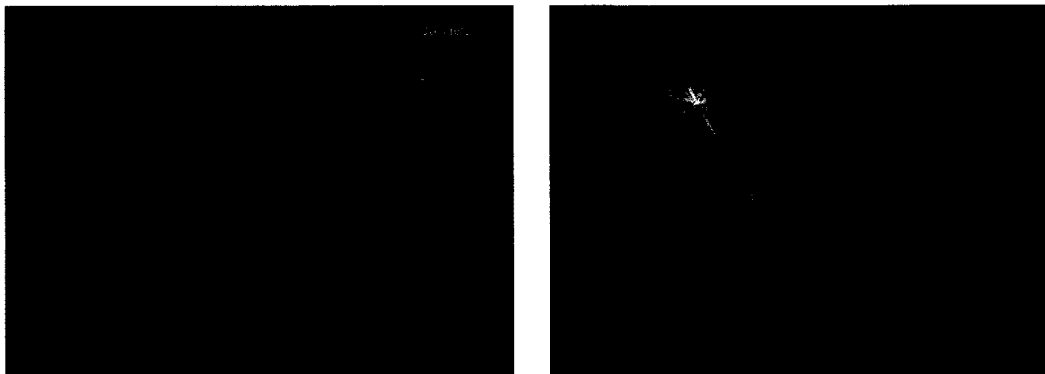
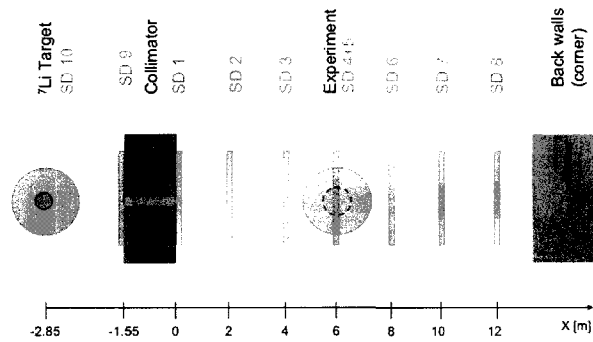


Figure 4–23: Schematic display of CNL neutron beam simulation (top). Visualization of simulation conditions within the beam cave. Experiment location (red) and neutron beam (green) are shown (bottom).

The beam diverges as it leaves the collimator exit to a width of  $\sim 15$  cm at the experiment location. Figure 4–24 shows the beam intensity and size when it exits the collimator ( $x = 0$  m) and at the approximate location ( $x = 6$  m) of FNIT SM2.

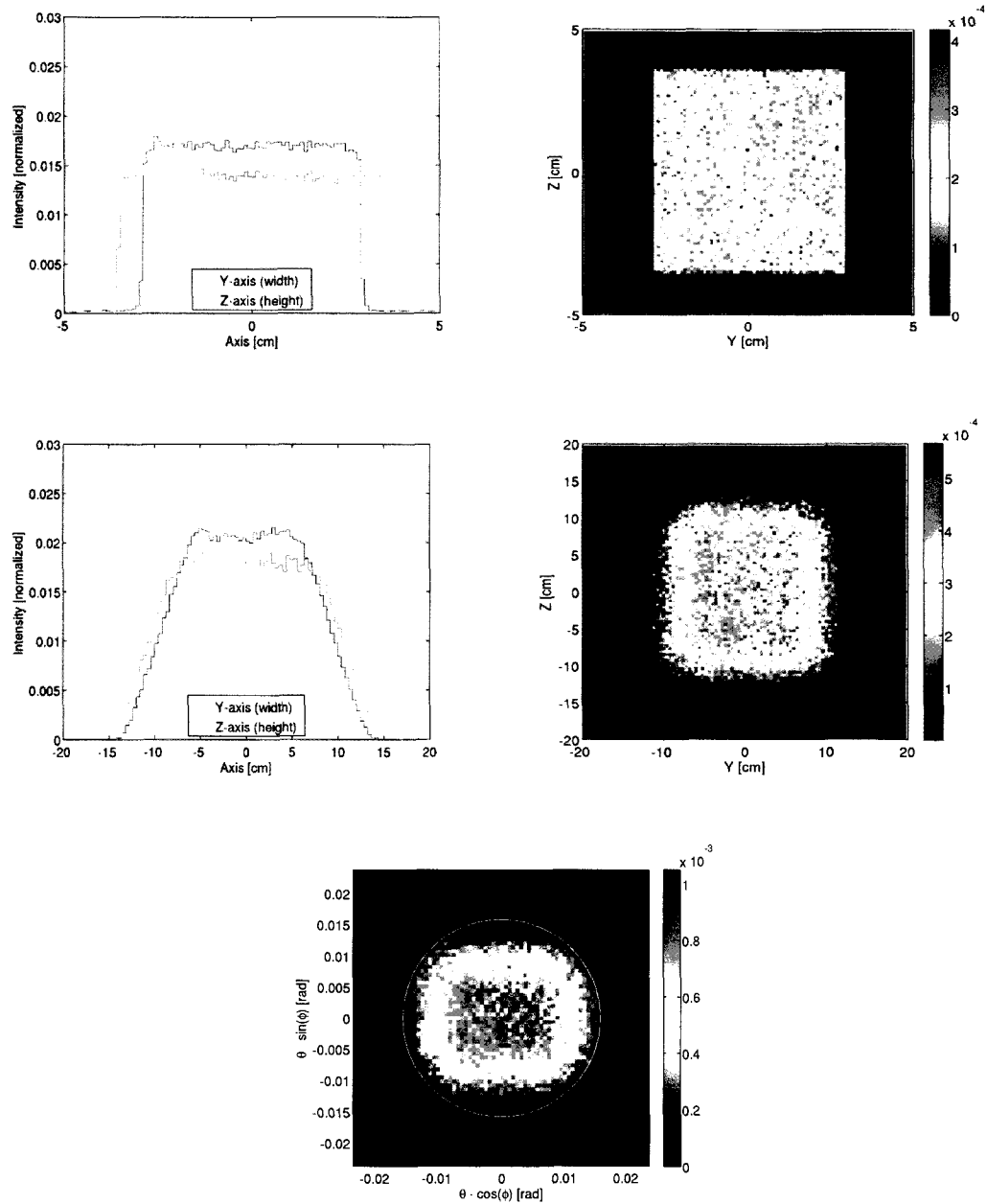


Figure 4–24: Neutron beam profile at collimator exit (top), 6 m from exit (center), and the 10-MeV primary neutron angular distribution at 6 m (bottom).

Neutron Energy	$x = 0$ m (col. exit)	$x = 2$ m	$x = 4$ m	$x = 6$ m	$x = 8$ m	$x = 10$ m	$x = 12$ m
1 MeV	100%	87.7%	83.8%	80.5%	77.6%	74.0%	68.2%
2 MeV	100%	94.5%	92.6%	90.9%	89.5%	87.1%	81.2%
5 MeV	100%	94.5%	92.9%	91.6%	90.5%	88.6%	82.9%
10 MeV	100%	93.7%	91.6%	90.0%	88.7%	86.4%	80.2%
19 MeV	100%	94.6%	92.1%	90.3%	88.8%	86.3%	79.7%

Table 4–2: Beam intensity at varying distances, normalized to collimator exit.

The angular size of the simulated 10-MeV neutron beam at 6 m from the point of emission is shown in Figure 4–24 (bottom). 10-MeV neutrons form a narrowly spread beam in the forward direction, translating into a cross-section at 6 m from the target of ~16 cm. Atmospheric reduction in the beam intensity of up to 10% at the experiment location was found over the 2–20 MeV energy range, with a 20% reduction at 1 MeV. Intensity was normalized to that measured at the collimator exit for all neutrons that pass through the sensitive detectors at each distance (Table 4–2). The distribution in energy and angle of the background (scattered) radiation is shown in Figure 4–25. The direction and energy distribution shown in Figure 4–25 are for neutrons and  $\gamma$  rays that scattered with the surroundings prior to passing through the spherical sensitive detector window ( $d = 30$  cm) located at  $x = 6$  m. The normalized intensity in each figure is with respect to the number of primary neutrons in the beam. Table 4–3 shows the percentage of primary neutrons scattered prior to reaching the experiment location and the intensity of the background (secondaries) produced from interactions with the walls, concrete, collimator, and air.

Neutron Energy	Primary neutrons w/ prev. interaction	Secondary neutrons	Secondary $\gamma$ rays
1 MeV	6.3%	0.1%	0.3%
2 MeV	4.8%	0.5%	0.3%
5 MeV	3.5%	0.6%	0.4%
10 MeV	4.2%	0.9%	0.7%
19 MeV	5.7%	1.1%	0.9%

Table 4–3: Intensity of induced background at 6 m.

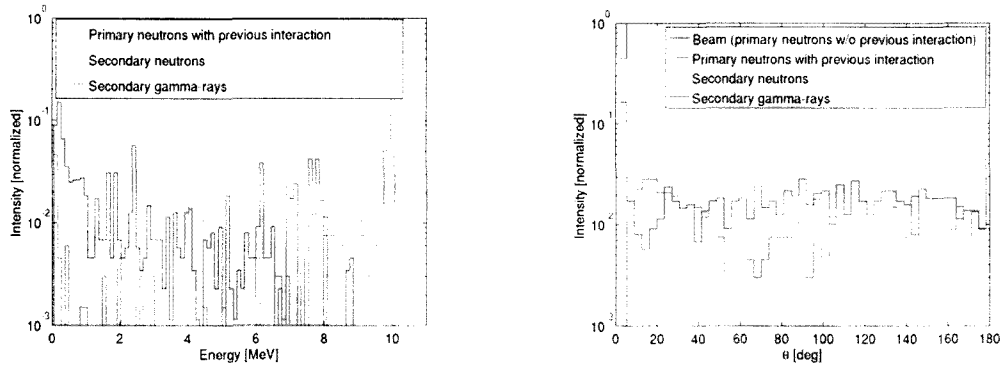


Figure 4–25: Energy (left) and directional (right) distribution of induced background at 6 m.

The primary neutron beam scattered more than once up to 7% of the beam intensity before reaching the prototype location, and was most severe at the lowest energy. The secondary neutron and  $\gamma$ -ray intensity comprised  $\sim 1\%$  of the total of primary beam neutrons. We chose the experiment location with the lowest background of secondary scatters. This location was approximately halfway between the beam exit and the rear concrete wall.

#### 4.4.1 DATA ANALYSIS

Calibration in the laboratory at UNH determined that the dynamic range of the prototype electronics was not sufficient for double scatter neutron measurements above 10 MeV. To accommodate the prototype dynamic range for neutron energies  $>10$  MeV, we developed a calibration plan to investigate the response (e.g. inelastic scattering contributions) by collecting the data with a different set of settings for high voltage, trigger and spectroscopy amplifier gain. Coincident events between detectors A–C or B–C trigger the data acquisition system and process the beam ToF, instrument ToF, pulse shape for A or B and C, and pulse height of A-PMT1, 2 or B-PMT1, 2 and C-PMT1, 2. The set up of the beam ToF logic was such that the beam pick-off initiated the STOP signal and either one of the front two detectors (A or B) provided a START. The STOP from the beam occurs much more frequently than an interaction in SM2. The beam ToF scale was set to a 1- $\mu$ s window to account for the long neutron transit time from the beam. Energy and incident angle dictated the integration time of each run such that a number of triggers – satisfying Gaussian statistics – could be recorded. To obtain the desired number of double scatter events, we aimed for  $\sim 1 \times 10^5$  triggers based on the simulated efficiency of the prototype. Instrument triggers constituted any interaction in the scintillator volume that produced a pulse height above threshold, i.e., single, double, and triple scatters. A scaler NIM module, whose input was from the four-fold logic unit, monitored the single, double, and triple scatter rate. We required count rates of 3 kHz (singles) and 3 Hz (doubles) in order to reduce the effects of pile-up and dead time in the

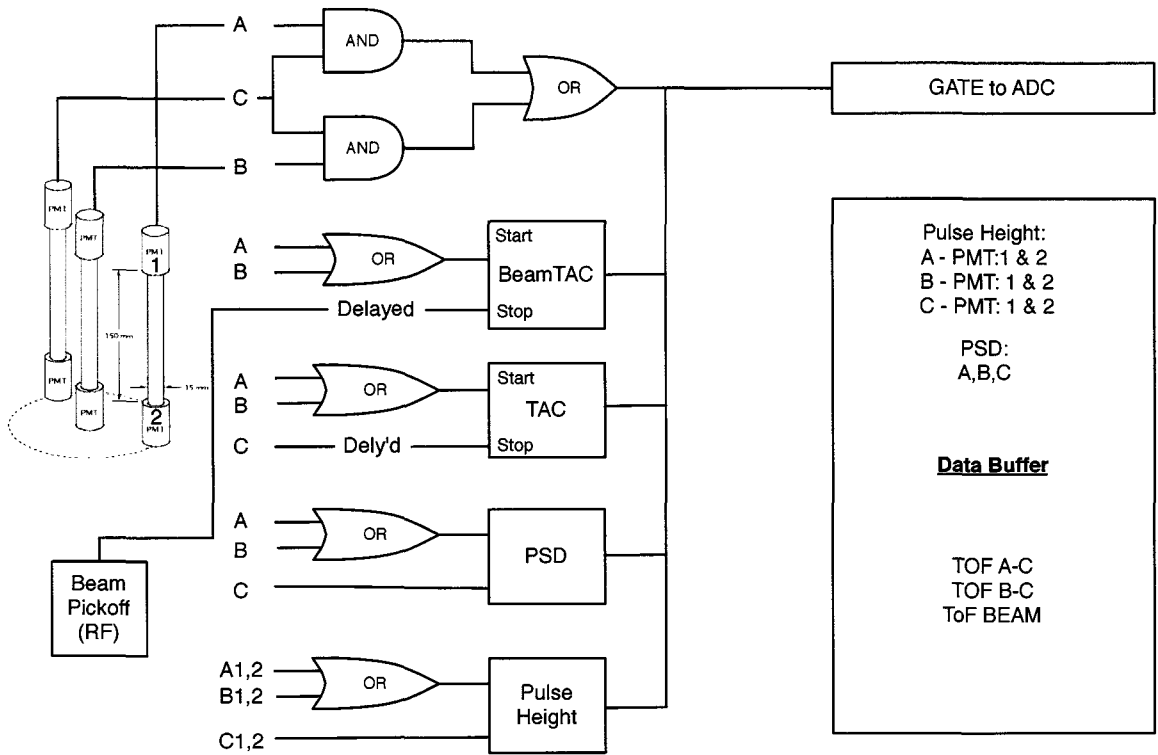


Figure 4-26: FNIT SM2 block diagram in double scatter mode.

data acquisition system; triple coincidence are rare and were not considered for these issues.

Beam time at CNL was reserved for five days over the week of 13–17 August 2007. We divided the beam schedule according to the required calibration settings. The first set of runs chosen were in the middle of the prototype range: 3.6–4.7 MeV. Due to the non-uniformity along the length of the rod (as discussed in section 4.3), the trigger level was lower near the ends than near the center. Doubly scattered neutrons near 4.7 MeV were at risk for saturating the system. We corrected for this by implementing a combination of both “high-energy” neutron and “low-energy” neutron calibration settings. However, due to the initial incorrect set up of the beam ToF, the results from this energy range were not used. The second, third, and part of the fourth day concentrated on

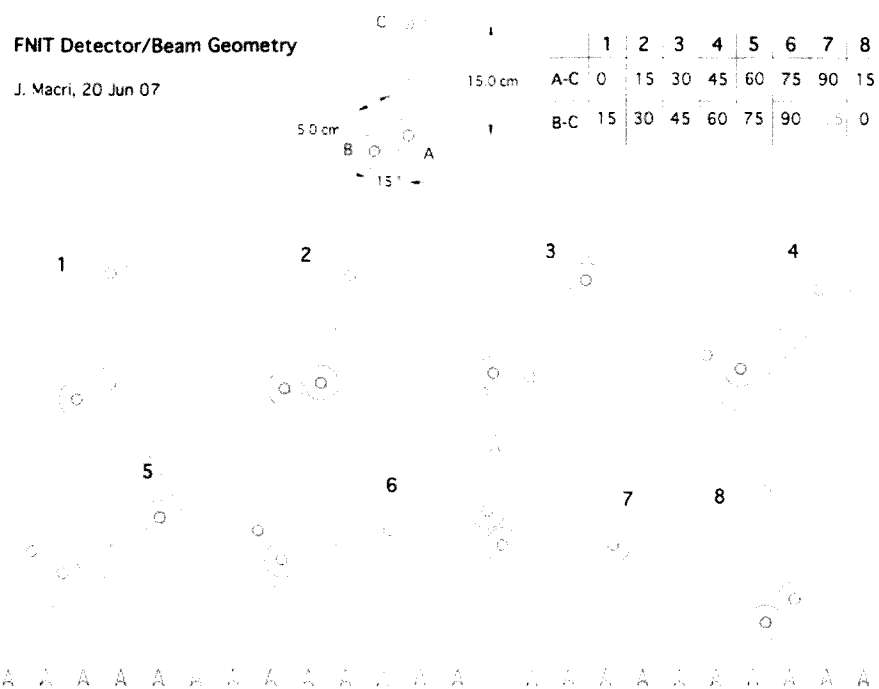


Figure 4–27: FNIT SM2 orientations with respect to the neutron beam.

the “low-energy” neutrons. These runs consisted of – energy: 1.0–2.9 MeV (orientation:  $0^\circ, \pm 15^\circ, 30^\circ, 45^\circ, 60^\circ$ ); 1.8–2.9 MeV ( $0^\circ, 30^\circ, 60^\circ$ ); and  $<1.0$ –2.9 MeV ( $0^\circ, 30^\circ, 60^\circ$ ). Run time and number of triggers acquired are summarized in Table 4–4. Time limits and angle dependent efficiency did not allow for all incident angles and energies to yield the desired number triggers of  $\sim 1 \times 10^5$ . A set of ToF and PSD parameters determined in the laboratory at UNH would govern the optimal event selections for valid neutron events. Additionally, event selections on the neutron beam ToF would be used as an additional tool for obtaining the beam neutron signal. However, at low-energy, the neutron production and immense number of 478-keV  $\gamma$  rays produced by inelastic proton scattering on  ${}^7\text{Li}$  nuclei (Bayanov et al. 2006) gave unexpected results in event selection

Angle	<1.0–2.9 MeV (Run Time; Triggers)	1.0–2.9 MeV (Run Time; Triggers)	1.8–2.9 MeV (Run Time; Triggers)
0°	1860 s; $1.0 \times 10^4$	2220 s; $1.0 \times 10^5$	1140 s; $2.4 \times 10^4$
15°	X	1560 s; $1.1 \times 10^5$	X
30°	2220 s; $2.0 \times 10^4$	1380 s; $1.1 \times 10^5$	3240 s; $1.3 \times 10^5$
45°	X	1500 s; $9.6 \times 10^4$	X
60°	2520 s; $1.0 \times 10^4$	2760 s; $9.5 \times 10^4$	1020 s; $1.0 \times 10^4$
-15°	X	1320 s; $7.1 \times 10^4$	X

Table 4–4: Run time and number of triggers obtained for “low-energy” neutron beams at varying orientations.

analysis. There was an absence of a narrow peak corresponding to neutrons in the beam ToF; instead a histogram of the raw beam ToF data produces the spectrum observed in Figure 4–28, where the peaks located near beam ToF values of ~5 ns and ~55 ns correspond to the 478-keV  $\gamma$  rays. A nearly featureless, flat spectrum is observed otherwise.



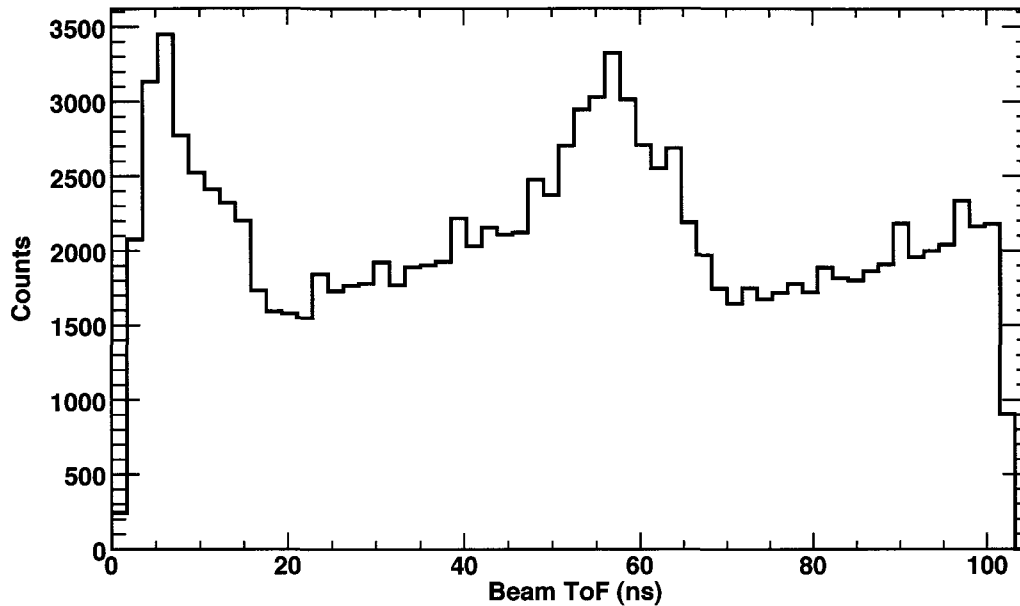


Figure 4–28: Beam ToF spectrum with no event selections applied.

However, if we consider the ToF measured by the instrument (either from A–C or B–C) the slower moving neutrons can be clearly separated from the  $\gamma$  rays. This can be seen in Figures 4–29 and 4–30 (top) which shows the instrument measured ToF A–C and scatter plots of ToF vs. pulse height for both front and rear detectors. Pulse shape in front and rear detectors vs. pulse height also shows the separation between neutrons and  $\gamma$  rays with the neutron events corresponding to pulse shape values  $>1000$  (Figure 4–30c and d).

We learned that first selecting on the instrument measured ToF (either ToF A–C or ToF B–C) could be used to obtain the beam neutron signal. By placing event selections on the ToF in Figure 4–29 between 5 ns and 22 ns – corresponding to neutrons – we obtain the results shown in Figure 4–31a and c, for the beam ToF and the  $D_1$  vs.  $D_2$  PSD, respectively. A scatter plot of the beam ToF vs. pulse shape in one of the front detectors

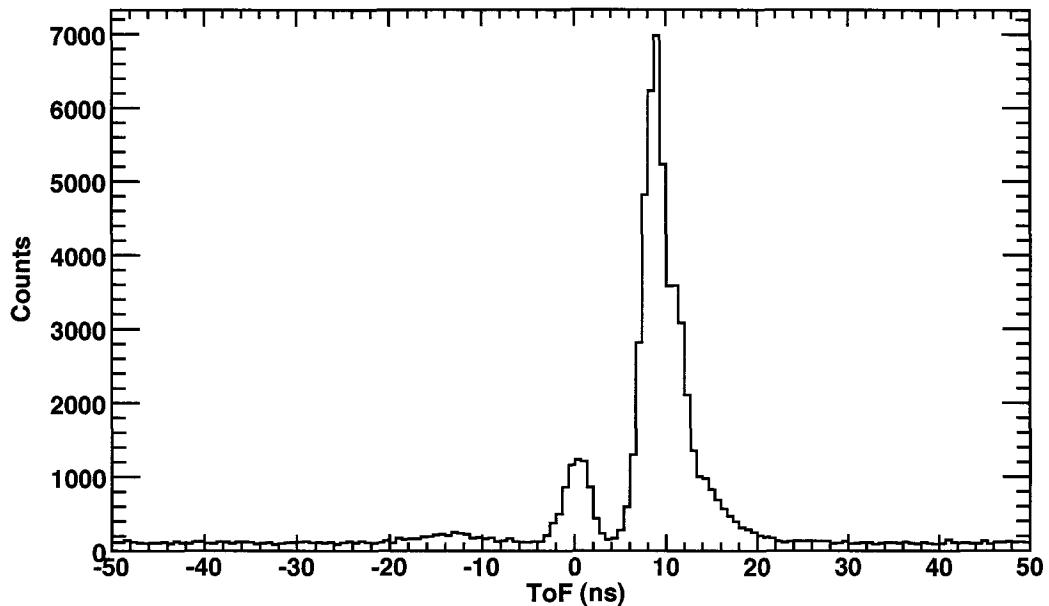
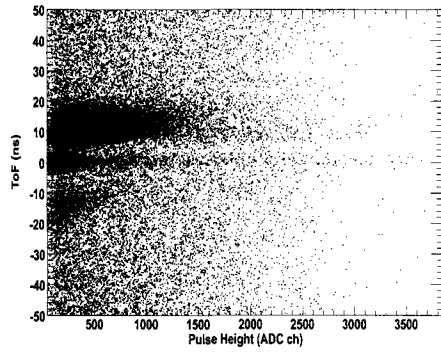
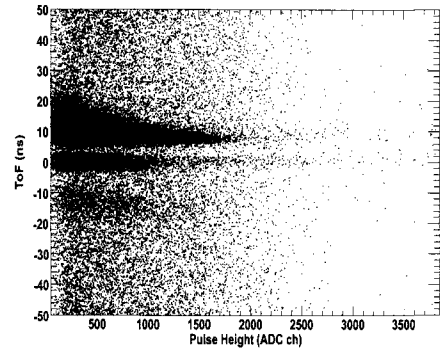


Figure 4–29: Instrument measured ToF for 1.0–2.9 MeV neutrons.  $\gamma$ -ray events peak around 0 ns and neutron events are observed with ToF values  $>5$  ns. Neutron back scatters can be observed with negative ToF values around  $-15$  ns.

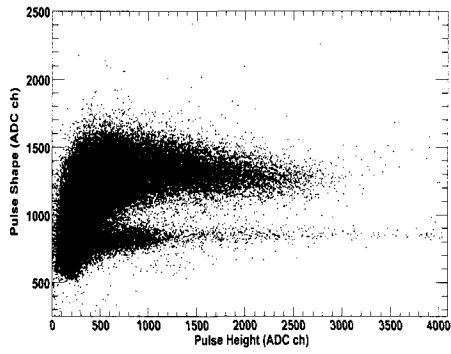
elucidates the quasi-monoenergetic neutrons (Figure 4–32 top) with pulse shape values between  $\sim 1000$ – $1200$  and beam ToF values between  $\sim 40$ – $55$  ns. 2-d selections on these beam ToF and PSD values were made to filter out the beam neutron signal. Additional selections were made on the PSD of the second scatter determined from a scatter plot of PSD in each detector (Figure 4–31c). For comparison, event selections on the ToF in Figure 4–29 between  $\pm 3$  ns – corresponding to  $\gamma$  rays – yields the results shown in Figure 4–31b and d. The importance of good ToF, PSD and beam ToF measurements are evident from the figures. Lastly, we note in Figure 4–32 the multiple distinct regions from the beam neutrons (top) and 478-keV  $\gamma$  rays (bottom) produced at the target as multiple beam cycles are measured within the beam ToF coincidence window.



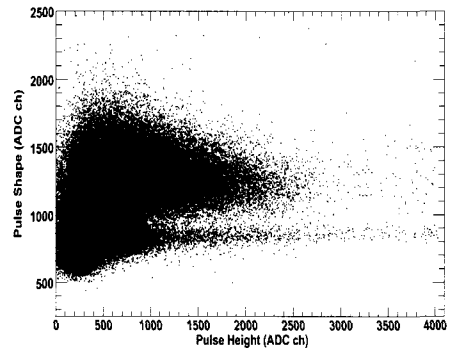
(a)



(b)

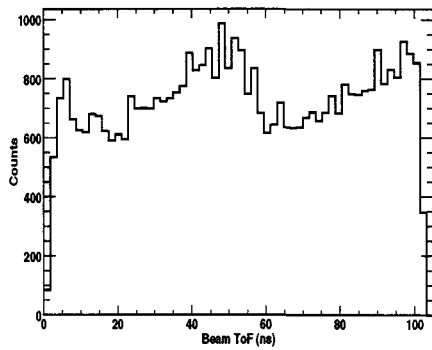


(c)

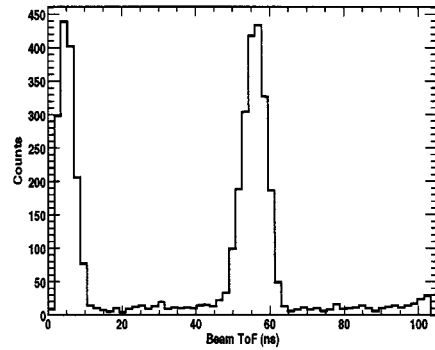


(d)

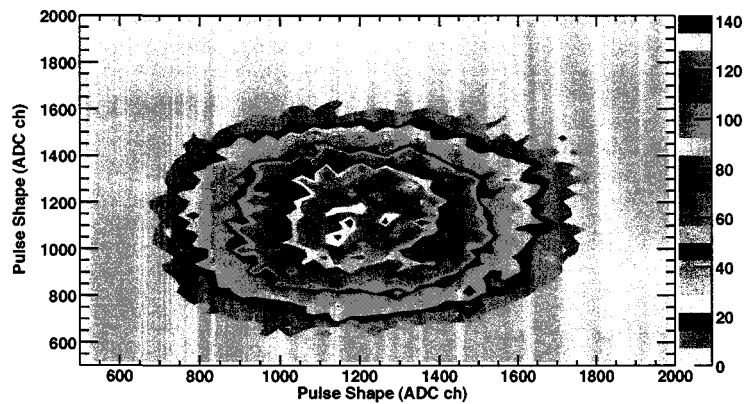
Figure 4–30: ToF A–C vs. (a) detector A pulse height, (b) detector C pulse height; (c) pulse shape vs. pulse height in detector A, (d) pulse shape vs. pulse height in detector C.



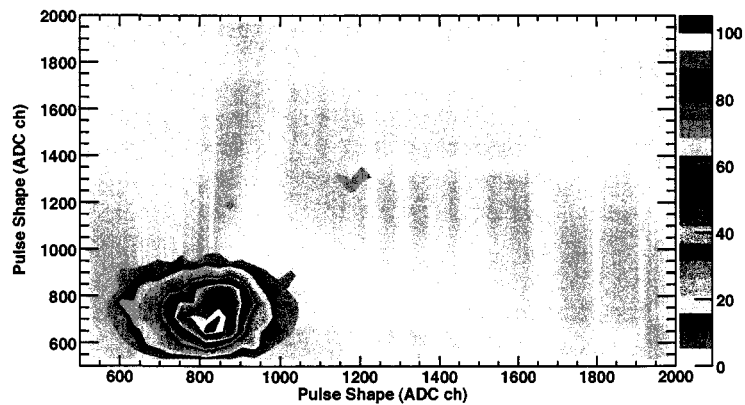
(a)



(b)



(c)



(d)

Figure 4–31: Beam ToF spectrum with instrumental ToF cuts for (a) neutrons, (b)  $\gamma$  rays, (c) PSD<sub>1</sub> vs. PSD<sub>2</sub> with neutron ToF cuts applied, (d) PSD<sub>1</sub> vs. PSD<sub>2</sub> with  $\gamma$ -ray ToF cuts applied.

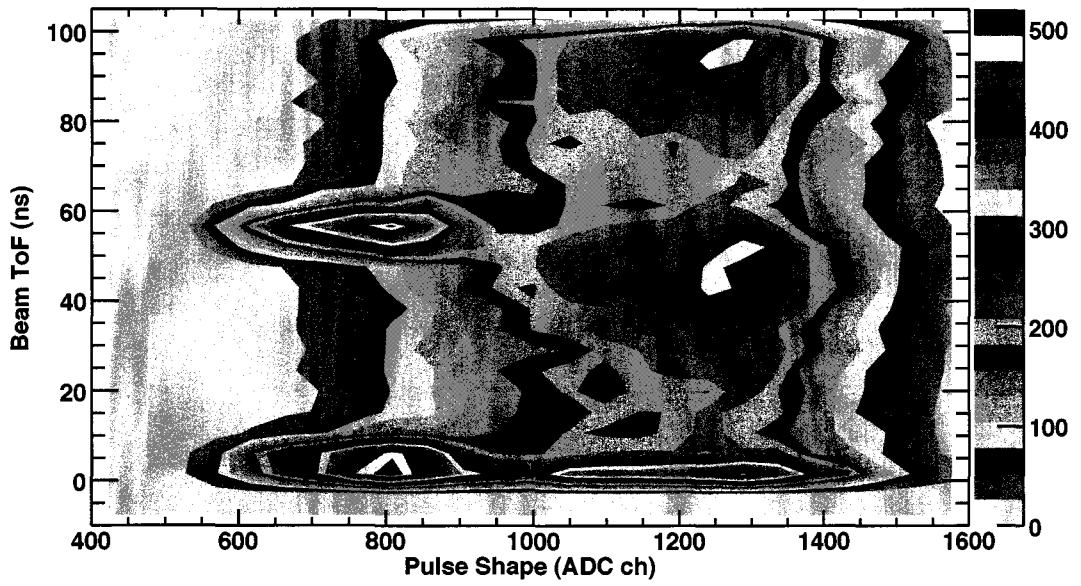
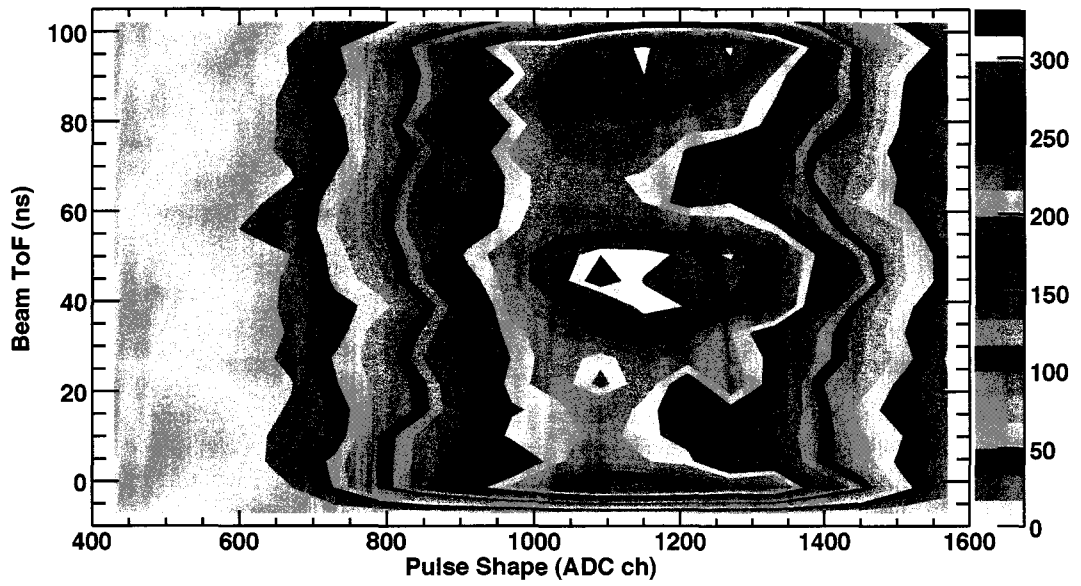


Figure 4–32: Beam ToF vs. PSD<sub>1</sub> with: instrumental neutron ToF cuts applied (top) and no instrumental ToF cuts applied (bottom).

For PSD that demonstrates high figure-of-merit,  $M(E)$ , an additional set of criteria can be imposed on the ToF spectrum with a high rate of false coincidence events. This was the case during times of high intensities from the beam. Equally sized windows for neutron ToF and false coincidence ToF events are selected and analyzed as 2-d scatters of  $D_1$  vs.  $D_2$  PSD for each window. Taking the difference between the false coincidence ToF events from neutron ToF events allows for PSD to display a clearer identification of the neutrons in PSD data space. The extra step of subtraction provides another level of scrutiny to the standard procedure of selecting on beam ToF vs.  $D_1$  PSD with only neutron ToF events selected. This analysis routine is best for high  $M(E)$  PSD, as we had for detectors A and C. However, this method was not employed for the PSD obtained with detector B (BC-519) as a result of the poor performance shown in section 4.3.5.

The total incident neutron energy is reconstructed based on the kinematic principles outlined in section 3.2.1 using the measured ToF (to obtain scattered neutron energy) and the recoil proton energy deposit in the first scatter. Attempts to reconstruct the total energy using a simple sum of the recoil proton energy in each detector – without scattered neutron energy – yields a systematically lower total neutron energy. However, the performance of the reconstructed neutron energy using ToF is degraded for short ToFs (i.e., scattered neutrons with energy upwards of 5 MeV). “Low-energy” neutrons traveling a distance of 15 cm (A-C)/17.6 cm (B-C) produce cleanly separated neutron and  $\gamma$ -ray ToF peaks (Figure 4-29). Scattered neutrons of higher energy produce ToF signals that more closely resemble  $\gamma$  rays. As the separation between neutrons and  $\gamma$  rays in the ToF spectrum decreases, ToF selections become more ambiguous. A method based

on a Maximum Likelihood Estimator (MLE) provided restrictions on the scattered neutron energy by using, not only the ToF, but also the recoil proton energy deposit in the second scatter and the neutron path length.

$$MLE(\Delta t, E_{p_2} | E_{n'}) = p(\Delta t | E_{n'}) \times (E_{p_2} | E_{n'}) \quad (4.12)$$

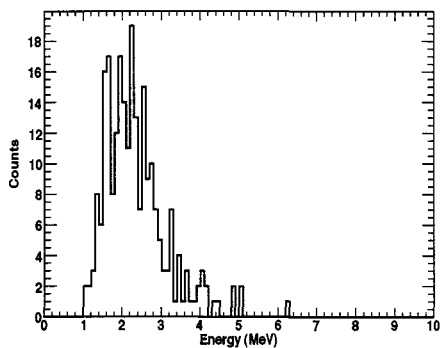
where

$$p(\Delta t | E_{n'}) = \frac{1}{\sigma_t \sqrt{2\pi}} \exp\left(-\frac{(\Delta t - \mu_t)^2}{2\sigma_t^2}\right) \quad (4.13)$$

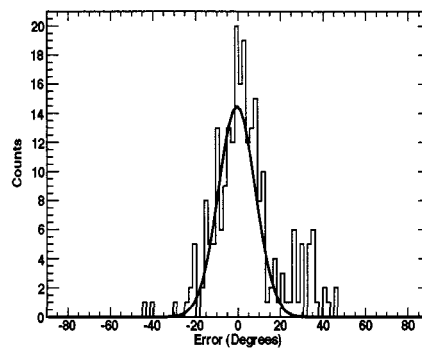
$$\mu_t = \frac{d}{c} \frac{1}{\sqrt{1 - \left(\frac{m_n c^2}{E_{n'} + m_n c^2}\right)^2}} \quad (4.14)$$

$$p(E_{p_2} | E_{n'}) = \frac{1}{E_{n'}} \quad (\text{for } 0 < E_{p_2} < E_{n'}) \quad (4.15)$$

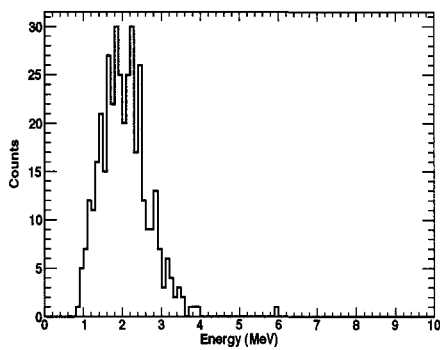
A restriction in the ToF value given the recoil proton energy deposit in the second scatter and the position of each scatter in each rod (path length) maximizes the probability of obtaining the true scattered neutron energy. Employing this method led to a more precise reconstruction of “high-energy” neutrons. Figures 4–33 through 4–36 show the A–C/B–C count spectra for a neutron beam energy of 1.0–2.9 MeV at the various rotation angles.



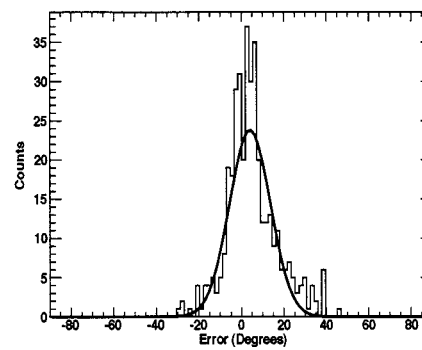
(a)



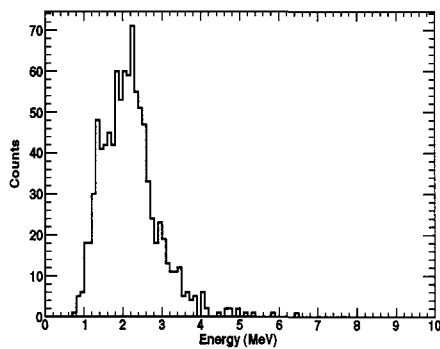
(b)



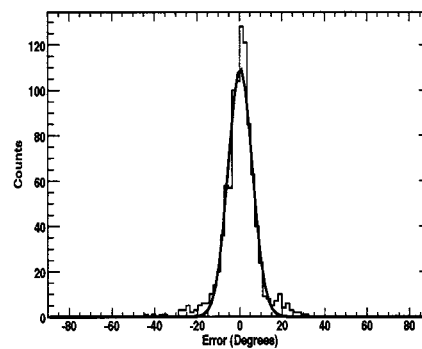
(c)



(d)



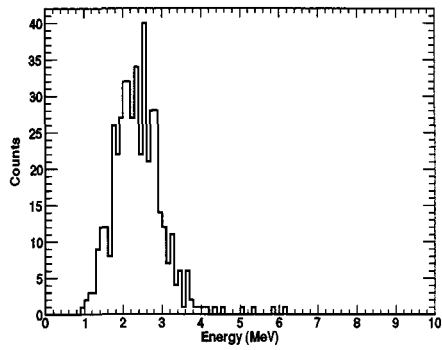
(e)



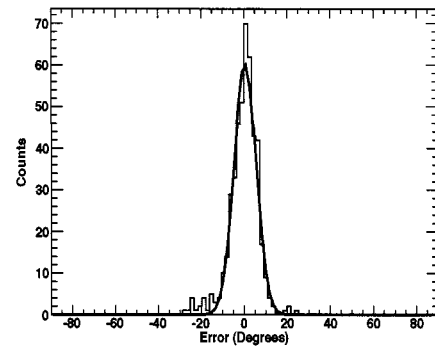
(f)

Figure 4-33: 1.0–2.9 MeV count spectrum and ARM for A–C orientations: 0° (a) and (b), 15° (c) and (d), 30° (e) and (f).

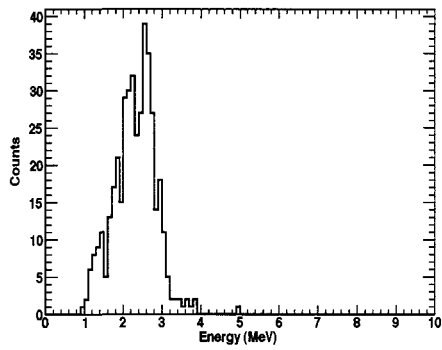




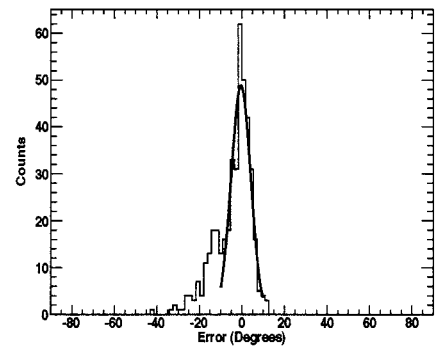
(a)



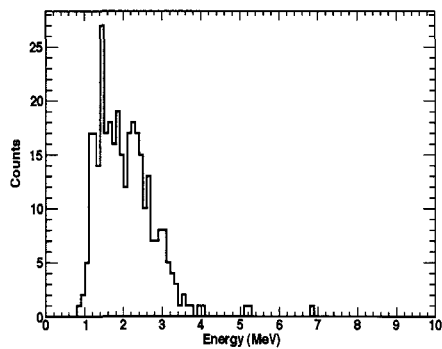
(b)



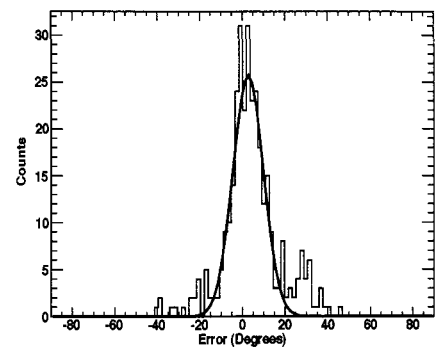
(c)



(d)

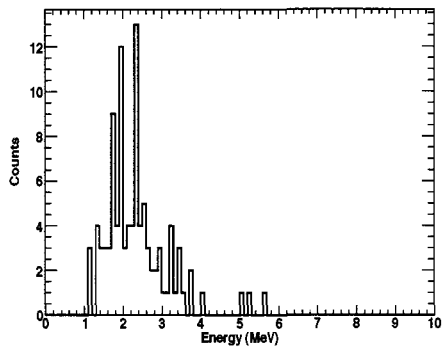


(e)

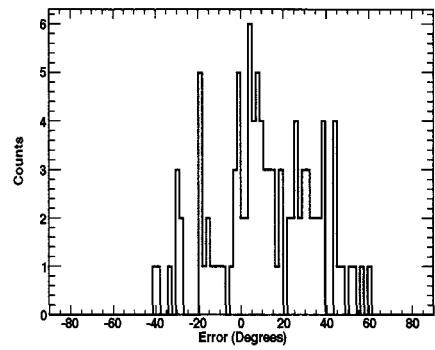


(f)

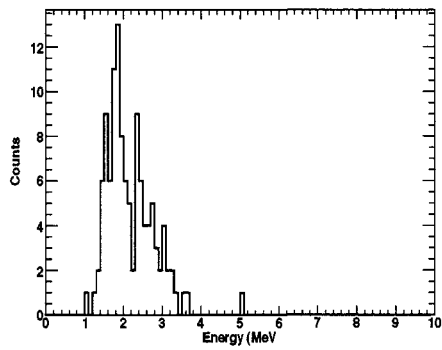
Figure 4–34: 1.0–2.9 MeV A–C count spectrum and ARM for A–C orientations: 45° (a) and (b), 60° (c) and (d), –15° (e) and (f).



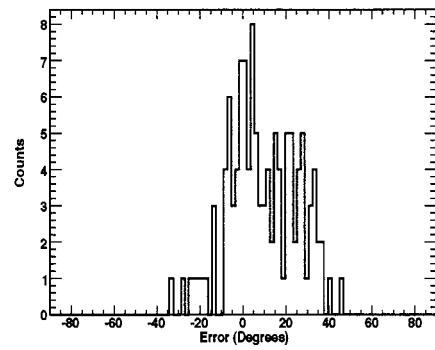
(a)



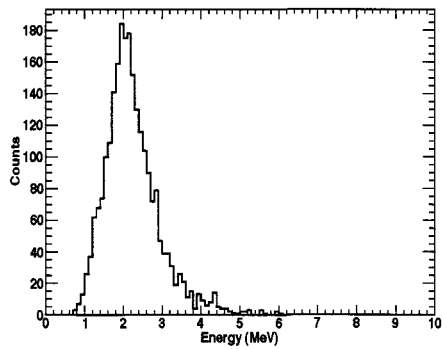
(b)



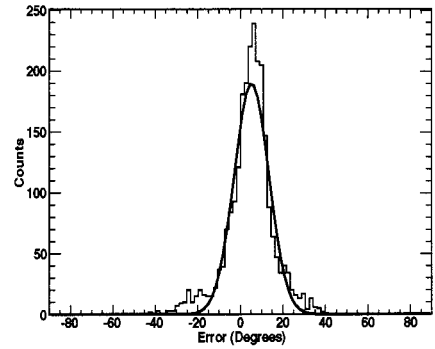
(c)



(d)

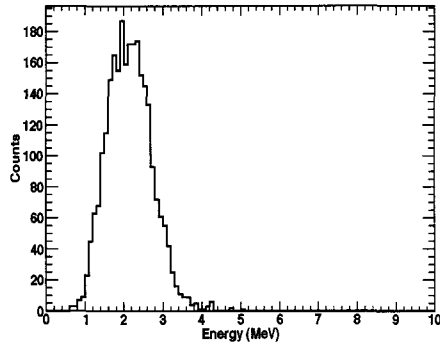


(e)

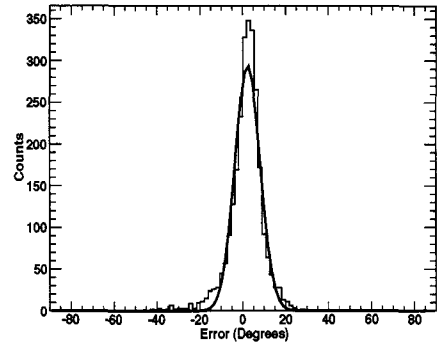


(f)

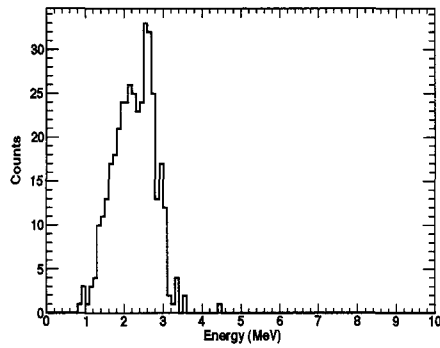
Figure 4–35: 1.0–2.9 MeV count spectrum and ARM for B–C orientations: 0° (a) and (b), 15° (c) and (d), 30° (e) and (f).



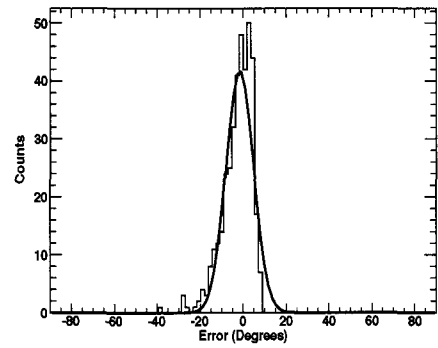
(a)



(b)



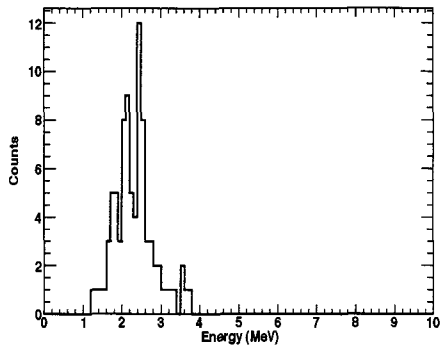
(c)



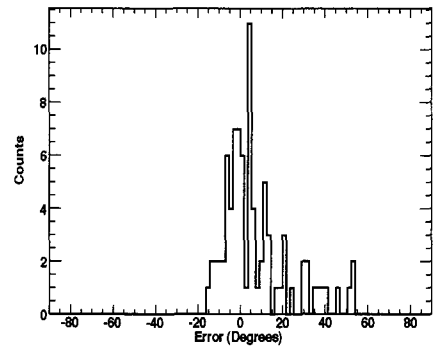
(d)

Figure 4–36: 1.0–2.9 MeV count spectrum and ARM for B–C orientations: 45° (a) and (b), 60° (c) and (d).

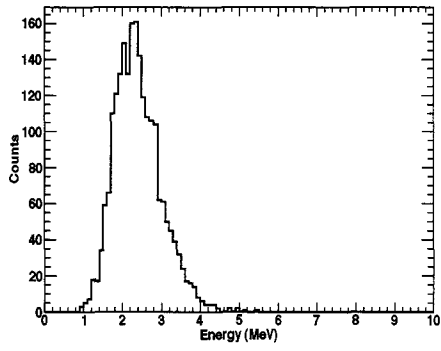
Figures 4–37 and 4–38 show the A–C/B–C count spectra for a neutron beam energy of 1.8–2.9 MeV at the various rotation angles. The sharper energy peak was obtained by changing the target thickness from 0.39 mm to 0.25 mm.



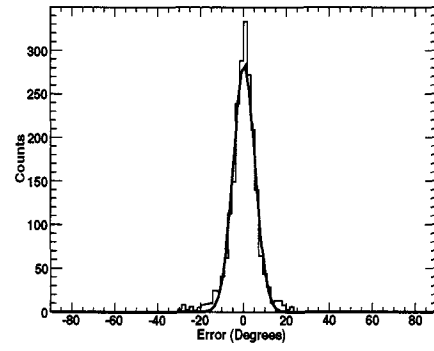
(a)



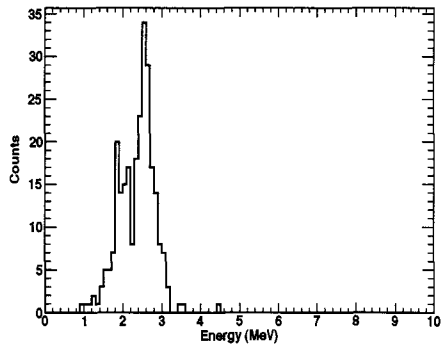
(b)



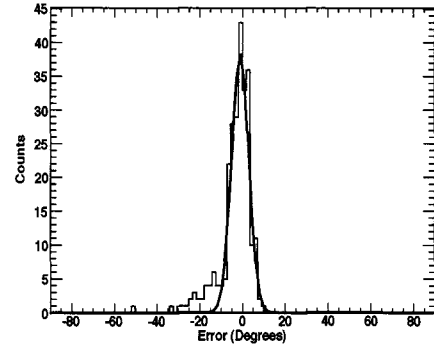
(c)



(d)

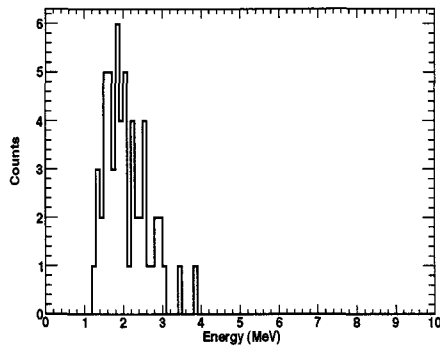


(e)

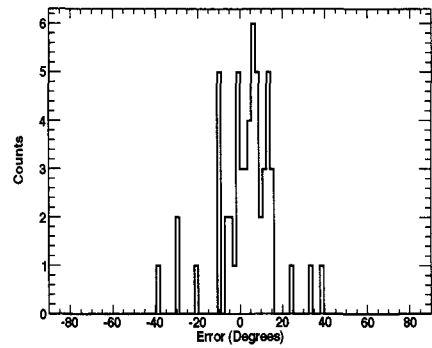


(f)

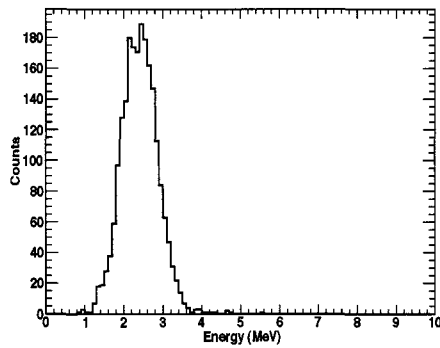
Figure 4–37: 1.8–2.9 MeV count spectrum and ARM for A–C orientations: 0° (a) and (b), 30° (c) and (d), 60° (e) and (f).



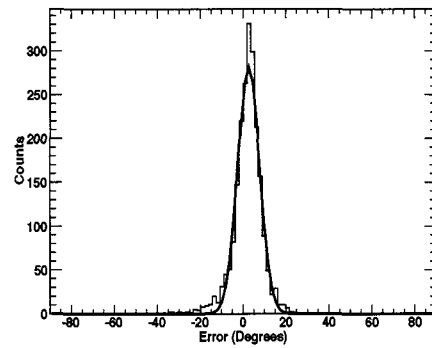
(a)



(b)



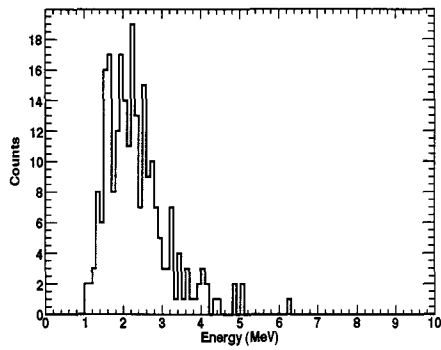
(c)



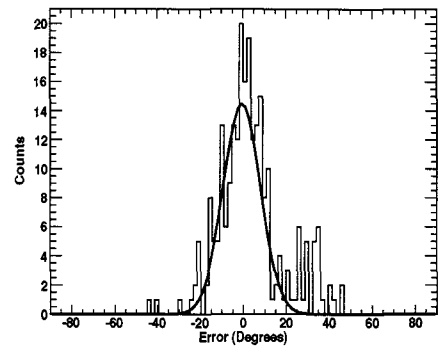
(d)

Figure 4–38: 1.8–2.9 MeV count spectrum and ARM for B–C orientations: 15° (a) and (b), 45° (c) and (d).

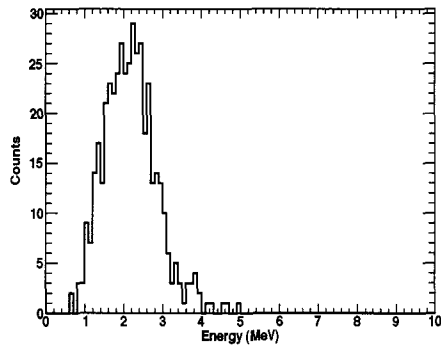
An unsuccessful attempt to produce ~1-MeV monoenergetic neutrons was made using 0.75-mm and 0.25-mm targets and a 5-MeV deuteron beam. The result was a hole burnt into the thin target. Instead a 0.89-mm target and a 9-MeV deuteron beam was used to produce neutrons from 2.9 MeV to below the prototype threshold. Figures 4–39 and 4–40 show the A–C/B–C count spectra for a neutron beam energy of <1.0–2.9 MeV at the various rotation angles.



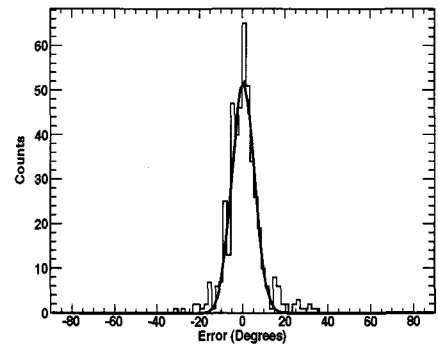
(a)



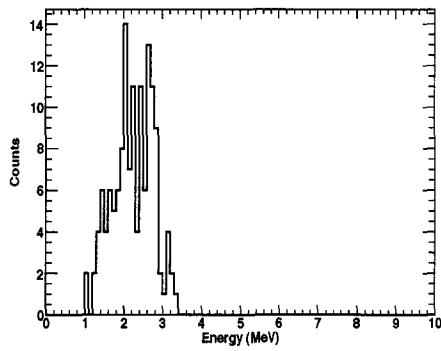
(b)



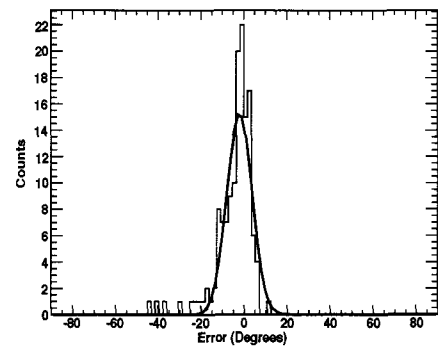
(c)



(d)



(e)



(f)

Figure 4-39: <math><1.0\text{--}2.9\text{ MeV}</math> count spectrum and ARM for A-C orientations:  $0^\circ$  (a) and (b),  $30^\circ$  (c) and (d),  $60^\circ$  (e) and (f).

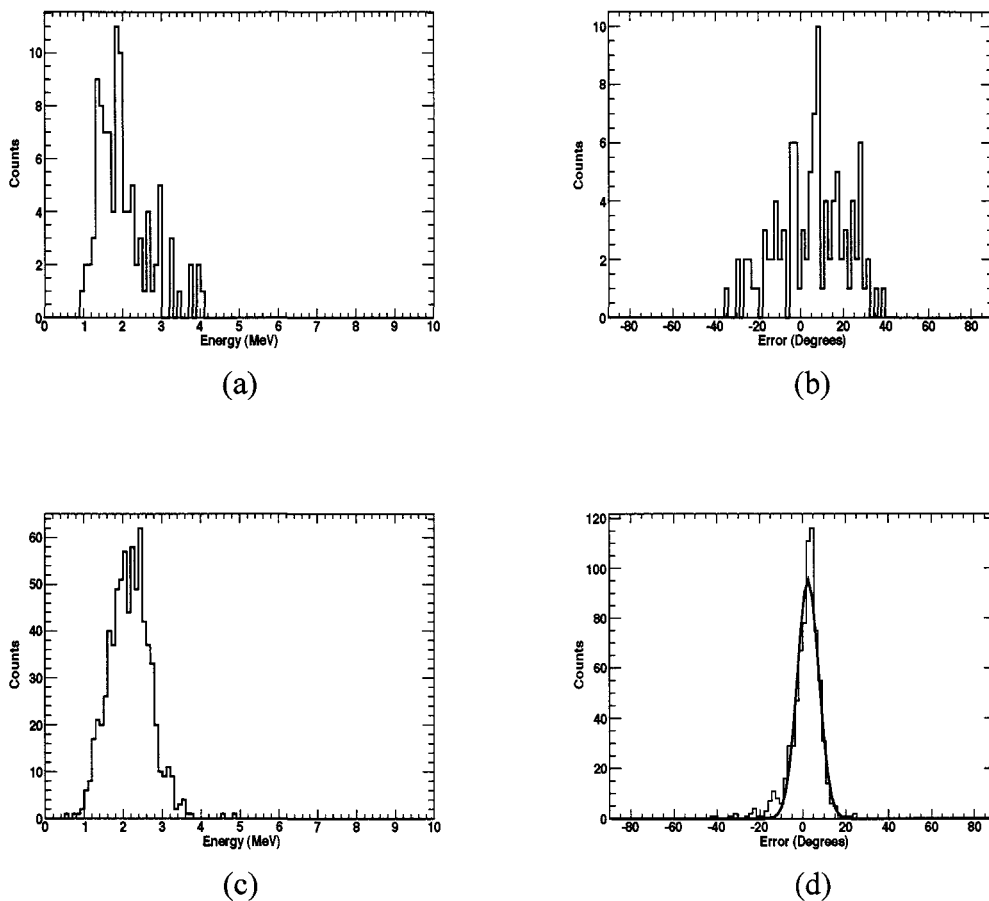


Figure 4-40: <math>\langle 1.0\text{--}2.9\text{ MeV}</math> count spectrum and ARM for B-C orientations: 15° (a) and (b), 45° (c) and (d).

Beam time during the latter half of the fourth and fifth day consisted of runs with neutron energies of 9.1–10.9 MeV and 17.6–18.9 MeV. The ToF spectrum recorded by the instrument for these “high-energy” runs is shown in Figure 4-41. Blurring of the  $n/\gamma$ -ray ToF is evident in the spectrum and the scatter plots of ToF vs. pulse height (Figure 4-42). The run times and number of triggers acquired for the high-energy runs are summarized in Table 4-5.

Angle	9.1–10.9 MeV (Run Time; Triggers)	17.6–18.9 MeV (Run Time, Triggers)
30°	8400 s; $1.0 \times 10^4$	4620 s; $3.1 \times 10^4$

Table 4–5: Run time and number of triggers obtained for “high-energy” neutron beams at 30°.

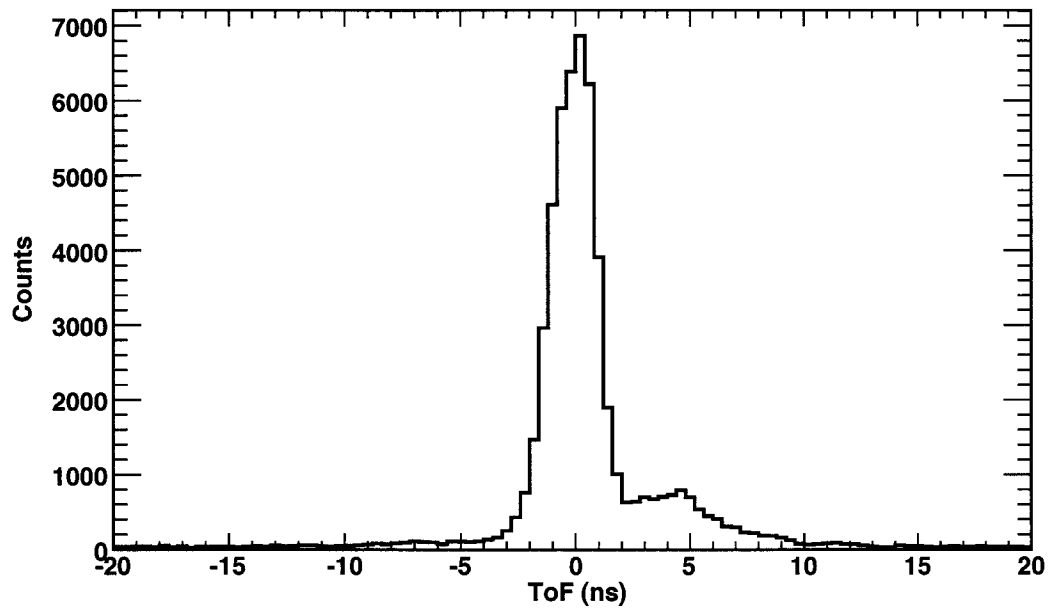


Figure 4–41: Instrument measured ToF for 9.1–10.9 MeV neutrons.



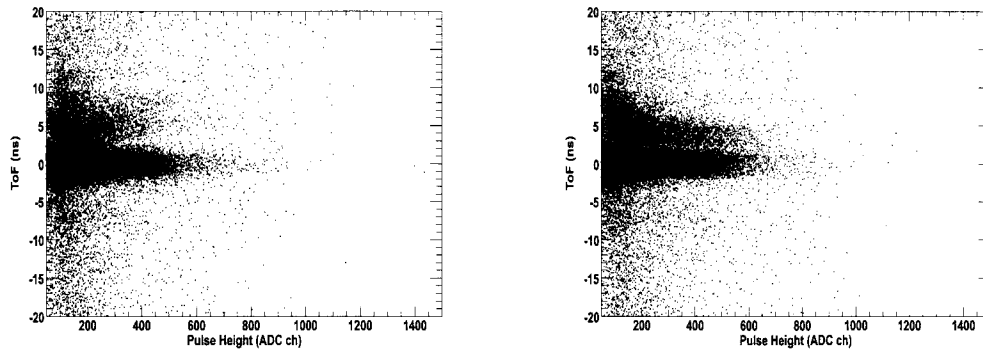
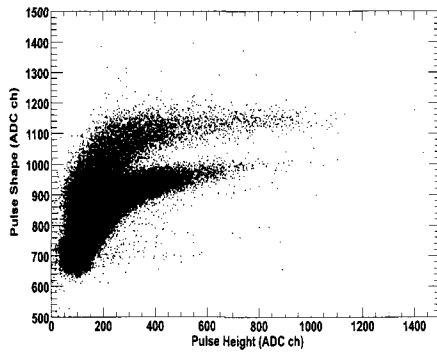
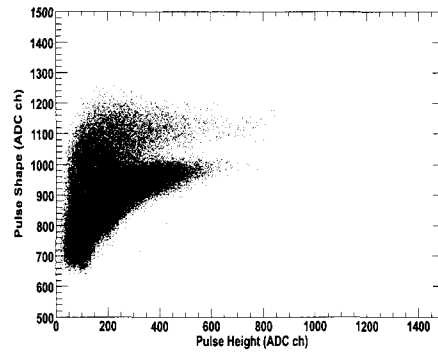


Figure 4–42: ToF A–C vs. detector A pulse height (left), detector C pulse height (right).

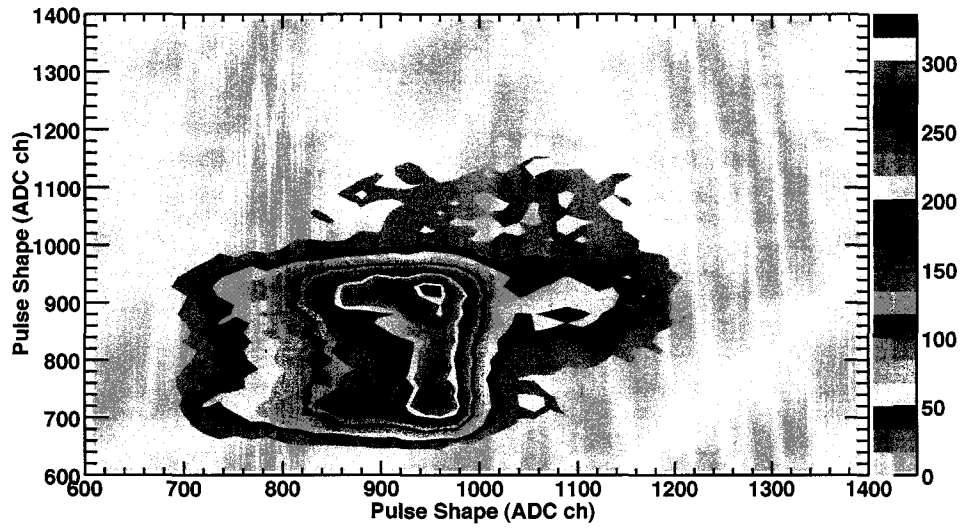
In addition to using the MLE method in the total energy reconstruction process, the  $\geq 10$  MeV neutrons produce large light pulses in each scatter, leading to improved pulse shape discrimination (Figure 4–43 top). A scatter of  $D_1$  vs.  $D_2$  PSD serves as a valuable diagnostic for obtaining the selections on ToF and beam ToF parameters needed for further event filtering (Figure 4–43 bottom). Neutron events emerge in the ToF signal – instrument and beam – with PSD cuts applied (Figure 4–44). Figures 4–45 and 4–46 show the A–C/B–C count spectra for a neutron beam energy of 9.1–10.9 MeV and 17.6–18.9 MeV at a rotation angle of  $30^\circ$ .



(a)



(b)



(c)

Figure 4-43: (a) Pulse shape vs. pulse height in detector A, (b) pulse shape vs. pulse height in detector C, (c) detector A pulse shape vs. detector C pulse shape.

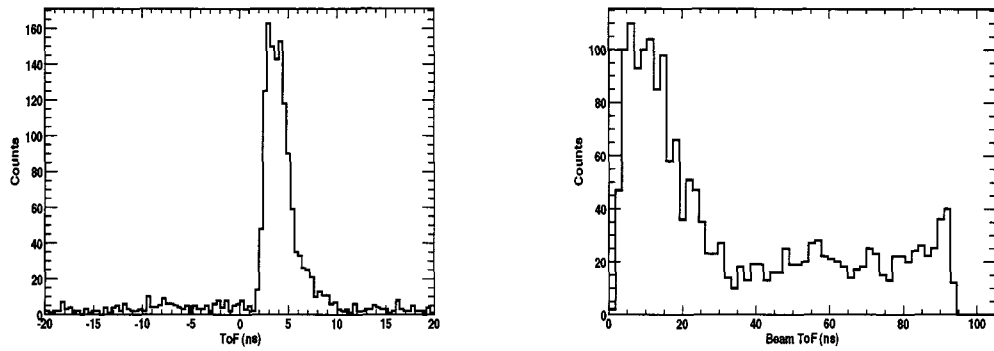


Figure 4-44: (Left) Instrument ToF A-C spectrum with detector A and C PSD cuts applied. (Right) Beam ToF spectrum with detector A and C PSD cuts applied.

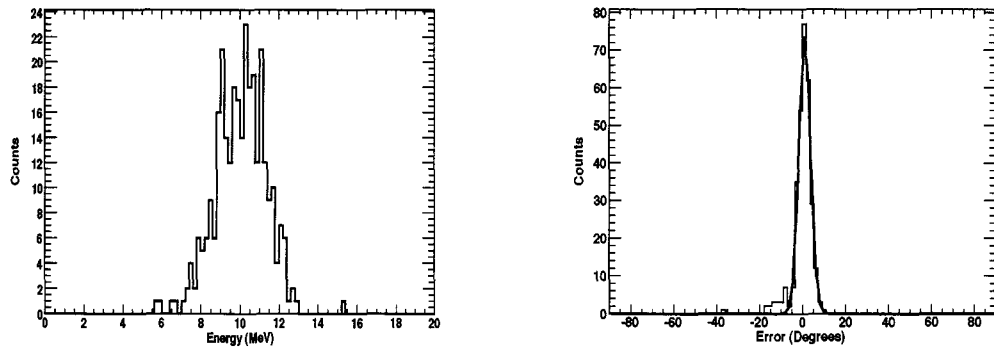
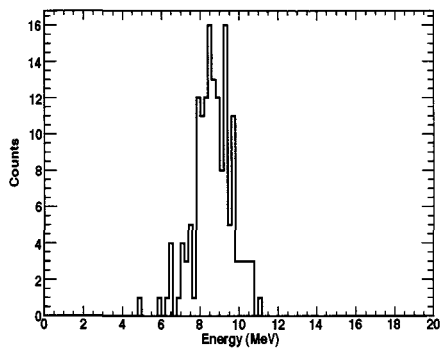
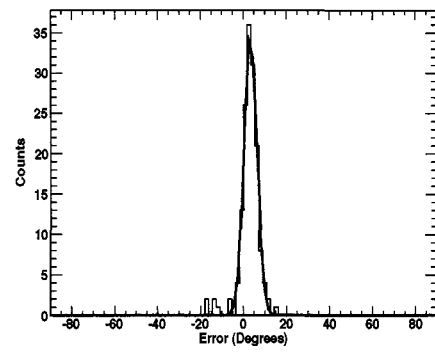


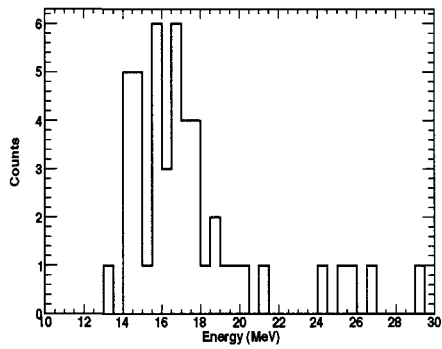
Figure 4-45: 9.1–10.9 MeV count spectrum (left) and ARM (right) for A-C orientation  $30^\circ$ .



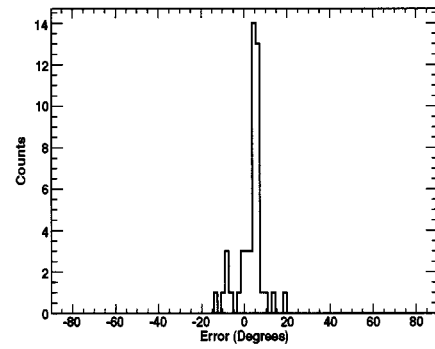
(a)



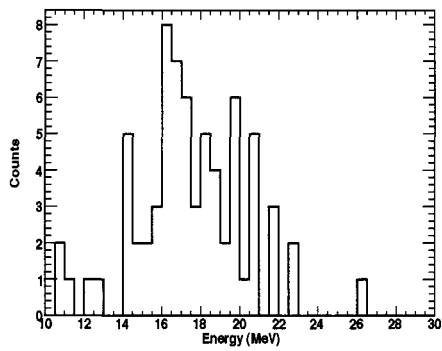
(b)



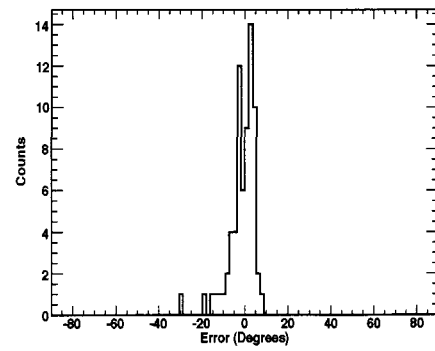
(c)



(d)



(e)



(f)

Figure 4-46: 9.1–10.9 MeV (a) count spectrum and (b) ARM for B–C orientation  $45^\circ$ . 17.6–18.9 MeV count spectrum and ARM for A–C orientation  $30^\circ$  (c) and (d), B–C orientation  $45^\circ$  (e) and (f).

The calibration at CNL reveals that the prototype yields a nearly diagonal response between the incident neutron energy and the reconstructed neutron energy. We will explore a comparison between the performance of A–C and B–C scatters in section 4.5.

#### 4.4.2 LIGHT OUTPUT FUNCTION FOR <1 MeV PROTONS

Converting from measured pulse height to meaningful proton equivalent energy is a two-step process – pulse height (digitized data channel) is first converted to electron equivalent energy, and then to proton equivalent energy. The former is a fairly straightforward process that is carried out with the known energy from  $\gamma$ -ray emitting isotopes and measuring the photopeak and/or approximately the Compton edge to obtain a calibration curve; the latter can be found elsewhere (Czirr et al. 1964; Cecil et al. 1979). However, the literature on conversion of electron equivalent to proton equivalent energy at low energy is based on extrapolation from measurements at higher energy (Figure 4–47). Extrapolating data from higher to lower energies is valid if the scintillator light output response is linear, but the unexplored low-energy, non-linear light output for protons makes this approach questionable. Williamson et al. (1999) states that the light output produced by recoil electrons is linear above 100–150 keV; Brannen and Olde (1962) and Taylor (1951) have shown that the recoil electron light output is linear below 100 keV. We used CNL data to check the conversion formula for proton recoils between  $60 \text{ keV}_{ee}$ – $150 \text{ keV}_{ee}$ , or correspondingly,  $200 \text{ keV}_{pe}$ – $1 \text{ MeV}_{pe}$ . The comparison was

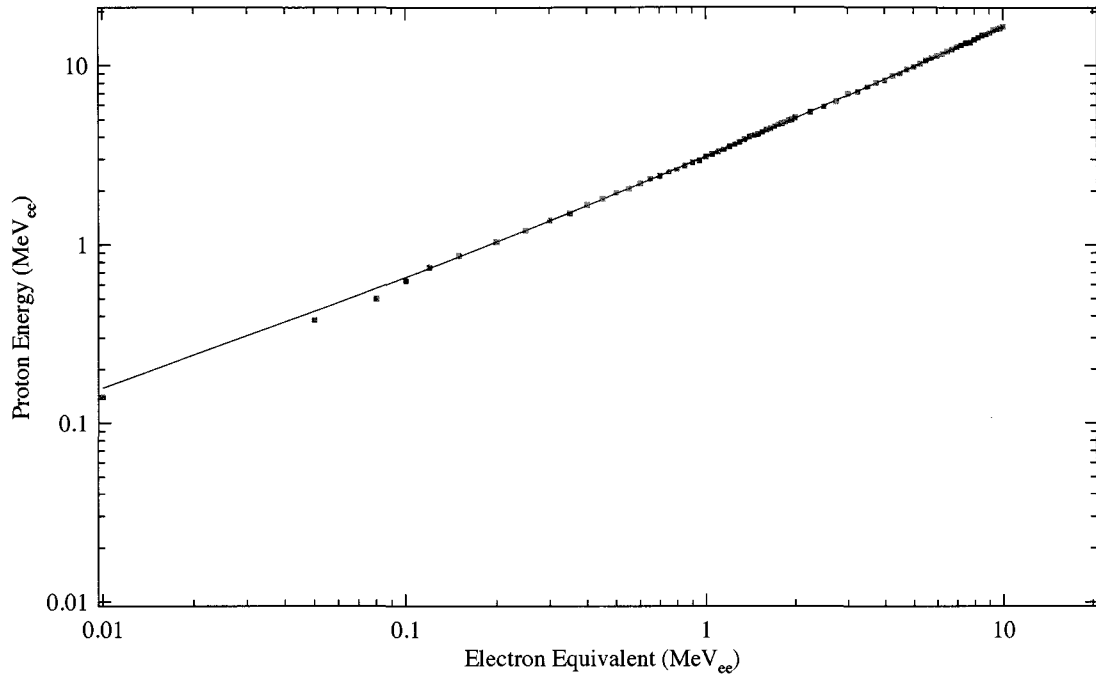


Figure 4–47: BC–501 electron equivalent energy to proton equivalent energy conversion data (Mascarenhas 2007).

carried out by measuring the electron equivalent energy of the recoil proton ( $E_{p1,ee}$ ) and calculating the proton equivalent energy of the recoil proton ( $E_{p1,pe}$ ) via

$$E_{p1} = E_{n'} \tan^2 \theta_n, \quad (4.16)$$

where  $\theta_n$  is the scattering angle as defined in section 3.2.1, and  $E_{n'}$  is the scattered neutron energy. The error associated when measuring the light output of the recoil proton comes from photoelectron statistics and noise, whereas the major contribution to the error in the calculated recoil proton energy is due to the ToF and spatial resolution, which also depends on statistics. Events that occurred within the same plane in the  $z$  dimension

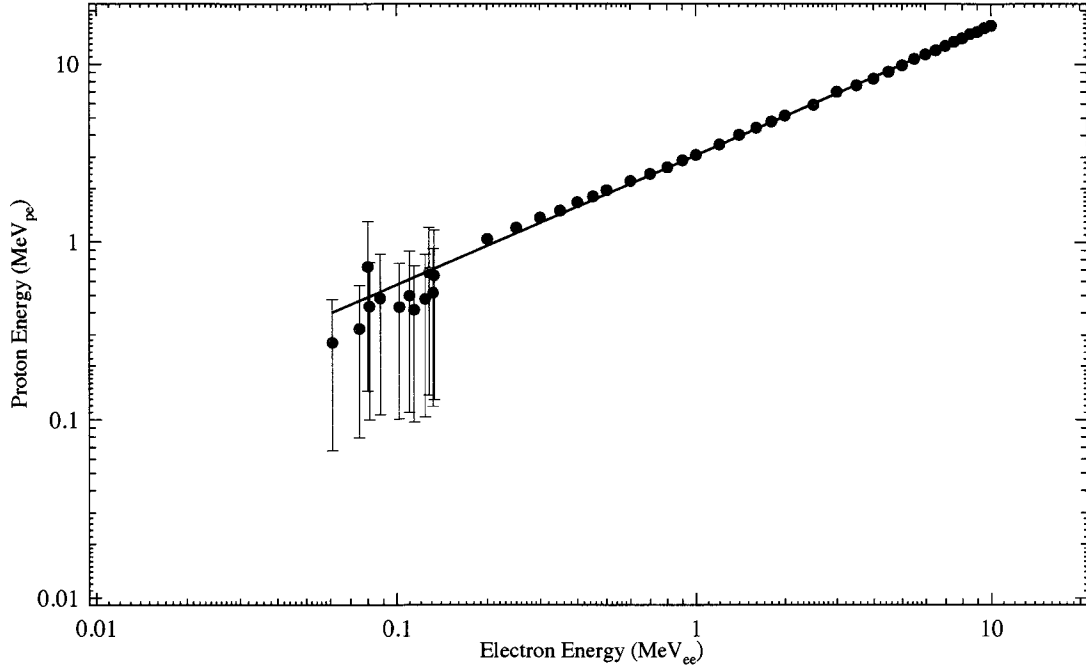


Figure 4–48:  $>1$  MeV<sub>p.e.</sub> data (from Figure 4–47, blue) plotted with  $<1$  MeV<sub>p.e.</sub> CNL data points and associated errors (red).

(to within  $\pm\sigma_z$ ) from  $<1.0$ – $2.9$  MeV data incident at  $30^\circ$  formed the basis for testing. The previous function for electron equivalent to proton equivalent energy conversion for BC–501 data was fit with our  $<1$  MeV<sub>pe</sub> data including  $1$ - $\sigma$  error bars (Figure 4–48). Errors in timing and position were propagated through the calculation to obtain these values. The large errors bars are driven by the low number of photoelectrons near threshold. Agreement is found, within error, between the functional form for the conversion and the  $<1.0$ – $2.9$  MeV CNL data, confirming the extraction from higher energies. The conversion from electron equivalent to proton equivalent energy is given by

$$E_p = A \exp(B \ln(E_e) + C \ln(E_e)^2), \quad (4.17)$$

where  $A = 3.1119 \text{ MeV}_{pe}$ ,  $B = 7.001 \times 10^{-1}$ , and  $C = 1.1339 \times 10^{-2}$  for BC-501. The values used for BC-519 were not verified with CNL data and are given by Saxena (1990) as:  $A = 3.2629 \text{ MeV}_{pe}$ ,  $B = 6.469 \times 10^{-1}$ , and  $C = 2.70 \times 10^{-2}$ .

#### **4.5 BC-501 vs. BC-519**

Scintillator choice in radiation detection is governed by the source one wishes to detect, the environment and the geometrical factor of the instrument. Liquid scintillator was chosen for the FNIT SM2 prototype since limited portability was needed, n/ $\gamma$ -ray discrimination could be achieved, and the rod geometry and light output coupling was favorable. As outlined throughout this chapter, two scintillators (BC-501 and BC-519) with differing properties were used in the FNIT SM2 rods and performance tested in a side-by-side comparison. From Table 4-6 we find that BC-501 has 33% higher light output than BC-519, each with a maximum wavelength emission of 425 nm. A reduction in the light output directly affects the performance of spatial reconstruction, energy resolution, and ToF since these parameters are governed by photoelectron statistics. However, BC-519 has a larger H:C ratio — 1.7 compared to 1.3 — than that of BC-501 and therefore has ~31% higher detection efficiency.

The choice of scintillator is application dependent, based on whether precise measurements of energy and angle are needed, or if less exposure time at the cost of degraded performance is adequate. We examine the performance of each scintillator in



Parameters	BC-501	BC-519
Light Output (% Anthracene)	80	60
Ratio H:C atoms	1.287	1.728
Wavelength Max. Emission	425 nm	425 nm
Decay Time	3.3 ns	4.0 ns
No. electrons per cc ( $10^{22}$ )	2.97	2.96

Table 4–6: Properties of organic liquid scintillators BC–501 (detectors A and C) and BC–519 (detector B) (Saint-Gobain Crystals n.d.).

terms of the angular resolution and the scintillator efficiency as a function of scatter angle from the CNL data. In Figure 4–49 the ARM (defined in section 4.3.6) is shown for beam energies of 1.0–2.9 MeV, 1.8–2.9 MeV, and <1.0–2.9 MeV. This quantity approaches a minimum at an angle  $45^\circ$  for both scintillators following a decrease in resolution at shallow scatter angles; BC–501 consistently outperforms BC–519. For angles  $>60^\circ$  the performance rapidly degrades for both scintillators (not shown).

Figure 4–50 shows the performance comparison in the number of counts obtained by BC–501 and BC–519 for varying incident scatter angle. Single and double scatters are given for 1.0–2.9 MeV. For single scatters, the counts in each rod were normalized to the single scatter counts in detector A. The double scatter efficiency comparison was made by normalizing the A–C and B–C raw counts to the total number of coincident counts recorded by the scaler module (Figure 4–51). The 1.0–2.9 MeV runs offer direct comparison of  $0^\circ$ ,  $15^\circ$ ,  $30^\circ$ ,  $45^\circ$  and  $60^\circ$  for A–C and B–C scatters. We find that B–C registers a higher percentage compared to A–C for incident angles between  $0^\circ$ – $30^\circ$ . The

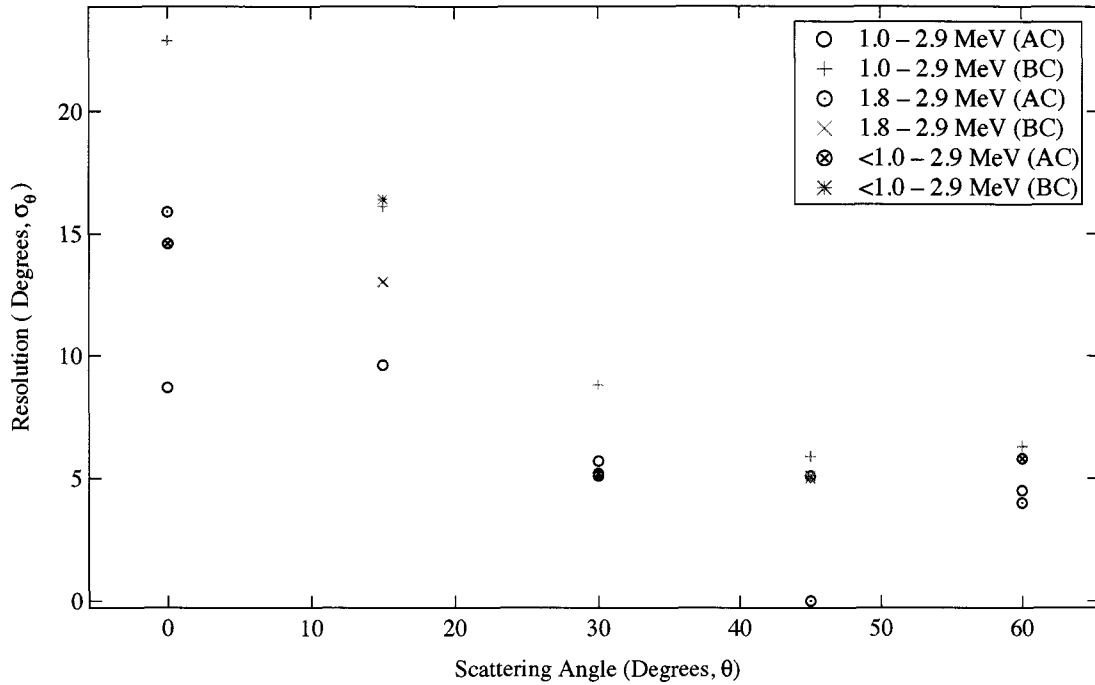


Figure 4–49: The ARM as a function of FNIT SM2 orientation with respect to varying energy neutron beams. Detector A (BC–501) with first scatter (black) and detector B (BC–519) with first scatter (red).

effect of partial detector shadowing can be observed in the single counts for shallow angles where either detector A and B lie directly in front of detector C; the same is true for detector B at large angles. The result of the detector B lying partially out of the beam path is evident from the reduction observed in the single scatter counts at 60° (75° for B–C). This effect, coupled with large angle scatter efficiency, can be used to explain the falloff in the number of double scatters in B–C for angles >30°.

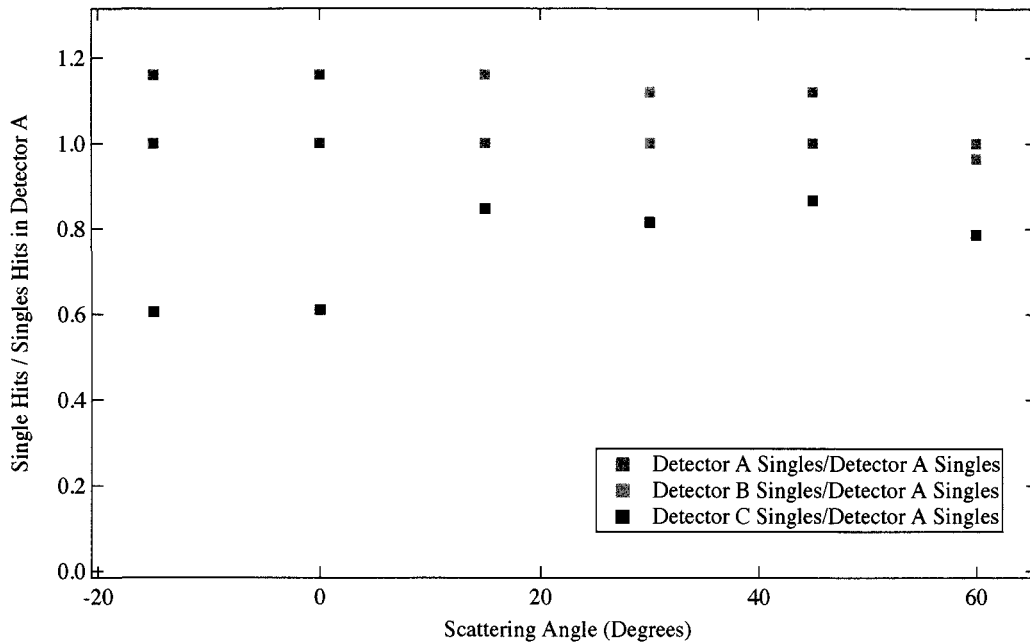


Figure 4-50: Single scatter counts in detectors A, B, and C normalized to the total single incident counts in detector A for 1.0–2.9 MeV CNL data.

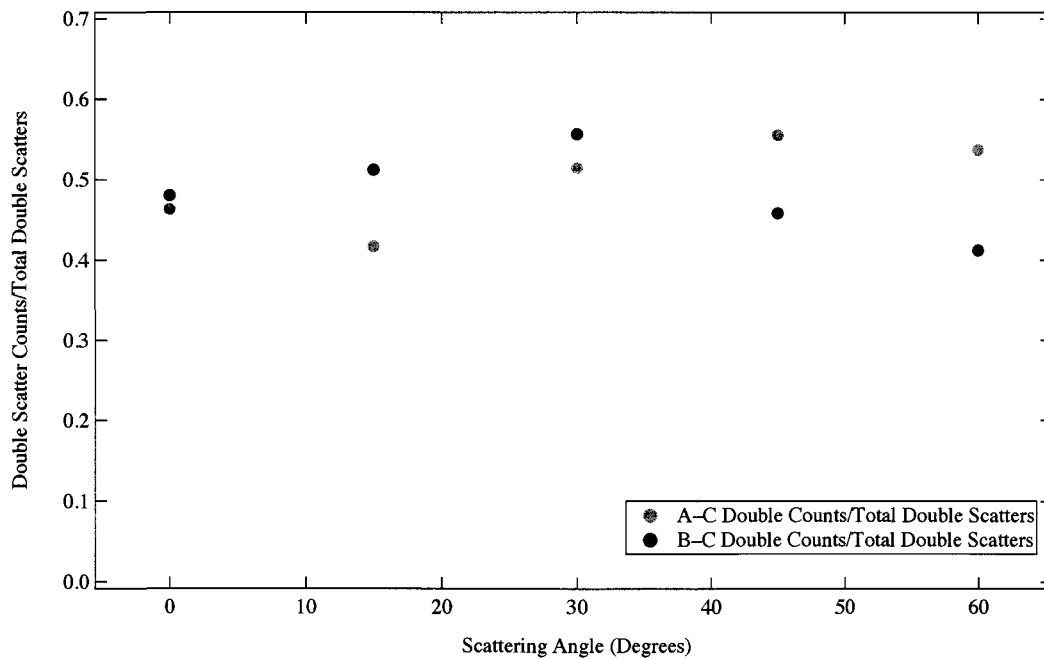


Figure 4-51: A-C (red) and B-C (black) double scatter counts normalized to the total number of double scatter counts recorded from 1.0–2.9 MeV CNL data. BC-501 is the scintillator in the first scatter for A-C and BC-519 is the scintillator in the first scatter for B-C.

## **4.6 FISSIONABLE MATERIAL**

A set of experiments were conducted in the field and in the laboratory at UNH to test the response of FNIT SM2 to fissile material. Both neutrons and  $\gamma$  rays from fission sources were used as test cases.

### **4.6.1 $^{239}\text{Pu}$**

In September of 2007 the FNIT SM2 was irradiated with neutrons from 98 g of  $\text{PuO}_2$  at the Pacific Northwest National Laboratory (PNNL) in Richland, WA. The sample used was 5.6%  $^{240}\text{Pu}$ ; this isotope is the primary source of neutron emission via spontaneous fission with a rate of  $0.91 \times 10^3 \text{ n g}^{-1} \text{ s}^{-1}$  and a half-life of 6560 years. The grade of Pu is determined by the percent composition of  $^{240}\text{Pu}$  in the total sample – the less  $^{240}\text{Pu}$  results in a higher amount of the fissile  $^{239}\text{Pu}$ , as shown in section 2.2.2. The grade used for the PNNL testing was Weapons-Grade (WG).  $^{239}\text{Pu}$  isotope emits neutrons via spontaneous fission at a rate of  $22 \times 10^{-3} \text{ n g}^{-1} \text{ s}^{-1}$  with a half-life of 24,100 years (Mark 1993). The spectral distribution of WGP neutron emission follows a Watt distribution with most probable energy of 1.6 MeV and an average energy of 2.1 MeV. The source was sealed in a slug and placed  $30^\circ$  off-axis a distance of 1 m away from the origin for a run time of 65 h. The main goal for this field experiment was to demonstrate the ability to detect and measure neutron source emission. Event selections on ToF and PSD in  $D_1$  and  $D_2$  produced a total of 79 and 54 doubly scattered neutrons from A–C and

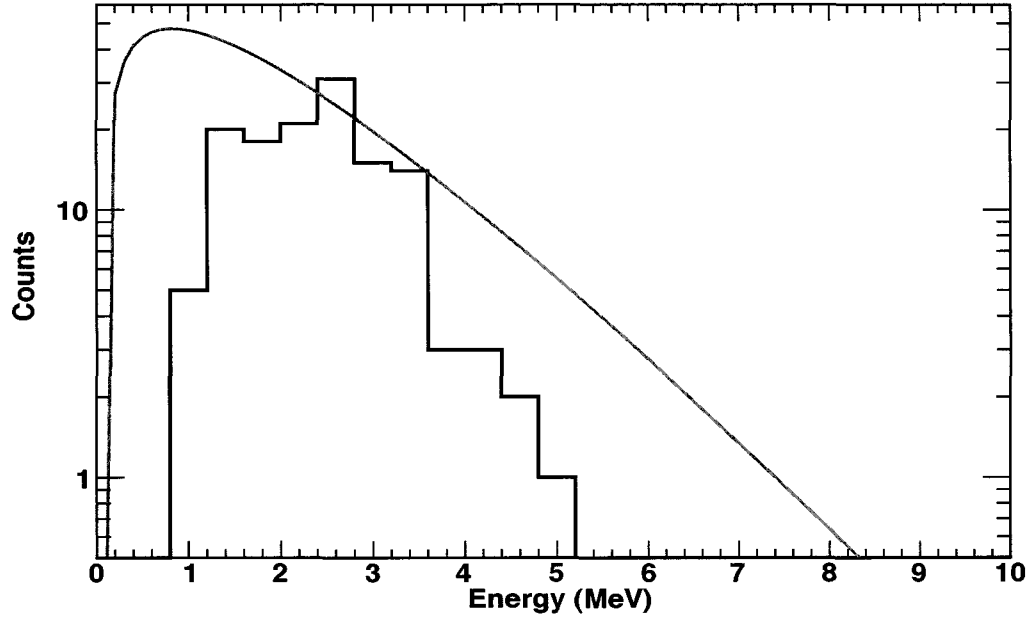


Figure 4-52:  $^{239}\text{Pu}$  fission neutron spectrum with normalized theoretical distribution shown in red.

B-C, respectively. The results were summed and are shown in Figure 4-52. The expected neutron density is described by the Watt distribution (Watt 1952) of the form:

$$N(E) = A \exp(-aE) \sinh(\sqrt{bE}) \quad (4.18)$$

given as red curve in Figure 4-52 with a normalization factor of  $A = 65$ ,  $a = 1$ , and  $b = 2$ .

#### 4.6.2 $^{252}\text{Cf}$

Laboratory testing was conducted with spontaneous fission neutrons from  $^{252}\text{Cf}$ . Decay via  $\alpha$ -particle emission (96.91% probability) and via spontaneous fission (3.09%)

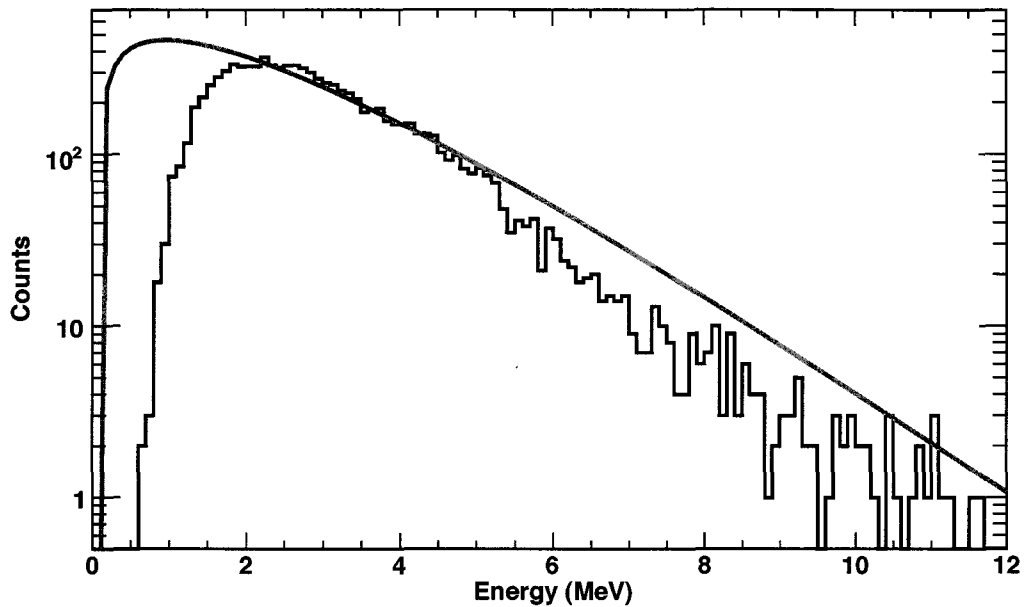


Figure 4–53:  $^{252}\text{Cf}$  fission spectrum combined from 38 different orientations. The normalized theoretical distribution is shown in red.

probability) results in a half-life of 2.65 years. The neutron emission rate is  $2.31 \times 10^{12} \text{ n s}^{-1} \text{ g}^{-1}$  with a specific activity of  $5.36 \times 10^5 \text{ mCi g}^{-1}$ . The neutron energy spectrum is similar to that of a fission reactor with a most probable energy of 0.7 MeV and an average energy of 2.1 MeV (Martin et al. 1999).  $^{252}\text{Cf}$  provides a measure of the performance of SM2 with fission neutrons with a spectral distribution that can be directly related to that of  $^{235}\text{U}$  (Smith et al. 1957). Although practical detection of highly-enriched uranium (HEU) would require a passive detection system, like FNIT, to work in tandem with an active interrogator due to the quiet nature of HEU (Myers et al. 2005). At the time of purchase in June of 2008, the  $^{252}\text{Cf}$  sample had a mass of  $5.1 \times 10^{-6} \text{ g}$  and an activity of 2.7 mCi, yielding  $\sim 15 \times 10^6 \text{ n s}^{-1}$ .

The main goal of this laboratory experiment was to perform measurements with  $^{252}\text{Cf}$  and the FNIT SM2 prototype by replicating a fully populated instrument viewing a fission neutron source from a distance of a few meters. The prototype was placed on the rotation table with  $0^\circ$  corresponding to an on-axis beam. A set of runs with FNIT SM2 oriented between  $\pm 90^\circ$  in  $10^\circ$  increments were completed to replicate the full range of potential scattering paths in the three-rod prototype. Front detector B is offset from the horizontal formed by detectors A and C by  $15^\circ$ , so the full range of incident scatter angles was covered every  $5^\circ$ . The  $^{252}\text{Cf}$  was placed at a distance of 3 m from the central point between the front and rear detector. A total of 19 separate runs, performed over equal live times and using identical event selections, were summed together for analysis. For a total 15-h live time, 9485 events fell within  $\pm$ FWHM ARM selections, corresponding to a rate of  $\sim 0.2 \text{ n s}^{-1}$ , or roughly one double scatter count every 5 s – a lower limit given the restrictions on the number of scattering paths that would be accessible in a full instrument and not available in this replication. Figure 4–53 shows the results from these measurements. The Watt distribution (shown in red for comparison) in this figure has values of  $A = 575$ ,  $a = 0.88$ , and  $b = 2$ .

Clandestine nuclear material concealing neutron emitting isotopes would most likely be enshrouded in passive hydrogenous material, such as wax or water (discussed in section 3.2.1). Neutrons that interact in such a passive material will scatter and deposit energy, leading to inaccurate energy reconstruction and a blurred source location when performing image identification. The total neutron transmission from passive material has an exponential decay dependent on the neutron mean free path in the medium and the

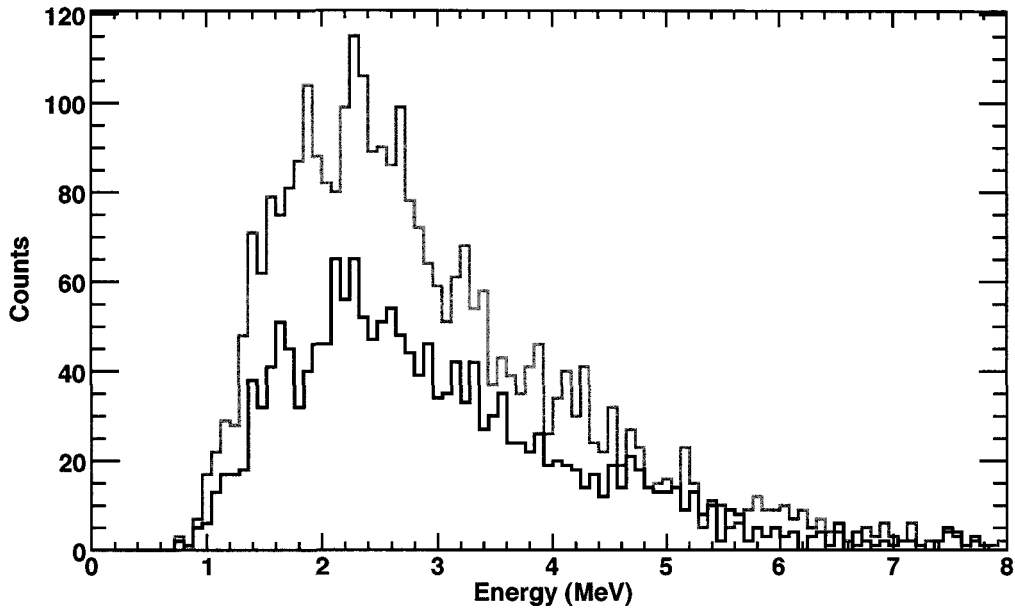


Figure 4–54:  $^{252}\text{Cf}$  fission neutron spectrum without shielding (red), and with  $1-\lambda$  of shielding (blue).

thickness of the medium. The transmitted intensity was given in equation 3.1. For bulk matter, the mean free path,  $1/\lambda = \Sigma_t$ , is:

$$\frac{1}{\lambda} = \sum_i N_i \sigma_i = N_H \sigma_{total,H} + N_C \sigma_{total,C} \quad (4.19)$$

where  $N_H$  is the density of hydrogen atoms [ $\text{cm}^{-3}$ ],  $N_C$  is the density of carbon [ $\text{cm}^{-3}$ ],  $\sigma_{total,H}$  is the total elastic cross-section for neutron-proton scattering, and  $\sigma_{total,C}$  is the total elastic cross-section for neutron-carbon scattering. An experiment to measure the neutron count spectrum transmitted through passive material was conducted to test the effects on the spectral shape and total number. The mean free path of the average energy neutron from  $^{252}\text{Cf}$  passing through paraffin wax is  $\sim 2.8$  cm. Household wax serves as an



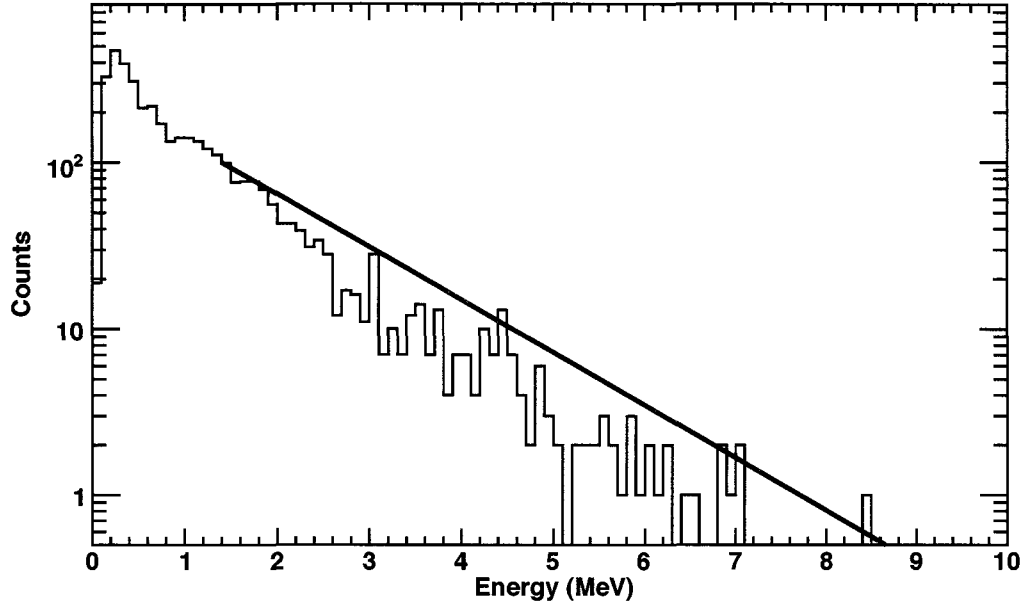


Figure 4-55:  $^{252}\text{Cf}$   $\gamma$ -ray spectrum as measured by FNIT SM2.

efficient moderator of neutrons due to its high hydrogen content. A network of household wax blocks were used for the shielding. Three 15-h runs were completed and compared with three equivalent live time runs with unshielded  $^{252}\text{Cf}$  at the same location. Spectral shape and the angular resolution ( $\sigma_{\text{shielded}} \sim \sigma_{\text{unshielded}} \sim 6^\circ$ ) are preserved, albeit lessened in the total number of events recorded. For one mean free path, the intensity should decrease by one  $e$ -folding length, or by 36%. In Figure 4-54 we find that the counts decrease from 3370 (without shielding) to 1787 (with shielding), or 53%. The higher transmission rate can be accounted for by neutrons that are emitted from the  $^{252}\text{Cf}$  with a higher than average energy, and hence a longer mean free path.

$\gamma$  rays associated with concealed nuclear material could possibly come in two forms: emission from the source itself and those produced from the intervening, passive

material. We shall concentrate on the former. The decay products of  $^{252}\text{Cf}$  de-excite through the emission of both neutrons and  $\gamma$  rays. On average  $\sim 20$  photons are emitted for each spontaneous fission, and 80% of these photons have energies of less than 1 MeV, exhibiting an evaporation spectrum similar to the neutron spectrum (Povh, et al. 2004). The FNIT SM2 was not optimized to make full energy double scatter  $\gamma$ -ray measurements; an organic scintillator for the first scatter coupled with an inorganic, high- $Z$  material to completely absorb the scattered  $\gamma$  ray in the second scatter has been used in past applications to make such measurements (Schönfelder et al. 1993). Additionally, due to the higher light output of the recoil electrons, the dynamic range of the prototype is limited to small energies and angles. Partial energy measurement will result in inconsistencies in the reconstructed  $\gamma$ -ray energy spectrum. The FNIT SM2  $\gamma$ -ray measuring abilities were tested with fission  $\gamma$  rays from the  $^{252}\text{Cf}$ . The dynamic range of the prototype was accounted for with a similar setup used in the beam measurements to avoid saturation. The source was placed  $30^\circ$  off-axis and run for a period of 15 h.  $\gamma$ -ray event data was processed in the same manner as the neutron events, selecting on ToF and PSD values. Compton scattering kinematics were applied and the incident energy and angle were reconstructed on an event-by-event basis. Saturation with the low-energy settings occurred  $\sim 1.5 \text{ MeV}_{ee}$ ; events above this threshold were measured with the lower gain settings. The distribution obtained in Figure 4-55 closely resembles that of a fission  $\gamma$ -ray spectrum. The data were fit with an exponentially decaying slope above 1.5 MeV and in relative agreement with results found previously (Glässel et al. 1989).

## CHAPTER 5

### INSTRUMENT RESPONSE

#### **5.1 GEANT4 SIMULATIONS**

The interaction of radiation with matter can be studied through computational numerical methods. The design of a detector and its response to various stimuli over a given energy range are tested and used to optimize and improve the design. The standard simulation packages used to study neutron interactions are the Monte Carlo N-Particle (MCNP) package developed by Los Alamos National Laboratory (Monte Carlo N-Particle (MCNP) 2003) and the Geometry and Tracking (GEANT) package developed by CERN (Agostinelli et al. 2003; Alison et al. 2006). Each package is based on Monte Carlo calculations. The Monte Carlo method – named after the city in Monaco famous for its casinos – is an iterative numerical method that randomly samples a probability distribution given the predefined experimental conditions on a regularly spaced grid. The GEANT4 environment is based in a C++ object-oriented package. The radiation (particle) type and physical processes that govern their interaction – electromagnetic and hadronic – with matter are prescribed in a user-defined physics list. The UNH group employs the cross sections for neutron physics developed at the University of Bern, now standard in GEANT4. We implemented version 9.0 with built-in GEANT neutron cross section data

(G4NDL 3.11). The physics list used for the simulation was QGSP\_BERT\_HP, which is based on the Quark-Gluon String Precompound (QGSP) that handles hadronic collisions and resulting de-excitations. For the energy range of interest, intra-nucleon transport reactions are modeled based on the Bertini (BERT) Cascade (Beringer 2004).

GEANT4 and published cross-section data were compared by injecting a monoenergetic pencil beam of 0.1–20 MeV neutrons into slabs of material with elemental relevance to the SM2 rods, i.e., H, C, N, O, Al, and Si. Discrete values for simulated elastic and inelastic cross sections for neutron-proton (n-p) and neutron-carbon (n-C) scatters as a function of energy were computed from the survival probability given in equation 3.1. The simulated and published results were in agreement (McLane, et al. 1988). Neutron beam attenuation was tested for standard scintillator material, composed of hydrogen and carbon in a ratio of 1.2:1. Simulated cross-section values, inserted into equations 3.1 and 4.19 for the survival probability and the mean free path of neutrons passing through a medium, respectively, yielded attenuation results in agreement with published data. These results were confirmed by former UNH undergraduate student, Mr. Joshua Wood.

#### 5.1.1 SIMULATING FNIT SM2

FNIT SM2 prototype materials included in the simulation were: liquid scintillator, Teflon™ wrapping and shims, Viton™ O-rings, aluminum casing, PMT housing and the

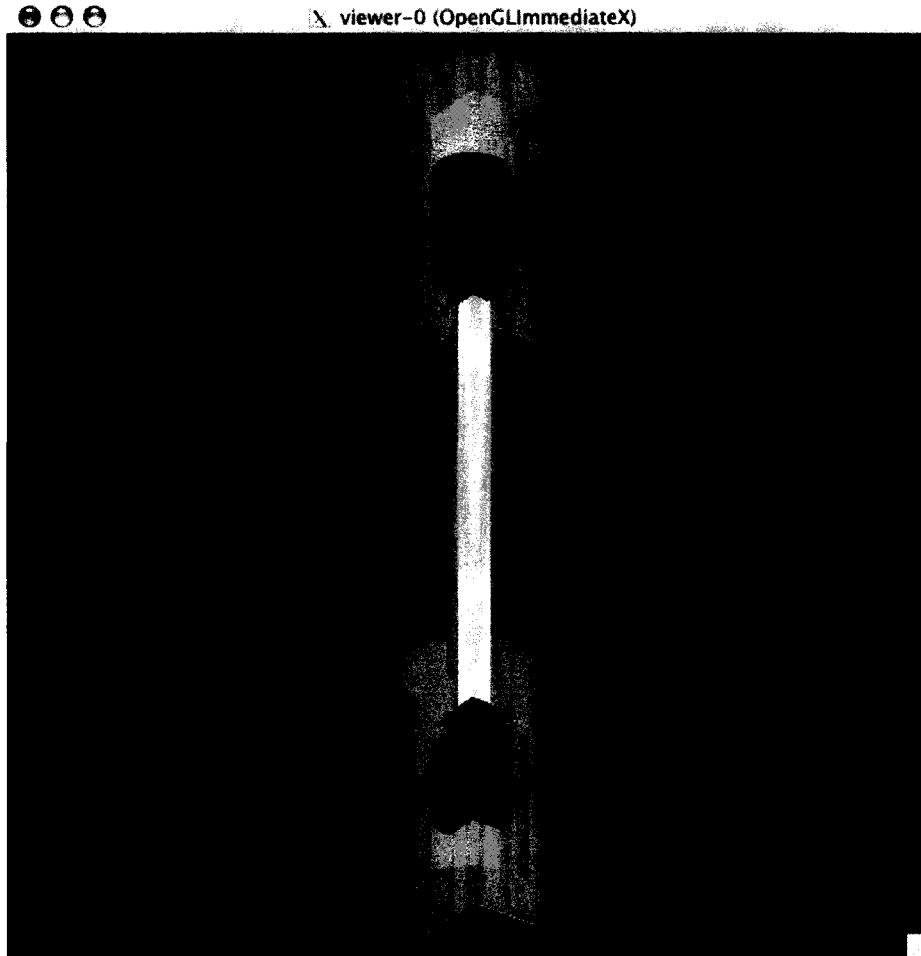


Figure 5–1: 90° cross-sectional cut out of the simulated FNIT SM2 rod. Liquid scintillator (yellow), borosilicate glass (blue), Teflon (white), aluminum (gray), and vacuum (black).

PMT (borosilicate glass). The effects of scintillation photon transport within the detector volume was not considered. The data generated were output in the form of an ASCII text file; each row of numbers representing a predefined set of parameters for each SM2 rod. Information regarding coincident level – single, double, or triple – were selected in post-processing.

<b>Simulation Output</b>
Event Number
Initial Position Vector ( $x, y, z$ )
Initial Momentum Vector ( $p_x, p_y, p_z$ )
Initial Energy
Time
Position Vector ( $x, y, z$ )
Energy Deposited (Proton Ionization Energy)
Number of Neutron Scatters (Elastic n-p, elastic & inelastic n-C)

Table 5–1: List of output parameters from the simulation for each SM2 rod.

Data filters were applied to select out events based on scattering sequence, number of elastic n-p scatters, and hadronic energy deposit ( $E_{pe}$ ) above a minimum threshold. Post-processing routines were developed to take the input from the simulation and smooth the data according to empirically determined instrumental parameters (Pirard et al. 2009). The functional form of the ToF, pulse height, and spatial location parameters were statistically broadened by algorithms that select out random numbers from a Gaussian distribution for a given mean and standard deviation. The energy deposited by recoil protons was smoothed by converting this value into an electron equivalent energy and broadened based on pulse height resolution and number of photoelectrons produced per MeV by the PMT photocathode. The position-dependent threshold along the length of each rod was accounted for in the routines. All events, smoothed in energy and above the position-dependent threshold, were then smoothed in ToF and interaction location. The

total neutron energy is reconstructed in the same manner as the laboratory data. The double scatter efficiency for FNIT SM2 is of order  $10^{-5}$ ; a typical simulation run was conducted with  $4 \times 10^7$  total input triggers. Beam characteristics were defined in a user-generated macro file. The specification of the beam spectrum (uniform or predefined function), size, shape and orientation allow for the full instrument energy response to be tabulated.

## **5.2 RESPONSE ANALYSIS**

A description of how an instrument reconstructs the energy and scattering direction for given stimulus is known as its response. A full 4-d response consists of the 2-d scattering direction, the scattering angle and the energy. One can slice or project the 4-d space to get lower dimensional response matrices of the quantity of interest. For FNIT SM2 our work focused on the instrument response in energy over the nominal energy range of the prototype instrument. To determine the energy response, we restricted the angle of orientation with respect to the neutron beam, recorded the input energy and computed the reconstructed output energy. In effect, we are collapsing the angle information down onto a 2-d energy point spread function (PSF). The 2-d response can be represented as a matrix,  $R_{ij}$ , where the elements are obtained from the binning and counting of neutrons in a 2-d scatter plot of the reconstructed output energy vs. the input energy. The response can be measured or computed by simulations. An ideal instrument response is diagonal – a 1:1 correspondence between the output and the input energy. However, there are competing factors that lead to off-diagonal elements in the response,

such as: multiple n-p scatters, n-C scatters, inelastic n-p and n-C scatters, and  $\gamma$ -ray contamination. The instrument geometry, size, light readout and resolution functions all contribute to the shape of the response. Simulation studies are used to unearth the relevant numbers for each of these reaction channels.

### 5.2.1 COMPARISON OF MEASURED AND SIMULATED DATA

A method for comparing the smoothed simulated data to the laboratory data is necessary, but a response matrix from laboratory data for a continuum source is not satisfactory given that the input energy of each individual neutron is not known. The method for comparison of the simulated and laboratory data was given by the two parameters that can be computed for each – the reconstructed total energy and the scattering angle,  $\theta_N$ . Simulated 1.8–2.9 MeV double scatter neutrons were used for comparison with the 1.8–2.9 MeV CNL neutron beam data incident at  $30^\circ$ . Figure 5–2 shows relative agreement between the two distributions. A more rigorous statistical test (e.g. Kolmogorov-Smirnov test) between the two distributions was not performed.



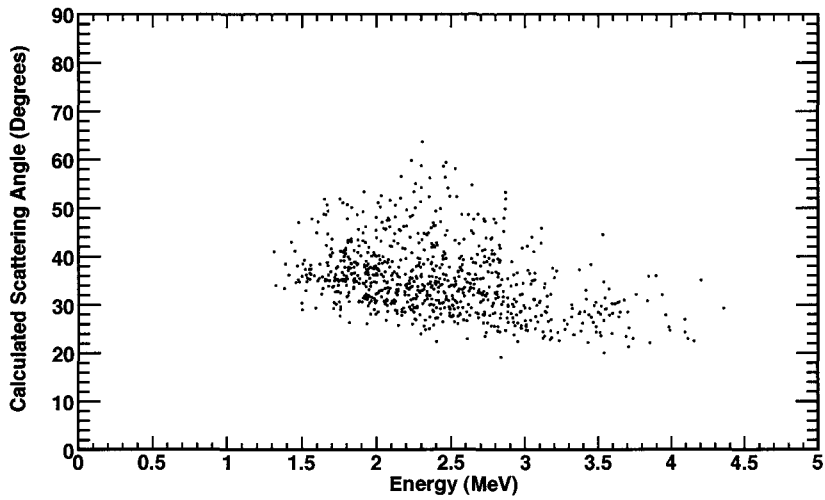
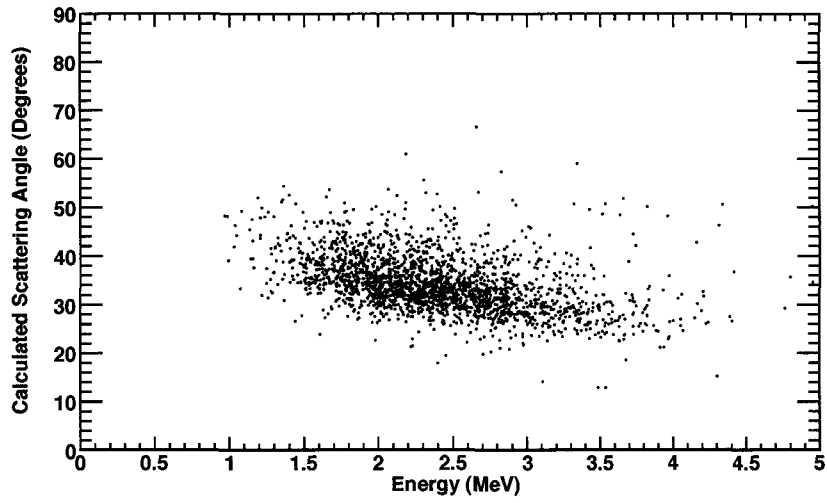


Figure 5–2: Scatter plot of the calculated scattering angle vs. reconstructed energy for measured (top) and simulated (bottom) neutrons.

### 5.2.2 FLAT (1–10 MeV) INPUT SPECTRUM

An on-axis simulated beam of neutrons with a flat spectrum from 1–10 MeV was input for the FNIT SM2 response. Of the  $4 \times 10^7$  event triggers input in the simulation, 1995 double scatters occurred. Figure 5–3 shows a scatter plot of the response without instrumental parameter broadening applied so that we could assess the off-diagonal elements. The majority of the events (87%) lies along the main 1:1 diagonal. Selecting the events that satisfy the forward-scattered neutron ToF criterion, 1585 events remain (Figure 5–4 top). By applying the windowed ToF selection, the events with reconstructed energy  $>$  input energy and along the baseline (reconstructed energy  $\sim$  a few keV), caused by large, negative ToF values, were removed. Further imposing single elastic n-p scatters in each rod limits the number of valid events to 514 (Figure 5–4 bottom).

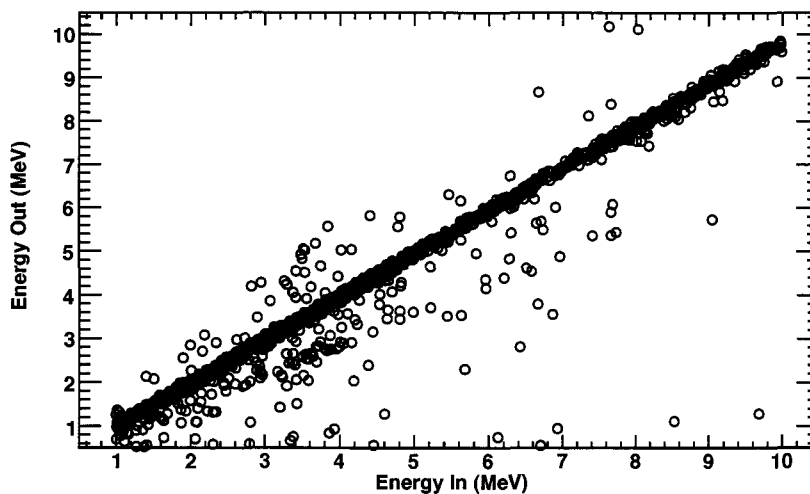


Figure 5–3: Calculated response for all double scatter events for an on-axis beam with a uniform energy spectrum.

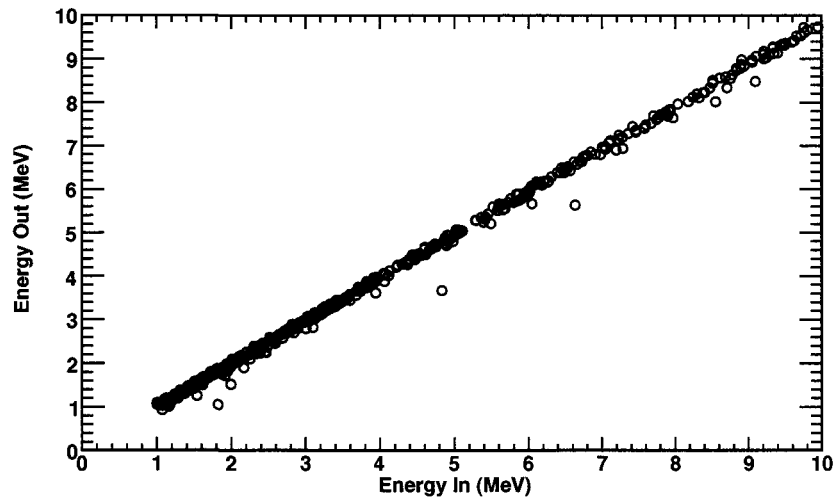
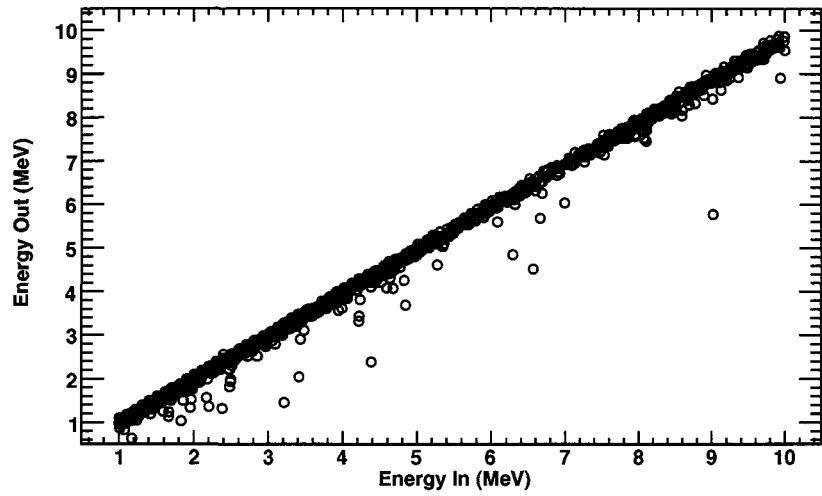


Figure 5-4: Calculated response for double scatter events with ToF cuts (top); additional constraints required one elastic n-p scatter in each rod (bottom).

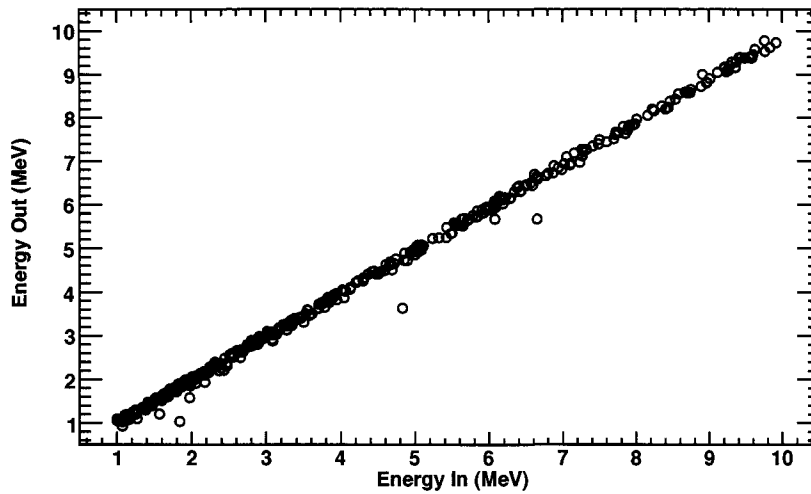


Figure 5–5: The data of Fig. 5–4 with ToF cuts, one elastic n-p and zero n-C total scatters in each rod.

The number of total n-C scatters in each rod that pass previous event selections and produce off-diagonal elements constitutes 7% of the total. Requiring that elastic and inelastic n-C scatters not be present in the data further reduces the total number of valid events to 428 (Figure 5–5). The remaining off-diagonal elements correspond to simulated events with systematically and anomalously long ToFs, which yields a lower energy for the scattered neutron, and hence a lower total reconstructed neutron energy. These events correspond to a small fraction of the total number (1%).

Beam rotations of 30°, 45°, and 60° were completed to obtain the response at greater incident angles. A total of 473, 392, 351 events remain with the same selections as Figure 5–5 for respective angles (Figures 5–6 & 5–7). Instrumental resolutions were applied to the simulated response data to obtain the expected nature of the instrument (outlined in section 5.1). Requirements on the type of scatter were relaxed since we do

not correct for this in the laboratory data. Threshold and smoothing reduce the number of on-axis events in the response to 184 due to the low energy deposit required in  $D_1$  (A or B) in order to satisfy the kinematics; the numbers at the larger angles were less affected. Although the data input were from 1–10 MeV, the smoothing procedure yields reconstructed values of  $<1$  and  $>10$  MeV. The (square) response matrix boundaries were from 0.6 MeV to 13.6 MeV. Binning strategy is based on the instrumental resolution and processing time available. 1-keV wide energy bins would oversample the data and require unnecessary processing; 1-MeV bins are too wide to reveal important features in the data. Linear and logarithmic bin step sizes have advantages that depend on the data being sampled; the response matrices were normalized based on the binning strategy chosen and will be discussed in Chapter 6.

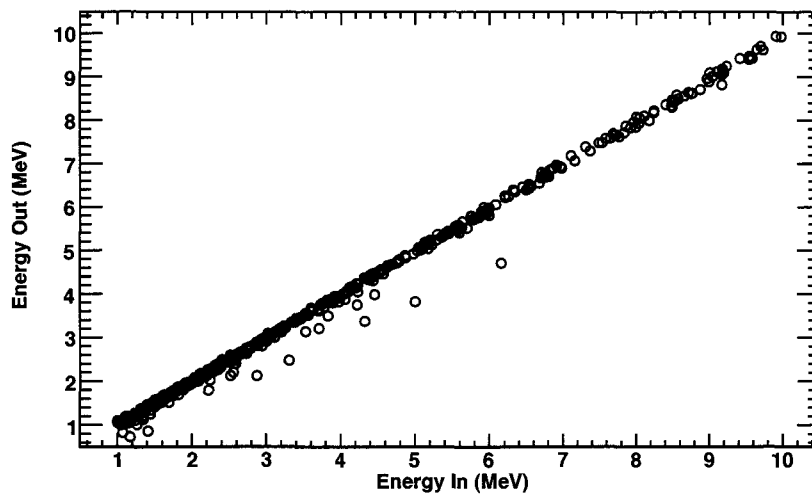


Figure 5–6: Response for double scatter neutrons, incident from  $30^\circ$ .

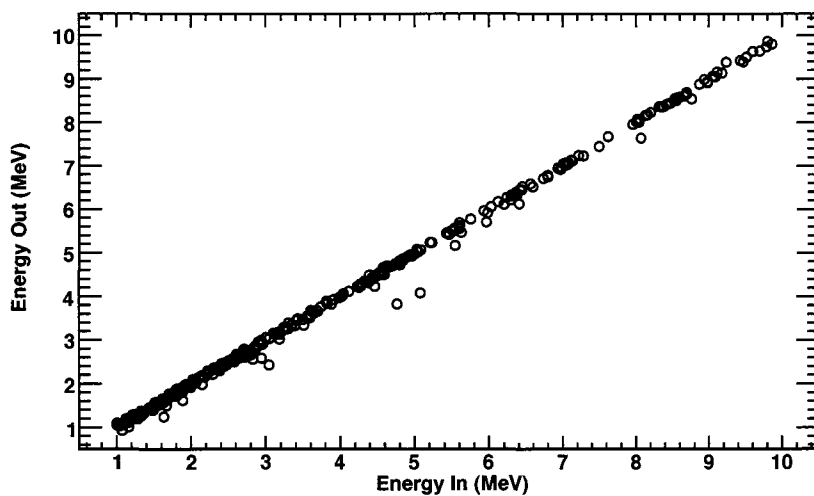
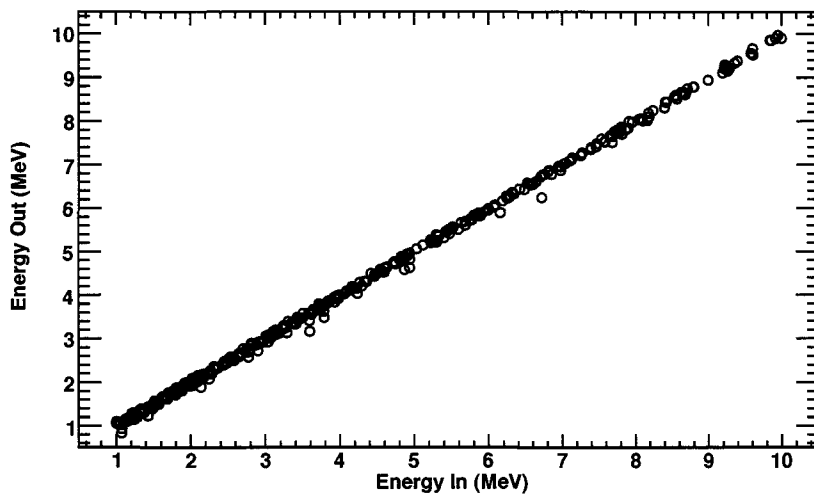


Figure 5–7: Response for double scatter neutrons, incident from 45° (top); 60° (bottom).

Poisson statistical fluctuations in the response were limited by rerunning each simulation for each angle, albeit with different random seeds at the onset, until ~5,000 double scatters were recorded. The number of runs differed for each angle due to rotation angle-dependent efficiency. The results were summed and are shown in Figures 5–8 through 5–12 for both A–C and B–C double scatters.

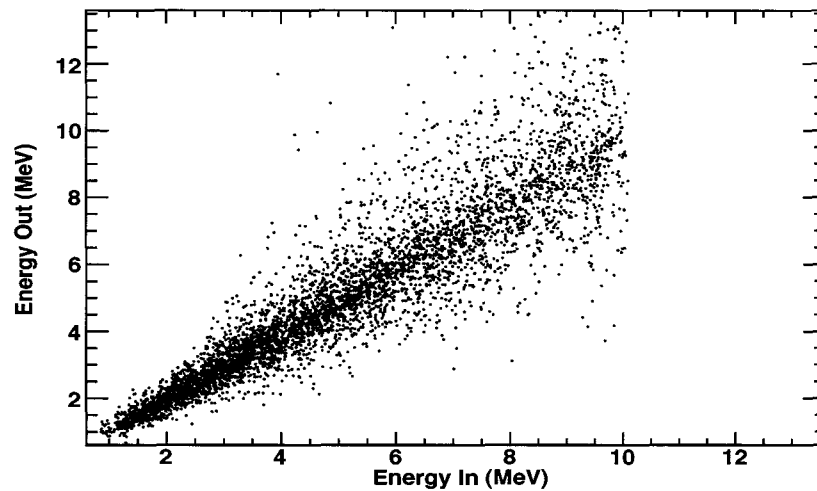


Figure 5–8: Dithered response for double scatter neutrons, incident from 0° A–C.

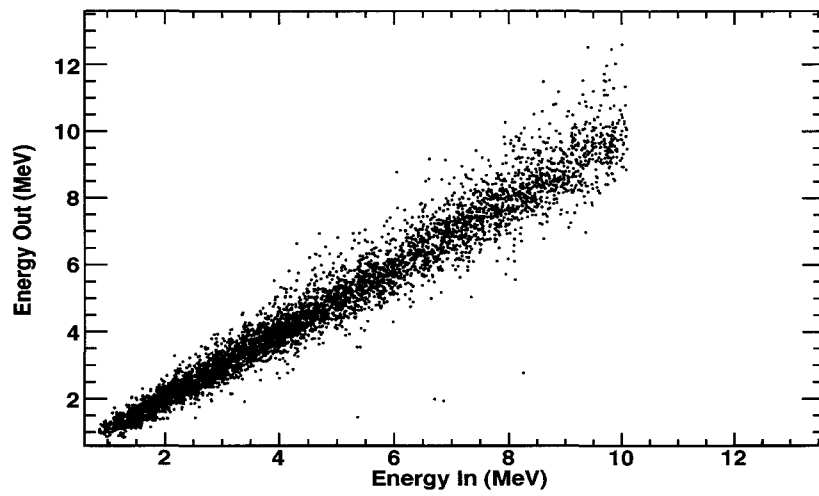
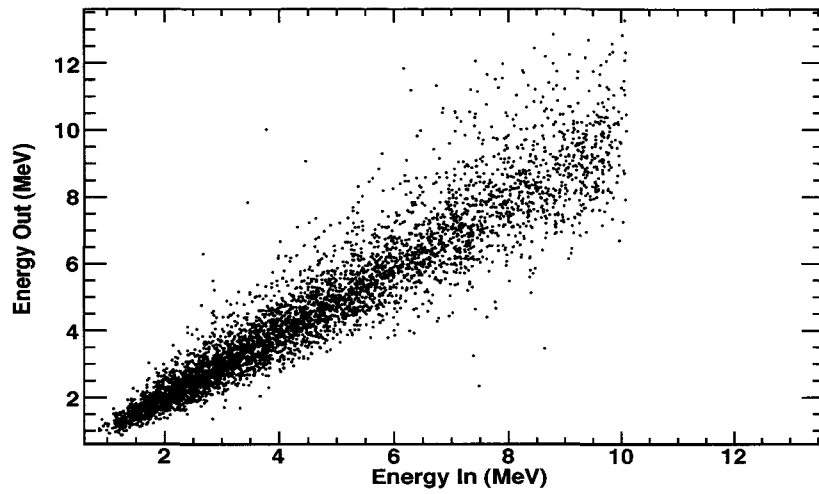


Figure 5-9: Dithered response for double scatter neutrons, incident from 30° A-C (top), 45° A-C (bottom).



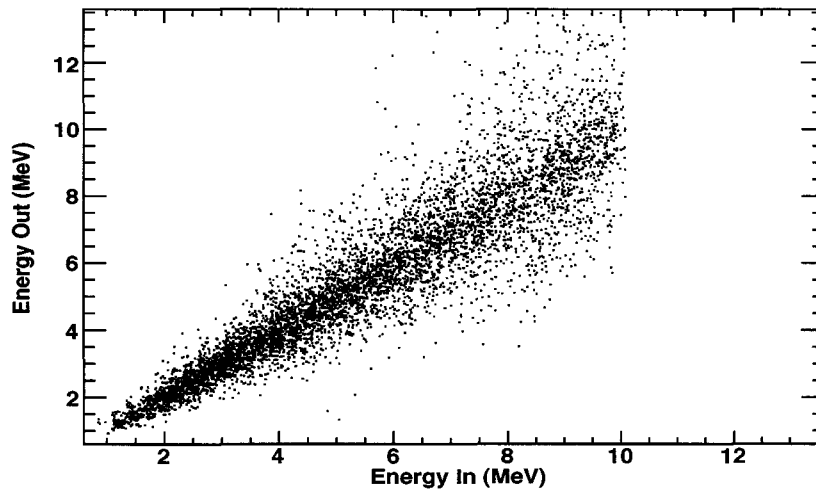
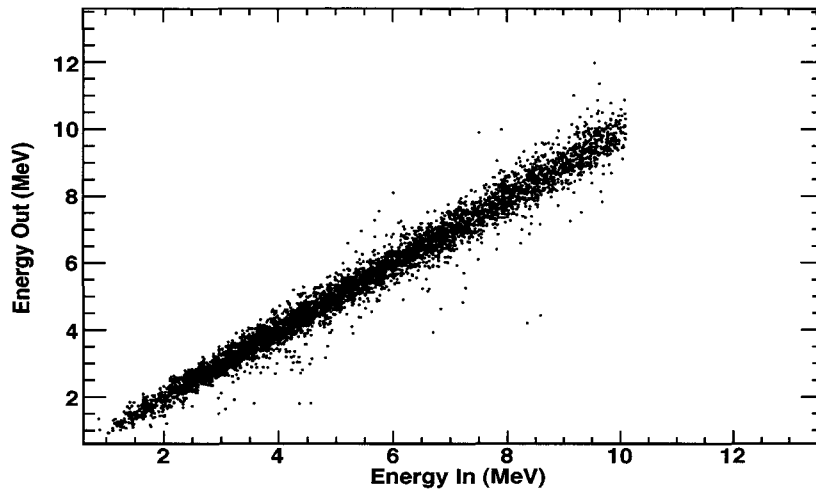


Figure 5-10: Dithered response for double scatter neutrons, incident from 60°  
A-C (center); 15° B-C (bottom).

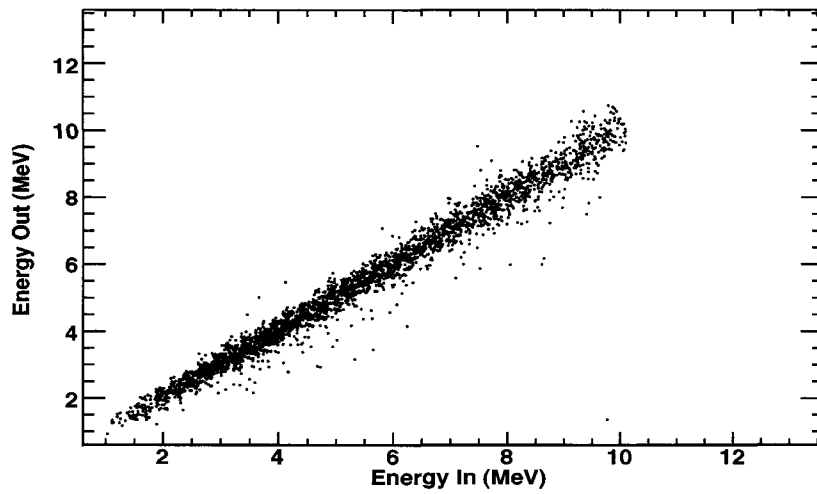
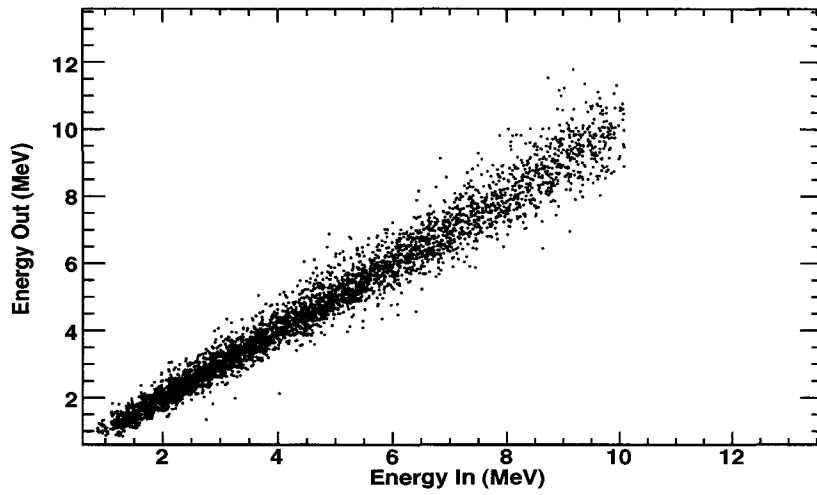


Figure 5-11: Dithered response for double scatter neutrons, incident from 45° B-C (top); 60° B-C (bottom).

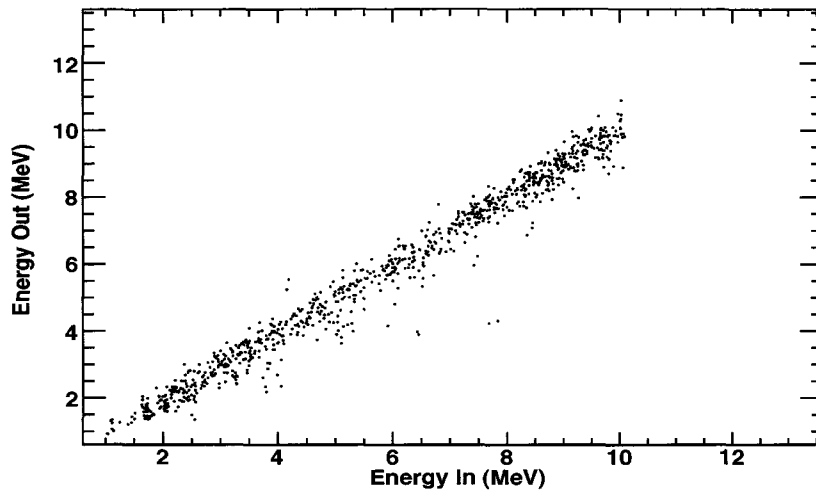


Figure 5–12: Dithered response for double scatter neutrons, incident from 75° B–C.

### 5.2.3 FIRST-ORDER EFFICIENCY CORRECTIONS

Figure 5–13 shows the measured count spectrum, the reconstructed simulated count spectrum and input spectrum used in the simulation. The input  $^{252}\text{Cf}$  spectrum was described in section 4.6.2. There is good agreement between the simulated continuous spectrum and the measured data. With this agreement, an estimate of the source flux was obtained by correcting the measured data to first order for the instrumental efficiency.

The input was normalized (Figure 5–14, red curve) for the efficiency, inherently a small quantity for the SM2 instrument. The integrated efficiency was computed bin-by-bin, in narrow bin step sizes such that the response did not vary greatly over the step size, by taking the ratio of the counts to the normalized input. This analysis is valid for an

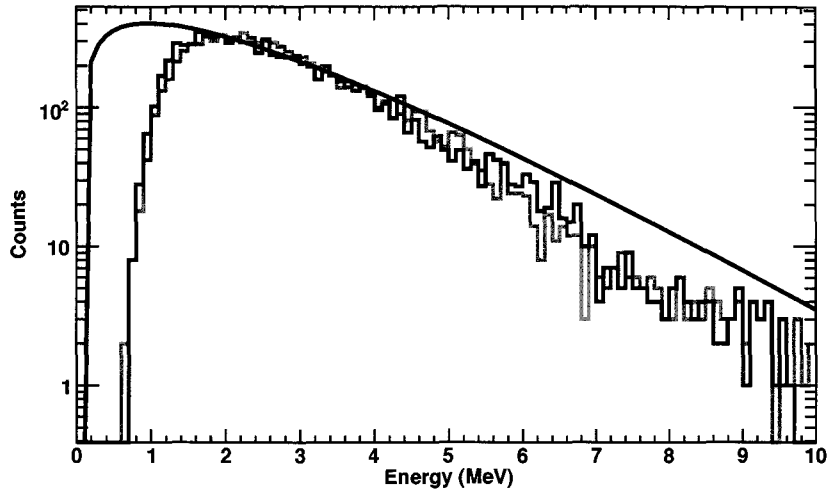


Figure 5–13:  $^{252}\text{Cf}$  spectra: input (black); uncorrected measured (red); simulated (blue).

instrument that demonstrates a nearly diagonal response and is slowly varying in energy. Figure 5–14 (black curve) shows the results of correcting the measured data to the input data using the calculated efficiency (Figure 5–14, blue curve). Above the  $\sim 1$ -MeV threshold the efficiency flattens out for increasing energies until  $>7$  MeV where statistics are limited. An analytical function was loosely fit to the efficiency ( $\epsilon$ ) data set and used to correct the measured data. The function is given as

$$\epsilon = (1 - a \times \exp(-E + a)) \times (bE + c) \quad (5.1)$$

where  $E$  has units of MeV,  $a = 0.85$ ,  $b = -3.34 \times 10^{-7} \text{ MeV}^{-1}$ , and  $c = 4.36 \times 10^{-6}$ . The first term in equation 5.1 is a threshold effect with the second term driven by the efficiency of the prototype instrument. The fluctuation of the corrected data about the input is the result of using the expression fit to the calculated efficiency. A more detailed

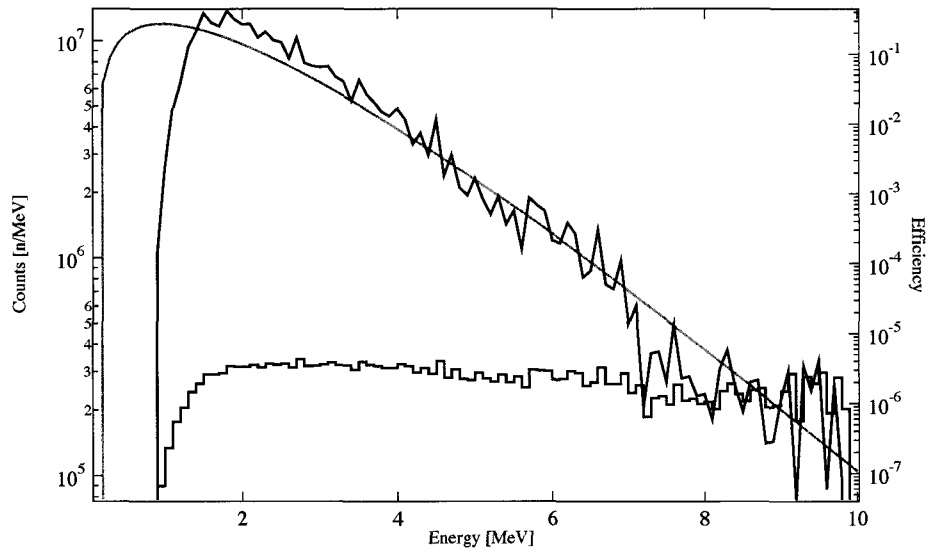


Figure 5–14: Simulated data (black) corrected for efficiency (blue) to the input spectrum (red).

approach to fitting, such as a cubic spline, could lead to less fluctuations. Without a full de-convolution procedure, this method to determine the source flux underestimates the total number of neutrons (Toner et al. 2001). With a complete understanding of the instrument response and agreement between the model and our data set, a de-convolution procedure for the prototype instrument data was developed and implemented and is the topic of Chapter 6.

## CHAPTER 6

### SPECTRAL AND IMAGING DE-CONVOLUTION FOR DOUBLE SCATTER NEUTRON TELESCOPES

#### **6.1 INVERSE AND ILL-POSED PROBLEMS**

Inverse problems arise when one intends to deduce source information from remotely sensed data, such as in the field of astronomy. There are, in general, four types of inverse problems, described as the: Interpretation Problem, Instrument Problem, Synthesis Problem, and Control Problem (Glasko 1986). For our purposes, we are concerned with the instrument problem where the underlying process is distorted by effects inherent to the instrument. The FNIT principle is not the direct detection of neutrons but the protons they interact with in the scintillator material. Indirect measurement of the quantity in question, by nature, is an inverse problem. The measurement of the neutron energy is thus affected by the measurement of scintillation light from the recoil proton to get a pulse height spectrum, path length and timing. Each of these parameters is a function of the light produced and varies with energy. When the underlying process to be uncovered is a true spectral distribution of the source in question, we can, in general, describe the forward problem as

$$\int_0^{\infty} R(E, E') S(E') dE' = C(E) \quad (6.1)$$

for  $0 < E < \infty$ . The count data,  $C(E)$ , measured in discrete energy bins, is a convolution of  $R(E, E')$ , the response of an instrument to  $E'$  resulting in  $E$ , and  $S(E')$  the true incident energy distribution. Measurements made with the FNIT instrument produce  $C(E)$ ; the simulation results outlined in section 5.2.1 are used to compute the energy response matrix  $R(E, E')$ , needed to find the true spectrum of the source  $S(E')$ . The integral equation can be solved if  $C(E)$  and  $R(E, E')$  have known exact and continuous solutions; this is the Fredholm integral of the first kind (Craig and Brown 1986; Hansen 1998). However, measured data are discrete in nature and not known as continuous functions, therefore the integral equation must be discretized and can be represented by the matrix equation

$$\sum_{j=1}^N R_{ij} S_j = C_i. \quad (6.2)$$

$S_j$  can be determined either by performing the method of linear least squares or by direct inversion. However, both approaches are unstable to errors in the data and lead to highly oscillatory, and often unphysical, results (Thompson and Craig 1992). These are known as ill-posed problems. A problem is said to be ill-posed if the solution is not unique or if it is not a continuous function of the data, i.e., arbitrarily small perturbation of the data can cause arbitrarily large perturbation of the solution (Hadamard 1923). When discretizing equation 6.1 for computation with a numerical solution, the problem is said to be a discrete ill-posed problem if: 1) the singular values of the response matrix decay

gradually to zero and 2) the ratio between the largest and smallest non-zero singular values is large, i.e. the response matrix is very ill-conditioned (Hansen 1990). The solution to problems with a very ill-conditioned response matrix are sensitive to perturbations to that solution (Hansen 2008). The idea, then, is to find a solution to a “nearby,” well-posed problem that is less sensitive to perturbations.

To stabilize the solution in a controlled manner the non-classical smoothing method of adding in a regularization term can be invoked. Regularization introduces an extra term (or function) to suppress irregular solutions. Several methods have been implemented for solving inverse problems and those of which will be discussed are: forward folding and Tikhonov regularization.

## **6.2 SPECTRAL ANALYSIS**

The two approaches we investigate to obtain spectral information are forward folding and non-classical data de-convolution (inversion). The former is a convolution of the input model spectrum with the instrument energy response that produces counts that are statistically compared to measured data,  $D$ . In non-classical inversion, the ill-posed problem is stabilized by introducing information regarding the assumed smoothness of the source to produce a source spectrum and flux.

Forward folding is parameter fitting based on an assumed input model. The input spectrum (or model),  $S_j$ , is folded into the instrument response,  $R_{ij}$ , to compute the count spectrum,  $C_i$ , given in matrix form as:  $C_i = R_{ij}S_j$ . A maximum of the log of the probability



(or minimizing  $\chi^2$  for Gaussian statistics) is performed between the computed count spectrum,  $C_i$ , and the measured count spectrum,  $D_i$ , to obtain a set of parameters associated with the model. The model is then adjusted such that there is convergence between  $C$  and  $D$ . The shortcomings of this procedure occurs when there is no realistic model or for low count statistics, necessary for minimizing  $\chi^2$  (Young et al. 2001).

Non-classical de-convolution aims to deduce the true spectrum from the instrument energy response and the measured data with a priori source information. As mentioned above, direct inversion of equation 6.1 typically amplifies the noise and yields unreliable, possibly unphysical results. The goal of non-classical “regularization” is to solve a least squares problem of the form

$$\|RS - C\|_2 \quad (6.3)$$

by adding in a term that simultaneously de-convolves and smoothes the solution. Tikhonov (1963) developed a highly regarded method for solving the minimization problem as

$$\|C - RS\|_2^2 + \lambda^2 \|LS\|_2^2 = \min, \quad (6.4)$$

where  $L$  is the regularization matrix,  $\lambda$  is a Lagrange multiplier known as the smoothing (or regularization) parameter, and  $\|\cdot\|_2$  is the Euclidean 2-norm. This is Tikhonov regularization. The combination of  $L$  and  $\lambda$  controls how much weight is given to the norm of the regularized solution compared to the norm of the residual vector (Hansen 1992). An efficient way to solve equation 6.5 and provide insight into the ill-conditioning of  $R$  is by employing a matrix decomposition. For a  $m \times n$  matrix  $R$ , the Singular Value

Decomposition (SVD) of the matrix can be achieved by a factorization in the form of

$$R = U\Sigma V^T = \sum_{i=1}^n u_i \sigma_i v_i^T \quad (6.5)$$

where  $U$  consists of the orthonormalized eigenvectors associated with the  $n$  largest eigenvalues of  $R^T R$  and  $V$  consists of the orthonormalized eigenvectors of  $RR^T$ .  $\Sigma_{n \times n} = \text{diag}(\sigma_1, \dots, \sigma_n)$  where  $\sigma_i$  are the non-negative square roots of the eigenvalues of  $R^T R$  called the singular values (Golub and Reinsch 1970). Van Loan (1976) outlined a more general form of this matrix decomposition called the Generalized Singular Value Decomposition (GSVD) where the response matrix  $R_{m \times n}$  and a regularization matrix  $L_{p \times n}$  with  $m \geq n \geq p$ , are simultaneously decomposed into

$$R = U\Sigma X^{-1} \quad L = V(M, 0)X^{-1}, \quad (6.6)$$

where  $U$  is a real  $m \times n$  matrix,  $V$  is a real  $p \times p$  matrix,  $X^{-1}$  is a nonsingular  $n \times n$  matrix, and  $\Sigma_{n \times n} = \text{diag}(\sigma_1, \dots, \sigma_n, 1, \dots, 1)$  and  $M_{p \times p} = \text{diag}(\mu_1, \dots, \mu_p)$  with the sum of the squares of the diagonalized entries of  $\Sigma$  and  $M$  normalized to unity for  $i = 1, \dots, p$  (Hansen 1992).

The regularized solution should provide a close approximation to the exact solution. For a given input data vector,  $C$ , if the Fourier coefficients of the response matrix, defined as the inner product  $(u_i, C)$ , on average decay to zero faster than the singular values ( $\sigma_i$ ), then the Discrete Picard Condition (DPC) is said to be satisfied if the following expression remains finite

$$\sum_{i=1}^{\infty} \left| \frac{(u_i, C)}{\sigma_i} \right|^2 < \infty. \quad (6.7)$$

Satisfying this condition ensures that the regularized solution is a close approximation to the exact solution. To what order Tikhonov regularization is carried out depends on the form of the regularization matrix  $L$  and the matrix decomposition. For zeroth-order Tikhonov regularization,  $L = I_n$  (the identity matrix of order  $n$ ), and the SVD is used to obtain the solution to equation 6.5 given as

$$S_\lambda = \sum_{i=1}^n f_i \frac{u_i^T C}{\sigma_i} v_i. \quad (6.8)$$

For higher-order Tikhonov regularization ( $L \neq I_n$ ), the GSVD is used to obtain the solution to equation 6.5 given as

$$S_\lambda = \sum_{i=1}^p f_i \frac{u_i^T C}{\sigma_i} S_i + \sum_{i=p+1}^n (u_i^T C) S_i. \quad (6.9)$$

$L$ , in this case, is a well-conditioned discrete approximation to some derivative operator, i.e.,  $L_1$  is a real  $(n-1) \times n$  matrix for first order and  $L_2$  is a real  $(n-2) \times n$  matrix for second order. The filter factors  $-f_i$  in equations 6.9 and 6.10 – are defined as

$$f_i = \frac{\alpha_i^2}{\alpha_i^2 + \lambda^2} \quad (6.10)$$

where  $\alpha$  depends on the order of the regularization. For zeroth order,  $\alpha$  is given by the singular values ( $\sigma_i$ ) for  $i = 1, \dots, n$  of the response matrix. For first and second order regularization,  $\alpha$  is given by the generalized singular values ( $\gamma_i = \sigma_i/\mu_i$ ) for  $i = 1, \dots, p$ . The filter factors effectively dampen the contribution of small singular values that are the cause of highly oscillatory solutions. While zeroth-order Tikhonov regularization is easier to implement, the higher-order Tikhonov regularization may provide better filtering of the

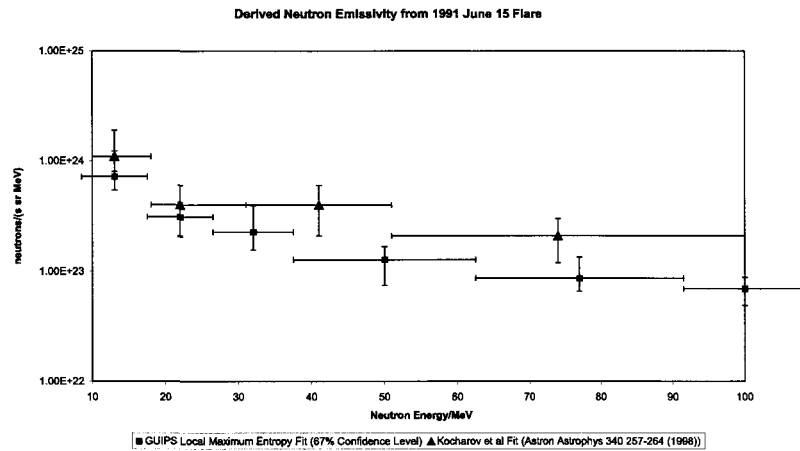


Figure 6–1: Neutron emissivity of the 15 June 1991 solar flare as a function of neutron energy, derived from COMPTEL data using a Maximum Entropy de-convolution (lower points) compared to the earlier results obtained using only diagonal elements of the response matrix.

errors and/or provide a better means for singling out a particularly attractive solution when  $R_{ij}$  is rank deficient (Hansen 1989).

There is no universal method for finding the optimal value of the regularization parameter ( $\lambda$ ). Statistical and numerical studies are often undertaken to determine the optimal value of  $\lambda$  depending on the degree of regularization and the problem at hand. Methods to determine  $\lambda$  are broken up into two categories that involve knowledge in the errors of the data vector, or that extract necessary information from the data vector (Hansen 2008). *L*-curve criterion, generalized cross validation (GCV) and the quasi-optimality criterion seek to minimize (or maximize) the regularized solution to find a balance between the perturbations and the regularized errors. In this work we used a method based on the discrepancy principle (Tikhonov et al. 1995) with knowledge of the errors in the data vector.

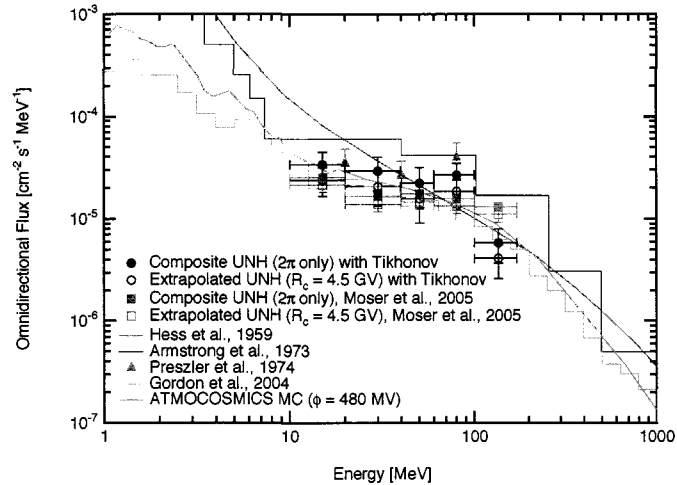


Figure 6–2: The cumulative mid-latitude sea level neutron energy spectrum. Results obtained using Tikhonov regularization (circles) and iterative methods (squares) are shown.

Several methods for obtaining true spectra have been carried out in the past for X-ray,  $\gamma$ -ray and neutron astronomy. Forward folding has been applied to  $\gamma$ -ray flare data from COMPTEL on the Compton Gamma Ray Observatory (Young 2001) and the Solar Maximum Mission (Share and Murphy 1995). The solar plasma electron spectrum can be de-convolved by measuring the X-ray bremsstrahlung distribution (Prato et al. 2006; Piana 1994; Kontar et al. 2004). Korchaov et al. (1998) performed de-convolution of solar flare neutron data for the X12 flare of 15 June 1991 measured by COMPTEL by direct inversion (assuming a response matrix with only diagonal elements). As we alluded to in section 5.2.3, this method underestimates the total neutron emissivity.

Toner et al. (2001) performed a full inversion using Maximum Entropy for the 15 June 1991 event that included off-diagonal elements of the response to derive a neutron emissivity, lower than that determined by Kocharov et al. (1998) (Figure 6–1). To incorporate off-diagonal response elements, a full de-convolution is needed. We chose to

work with the regularization method developed (outlined above) by Tikhonov. Zeroth-order Tikhonov regularization was applied to UNH ground-level neutron telescope data to obtain the sea level neutron energy distribution (Moser et al. 2005). The results agree with other measurements and predictions (Figure 6–2). The UNH telescope has enough qualitative similarities to FNIT SM2 (and facsimiles) to pose a deconvolution problem of similar character.

### **6.3 IMPLEMENTATION**

In this section we will discuss the implementation of forward folding and Tikhonov regularization for measured and simulated data from quasi-monoenergetic and fission neutrons. The scope of this work was not to use forward folding as a means to obtain model parameters, but rather to test the agreement between measured data ( $D_i$ ) and the computed data ( $C_i$ ) resulting from folding the input (model) spectrum into the broadened instrument response ( $R_{ij}$ ). Statistical analysis between  $C_i$  and  $D_i$  was performed by computing the reduced chi-square parameter and the weighted mean (and error) of each distribution. Ultimately, a measure of the true incident energy spectrum is desired. In section 6.3.2 we show the results of using Tikhonov regularization to de-convolve the incident spectrum from the data, the method used to determine the optimal regularization parameter ( $\lambda$ ), the sensitivity of  $\lambda$ , and the errors associated with the regularization procedure.

### 6.3.1 FORWARD FOLDING

The model (input) spectrum used for the neutron beam calibration data was a flat (uniform) distribution over a given energy range to generate  $C_i$ . A reduced chi-square test determined whether or not the convolved data set,  $C_i$ , was indicative of the measured set,  $D_i$ . The chi-square parameter is given as

$$\chi^2 = \sum_{i=1}^n \frac{[D_i - C_i]^2}{\sigma_D^2 + \sigma_C^2}, \quad (6.11)$$

where the denominator is the variance of the difference  $D_i - C_i$  (Bevington and Robinson 2003). The reduced chi-square is given by

$$\chi_v^2 = \frac{\chi^2}{\nu}, \quad (6.12)$$

where  $\nu$  is the number of degrees of freedom. The weighted mean and variance of the input model and measured data set provides an additional quantitative measure of the energy reconstruction method, instrument model and broadening, and input spectrum. We accepted distributions of  $C$  and  $D$  whose means were in agreement to within  $\pm 1\text{-}\sigma$ . Shown in Figures 6–3 through 6–5 are  $D$  (laboratory measured data: black),  $C$  (convolved data generated from the model: red), and the  $\chi^2$  parameter for each energy bin (blue). The response matrices used are shown in section 5.2.2 and are for A–C ( $0^\circ$ ,  $30^\circ$ ,  $45^\circ$ , and  $60^\circ$ ) and B–C ( $15^\circ$ ,  $45^\circ$ , and  $60^\circ$ ) double scatters. We used a 200 keV binning strategy, which is of the order of the pulse height resolution at low energy.

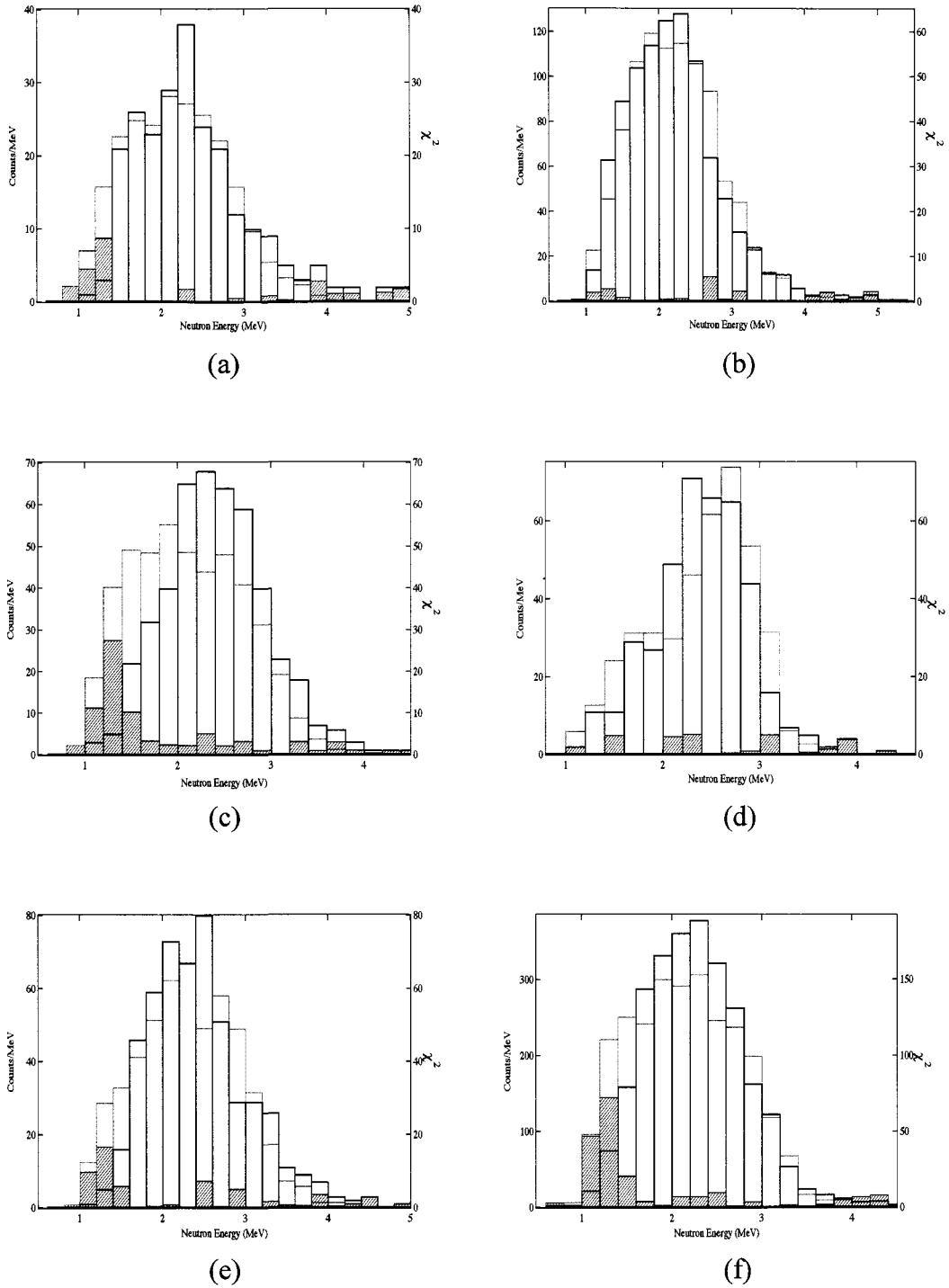
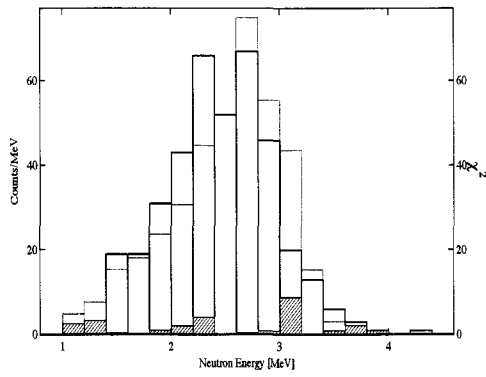
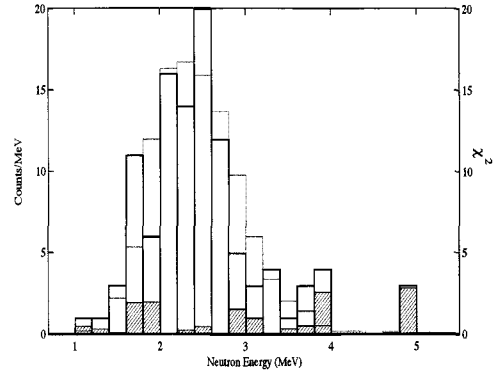


Figure 6-3: 1.0–2.9 MeV neutron beam, A–C (a) 0°, (b) 30°, (c) 45°, (d) 60°; B–C (e) 15°, (f) 45°. Convolved data generated from the model and instrument response, *C* (red); laboratory measured data, *D* (black); chi-square value per bin (blue).

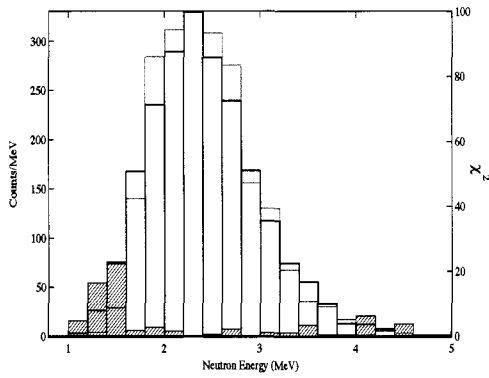




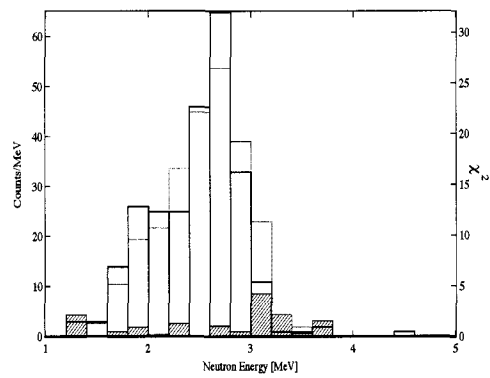
(a)



(b)



(c)



(d)

Figure 6-4: 1.0–2.9 MeV neutron beam, B–C (a) 60°; 1.8–2.9 MeV neutron beam, A–C (b) 0°, (c) 30°, (d) 60°. Convolved data generated from the model and instrument response, *C* (red); laboratory measured data, *D* (black); chi-square value per bin (blue).

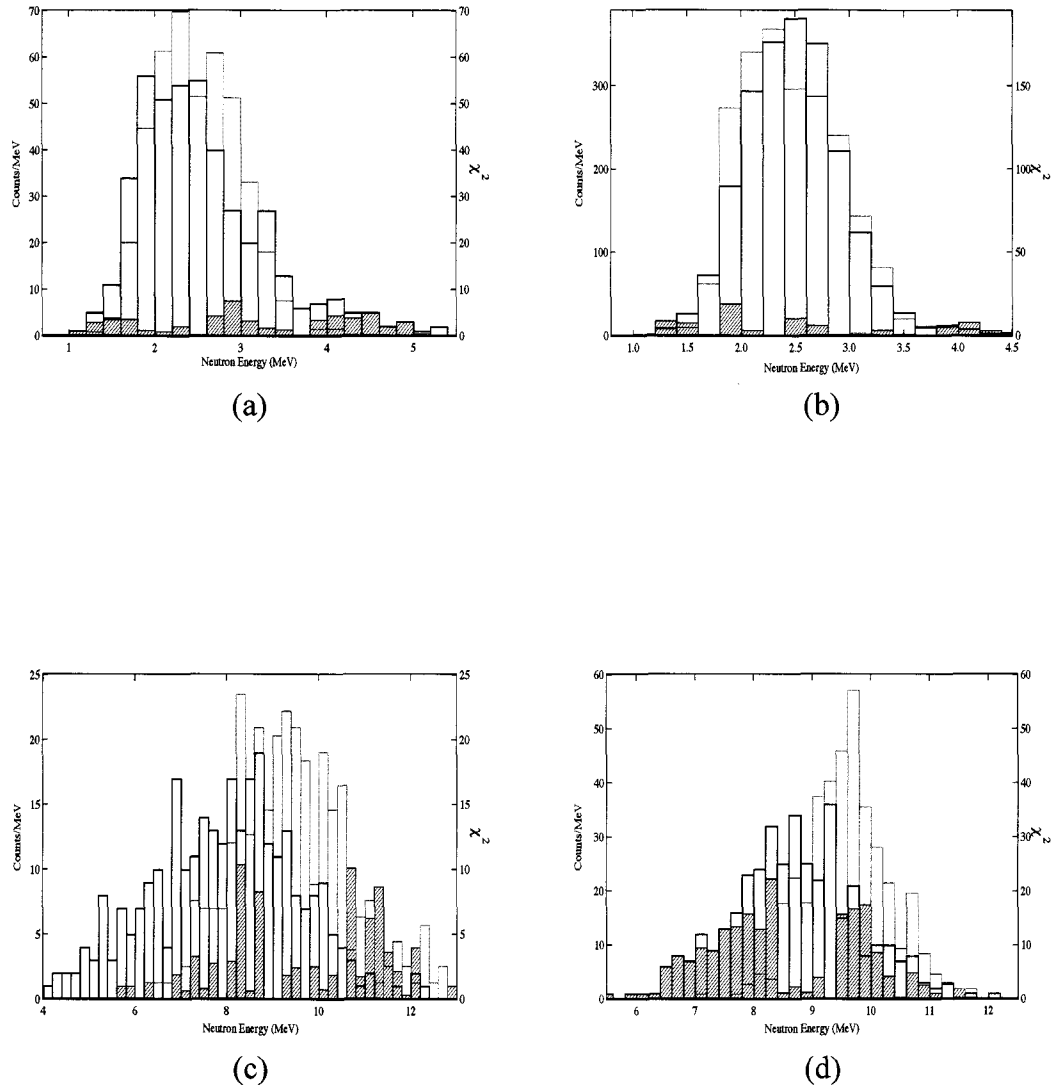


Figure 6-5: 1.8–2.9 MeV neutron beam, B–C (a) 15°, (b) 45°. 9.1–10.9 MeV neutron beam, A–C (c) 30°; B–C (d) 45°. Convolved data generated from the model and instrument response, *C* (red); laboratory measured data, *D* (black); chi-square value per bin (blue).

Energy (Pair) & Angle	$C$	$D$	$\chi_v^2$
<b>1.0 – 2.9 MeV (AC): 0°</b>	2.2 ± 0.6	2.4 ± 0.8	1.4
30°	2.2 ± 0.6	2.2 ± 0.7	1.1
45°	2.1 ± 0.6	2.4 ± 0.6	4.1
60°	2.4 ± 0.5	2.4 ± 0.5	2.0
<b>1.0 – 2.9 MeV (BC): 15°</b>	2.3 ± 0.6	2.5 ± 0.6	3.0
45°	2.2 ± 0.6	2.3 ± 0.6	10.0
60°	2.5 ± 0.5	2.5 ± 0.5	1.9
<b>1.8 – 2.9 MeV (AC): 0°</b>	2.5 ± 0.5	2.5 ± 0.7	0.8
30°	2.4 ± 0.5	2.4 ± 0.6	3.4
60°	2.5 ± 0.4	2.5 ± 0.5	1.2
<b>1.8 – 2.9 MeV (BC): 15°</b>	2.5 ± 0.5	2.6 ± 0.8	2.8
45°	2.5 ± 0.4	2.5 ± 0.5	4.5
<b>9.1–10.9 MeV (AC): 30°</b>	9.4 ± 1.3	10.0 ± 1.3	2.3
<b>9.1–10.9 MeV (BC): 45°</b>	9.6 ± 0.7	8.7 ± 1.1	6.4

Table 6–1: Weighted mean and error for convolved data generated from the model and instrument response,  $C$ ; laboratory measured data,  $D$ ; chi-square value per bin with  $\chi_v^2$  value for each energy and angle.

The means of the distributions outlined in Table 6–1 are in agreement in the 1–3 MeV range with reasonable values for the reduced chi-square. A value of the reduced chi-square  $\sim 1$  indicates that the model adequately describes the spread in the data points well, provided there are sufficient statistics. Larger or smaller values than unity indicate measurement uncertainties incorrectly accounted for, or a misunderstanding in the assumed model (Bevington and Robinson 2003). For increasing incident neutron energy,

the agreement between the means of each distribution start to diverge, caused by the effect discussed in section 4.4.1 – the short ToF of the high-energy scattered neutron blending in with  $\gamma$  rays, making it difficult to select out a clean neutron signal.

Figure 6–6 shows the results for fission neutrons. The binning of the data and the response matrices are in terms of lethargy,  $u$  (discussed in section 3.2.1). Lethargy allows for the naturally less populated bins – due to the scatters at high energies and a decrease in cross section – to be counted without a reduction in the resolution and avoids an excess in low frequency bin counts. The lethargy binned response matrix and theoretical  $^{252}\text{Cf}$  fission neutron spectrum (see section 4.6.2) are used to construct the count spectrum,  $C$ . Comparison of  $C$  (red) and  $D$  (black) for A–C ( $0^\circ$ ,  $30^\circ$ , and  $60^\circ$ ) and B–C scatters at  $15^\circ$ ,  $45^\circ$ , and  $75^\circ$  is shown in Figure 6–6. The reduced chi-square for each bin is shown in blue. There is good agreement between  $C$  and  $D$  when measuring the continuous spectrum.

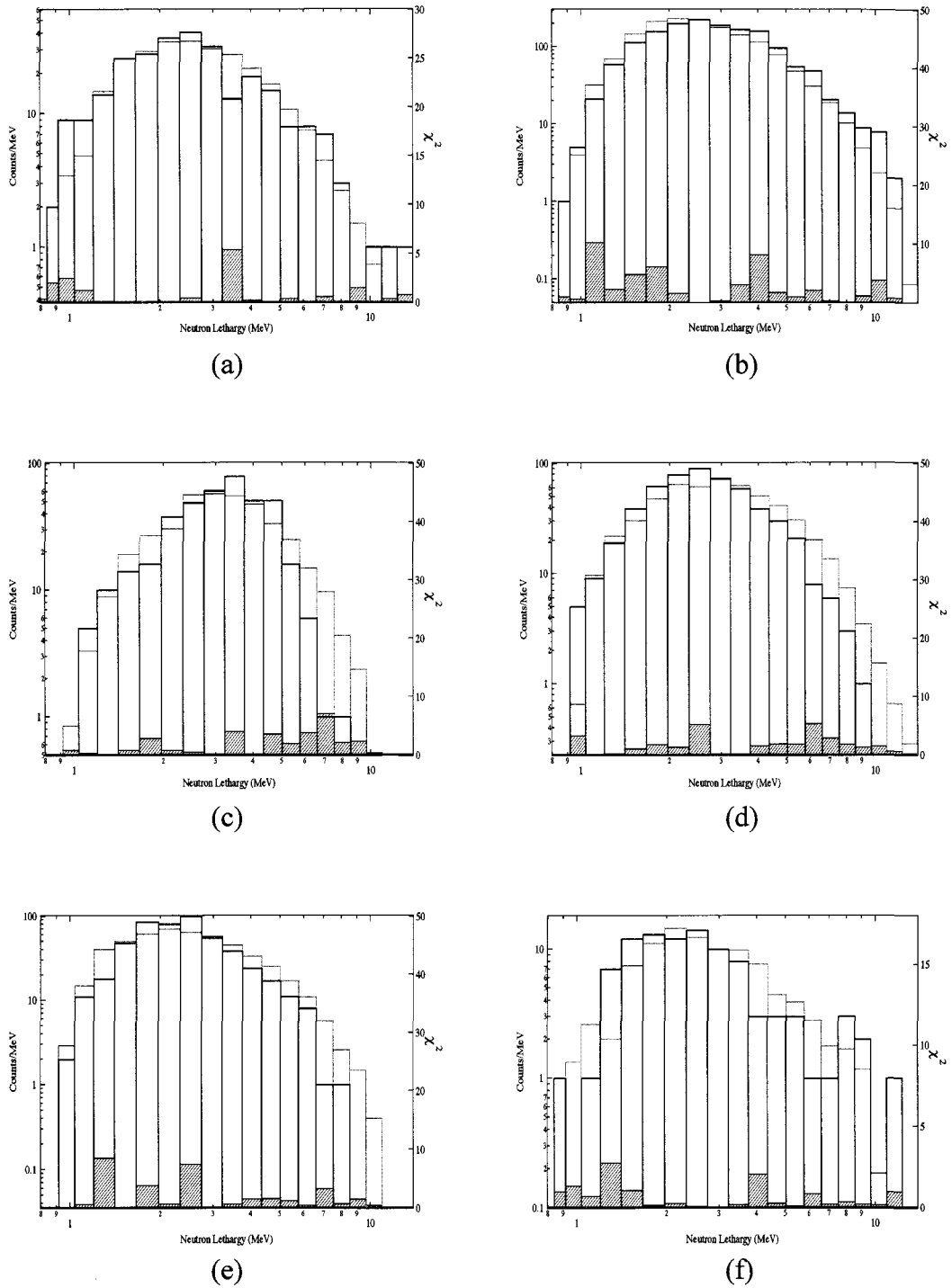


Figure 6–6:  $^{252}\text{Cf}$  count spectrum for A–C orientations: (a)  $0^\circ$ , (b)  $30^\circ$ , (c)  $60^\circ$ ; B–C orientations: (d)  $15^\circ$ , (e)  $45^\circ$ , (f)  $75^\circ$ . Convolved data generated from the model and instrument response, *C* (red); laboratory measured data, *D* (black); chi-square value per bin (blue).

Rotation Angle	$C$	$D$	$\chi_v^2$
AC: 0°	$3 \pm 1.6$	$2.9 \pm 1.8$	0.8
30°	$2.8 \pm 1.4$	$3.1 \pm 1.5$	2.6
60°	$3.4 \pm 1.5$	$3.3 \pm 1.1$	1.9
BC: 15°	$3.3 \pm 1.7$	$2.9 \pm 1.3$	1.8
45°	$2.7 \pm 1.4$	$2.6 \pm 1.1$	1.9
75°	$3.1 \pm 1.7$	$2.9 \pm 2.0$	0.7

Table 6–2: Weighted mean and error for convolved data generated from the model and instrument response,  $C$ ; laboratory measured data,  $D$ ; chi-square value per bin with  $\chi_v^2$  value for each energy and angle.

### 6.3.2 TIKHONOV REGULARIZATION

We plotted the Fourier coefficients and singular values for linear and lethargy binned response matrices to determine whether or not the Discrete Picard Condition (DPC) – defined in section 6.2 – is satisfied. This is represented graphically in Figure 6–7 with the singular values of the response matrix (blue), the Fourier coefficients (green), and the ratio of the Fourier coefficients to the singular values (red). The measured data vector,  $D$ , used for input into equation 6.8 demonstrated that, on average, the behavior of the singular values with respect to the Fourier coefficients satisfies the DPC. To carry out the de-convolution of measured neutron data, we chose A–C scatters incident at 30°.

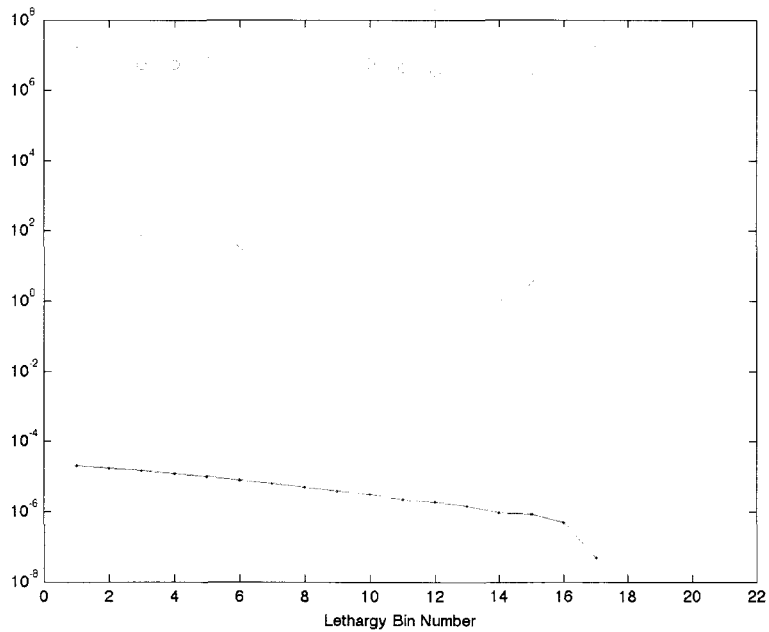
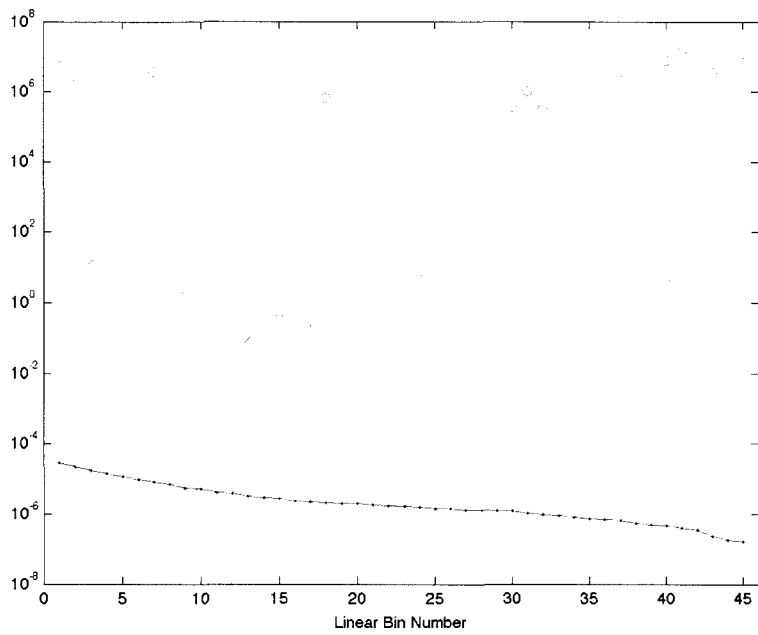


Figure 6–7: Response matrix singular values (blue), Fourier coefficients (green), and the ratio of the Fourier coefficients to the singular values (red) for response matrix at a  $30^\circ$  rotation with 200-keV linear bins (top) and lethargy bins (bottom). Plotting tools courtesy of P. C. Hansen.

Mallik (2009) experimented with zeroth, first and second order Tikhonov regularization strategies using the on-axis FNIT SM2 double scatter neutron telescope response matrix. The input used for the test was a “fake” data set representative of a continuous spectrum with jagged (sharp) features. The de-convolved output was then compared to the original input. It was found that the first and second order solutions were more smooth and able to pick out subtle features in the data, where zeroth order tends to under-smooth the solution. However, the Picard Condition was not satisfied for first and second order (using the GSVD) and thus could not automate a value for the smoothing parameter. Thus, for our de-convolution studies we concentrated on zeroth order Tikhonov regularization. The main focus of the work was the 1.8–2.9 MeV quasi-monoenergetic neutron beam and  $^{252}\text{Cf}$  fission neutron data. The regularized solution is given in equation 6.9, where the orthonormal matrices  $U$  and  $V$  and the singular values  $\sigma$  were generated using the singular value decomposition algorithm in MATLAB. We then determined the optimal value of the regularization parameter,  $\lambda$ , following the discrepancy principle method outlined in Turchin (1967). The value of  $\lambda$  is given such that the square of the residual norm is equal to the norm of the error vector

$$\|D - RS_\lambda\|^2 = \sum \sigma_D^2, \quad (6.13)$$

where the right hand side is simply the sum of the components of the data vector for Gaussian statistics. The value of  $\lambda$  that satisfies equation 6.14 ensures that the regularized solution  $S_\lambda$  is the nearest approximation to the exact solution,  $S$ .



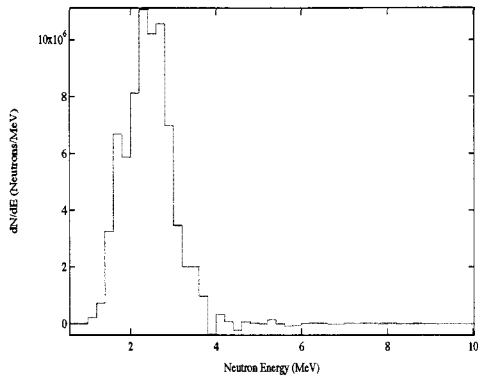
With the determination of the optimal value of  $\lambda$ , we investigated how the response matrix precision affects the regularized solution and the value of  $\lambda$ . We performed this test by starting with data sets that were equally noisy, i.e.,  $D$  and  $R$  with roughly the same number of counts, and then systematically increased the precision of  $R$  (more counts) while holding  $D$  constant (summarized in Table 6–3 for 1.8–2.9 MeV neutrons, and Table 6–4 for fission neutrons).

$D$ (No. of Events)	$R$ (No. of Events)	$\lambda$
$2.2 \times 10^3$	$2.3 \times 10^3$	$5.60 \times 10^{-6}$
$2.2 \times 10^3$	$4.6 \times 10^3$	$5.30 \times 10^{-6}$
$2.2 \times 10^3$	$7.7 \times 10^3$	$6.67 \times 10^{-6}$
$2.2 \times 10^3$	$1 \times 10^4$	$6.65 \times 10^{-6}$

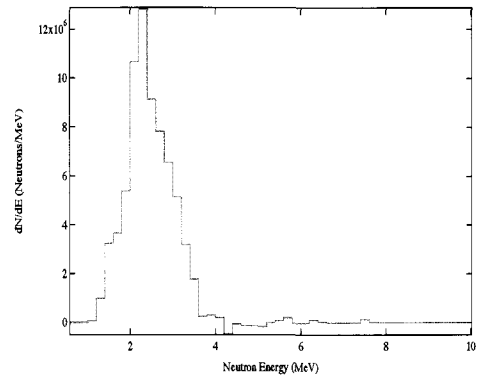
Table 6–3: Variation of the response matrix precision with respect to a constant number of 1.8–2.9 MeV neutron beam events to determine how the optimal value of the smoothing parameter varied.

$D$ (No. of Events)	$R$ (No. of Events)	$\lambda$
$1.6 \times 10^3$	$1.9 \times 10^3$	$3.85 \times 10^{-6}$
$1.6 \times 10^3$	$3.2 \times 10^3$	$4.06 \times 10^{-6}$
$1.6 \times 10^3$	$6.3 \times 10^3$	$4.04 \times 10^{-6}$
$1.6 \times 10^3$	$1 \times 10^4$	$4.23 \times 10^{-6}$

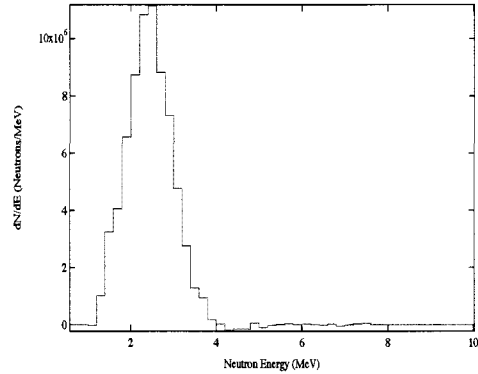
Table 6–4: Variation of the response matrix precision with respect to a constant number of fission neutron events to determine how the optimal value of the smoothing parameter varied.



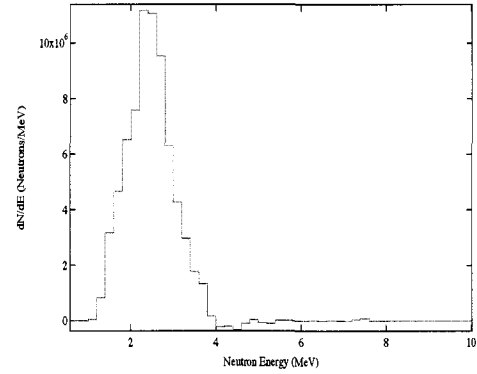
(a)



(b)

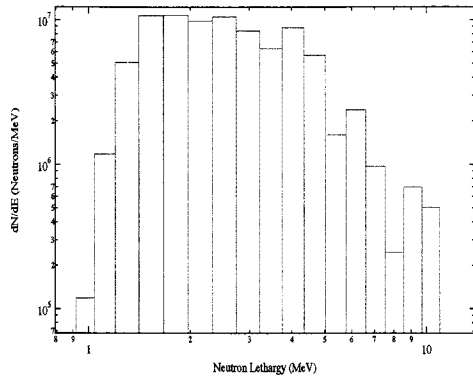


(c)

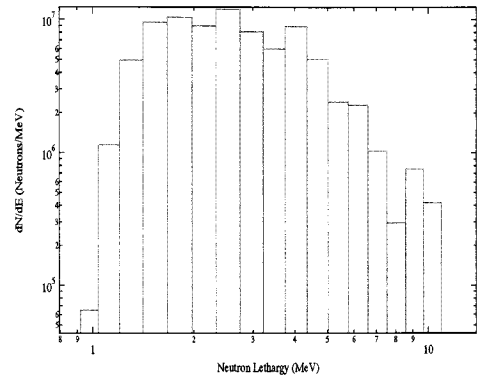


(d)

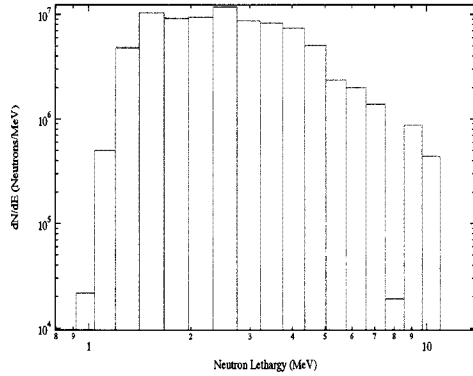
Figure 6–8: De-convolved 1.8–2.9 MeV neutron beam spectrum for (a)  $\sim$ equal, (b)  $2\times$ , (c)  $3.5\times$ , (d)  $4.5\times$  the number of counts in the data set as is in the 200-keV linear binned response matrix at  $30^\circ$ .



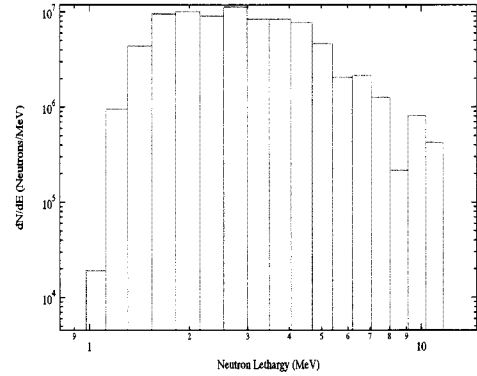
(a)



(b)



(c)



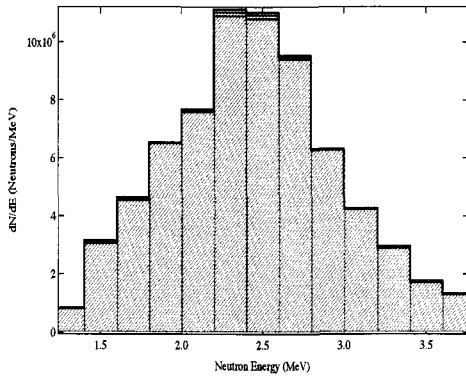
(d)

Figure 6–9: De-convolved fission neutron spectrum for (a)  $\sim$ equal, (b)  $2\times$ , (c)  $3.5\times$ , (d)  $\sim 6\times$  the number of counts in the data set as is in the lethargy binned response matrix at  $30^\circ$ .

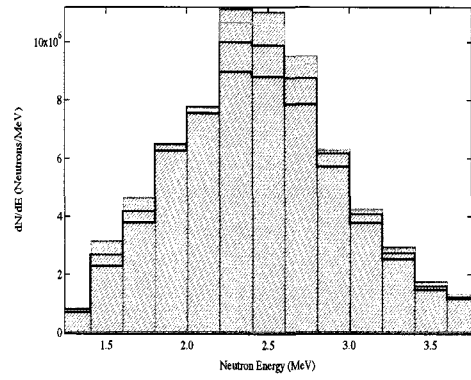
The results show that the value of  $\lambda$  is sensitive to change in the precision of  $R$ . Given this, we investigated the spectral sensitivity to percentage changes in  $\lambda$ . The response matrix with  $1 \times 10^4$  events (last row of Tables 6–3 and 6–4) was used, corresponding to  $\sim 5\text{--}6\times$  the number of counts in the data vector from measurements. The value of  $\lambda$  was varied by  $\pm 1\%$ ,  $\pm 5\%$ ,  $\pm 10\%$ ,  $\pm 20\%$ ,  $\pm 50\%$ , and  $100\%/ -99\%$  for both data sets. In Figures 6–10 through 6–14 the varied regularized solution is plotted with the “optimal” spectrum for comparison. The absolute value of the relative error between the optimal and varied spectrum (per bin) was also computed in each case to show where the largest deviations between the varied and optimal spectrum occur. The values for  $\lambda$  are summarized in the table below; the value of the square of the residual norm,  $\rho$ , was computed for each new  $\lambda$ . We showed that  $\lambda$  was determined such that the value of  $\rho$  was equal to the summed number of events in the data vector (see equation 6.14).

	Optimal	+1%	+5%	+10%	+20%	+50%	+100%
$\lambda$	$6.646 \times 10^{-6}$	$6.712 \times 10^{-6}$	$6.978 \times 10^{-6}$	$7.310 \times 10^{-6}$	$7.975 \times 10^{-6}$	$9.968 \times 10^{-6}$	$1.329 \times 10^{-5}$
$\rho$	2,147	2,211	2,477	2,843	3,691	7,311	17,560
	Optimal	-1%	-5%	-10%	-20%	-50%	-99%
$\lambda$	$6.646 \times 10^{-6}$	$6.579 \times 10^{-6}$	$6.313 \times 10^{-6}$	$5.981 \times 10^{-6}$	$5.316 \times 10^{-6}$	$3.323 \times 10^{-6}$	$6.646 \times 10^{-8}$
$\rho$	2147	2086	1852	1588	1148	367	8

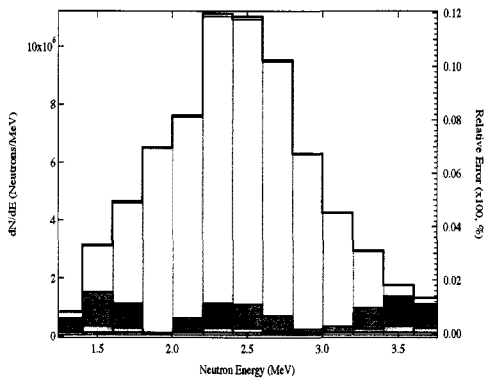
Table 6–5: Values of  $\lambda$  and  $\rho$  for (+/–) percent changes to the optimal value of  $\lambda$  with 1.8–2.9 MeV neutron beam data at  $30^\circ$ .



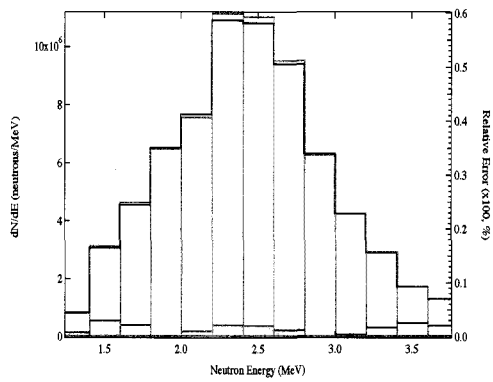
(a)



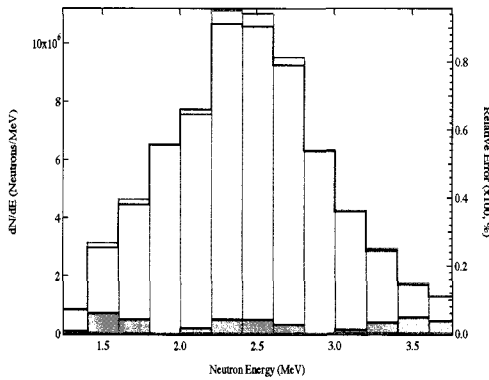
(b)



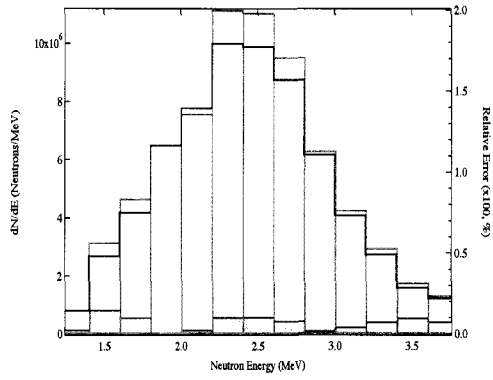
(c)



(d)

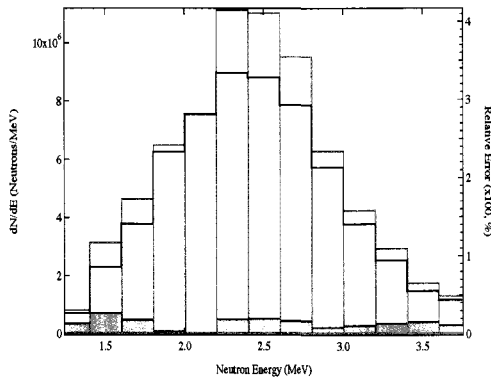


(e)

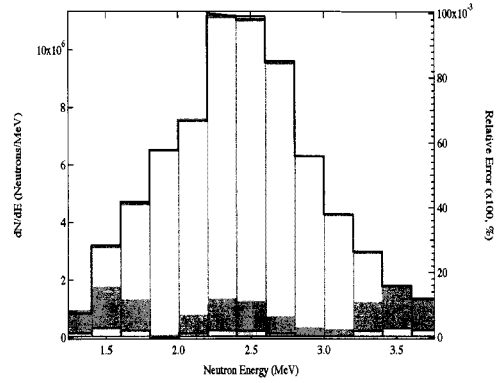


(f)

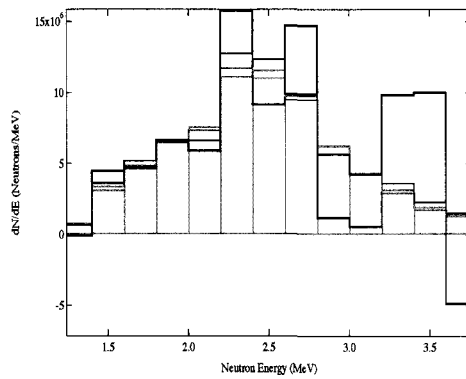
Figure 6–10: De-convolved 1.8–2.9 MeV neutron beam with optimal value of smoothing parameter (red). Variations of (a): 1% (green), 5% (blue), 10% (black); (b): 20% (green), 50% (blue), 100% (black); (c) 1% (green, with relative error in purple), 5% (blue, with relative error in gray); (d) 10% with relative error (blue); (e) 20% with relative error (blue); (f) 50% with relative error (blue).



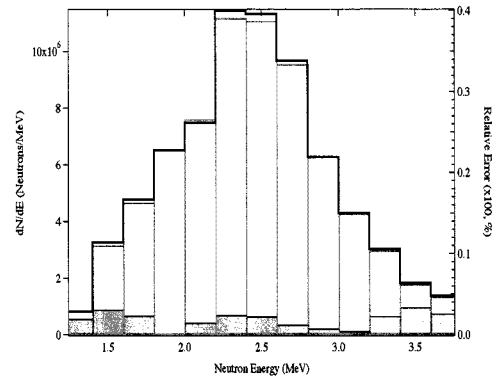
(a)



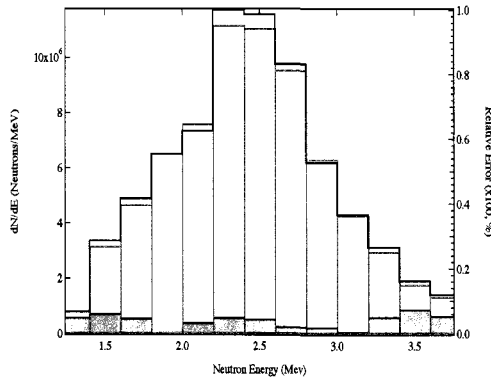
(b)



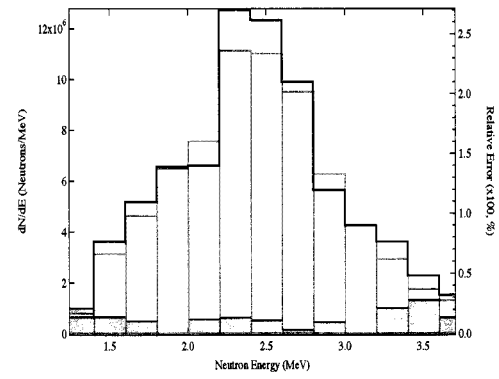
(c)



(d)



(e)



(f)

Figure 6–11: De-convolved 1.8–2.9 MeV neutron beam with optimal value of smoothing parameter (red). Variations of (a) 100% with relative error (blue); (b) –1% (green, with relative error in light green), –5% (blue, with relative error in magenta); (c) –20% (green), –50% (blue), –99% (black); (d) –10% with relative error (blue); (e) –20% with relative error (blue); (f) –50% with relative error (blue).

	Optimal	+1%	+5%	+10%	+20%	+50%	+100%
$\lambda$	$4.225 \times 10^{-6}$	$4.267 \times 10^{-6}$	$4.436 \times 10^{-6}$	$4.648 \times 10^{-6}$	$5.070 \times 10^{-6}$	$6.337 \times 10^{-6}$	$8.450 \times 10^{-6}$
$\rho$	1,556	1,599	1,777	2,016	2,547	4,603	9,751
	Optimal	-1%	-5%	-10%	-20%	-50%	-99%
$\lambda$	$4.225 \times 10^{-6}$	$4.183 \times 10^{-6}$	$4.014 \times 10^{-6}$	$3.803 \times 10^{-6}$	$3.380 \times 10^{-6}$	$2.113 \times 10^{-6}$	$4.225 \times 10^{-8}$
$\rho$	1556	1514	1351	1165	839	222	14

Table 6-6: Values of  $\lambda$  and  $\rho$  for (+/-) percent changes to the optimal value of  $\lambda$  with fission neutron data at  $30^\circ$ .

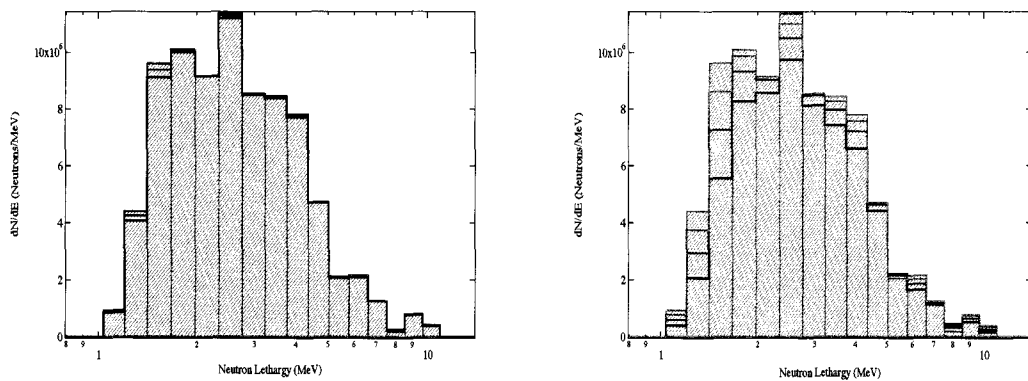


Figure 6-12: De-convolved fission neutrons with optimal value of smoothing parameter (red). Variations of (left): 1% (green), 5% (blue), 10% (black); (right): 20% (green), 50% (blue), 100% (black).

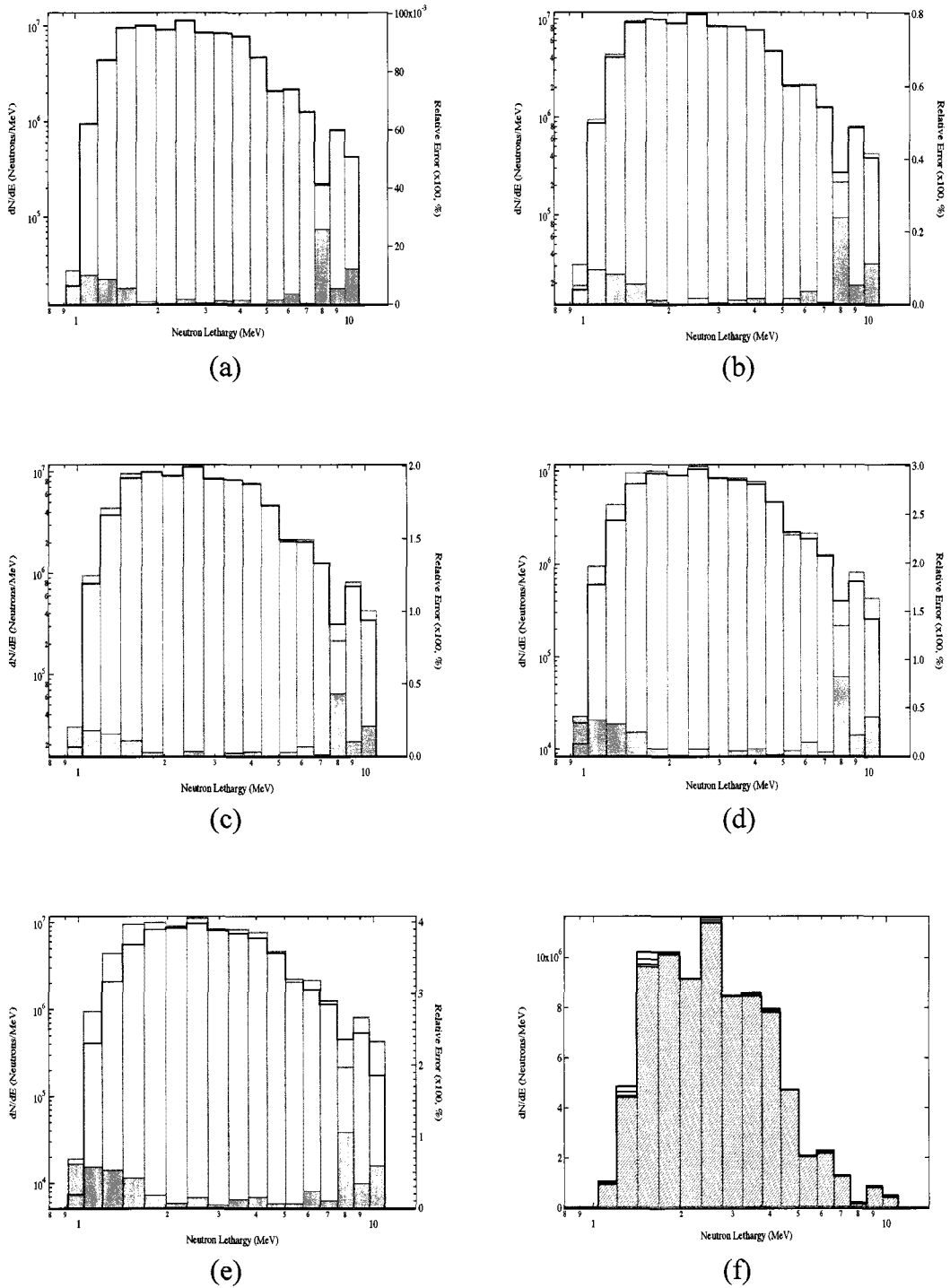
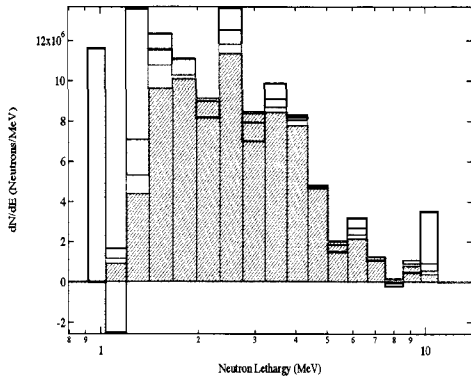
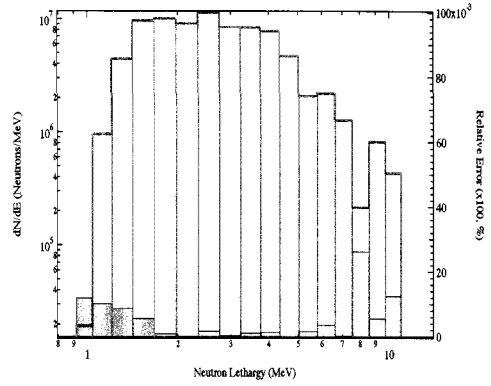


Figure 6-13: De-convolved fission neutron spectrum with optimal value of smoothing parameter (red). Variations of (a) 1% with relative error in (blue); (b) 10% with relative error in (blue); (c) 20% with relative error in (blue); (d) 20% with relative error in (blue); (e) 20% with relative error in (blue); (f): -1% (green), -5% (blue), -10% (black).

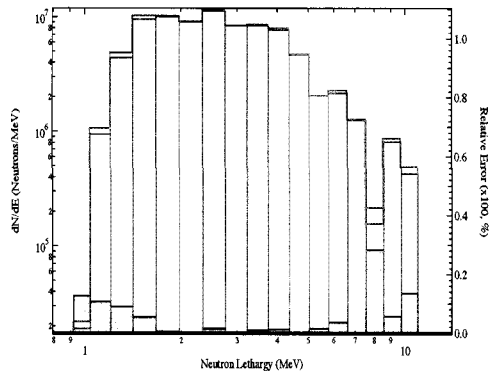




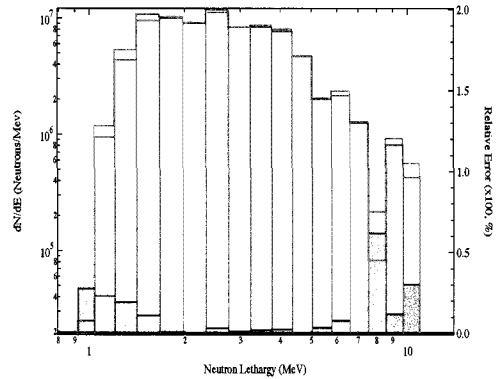
(a)



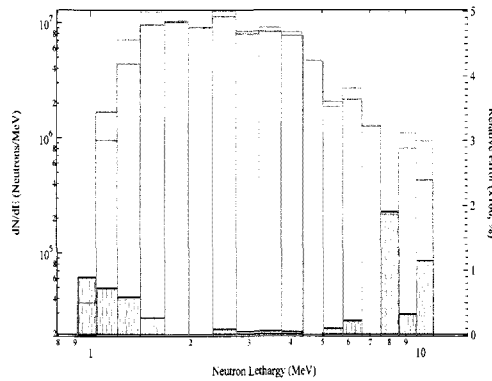
(b)



(c)



(d)



(e)

Figure 6-14: De-convolved fission neutron spectrum with optimal value of smoothing parameter (red). Variations of (a): -20% (green), -50% (blue), -99% (black); (b) -1% with relative error in (blue); (c) -10% with relative error in (blue); (d) -20% with relative error in (blue); (e) -50% with relative error in (blue).

Increasing  $\lambda$  results in spectra with lower counts per bin ( $dN/dE$ ) and hence a lower overall total number of neutrons. Typically, the opposite is true. As the value of  $\lambda$  approaches zero – nearing direct inversion – the solution becomes unstable resulting in (comparatively) large negative  $dN/dE$  values in some bins. To determine the error in  $\lambda$  we computed the fluctuations in the number of counts obtained for repeated simulations (with different random seeds) of the same conditions. One simulation produces a given number of counts; a set of simulations repeated 10× yielded numbers that fell within  $\pm 3\text{-}\sigma$  of the original number of counts. Using this information we computed the corresponding 1- $\sigma$  error in  $\lambda$  based on the observed variation of  $\rho$  with respect to  $\lambda$ . For the quasi-monoenergetic neutrons we find an optimal value for  $\lambda$  of:  $(6.65 \pm 0.13) \times 10^{-6}$ ; for fission neutrons we find  $\lambda$ :  $(4.23 \pm 0.09) \times 10^{-6}$ . In Figure 6–15 we show the optimal spectrum (red) with  $\pm 1\text{-}\sigma$  error (black dots).

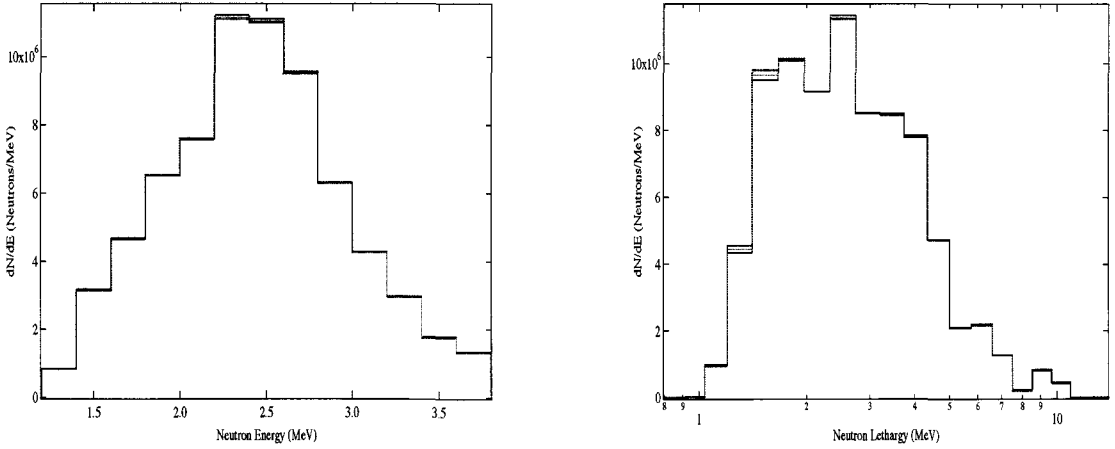


Figure 6–15:  $\pm 1\text{-}\sigma$  error (black) in the optimal value of the smoothing parameter (red) for the de-convolved: 1.8–2.9 MeV neutron beam (left) and fission neutrons (right).

## 6.4 NEUTRON IMAGING

Imaging of double scatter neutrons requires that the path of the recoil neutron between each scatter is known. The methods to acquire such information were outlined in section 3.2.1 and demonstrated in section 4.3. With full neutron energy measurement from the pulse height in the first scatter and the ToF between the first and second scatter, the track of the incident neutron is restricted to lie on the mantle of a cone whose axis is the momentum vector of the recoil neutron, hereafter known as the scattered neutron vector (SNV). The neutron scatter angle  $\phi$  – previously defined as  $\theta_N$  – is used to define the half-angle of the “event cone” as shown in Figure 6–16.

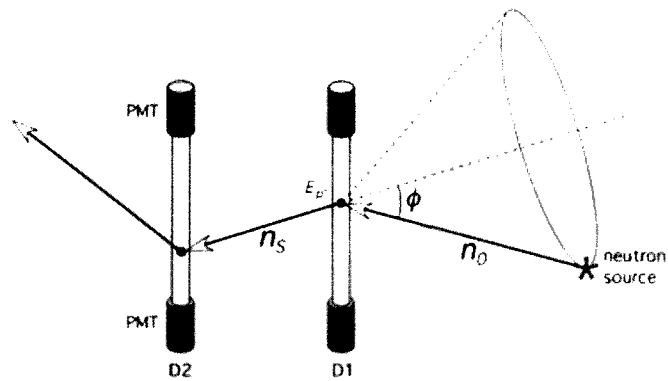


Figure 6–16: Double scatter neutron event in FNIT SM2 producing an event cone.

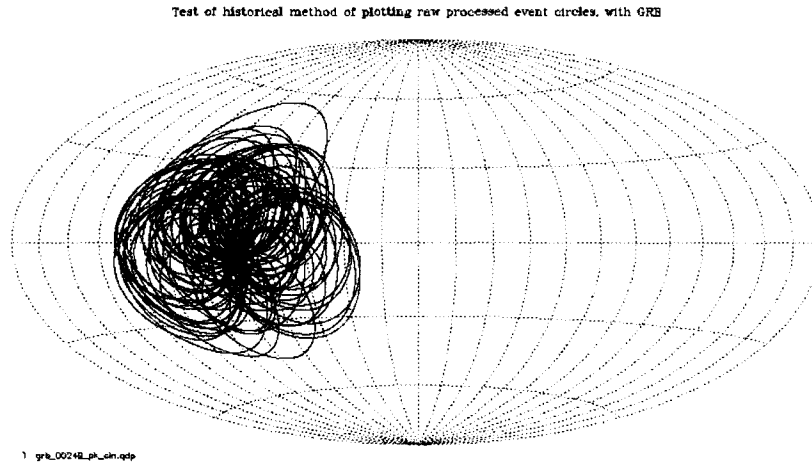


Figure 6–17:  $\gamma$ -ray event circle imaging from GRB910503 measured with COMPTEL (Winkler et al. 1993).

To perform imaging, the event cone is back-projected onto the image plane where it intersects to form a 2-d “event circle.” The superposition of many event circles can produce an image. This procedure is analogous to that used successfully by the COMPTEL instrument (Winkler et al. 1993) aboard the Compton Gamma-Ray Observatory (CGRO) to locate a source of extragalactic  $\gamma$  rays (Figure 6–17) and also to image the Sun (Figure 6–18) in 15–80 MeV neutrons (McConnell 2010). Without a full energy measurement, the radius of the event circle derived from the two recoil proton pulse heights would be too large. The source under investigation would then have to lie within the interior of the expanded event circle. The energy measure would thus be a lower limit and the event circle becomes an event disk where the circumference of the disk would be the computed event circle.

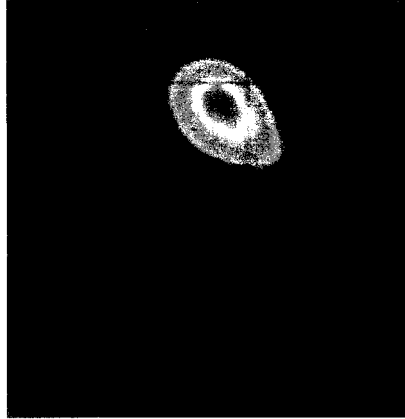
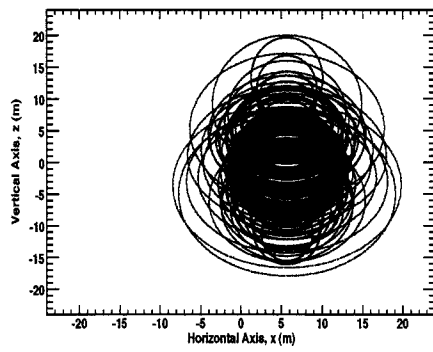


Figure 6–18: Image of the Sun in 15–80 MeV neutrons from 15 June 1991 X12 flare (McConnell 2010).

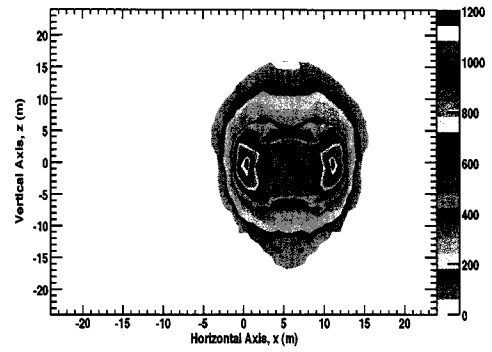
The point spread function coordinates are defined on a Cartesian plane with  $(x, z)$  defining the direction of the scattered neutron and  $\phi$  defining the neutron scatter angle. The direction of the scattered neutron (and hence the center of the event circle) is determined by using direction cosines and normalized unit vectors from the location information in the position sensitive rods and the distance to the image plane. Euler angles rotate the event circle to intersect the image plane dependent on the incident scatter angle. A set of 360 points – one for each degree of the circle – are plotted on the image plane to create an unbiased probability distribution for possible source location. The image plane is segmented into small-scale bins; for each point of the event circle that crosses the bin boundary, that bin is incremented and counted for intersections with the most intersections corresponding to the most probable location of the source. Imaging instruments searching the data space for location information require more advanced algorithms because simply counting the intersections of event circles on the image plane integrates over much useful information. A full knowledge of the image space response

(i.e. the PSF) would be needed to employ imaging algorithms, such as the Maximum Entropy method (Strong et al. 1992), the Maximum Likelihood method (deBoer et al. 1992), or iterative-based Bayesian techniques (Lucy 1972; Richardson 1972). However, the purpose of a double scatter telescope is to select out events that are consistent with the Sun and suppress the background from directions other than the Sun, providing data with high signal-to-noise (S/N). For the work of this thesis, the main focus for imaging is of solar origin where a high S/N is expected. Algorithms of higher-order invoking a full imaging de-convolution are beyond the scope of this work.

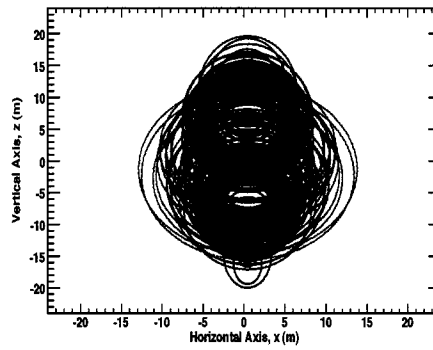
We use the double scatter event data from CNL measurements (section 4.4) and fission neutron measurements (section 4.6.2) to demonstrate event circle imaging. The image plane is in the  $x$ - $z$  plane; the  $y$ -direction — the distance between the image plane and the prototype origin — is collapsed onto the plane. For all data presented within, the source location was the origin:  $(x_0, z_0) = (0, 0)$ . In CNL measurements, we demonstrated an ambiguity in identifying source location that arises when viewing from one orientation ( $+30^\circ$  in this example, Figure 6–19*a* and *b*). At CNL, the image plane was 10 m away from the prototype origin. The location of the most event circle intersections leads to two possible source locations. The image plane is shown with event circles and the associated intensity (contour) plot for clarity. Implementing an additional viewing angle resolves the ambiguity with one detector pair. Figures 6–19*c–f* through 6–22 shows the event circle projections for  $0^\circ$ ,  $\pm 15^\circ$ ,  $\pm 30^\circ$ ,  $\pm 45^\circ$ , and  $\pm 60^\circ$  where the experiment symmetry is employed to simulate measurements at  $-15^\circ$ ,  $-30^\circ$ ,  $-45^\circ$ , and  $-60^\circ$ . Both A–C and B–C scatters are shown at each angle.



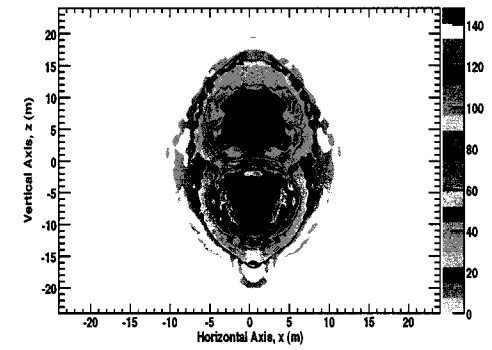
(a)



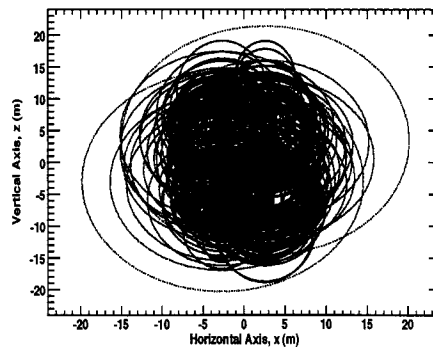
(b)



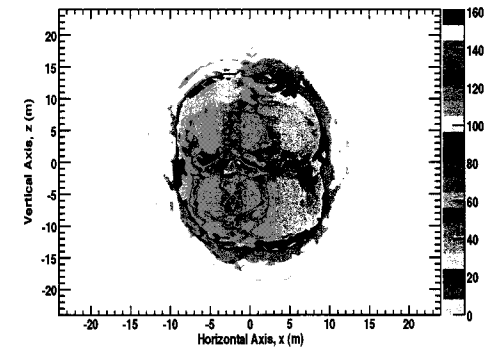
(c)



(d)

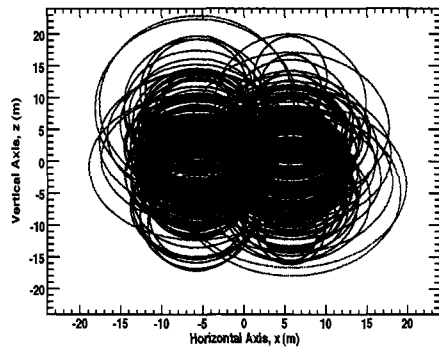


(e)

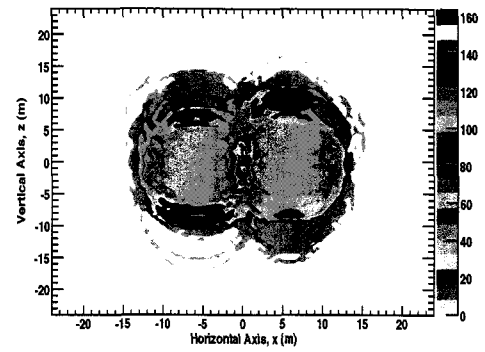


(f)

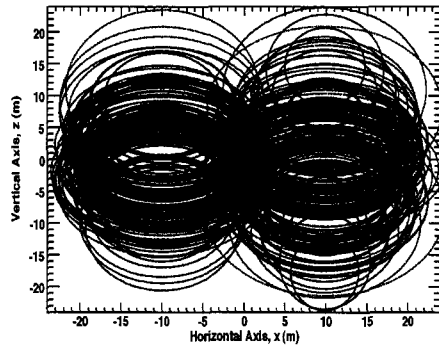
Figure 6–19: Event circle imaging (left) and corresponding intensity plots (right) for a 1.0–2.9 MeV neutron beam at 10 m away. For A–C scatters: viewing the source from one orientation of  $+30^\circ$  (a) and (b);  $0^\circ$  (c) and (d);  $\pm 15^\circ$  (e) and (f).



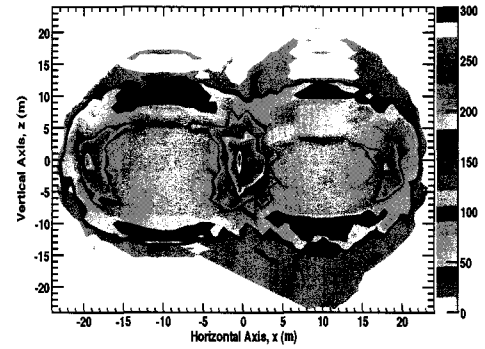
(a)



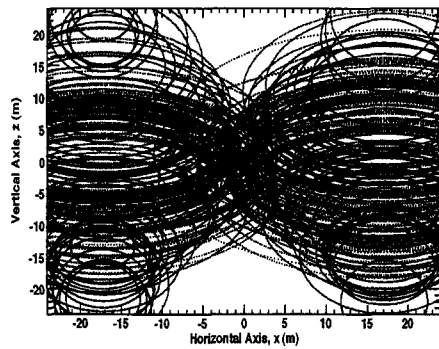
(b)



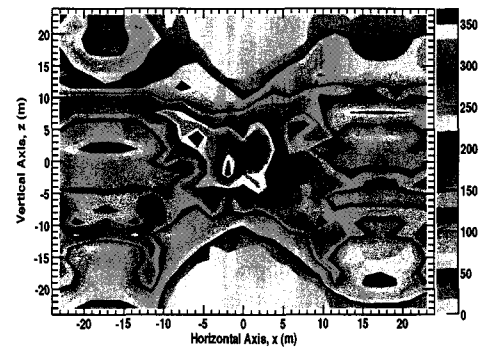
(c)



(d)



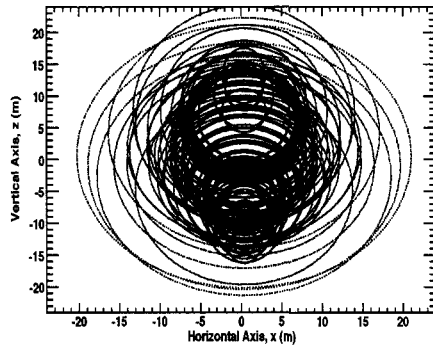
(e)



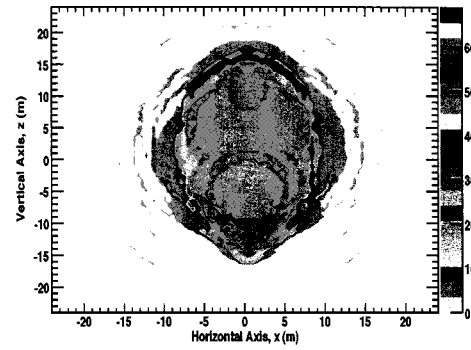
(f)

Figure 6–20: Event circle imaging (left) and corresponding intensity plots (right) for a 1.0–2.9 MeV neutron beam at 10 m away. For A–C scatters:  $\pm 30^\circ$  (a) and (b);  $\pm 45^\circ$  (c) and (d);  $\pm 60^\circ$  (e) and (f).

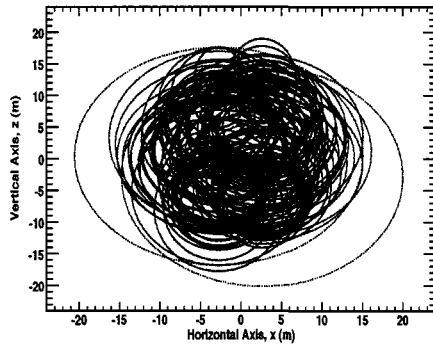




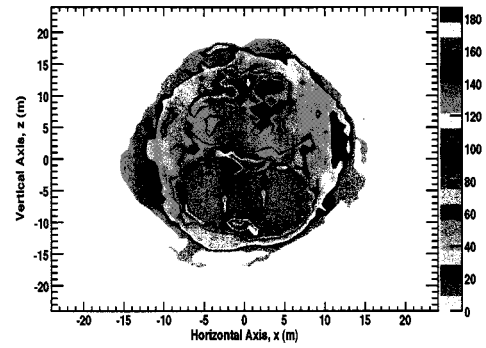
(a)



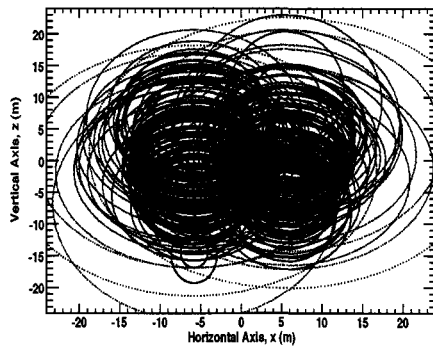
(b)



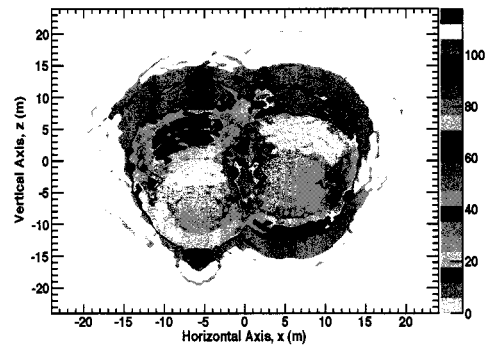
(c)



(d)

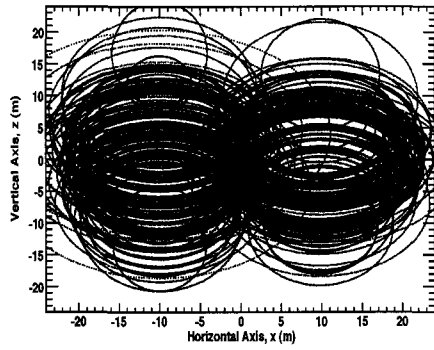


(e)

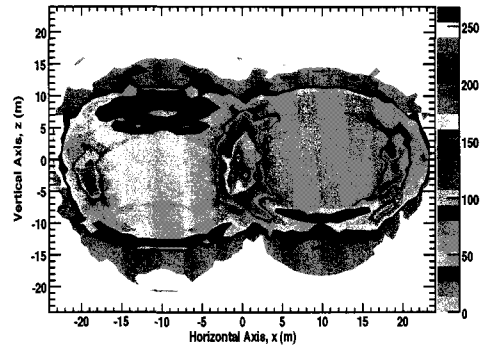


(f)

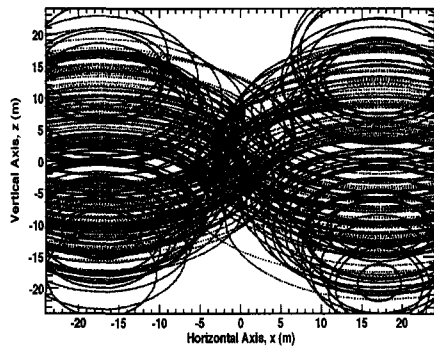
Figure 6–21: Event circle imaging (left) and corresponding intensity plots (right) for a 1.0–2.9 MeV neutron beam at 10 m away. For B–C scatters:  $\pm 0^\circ$  (a) and (b);  $\pm 15^\circ$  (c) and (d);  $\pm 30^\circ$  (e) and (f).



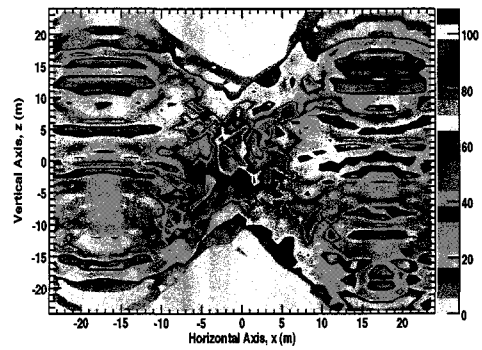
(a)



(b)



(c)



(d)

Figure 6–22: Event circle imaging (left) and corresponding intensity plots (right) for a 1.0–2.9 MeV neutron beam at 10 m away. For B–C scatters:  $\pm 45^\circ$  (a) and (b);  $\pm 60^\circ$  (c) and (d).

The 3-d representation of the image data does not suppress the y-dimension (as the 2-d view does) of image space. This view displays the number of intersections (counts) in each bin as the vertical dimension where the highest bins correspond to most probable source location. Figures 6–23 through 6–25 show the 3-d representation of image space and associated 2-d representation for the 1.0–2.9 MeV CNL neutron beam data viewed from angles varying between  $\pm 60^\circ$  in increments of  $15^\circ$  for A–C and B–C scatters.

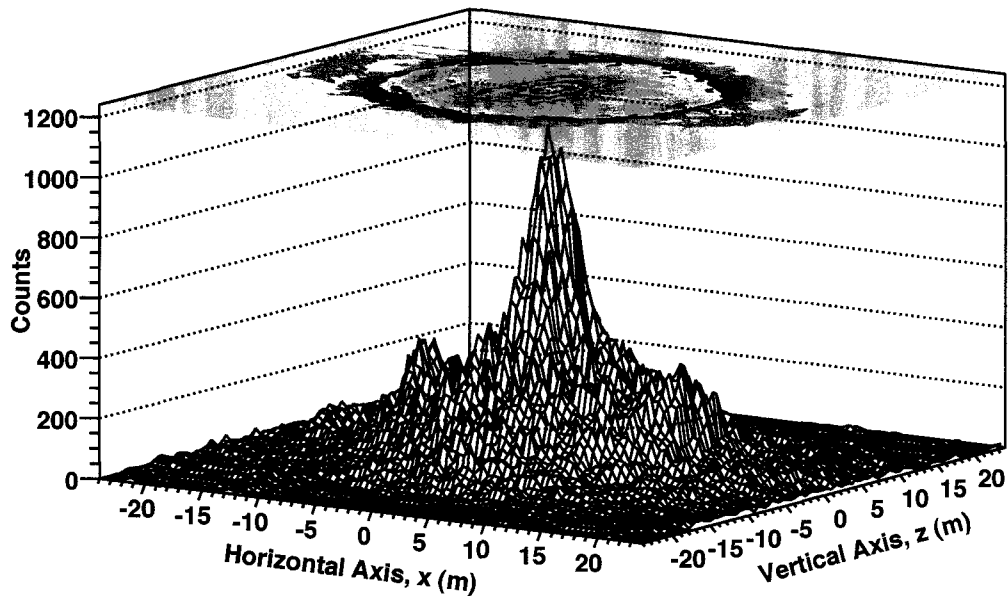


Figure 6–23: Composite image with 3-d view of the image plane for 1.0–2.9 MeV neutron beams from A–C angles varying between  $\pm 60^\circ$  in increments of  $15^\circ$ .

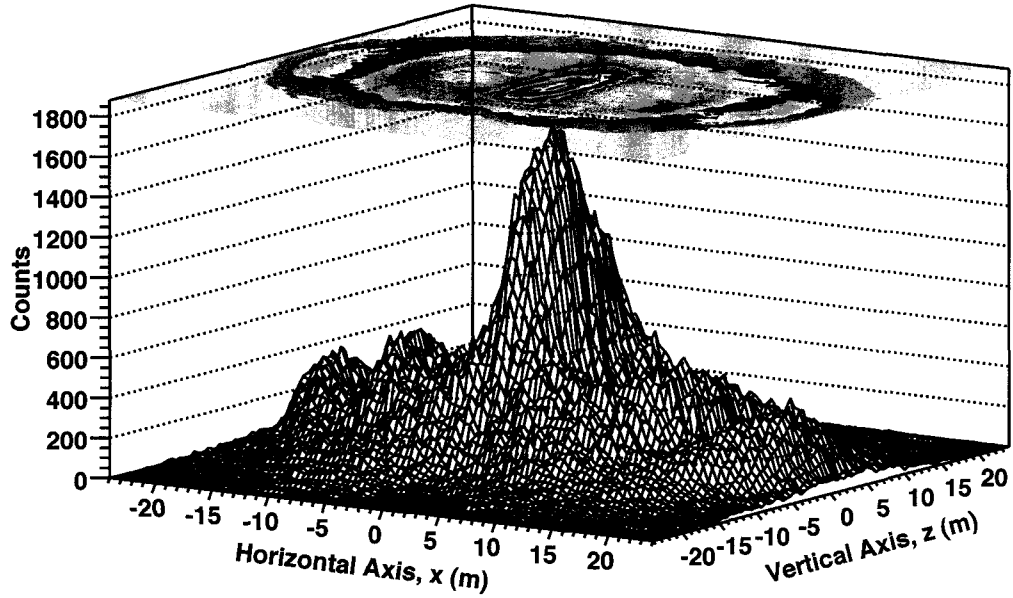


Figure 6–24: Composite image with 3-d view of the image plane for 1.0–2.9 MeV neutron beams from B–C angles varying between  $\pm 60^\circ$  in increments of  $15^\circ$ .

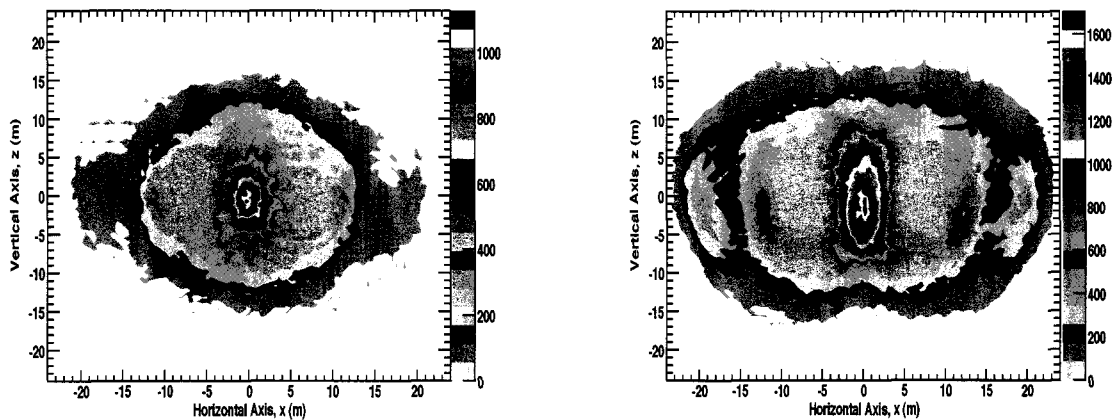


Figure 6–25: 2-d view of the image plane for 1.0–2.9 MeV neutron beams from A–C (left) and B–C (right) angles varying between  $\pm 60^\circ$  in increments of  $15^\circ$ .

Image reconstruction principles outlined above demonstrated its ability in a narrow energy band. For neutrons with a continuous energy spectrum, we apply the image reconstruction algorithm to data obtained from fission neutrons –  $^{239}\text{Pu}$  and  $^{252}\text{Cf}$ . Figure 6–26 shows the reconstructed  $^{239}\text{Pu}$  image without employing instrument symmetry, but instead the summed events from both detector A–C and B–C pairs to offer two separate viewing angles of  $30^\circ$  and  $45^\circ$ , respectively, from one exposure. The  $^{239}\text{Pu}$  was at a distance of 1 m from the axis of rotation. Although two possible source locations appear visible in the intensity plot, the density around (0, 0) has  $\sim 20\%$  more counts than (1, 0). The  $^{252}\text{Cf}$  data runs were described in section 4.6.2. In this section we use the data from the instrument viewing the source from 3 m for A–C/B–C rotation angles varying between  $\pm 90^\circ$  in increments of  $5^\circ$ . The 2-d and 3-d views of the image data are shown in Figure 6–27.

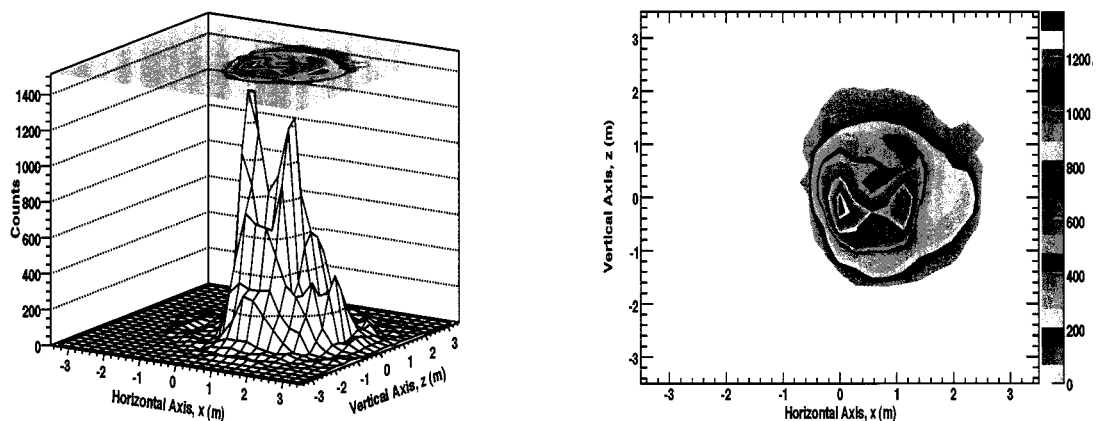


Figure 6–26: 3-d (left) and 2-d (right) views of the image plane for  $^{239}\text{Pu}$  neutrons from A–C and B–C events summed together.

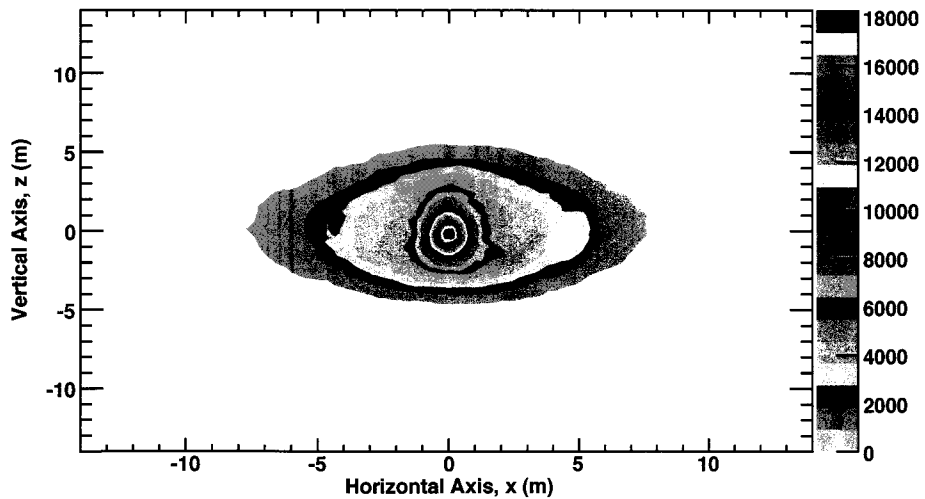
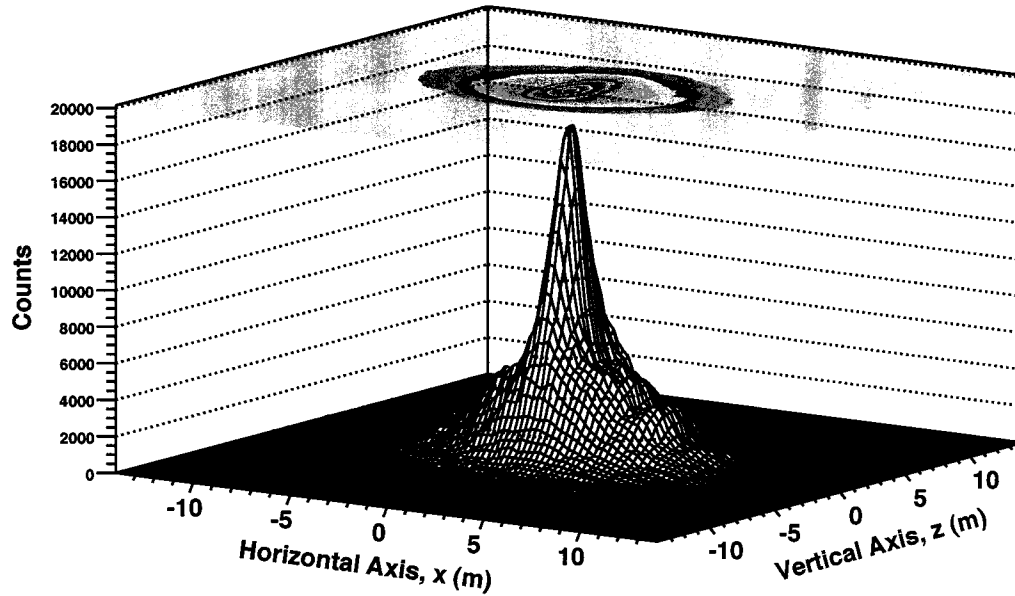


Figure 6–27: Composite image with 3-d (top) and 2-d (bottom) view of the image plane for fission neutrons from A–C/B–C angles varying between  $\pm 90^\circ$  in increments of  $5^\circ$ .

Errors in the spatial location and energy result in the distribution about the true location observed in the image. These instrumental effects are the main source of blurring in the image reconstruction process, much like what we found with energy reconstruction. The variation of the SNV in the  $z$ -dimension is due to the variety of locations a scatter can occur in each 15-cm rod whereas the  $x$ -dimension is fixed based on the orientation. The error in this quantity depends on the pulse height measurement in successive scatters. Errors in the energy drives the total width of the event circle annulus. We have assumed idealized, point-like precision when drawing each portion of the event circle, whereas in reality, each event circle has a resolution-dependent width. The annulus width should be folded into the PSF for higher-order algorithms.

#### 6.4.1 MINIMAL NUMBER OF EVENT CIRCLES FOR LOCATION IDENTIFICATION

The above results show clear source identification between a few hundred to a few thousand double scatter events. In a less controlled environment, observation time and source flux could be limited and statistics of this magnitude, in general, are not feasible. With event selections on threshold, ToF, and PSD made, and the distance to the source known, we addressed the question of: how many events circles are needed to identify a source location. 10, 20, 40, and 100 random events were selected out from  $^{252}\text{Cf}$  data at a distance of 3 m between rotation angles of  $\pm 60^\circ$ . A measure of the performance for imaging with a minimal number of event circles is given by analyzing the mean and width of the  $x$  and  $z$  image plane distributions projected onto their

respective axes. The mean of the distribution in  $x$  varied between 20 and 40 cm from the origin with  $1-\sigma$  width of  $2.8 \pm 0.1$  m;  $z$  varied between  $-10$  and  $20$  cm from the origin with  $1-\sigma$  width of  $2.4 \pm 0.1$  m. Randomly sampled events show no improvement in performance using this metric with an increase in the number of events. Figures 6–28 and 6–29 show that as more events populate the central region where the source is located, the overall width and shape of that region remains identifiable down to 10 events.

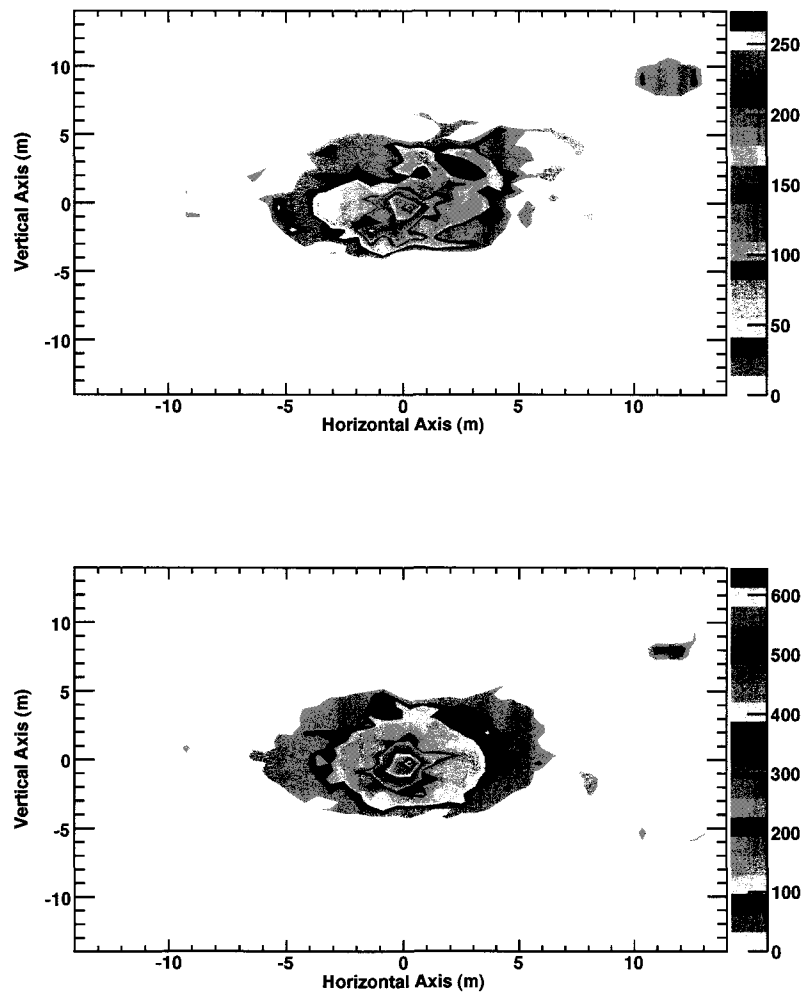


Figure 6–28: Imaging a source with: 100 event circles (top), 40 event circles (bottom).



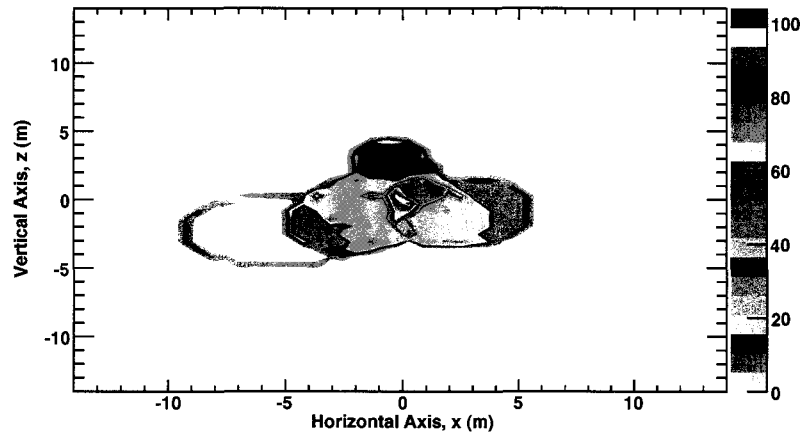
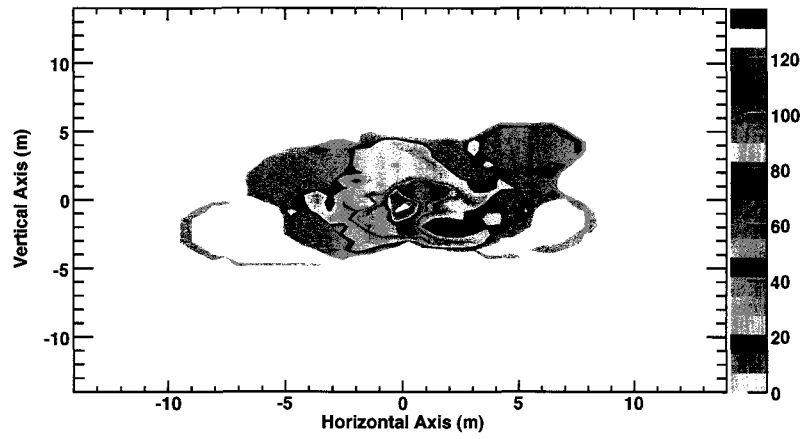


Figure 6–29: Imaging a source with: 20 event circles (top), 10 event circles (bottom).

## CHAPTER 7

### PERFORMANCE MEASUREMENTS AND ESTIMATES FOR SOLAR AND TERRESTRIAL NEUTRON TELESCOPES

The next generation of the double scatter neutron telescope described in this work is intended for a near-Sun mission (Woolf et al. 2009) or a field instrument searching for nuclear material (Ryan et al. 2010). A mission to go to within 10 solar radii of the Sun is planned for launch near the end of the 2010–2020 decade and interest in detection of nuclear material should not wane in the foreseeable future. The FNIT SM2 instrument outlined relies on neutron detection and the discrimination between neutrons and  $\gamma$  rays via pulse shape discrimination (PSD) with the use of liquid scintillator. However, this material is caustic, flammable and toxic. It requires extra mass in the form of safety approaches for a space mission. We, therefore, consider an alternative solid scintillator, such as plastic. Reliable PSD cannot be obtained from plastic scintillator. If we consider limiting the instrument PSD capabilities to one of the two detection planes ( $D_1$  or  $D_2$ ), then the immediate question is whether or not one layer of PSD is sufficient for effective discrimination. We could test this configuration with FNIT SM2 prototype data obtained in a neutron/ $\gamma$ -ray environment.

The FNIT SM2 data has a pulse shape value for each scatter within the rod. The data analysis described in Chapter 4 discriminated neutrons from  $\gamma$ -ray events by placing

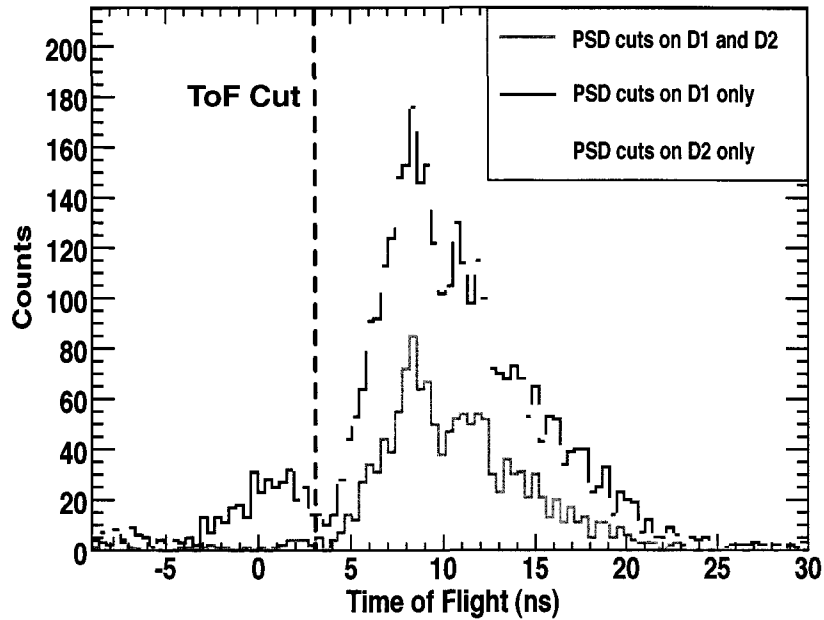


Figure 7-1: Effective  $\gamma$ -ray discrimination with ToF cuts.

restrictive pulse shape selections in both of the rods. To test whether or not effective discrimination of neutrons and  $\gamma$  rays could be achieved by having pulse shape selections turned on in one plane, we used the data obtained from A-C scatters at  $0^\circ$ ,  $30^\circ$ , and  $60^\circ$  for  $^{252}\text{Cf}$  fission neutrons. The discrimination performance from applying pulse shape cuts to one or both layers of the raw data is shown in the ToF spectrum in Figure 7-1. The red curve is produced by selecting on previously determined neutron pulse shape values in both  $D_1$  and  $D_2$  planes; the blue curve is only  $D_1$  neutron pulse shape selected events and the green curve is only  $D_2$  neutron pulse shape selected events. The ToF cut demarcation indicates where neutron ToF selections are made for values greater than this to eliminate events with  $\gamma$ -ray ToF. We observe a reduction in counts in the ToF spectrum when placing neutron pulse shape selections on both scatters compared to neutron pulse shape selections in  $D_1$  (or  $D_2$ ) only.

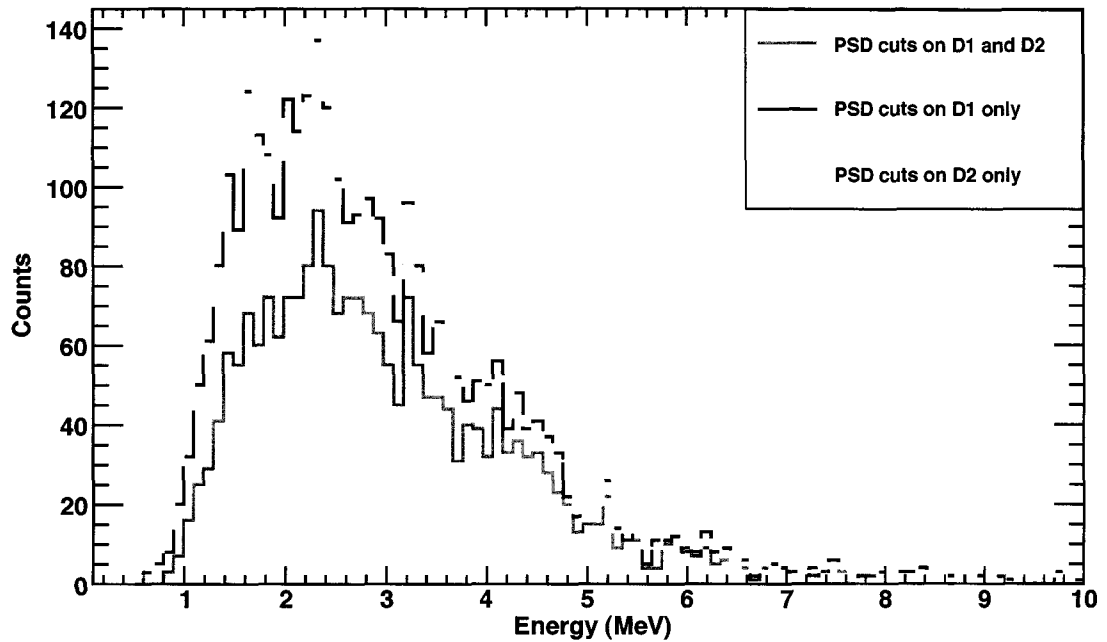


Figure 7-2: Count spectra for fission neutrons with varying levels of selections on PSD.

The difference between the curve with D<sub>2</sub> neutron pulse shape selections only and selections on both D<sub>1</sub> and D<sub>2</sub> is the absence of a D<sub>1</sub> neutron pulse shape selection. We analyze the D<sub>1</sub> pulse shape events that remain after D<sub>2</sub> neutron pulse shape and neutron ToF values are selected. Evaluation reveals that remaining events lie both within and outside of the nominal D<sub>1</sub> neutron pulse shape selection window. The events outside the neutron pulse shape window register either  $\gamma$ -ray type pulse shape values or large values caused by the long, decaying tail of the pulse triggering the stop in the PSD circuit. When placing windowed selections on D<sub>2</sub> neutron pulse shape and neutron ToF, the total number of D<sub>1</sub> pulse shape events outside the D<sub>1</sub> neutron pulse shape values is 62%. This value is the number of events discarded by D<sub>1</sub> neutron pulse shape selections (the distribution in Figure 7-1 for selections on D<sub>1</sub> pulse shape shows similar results). However, we find that accepting events in the D<sub>1</sub> pulse shape that lie outside the nominal

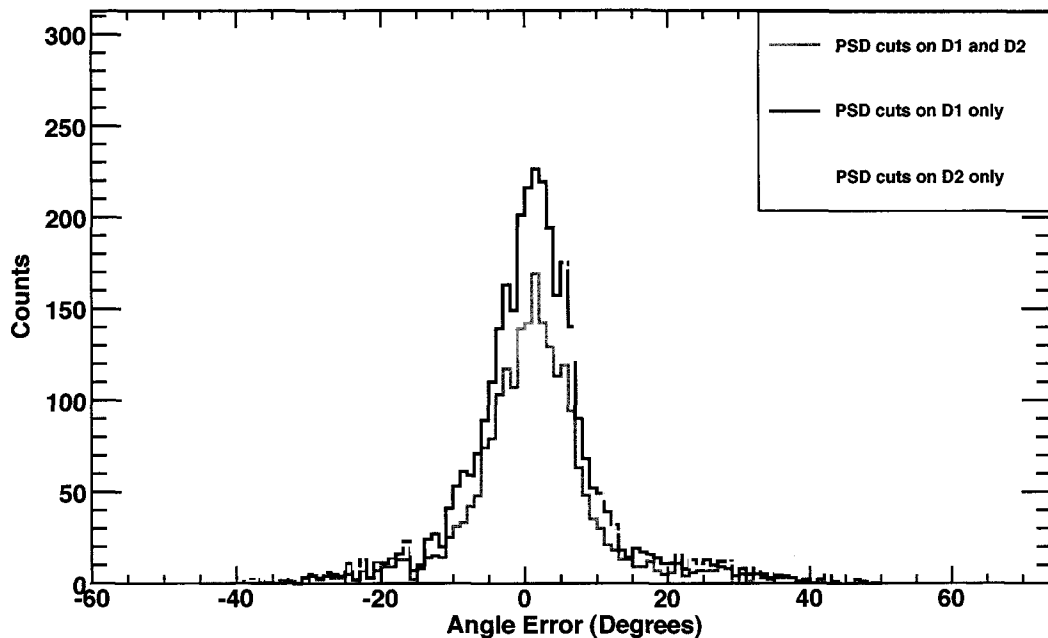


Figure 7-3: ARM for fission neutrons with varying levels of selections on PSD.

range of neutron pulse shape cuts has little effect on the reconstruction process and, in fact, increased the number of “good” events in our data stream, increasing the efficiency since the data were not subject to stringent selections.

Comparison of  $^{252}\text{Cf}$  FNIT SM2 data with varying degrees of PSD selections are shown in Figures 7-2 and 7-3. The fission count spectrum (Figure 7-2) retains the Watt distribution albeit with fewer total events when PSD selections are applied to both layers. The angular resolution (Figure 7-3) produced a mean and  $\sigma$ -width of:  $0.9^\circ \pm 6.0^\circ$  (neutron pulse shape selections in both planes);  $0.9^\circ \pm 6.3^\circ$  (neutron pulse shape selection in  $D_1$  only); and  $0.6^\circ \pm 6.6^\circ$  (neutron pulse shape selection in  $D_2$  only). Any resulting image should be unaffected. Given the results of Figures 7-2 and 7-3 we decided to move in the direction of having plastic scintillator in one layer with PSD capabilities in the other. In this section we will discuss the proposed space and field instruments and their

performance testing through laboratory and simulation studies with the aforementioned instrument configuration.

### **7.1 SOLAR NEUTRON TELESCOPE SENSITIVITY**

Originally we designed an instrument for Solar Probe Plus consisting of a three-plane detection system composed of organic and inorganic scintillator to measure solar neutrons (1–20 MeV) and  $\gamma$  rays (0.1–20 MeV). However, the original instrument underwent a redesign because of strict mass ( $\sim 2$  kg) requirements for a deep space mission and the results determined from tests with a laboratory prototype. We show the simulation results of the original instrument observing a large flare. The instrument has enough qualitative similarities to that of the newly proposed instrument to be relevant. Independent of instrument design, the neutron background produced locally by the spacecraft was considered. Understanding the background flux is important for determining the overall sensitivity of the instrument, especially to weak fluxes. We present the results of modeling the spacecraft background for three potential instrument locations on the spacecraft, the background intensity as a function of instrument viewing angle, and the sensitivity above a given background to weak fluxes.

The original instrument consisted of three circular disks – the  $D_1$  and  $D_2$  layers composed of organic scintillator for neutron and  $\gamma$ -ray measurements, and a  $D_3$  layer of inorganic scintillator for  $\gamma$ -ray measurements. The separation between each layer was 15 cm. The radius of each disk is 3.81 cm with a thickness of 3 cm. Abutted opposite the

Sun facing side of  $D_1$  is a layer of plastic scintillator (0.5-cm thick, 3.81-cm radius) acting as a charged particle veto. PMTs are coupled to the circumference of each disk to measure the scintillation light. Each cell would be contained in Mg housing with 0.1-cm thick walls on the top and bottom and 3-cm thick on the side. The redesigned instrument proposed for Solar Probe Plus – the Solar PRobe Ion, Neutron and Gamma Spectrometer (SPRINGS) – consists of a two-plane detection system composed of organic scintillator, separated by 12 cm, to measure double scatter neutrons and  $\gamma$  rays and can be used as a  $dE/dx$  vs.  $E$  detector to measure ions of 60–100 MeV/nucleon. Instead of circular disks with PMTs mounted around the circumference, the  $D_1$  and  $D_2$  layer are segmented into four blocks of scintillator (3.5 cm  $\times$  3.5 cm  $\times$  3.5 cm) optically separated by 0.5 cm on abutting sides. PMTs are mounted on the side of each scintillator block for direct light readout. Comparatively, the total volume of the SPRINGS instrument is 147 cm<sup>3</sup> per layer, while the total volume of the original design is 136.8 cm<sup>3</sup>. Dissimilarities between the two instrument comes as a result of the active volume and separation between layers.

We simulated the performance of the instrument mass model observing a large flare in the inner heliosphere. The instrument was mounted on a simulated Solar Probe Plus spacecraft (Figure 7–6). The simulation package used for instrument and spacecraft modeling was developed at the University of Bern by Drs. Michael Moser and Benoît Pirard. An omnidirectional galactic cosmic-ray flux was the main source of background (see below for complete description of spacecraft simulations). We used simulations to estimate the instrument effective area – a product of the geometric area and the efficiency

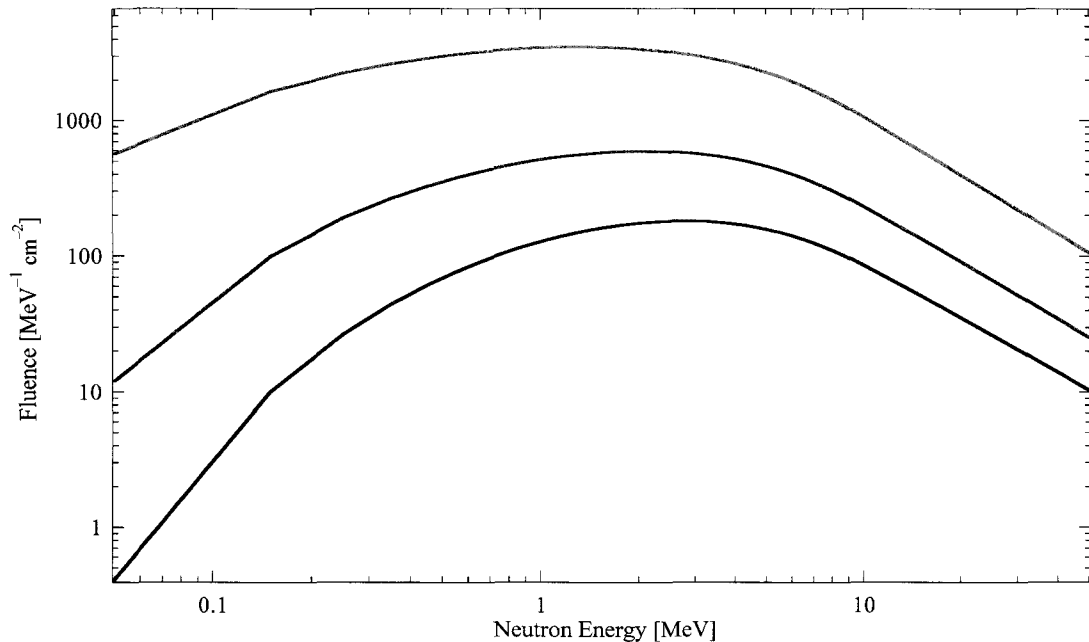


Figure 7-4: Solar neutron fluence for the 15 June 1991 X12 flare at 10 (red), 20 (green) and 30 (blue) solar radii.

– from a uniform input of 1–15 MeV neutrons with selections on double scatters and the ARM distribution. An integrated efficiency of  $3.3 \times 10^{-4}$  yielded an effective area for the original design of  $1.5 \times 10^{-2} \text{ cm}^2$ .

In June of 1991 a large class of X-flares erupted from the Sun during a two-week time period. One of these events, occurring on June 15, produced an X12/3B class flare that was well measured with the CGRO (Rank et al. 2001). Neutrons in the 15–80 MeV energy range were detected and measured for this event from a distance of 1 AU (Kocharov et al. 1998; Debrunner et al. 1993). The time-integrated directional neutron emissivity spectrum was derived from the number of counts COMPTEL on CGRO registered with a value of  $8.8 \times 10^{27} \text{ n sr}^{-1}$  and a spectral index  $s = 1.5$  (Debrunner et al. 1993). This information was used to predict the neutron fluence below 15 MeV and at



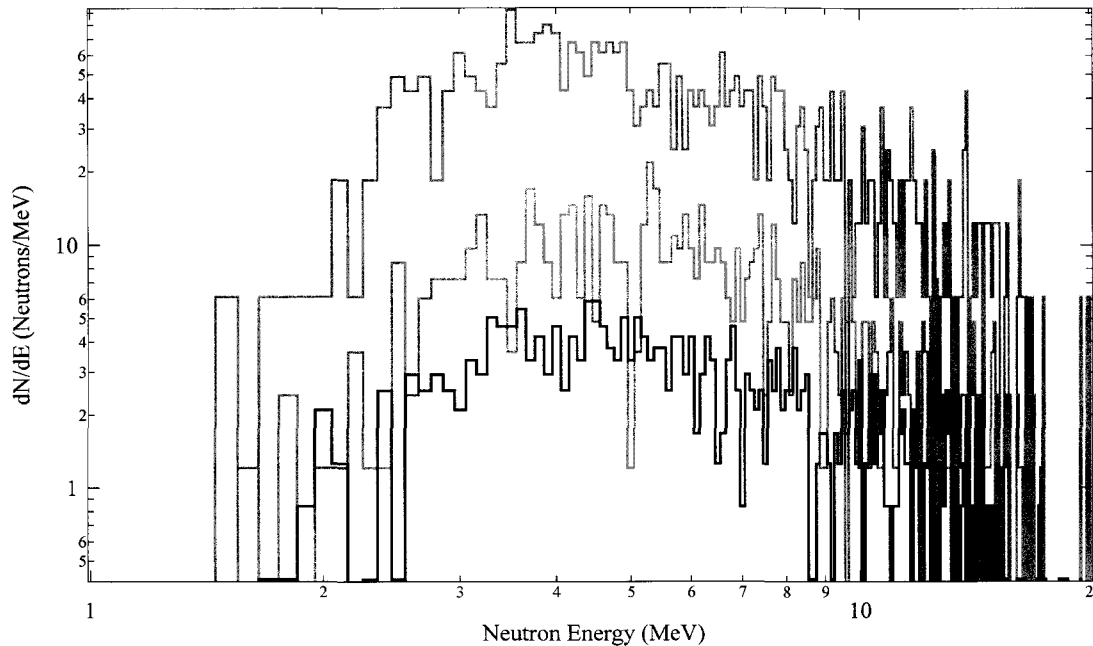


Figure 7-5: Reconstructed solar neutron spectrum for the 15 June 1991 X12 flare at 10 (red), 20 (green) and 30 (blue) solar radii with original instrument design.

different heliocentric distances. Figure 7-4 shows the results of the solar neutron fluence spectrum at 10, 20, and 30 solar radii for a 2100-s integration time. The intensity of 1-MeV neutrons at Solar Probe Plus perihelion is  $4.2 \times 10^7$  greater than the intensity at 1 AU, and  $1.6 \times 10^4$  greater for 10 MeV neutrons. Each flare spectrum shown in Figure 7-4 was used to compute the instrument response. Simulated data were analyzed in the same manner as outlined in section 5.2, i.e., we selected double scatter events that adhere to scatter, ToF, and threshold requirements and then broadened the distribution based on the extrapolation of resolution values from instrumental parameters measured by FNIT SM2. Figure 7-5 shows the differential response of the instrument at various heliocentric distances. The integrated total neutron counts are: 395 at 10 solar radii, 77 at 20 solar radii, and 29 at 30 solar radii.

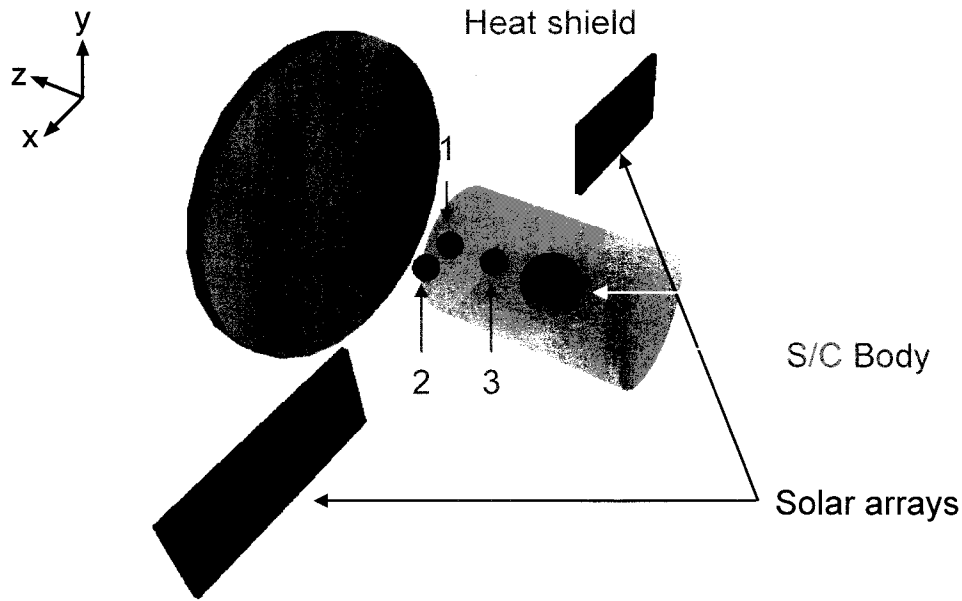


Figure 7–6: Solar Probe Plus spacecraft mass model.

The prototype instrument sensitivity is crucial for assessing the instrument performance. To determine the sensitivity, the background neutron counts were considered in the measurement window. A mass model of the Solar Probe Plus spacecraft (Figure 7–6) was built into the simulation code based on the specifications given by the Solar Probe Plus Science and Definition Team document (Solar Probe STDT 2008). The spacecraft consists of a heat shield (mass: 70 kg, composition: 62% C, 38% Al), spacecraft body (mass: 313 kg, composition: 41% Al, 13% N, 12% Cu, 8% Si, ...), solar arrays (mass: 100 kg, composition: TBD), and hydrazine fuel tanks (mass: 50 kg, composition: 87% N, 13% H). To replicate the local spacecraft background expected in the harsh radiation environment of deep space, a proton-only, omnidirectional cosmic-ray flux from 10 MeV–100 GeV was used ( $\alpha$  particles and heavier ions were neglected). The interplanetary field and solar wind in the heliosphere affect the total flux and spectrum of

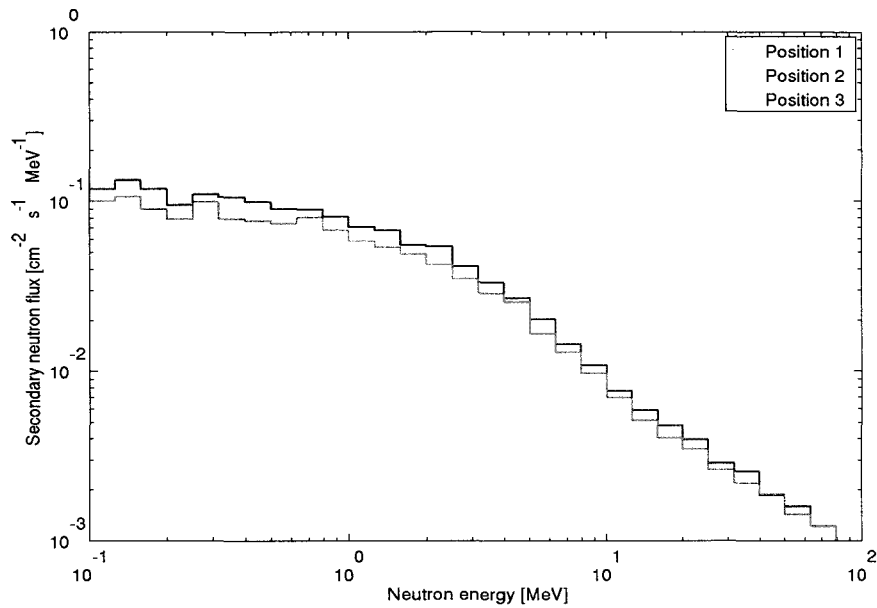


Figure 7–7: Background fast neutron flux from primary GCRs for varying positions on the Solar Probe Plus spacecraft.

the galactic cosmic rays (GCRs). This effect is not constant and creates a variable spectrum of GCRs throughout the heliosphere. The variation of the modulation is related to the variation of the solar activity, commonly described by the so-called force field model (Gleeson and Axford 1968). The only model parameter is the modulation potential,  $\phi$ , given in units of MV. For conditions of solar minimum a value of  $\phi = 400$  MV was used to generate a differential GCR spectrum in the inner heliosphere.

Figure 7–7 shows the secondary background neutrons produced from nuclear interactions between the GCR proton flux and the spacecraft material. We considered the secondary background neutrons coming from solar and non-solar origin. Regions selected for analysis were a  $45^\circ$  cone centered about the direction of the Sun and varying slices of the field of view coming from  $90^\circ$  off-axis of the Sun to the anti-sunward point in  $30^\circ$  increments. The mass model of the spacecraft contained three spherical detectors to

measure the energy and direction of secondaries that passed through the volume. For each position on the spacecraft, we computed the secondary background neutron intensity in the 1–20 MeV range, the expected count rate for the double scatter effective area and the total number of neutrons expected for a 1000-s integration time.

Figures 7–8 and 7–9 show intensity Aitoff projection plots of the spacecraft mapped out in secondary neutrons from the vantage of position 1, 2, 3, respectively (Figure 7–6). In each figure the Sun is located at  $(\Theta, \Phi) = (90^\circ, 0^\circ)$ . At position 1 and 2 the heat shield appears as  $(\Theta, \Phi) = (>40^\circ, \pm 180^\circ)$  and the solar arrays can be seen at:  $(\Theta, \Phi) = (-10^\circ, \pm 90^\circ)$ .

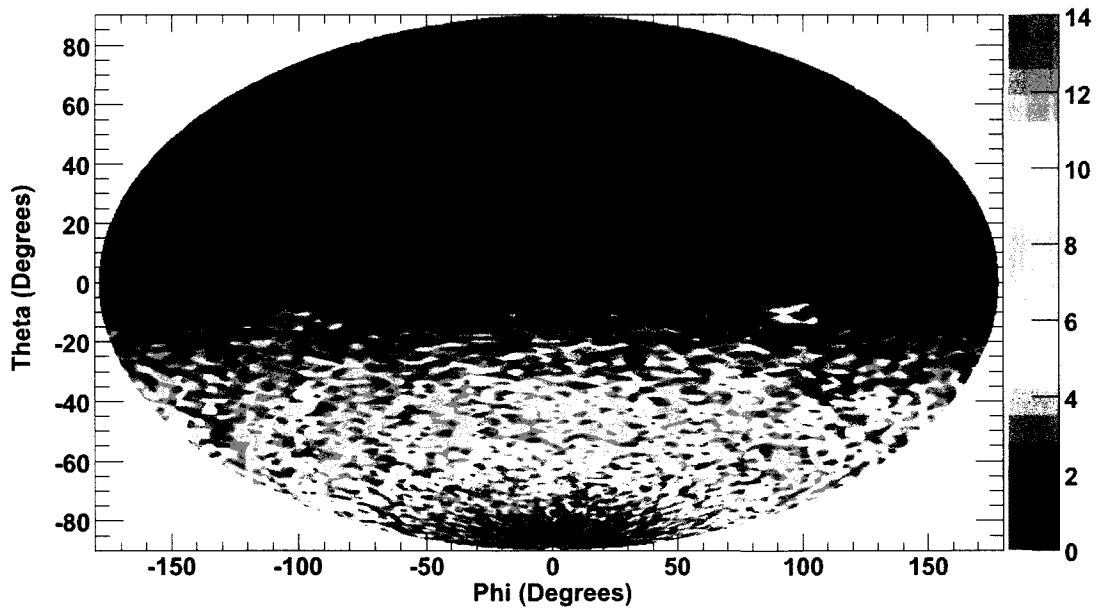


Figure 7–8: Spacecraft mapped out in secondary 1–20 MeV neutrons from the vantage of position 1.

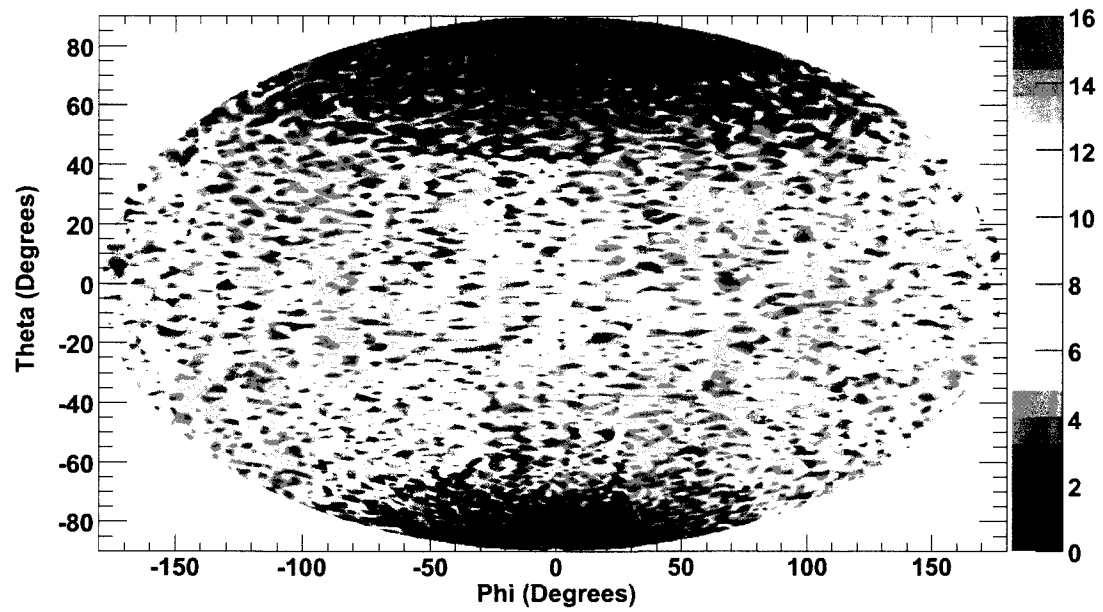
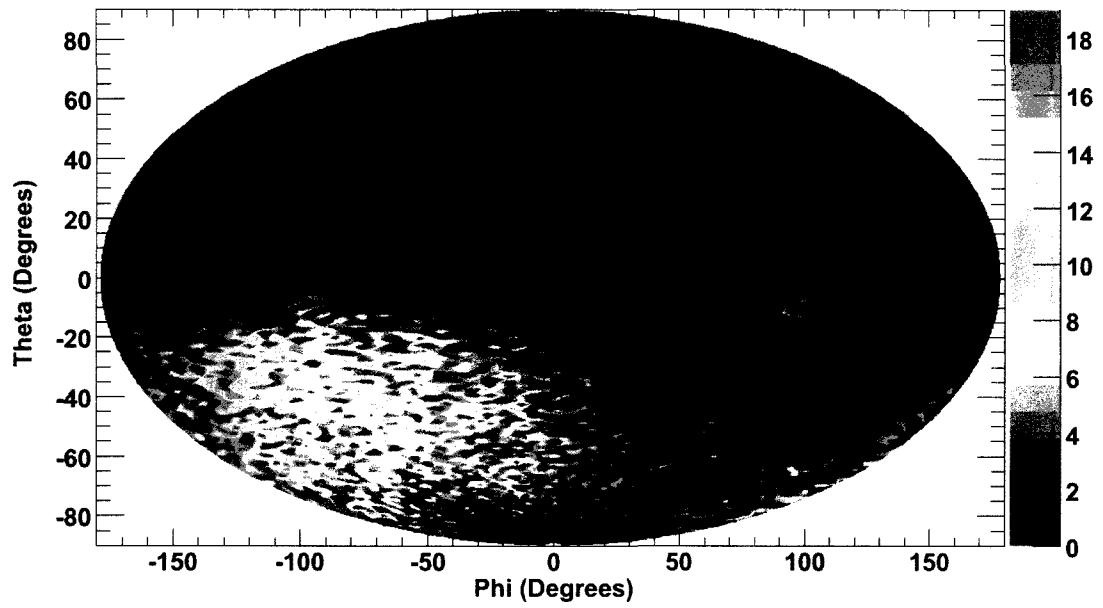


Figure 7–9: Spacecraft mapped out in secondary 1–20 MeV neutrons from the vantage of position 2 (top) and position 3 (bottom).

Selecting events that fell within a 45° half-angle cone,  $\Theta$ : ( $>45^\circ$ ),  $\Phi$  ( $-180^\circ, 180^\circ$ ), of the solar direction for each position we compute a background flux vs. energy (Figure 7–10). In the tables that follow, the tabulated neutron intensity from 1–20 MeV (Table 7–1), the count rate for the instrument double scatter effective area (Table 7–2), and the total number of neutrons counted over a 1000-s integration time (Table 7–3) are shown.

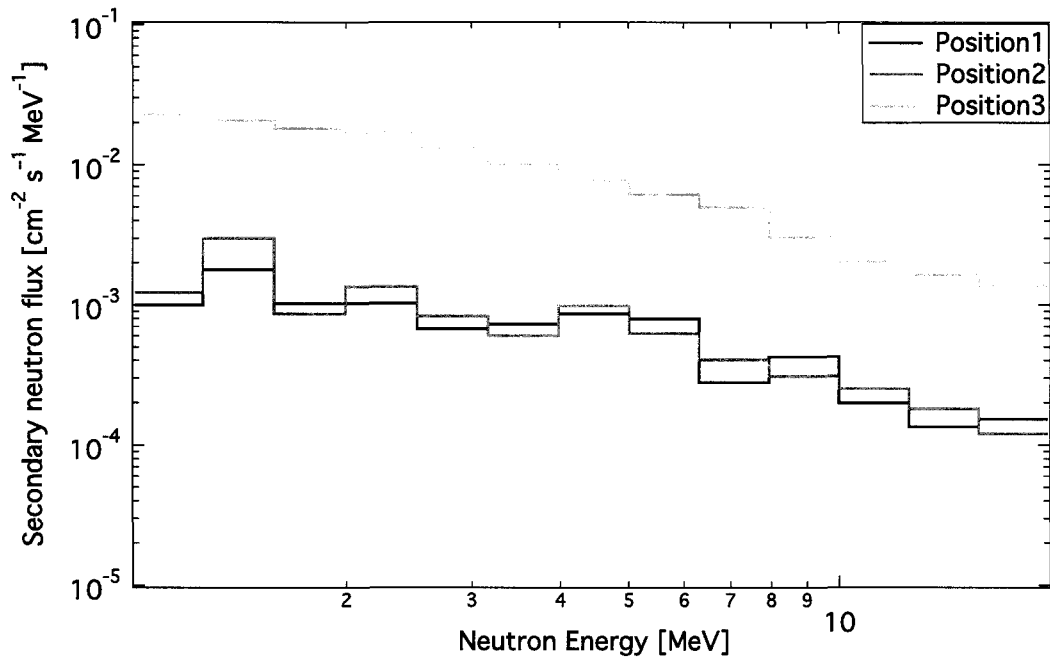


Figure 7–10: Secondary neutron intensity from a 45° half-angle cone centered on the sunward direction.

Position	Integrated Neutron Intensity [cm⁻² s⁻¹]
1	$7.7 \times 10^{-3}$
2	$8.2 \times 10^{-3}$
3	$9.2 \times 10^{-2}$

Table 7–1: The 1–20 MeV integrated neutron intensity for a 45° cone centered on the sunward direction for each spacecraft position.

Position	Count Rate [Hz]
1	$1.2 \times 10^{-4}$
2	$1.2 \times 10^{-4}$
3	$1.4 \times 10^{-3}$

Table 7–2: Count rate for an effective area of  $1.5 \times 10^{-2} \text{ cm}^2$  at each position on the spacecraft.

Position	Total Number of Neutrons
1	0.1
2	0.1
3	1.4

Table 7–3: Total number of neutrons for an integration time of 1000 s at each position on the spacecraft.

Repeating the analysis outlined above, Tables 7–4 through 7–6 shows the integrated neutron intensity for the background coming from  $\Theta = 0^\circ$  to the anti-sunward, azimuthally symmetric in  $\Phi$ , in  $30^\circ$  increments for positions 1, 2, and 3 for events within the 1–20 MeV energy range.

$\Theta: (0, -30^\circ), \Phi (-180^\circ, 180^\circ)$

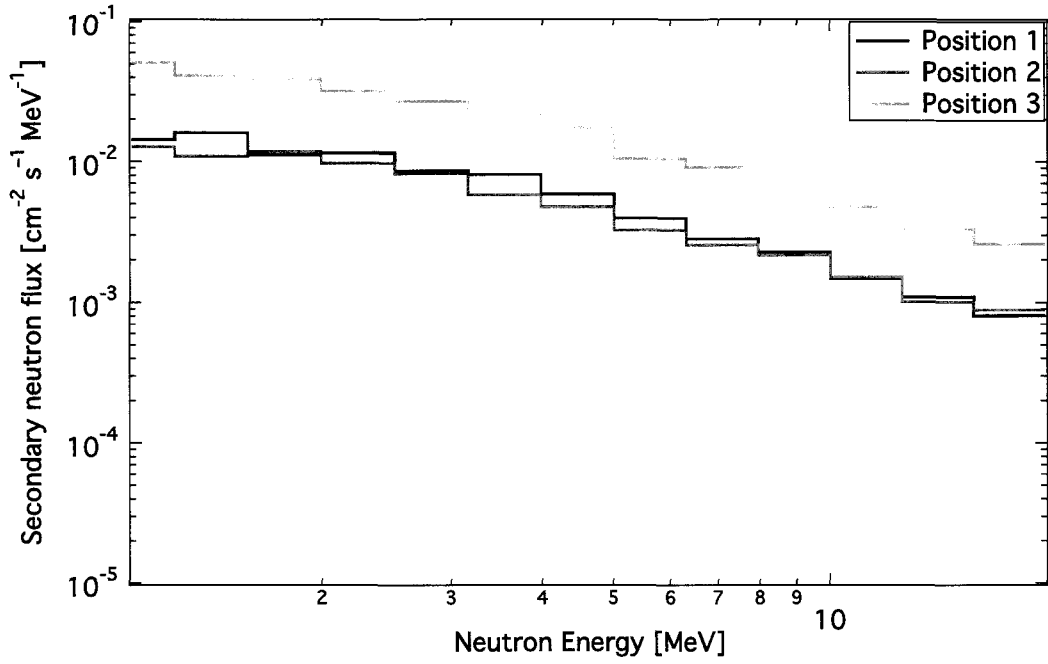


Figure 7–11: Secondary neutron flux with selections  $\Theta: (0^\circ, -30^\circ), \Phi: (-180^\circ, 180^\circ)$ .

Position	Integrated Neutron Intensity [ $\text{cm}^{-2} \text{s}^{-1}$ ]
1	$6.3 \times 10^{-2}$
2	$5.5 \times 10^{-2}$
3	$18.8 \times 10^{-2}$

Table 7–4: The 1–20 MeV integrated neutron intensity for selections on spacecraft coordinates of  $\Theta: (0^\circ, -30^\circ), \Phi: (-180^\circ, 180^\circ)$ .



$\Theta: (-30^\circ, -60^\circ), \Phi: (-180^\circ, 180^\circ)$

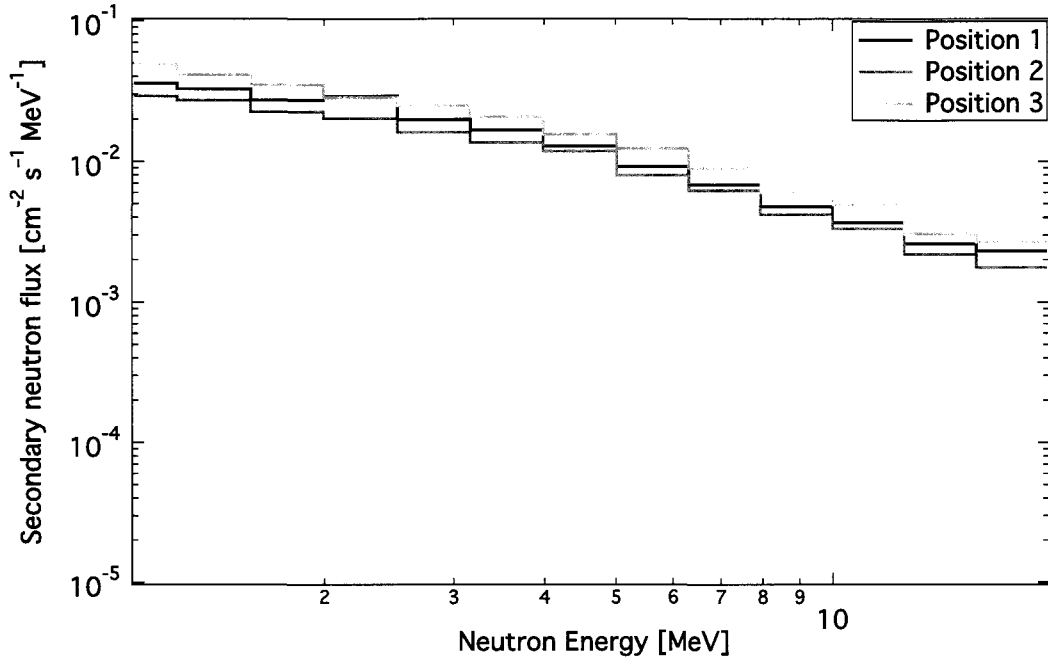


Figure 7-12: Secondary neutron intensity with selections  $\Theta: (-30^\circ, -60^\circ), \Phi: (-180^\circ, 180^\circ)$ .

Position	Integrated Neutron Intensity [cm <sup>-2</sup> s <sup>-1</sup> ]
1	$1.5 \times 10^{-1}$
2	$1.2 \times 10^{-1}$
3	$1.8 \times 10^{-1}$

Table 7-5: The 1-20 MeV integrated neutron intensity for selections on spacecraft coordinates of  $\Theta: (-30^\circ, -60^\circ), \Phi: (-180^\circ, 180^\circ)$ .

$\Theta: (-60^\circ, -90^\circ), \Phi: (-180^\circ, 180^\circ)$

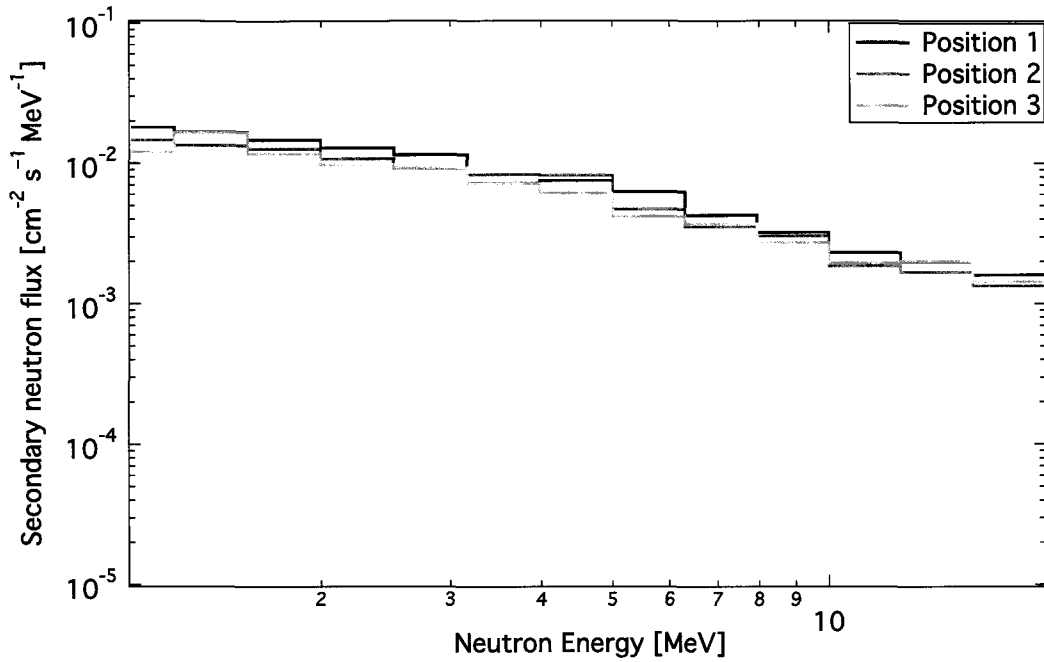


Figure 7-13: Secondary neutron intensity with selections  $\Theta: (-60^\circ, -90^\circ), \Phi: (-180^\circ, 180^\circ)$ .

Position	Integrated Neutron Intensity [cm <sup>-2</sup> s <sup>-1</sup> ]
1	$8.5 \times 10^{-2}$
2	$7.4 \times 10^{-2}$
3	$7.1 \times 10^{-2}$

Table 7-6: The 1-20 MeV integrated neutron intensity for selections on spacecraft coordinates of  $\Theta: (-60^\circ, -90^\circ), \Phi: (-180^\circ, 180^\circ)$ .

We determined that the optimal position of the instrument on the spacecraft is the one that provides the least amount of intervening material in the viewing direction of the Sun. Independent of position the spectrum of secondary background neutrons produces a hard spectrum of  $E^{-1}$ . The location with the highest neutron intensity is position 3. The intensity remains relatively unchanged as a function of the viewing angle. This is caused by the location of position 3 inside the spacecraft body. At this location the instrument is surrounded in all directions by spacecraft material. We see this effect for positions 1 and 2. Both of these positions are situated on the front of the spacecraft body, directly behind the heat shield, with position 1 directly behind the center and position 2 to the side. The intervening material of the heat shield is the only interference when viewing the Sun. A reduction in the neutron intensity with respect to position 3 for observing the Sun's direction is shown in Figure 7–10. However, the neutron intensity at positions 1 and 2 begins to match that of position 3 as the viewing angle is increased towards the region anti-sunward due to the GCRs passing through a greater amount of spacecraft material (Figures 7–11 through 7–13). Our choice for the Solar Probe Plus mission would be to have the instrument situated at position 1.

We show the neutron intensity from each position that passes within  $\pm 20^\circ$  (FWHM ARM cuts) of the Sun direction (Figure 7–14). This restriction and selectivity severely reduces the count rate. The sensitivity of the prototype instrument is given in terms of the signal-to-noise ratio, expressed as the signal divided by the square root of the background. For the energy range of 1–20 MeV, at perihelion a detection of  $\sim 240 \sigma$  (given for the red curve in Figure 7–4 as the signal) is obtained by suppressing the back-

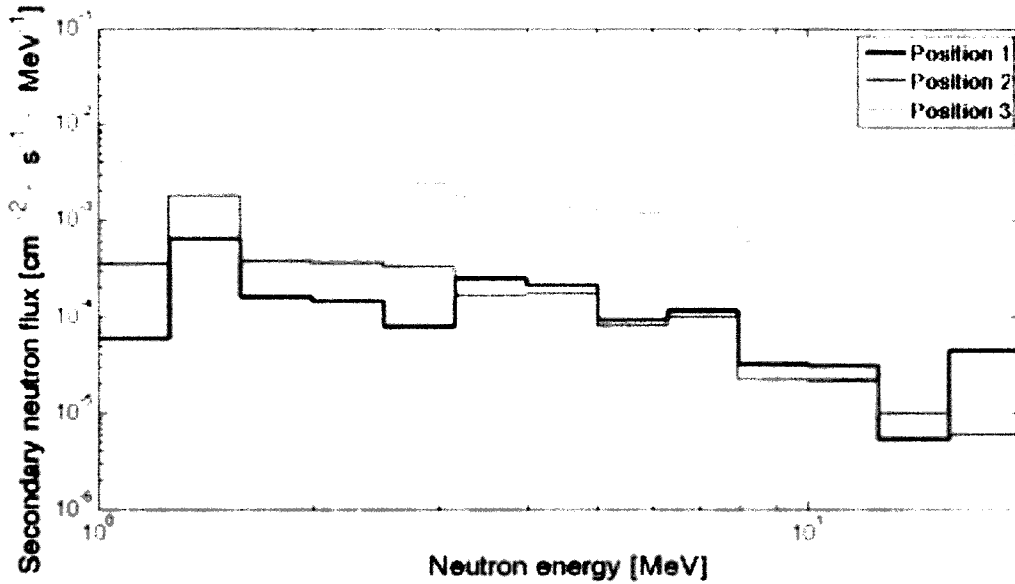


Figure 7-14: Secondary neutron intensity from a 20° half-angle cone centered on the sunward direction.

ground using imaging.

With this expected background intensity that satisfies the ARM cuts, we estimated the quiescent solar neutrons to determine what measurable effects of coronal heating may be detected by an instrument in the inner heliosphere. For a two-week observation time – the approximate time within 20 solar radii – one would expect a total of 35 background neutron counts with the instrument at a position on the spacecraft where the background is minimized (Figure 7-13, blue curve). A 3- $\sigma$  detection would then correspond to an additional 20 counts. If the instrument were to measure 20 background counts, we calculate a source rate of  $1.8 \times 10^{-5}$  counts  $s^{-1}$  yielding a source emissivity at the Sun of  $2.4 \times 10^{18}$  n  $s^{-1}$  sr $^{-1}$  given the surface area of both the Sun and the instrument. The effects of  $\beta^-$  decay and flux divergence have been included. For this emissivity, it was then considered how many neutrons near threshold – 15 MeV – COMPTTEL would have been

expected to observe over a two-week period of quiescence.  $\beta^-$  decay does not play as strong of a role for 15-MeV neutrons as it does at 1 MeV, but flux divergence of these near threshold neutrons at 1 AU is significant. Given an exponential-like neutron spectrum from small-scale flaring and a neutron effective area of  $\sim 5 \text{ cm}^2$ , COMPTEL would have expected to see of the order  $\sim 10^{-9} \text{ n sr}^{-1}$  over a two-week integration time, indicating a flux of this magnitude would have been unobservable by COMPTEL at 1 AU. This emissivity, given the background rate, is based on the assumption that a population of accelerated  $\alpha$  particles with a soft energy spectrum interacting with a heavy target consisting of CNO–Fe produced the resulting neutrons.  $\alpha$  particles that do not produce neutrons via these interactions will subsequently range out and deposit their energy in the corona via Coulomb collisions after they have been accelerated during solar activity. The fraction of these  $\alpha$  particles is dependent on the density, cross-section, and the non-relativistic Bethe-Bloch expression for a given elemental composition in the corona. We calculate that the  $\alpha$ -particle emissivity needed would be of the order  $8.6 \times 10^{21} \alpha \text{ particles s}^{-1} \text{ sr}^{-1}$ , yielding an energy flux imparted to the corona of  $2.3 \times 10^{-6} \text{ ergs s}^{-1} \text{ sr}^{-1} \text{ cm}^{-2}$ . The quiet Sun solar wind flux requirement for the observed plasma temperature in the corona of 1.1 to  $1.6 \times 10^6 \text{ K}$  is an energy loss of  $\sim 5 \times 10^4 \text{ ergs cm}^{-2} \text{ s}^{-1}$  (Withbroe and Noyes 1977). One can verify this result by computing the bulk kinetic energy flux of the solar wind for a typical density of  $10 \text{ protons cm}^{-3}$  and a solar wind speed of  $400 \text{ km s}^{-1}$ . A  $3\text{-}\sigma$  detection of 20 neutrons above background would correspond to an energy flux  $\sim 10$  orders of magnitude smaller than this requirement. This provides

that if an instrument were sensitive to 20 neutron counts above background over a two-week observation time, then it would be sensitive to an energy flux of this magnitude.

The total coronal energy loss for the quiet Sun is  $3 \times 10^5$  ergs  $\text{cm}^{-2} \text{s}^{-1}$ . For 1% coronal heating by particles alone, an input energy flux of  $3 \times 10^3$  ergs  $\text{cm}^{-2} \text{s}^{-1}$  would be needed. This translates into  $8.5 \times 10^{26}$  n  $\text{s}^{-1} \text{sr}^{-1}$  yielding a neutron count rate of 98 counts  $\text{s}^{-1}$  at 10 solar radii, 19 counts  $\text{s}^{-1}$  at 20 solar radii and 6 counts  $\text{s}^{-1}$  at 30 solar radii. During quiet times on the Sun the instrument outlined in this section (or one of similar character) would detect neutron emission from coronal heating by particles at the 1% level that are unobservable at 1 AU with high statistical significance. Over a two-week observation time inside 20 solar radii,  $\sim 2 \times 10^7$  counts would be expected. While it is not known what can be expected within close proximity to the Sun, the count rate estimates made in this section show that the particle contribution to coronal heating would be identified with a double scatter neutron telescope in close proximity to the Sun.

## **7.2 NEUTRON SPECTROSCOPE**

The Neutron SPECTroscope, or NSPECT, is a portable incarnation of a double scatter neutron telescope based on the work done with FNIT. NSPECT is a collaborative effort with Michigan Aerospace Corporation and is funded through the Defense Threat and Reduction Agency (DTRA) branch of the Department of Defense. The NSPECT prototype is a two-plane detection system with 1" organic scintillator cells populating each plane (Figure 7–15). Each scintillator cell is directly coupled to a PM tube with fast

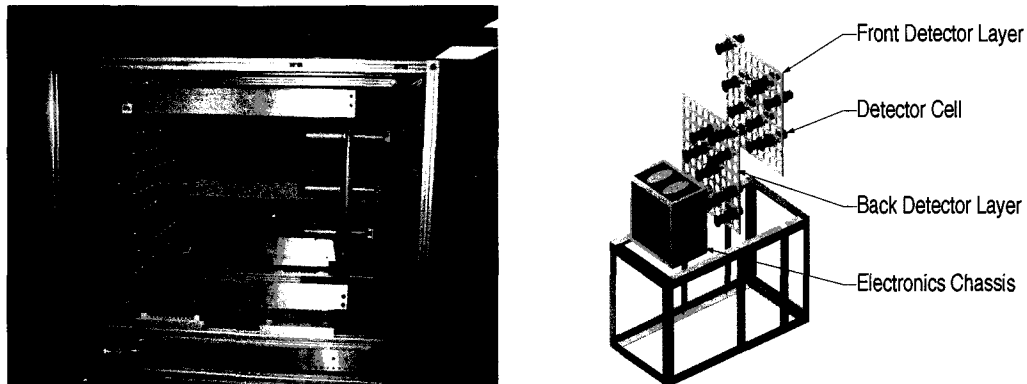


Figure 7–15: Laboratory set up of the NSPECT prototype with three-cells per layer (left), prototype design schematic (right).

signals individually read out into a summing circuit. Each cell trigger produces a output signal that is read into NIM and VME electronics for pulse height and shape, trigger and timing analysis. At the time of writing, the prototype was in the testing phase with three cells per layer. By the end of 2010 the NSPECT prototype will be populated with 10 cells per layer. The ultimate goal of the final, fully populated instrument is 77 cells per layer and to operate eight hours on battery power (Ryan et al. 2010). The NSPECT instrument is designed to be used in an environment outside of the laboratory, potentially for the detection of nuclear material. We calibrated the NSPECT prototype in the same manner as was outlined in section 4.3 for FNIT and performed measurements of fission neutrons and  $\gamma$  rays. We determined a ToF resolution with  $^{60}\text{Co}$   $\gamma$ -ray photons to be 0.5 ns (Figure 7–16 top) and a pulse height resolution of 10%–18% ( $\sigma_E/E$ ) at 60 keV for the  $^{241}\text{Am}$  photopeak, depending on the cell. Figure 7–16 (bottom) shows the fit to the  $^{241}\text{Am}$  photopeak with 15% resolution. The interaction location is determined by cell identification, thus a spatial resolution of 1" is expected for a corresponding cell.

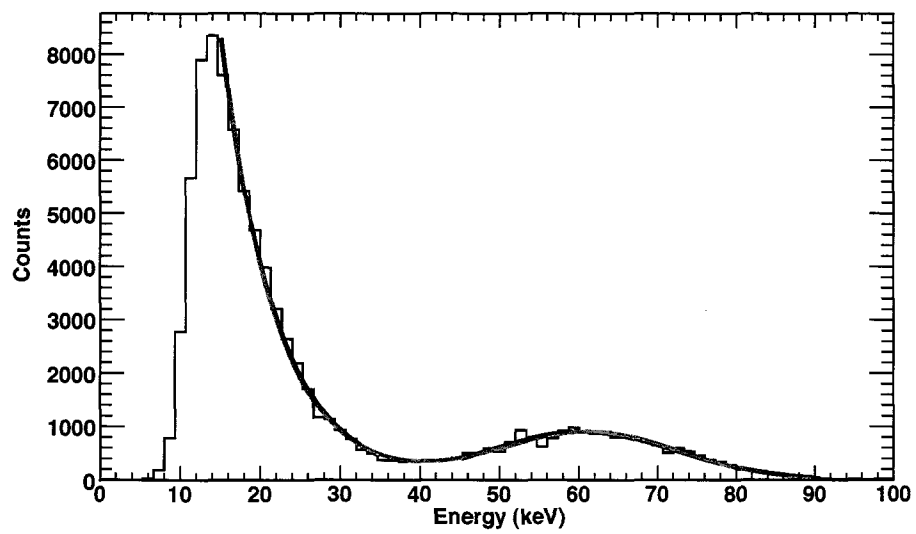
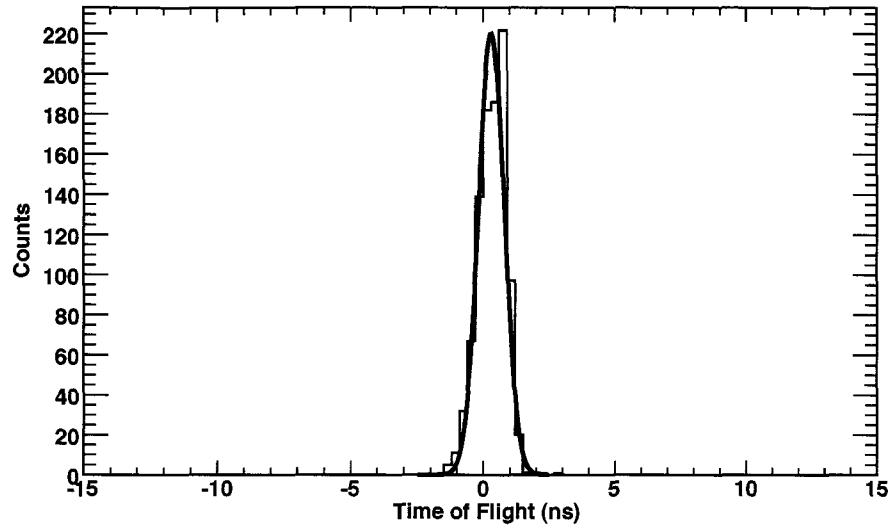


Figure 7–16:  $^{60}\text{Co}$  ToF (top) and  $^{241}\text{Am}$  pulse height (bottom) for a single cell of the NSPECT prototype.



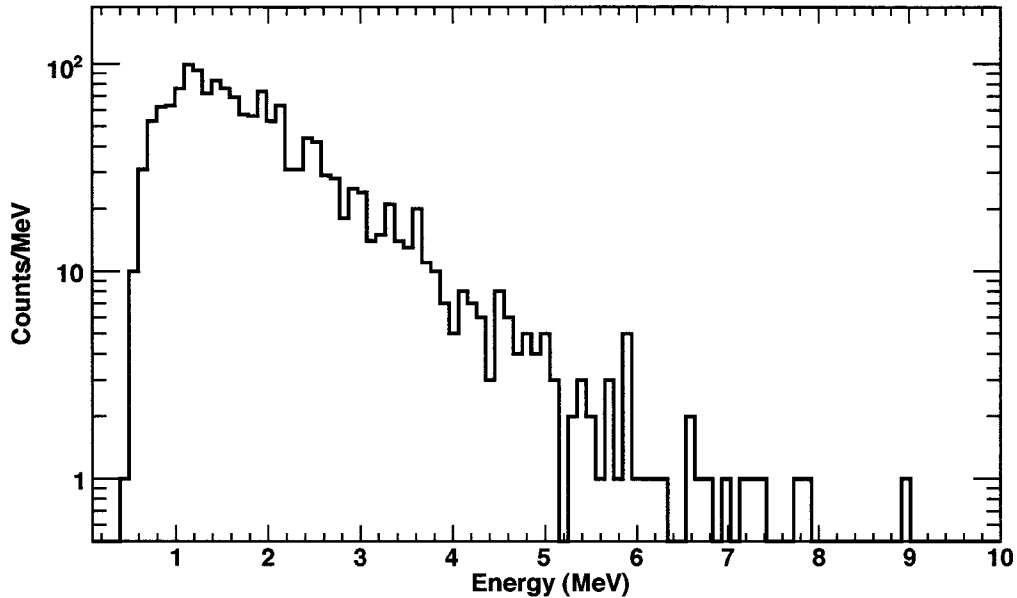


Figure 7–17: Count spectrum from fission neutrons measured by NSPECT.

For a  $^{252}\text{Cf}$  source on-axis at a distance of 3.4 m, 1727 events were collected over a run time of 62 h. The distribution in Figure 7–17 is the count spectrum with  $\pm\text{FWHM}$  ARM cuts, resulting in 1586 double scatters. The ARM distribution (mean:  $-0.3^\circ$ ,  $\sigma$ -width:  $5.2^\circ$ ) and reconstructed image from the  $^{252}\text{Cf}$  point source are shown in Figure 7–18. The performance of the NSPECT three-cell per layer prototype is comparable to that achieved in FNIT albeit with less exposure time needed for comparable statistics. With a greater number of potential scatter paths (three cells per layer yielding nine combinations), asymmetry effects are small.

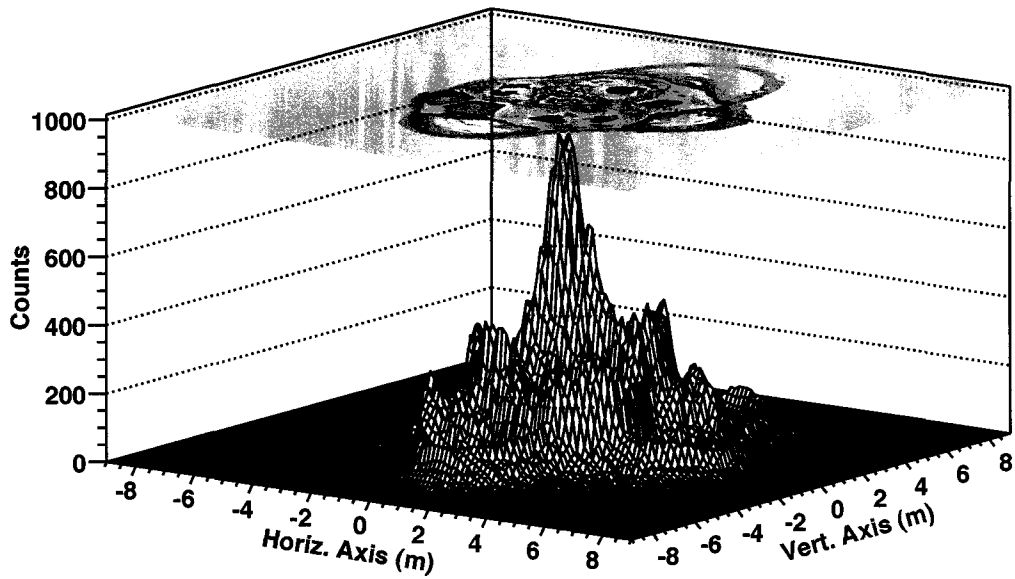
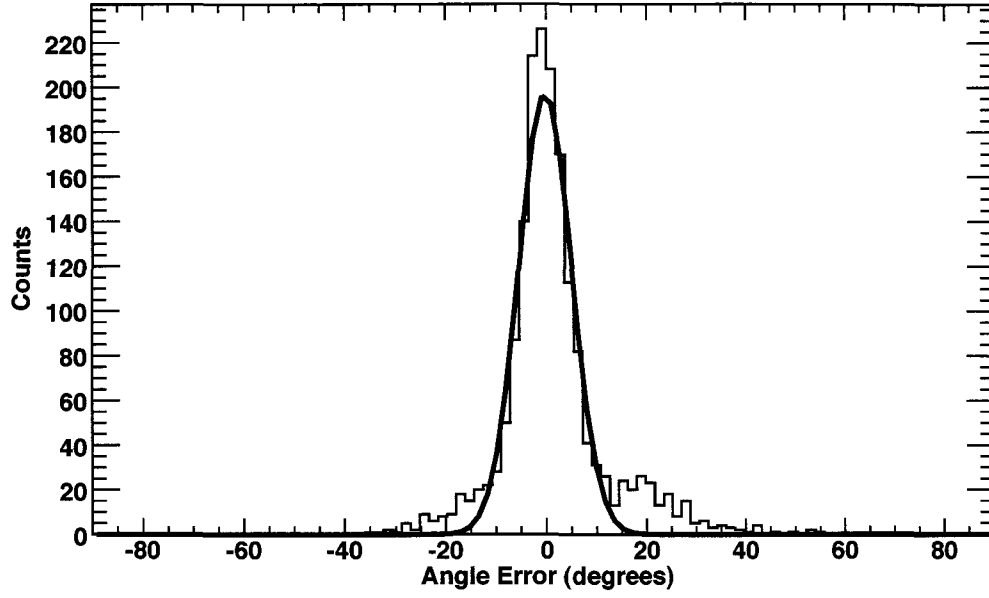


Figure 7-18: ARM (top) and image (bottom) for fission neutrons measured by the NSPECT prototype.

We performed two tests not completed with the FNIT SM2 prototype to identify a source located off-axis and in the presence of a high  $\gamma$ -ray background. The  $^{252}\text{Cf}$  was placed at four different locations at a distance of 3.4 m to the image plane from the instrument origin: 1 m below the image plane origin, 0.9 m above the image plane origin (laboratory height restriction), 2 m to the left of the image plane origin and  $20^\circ$  off-axis (0.7 m below the image plane origin, and 1 m to the left of the image plane origin). Each run was performed for equal live times of 15 h and the results were summed together to mimic the instrument viewing four separate, equal strength sources during one observation period. Figure 7–19 shows that two image locations are clearly visible above and below the origin. The source off-axis by  $20^\circ$  is visible while the source at 2 m to the left has fewer events and thus less discernible due to the intervening obstacles in the laboratory, potentially scattering neutrons before the measurement or completely out of the beam path.

We considered the imaging of fission neutrons in the presence of a high  $\gamma$ -ray background. Unlike an alternative neutron detection instrument composed of  $^3\text{He}$  in a proportional counter, scintillation detectors are sensitive to both neutrons and  $\gamma$  rays. Sensitivity to both stimuli is advantageous in nuclear security when potential threat isotopes have high  $\gamma$ -ray emission but also has proved to be problematic when trying to distinguish between the two. The  $^3\text{He}$  proportional counter is insensitive to  $\gamma$  rays and only registers  $\gamma$ -ray effects on the instrument as pileup in a high background environment ( $\sim 1$  R/h). However, in recent years, the availability of  $^3\text{He}$  has diminished making the use

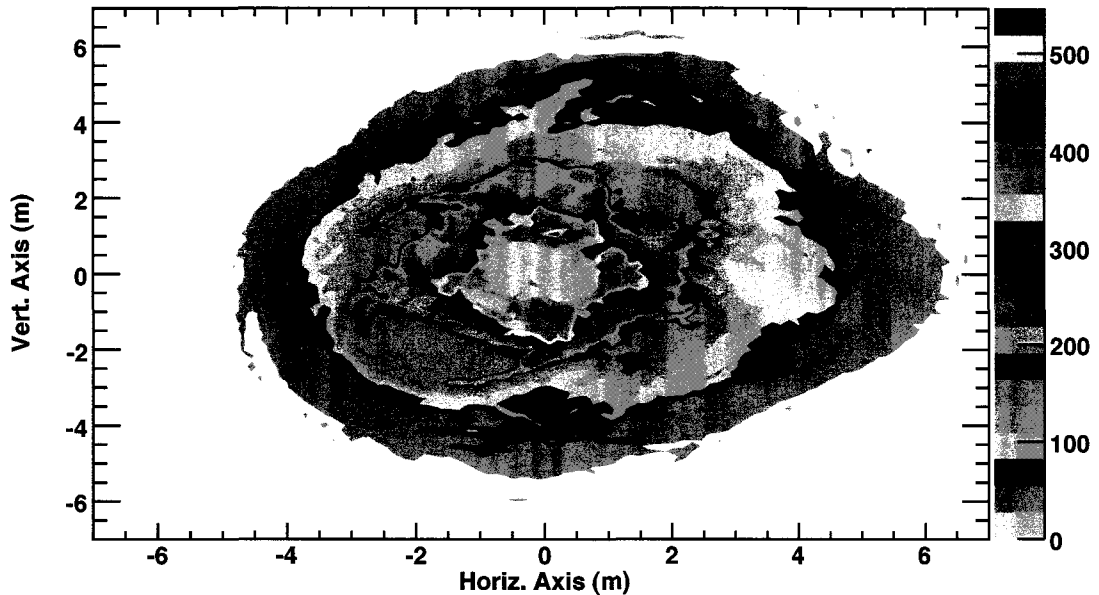


Figure 7–19: Composite image of  $^{252}\text{Cf}$  at four separate locations.

of this gas in neutron detection scarce in coming years.  $^3\text{He}$  is obtained from the decay of  $^3\text{H}$  (tritium) – an isotope abundant in nuclear weapons. The shortage of  $^3\text{He}$  comes as a result of the high demand by the Department of Homeland Security and the reduction of the nuclear weapon stockpile thus lowering the need of tritium to maintain the stockpile (Kouzes 2009). Scintillation detectors with the ability to detect neutrons in a high  $\gamma$ -ray environment is paramount for successful operation.

We tested the robustness of the NSPECT prototype for the measurement and imaging of neutrons in a high  $\gamma$ -ray environment. The source of  $\gamma$  rays was from  $^{137}\text{Cs}$  – an isotope with the potential to be used as a dirty bomb component (CsCl in powder form). This isotope thus serves as an important test source when viewed in conjunction with fission neutrons. The  $^{252}\text{Cf}$  was placed at 3.4 m away from the instrument origin and

20° off-axis (0.7 m below the image plane origin, and 1 m to the left of the image plane origin), while a 796- $\mu\text{Ci}$   $^{137}\text{Cs}$   $\gamma$ -ray source was placed midway between the two planes, a distance of 27 cm above the instrument horizontal axis. At a distance of 27 cm, the biological effective dose from the  $^{137}\text{Cs}$  source is  $\sim 3.2$  mrem  $\text{h}^{-1}$ , a value that is  $\sim 315\times$  the room  $\gamma$ -ray background. Two equal live time runs of 15 h were performed with and without the  $^{137}\text{Cs}$  present. The standard event selections were made on ToF, pulse height and shape. A total of 918 events with, and 445 events without, the  $\gamma$ -ray source present passed through the neutron event selection criteria. The ToF spectrum reveals a high number of accidental events – uncorrelated events that fall within the coincidence time window. We observed a high accidental rate in the ToF spectrum obtained from CNL calibration data (see section 4.4.1 for an explanation of how we corrected the data). The rate of accidental events is  $2r_1r_2\tau$  where  $r_1$  is the rate in the first detection plane,  $r_2$  is the rate in the second detection plane and  $\tau$  is the coincidence time window. For the NSPECT prototype  $\tau = 90$  ns; the singles rate for each plane in this experiment (sum total of all cells per layer) was  $\sim 5.5$  kHz with the  $^{137}\text{Cs}$  present, yielding an accidental rate of  $5.5$   $\text{s}^{-1}$ . Although we recorded a rate of accidentals at this level, without corrections, Figure 7–20 shows that imaging of the neutron selected ToF and PSD (in  $\text{D}_2$ ) events with and without a  $\gamma$ -ray source present demonstrates the instrument’s ability to identify source location in an extremely high background environment. Figure 7–20 (top) is the image plane distribution without the  $\gamma$ -ray source present; Figure 7–20 (bottom) is with the source present.

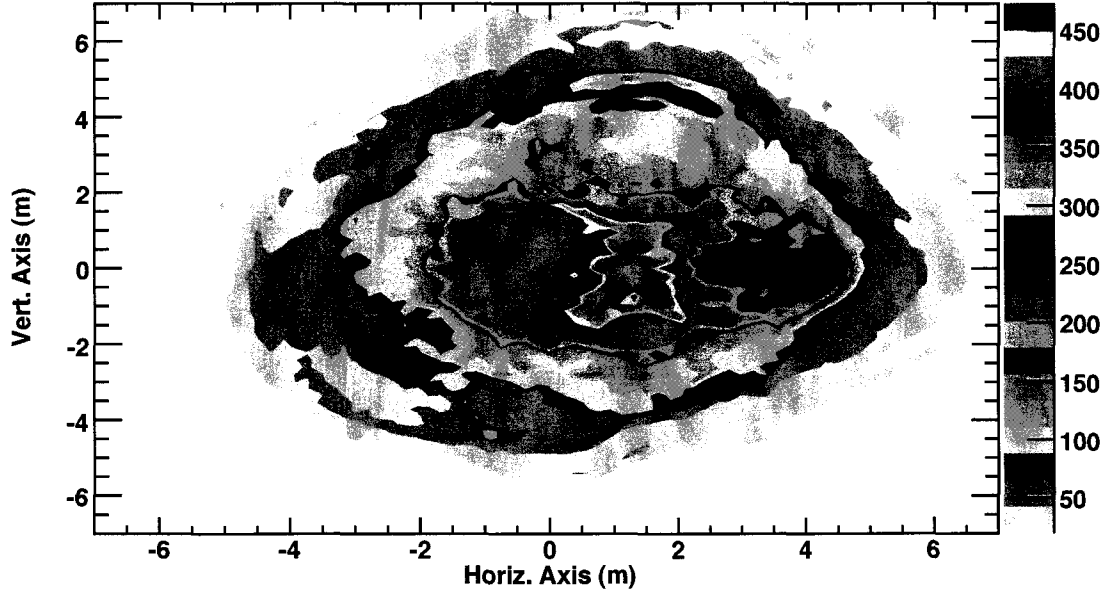
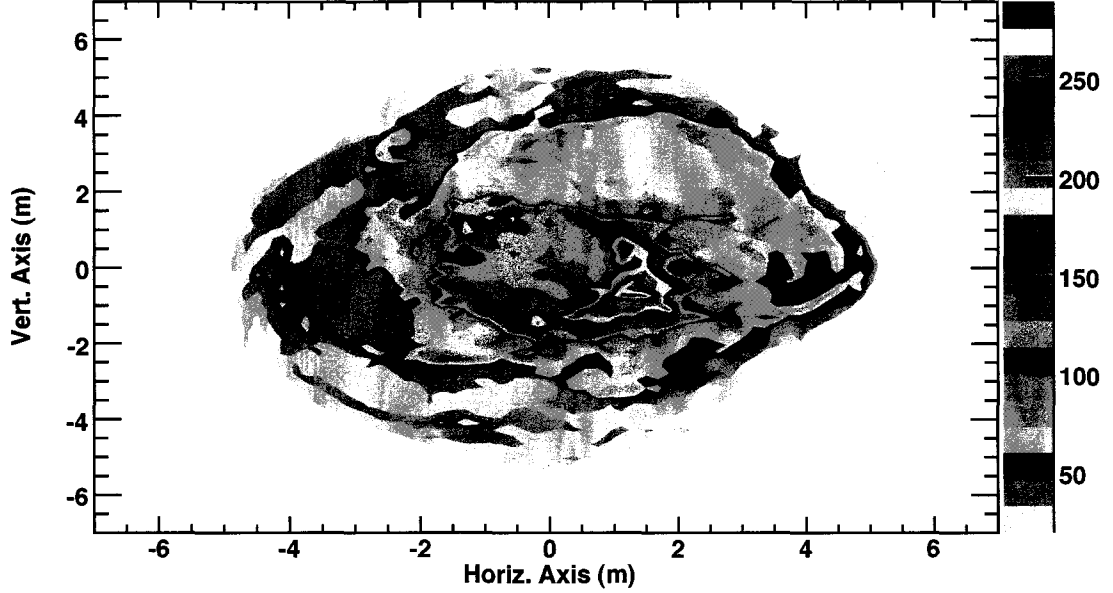


Figure 7–20:  $^{252}\text{Cf}$   $20^\circ$  off-axis (top) without strong  $\gamma$ -ray source present and (bottom) with strong  $\gamma$ -ray source present.

## CHAPTER 8

### DISCUSSION AND CONCLUSIONS

Neutrons below 10 MeV serve as an important diagnostic in solar physics and nuclear security. Detection and measurement of neutrons below this energy threshold serve as an important diagnostic to help understand the processes of the high-energy Sun, while detection of neutron emission by a ground-based instrument could be a clear-cut indication that manufactured nuclear material is present. For this purpose, the Fast Neutron Imaging Telescope (FNIT) instrument was designed, built and calibrated at UNH to measure the energy and direction of incident neutrons.

FNIT is a multi-center, double scatter instrument composed of scintillation material for the production and measurement of scintillation light produced by ionizing recoil particles. The critical parameters to calibrate for precise energy and directional measurements are pulse height and pulse shape of the scintillation light components. The pulse height allows for the energy, position, ToF, and triggering (coincidence) measurements; pulse shape can be used for the determination of whether or not the stimulus is either a neutron or  $\gamma$  ray. A scintillation light measurement is affected by light loss at surfaces and the scintillator attenuation coefficient. Performance depends on these quantities as well as the scintillator-dependent light output and the agreement of PMT characteristics (when multiple PMTs are used to measure the total light output) with the

scintillation. Each of the FNIT SM2 15-cm rods proved to be an effective size for a prototype instrument without great light losses due to length. Detector A – filled with the liquid scintillator BC-501 – outperformed detectors B and C of the full prototype due to the high light output of the scintillator, well-matched PMTs characteristics and the combination of a reflective paint and Teflon lining. Pulse height, time-of-flight (ToF) and spatial resolution vary with incident energy and the performance of each parameter is shown graphically in Figures 4-10 (ToF), 4-11 (spatial) and 4-17 (energy).

The FNIT prototype is designed to have measurement capabilities in the 1–20 MeV range and was tested accordingly during the neutron beam calibration. Results show count spectra resolution of ~20% in the 2 MeV range, improving to 17% in the 10 MeV range. While 10-MeV neutrons are reconstructed fairly well, 18-MeV neutrons cannot be cleanly distinguished from  $\gamma$  rays and hence produce a wide spread in “neutron” energy from ~10–25 MeV. Neutron beam calibration data indicates that the FNIT instrument in its current design performs optimally in energy below ~12–13 MeV down to a threshold of ~500 keV in double scatter mode. The angular resolution measurements, on average, yield a  $\sigma$ -width of ~5° for rotation angles between 15° and 60° for A–C scatters and 6–8° for B–C scatters of similar angles. Shallow angle scatters result in ARM values that are broad. The small energy deposit in the forward detector results in a low number of photoelectrons and leads to error in the measurement of the recoil proton energy. Large angle scatters display distributions that are skewed toward negative values. Counting efficiency depends on the rotation angle with respect to a beam of neutrons. Comparing equal run times in the laboratory, good statistics were obtained between the angles of



15°–60° with the most efficient scattering angles occurring between 30°–45°.

The performance of the BC-501 scintillator compared to that of the BC-519 scintillator as the first scattering rod did not show a significant performance degradation in ARM and energy. Testing with a two-center instrument of BC-519 was not conducted. The scintillating material of choice is ultimately application dependent, but as we have shown, the use of BC-519 should not deter one from exploring this scintillator as a viable option. If one could improve the PSD obtained from the BC-519 scintillator, such as the results found in previous work (Horvath et al. 2000; Saxena 1990), then the ARM distribution, and hence energy, may result in performance comparable to that obtained with BC-501.

Response matrices from a simulated 1–10 MeV flat, uniform, incident neutron beam possess a large diagonal component in the reconstructed energy space with a ~250 keV width at low energies increasing to ~3 MeV at higher energies for shallow angle scatters. As the incident scattering angle is increased to larger angles, the instrument response in energy narrows as more energy from the incident neutron is imparted to the first recoil proton. Because the amount of scintillation light increases for a larger energy deposit in the first scatter, one should expect better performance in the energy reconstruction process for increasing neutron energy. However, simulations show that inaccuracies in energy reconstruction at higher energy, without considering  $\gamma$ -ray contamination, are due to the short ToF values leading to errors in the reconstructed energy of the scattered neutron from ToF. For the D<sub>1</sub>–D<sub>2</sub> planes separated by 15 cm, as they are in the FNIT SM2 prototype, the ToF of a 10-MeV neutron is 3.5 ns whereas the

ToF of a 1-MeV neutron is 11 ns. For short ToFs, an error in the ToF measurement of  $<2$  ns could result in a scattered neutron with an energy upwards of 15 MeV. Reducing the error in ToF measurements for increasingly short ToF values reduces the errors in the energy measurements. One could increase the separation of the  $D_1$  and  $D_2$  planes allowing for a more accurate measurement of neutrons at higher energy, but the efficiency then suffers from the smaller solid angle that  $D_2$  subtends. It also implies that the thickness of each plane would need to be increased from 1.5 cm to reduce edge effects. An increase in detector thickness would lead to a reduction in the spatial resolution with an instrument of similar design.

The count spectra obtained at various angles for beam measurements were compared with simulated beam data via the method of forward folding. The errors of the weighted means for measured and simulated data varied between 21% – 33% at low energies, improving to 8% – 13% at higher beam energies. The mean and width at low energies are in good agreement and show that the energy reconstructed response matrix and the assumed beam input that was used were accurate to within error. Although the percentage errors are smaller for increasing energy, the means of the distributions show a 1-MeV variation between the simulated and measured data, as opposed to a variation of a few hundred keV at low energy. This is the result of the difficulty of selecting out the high-energy neutron events discussed earlier. Overall good agreement within error was found for fission neutron data. The reduced chi-square parameter used for comparison between the two resulting distributions served as a good diagnostic when the total number of counts in each was low. As the number of events increased, large chi-square

values resulted due to the nature of the way the distribution is calculated.

For spectral de-convolution studies we used zeroth-order Tikhonov regularization to obtain a measure of the true source spectrum. The response matrix obtained at a rotation angle of  $30^\circ$  with linear and logarithmic bin step sizes was used to test the de-convolution method with beam and fission neutrons, respectively. The singular values and the left singular vectors of the response matrix with linear and logarithmic bin step sizes show that the DPC was satisfied for beam and fission neutron data. This condition ensures that the regularized solution is the best approximation of the exact solution.

The optimal value of the smoothing parameter – coupled with the identity matrix in zeroth-order Tikhonov regularization – provides the most stable solution. We determined the optimal value of the smoothing parameter with the discrepancy principle originally outlined by Turchin (1967). The value of the smoothing parameter is of order  $10^{-6}$ . We then tested how the variation of the precision (number of counts) of the response matrix affected the value of the smoothing parameter, and how percentage changes in the smoothing parameter affected the regularized solution (reconstructed energy spectrum).

The response matrix precision was increased from a starting set of equally noisy data sets ( $\sim$ equal number of counts in the response and data vector) to  $\sim 4-5\times$  the number of neutron counts in the response matrix compared to that in the data vector. We determined a variation of 21% for beam data and 9% for fission data in the value of the optimal smoothing parameter. Greater variation in the smoothing parameter for neutron beam data is due to the nature of the beam distribution with sharp edges at endpoint energies. The fission data are continuous over a wider energy range and errors in the de-

convolution procedure are not as apparent. By varying the smoothing parameter associated with the highest precision response matrix in our test, we computed the variation in the total number of counts in the reconstructed spectrum for percentage changes to the optimal value of the smoothing parameter. For the beam and fission data a variation of  $\pm 1\%$ ,  $\pm 5\%$ , and  $\pm 10\%$  led to a percent change of 3%, 15%, and 30% in the total number of data counts, respectively, compared to the original data set with optimal smoothing parameter. The factor of 3.0 difference between the variation in the smoothing parameter and total count difference diverges more rapidly with larger percent variations. For greater than 10% variation, the total number of neutron counts varied by: 72% beam, 64% fission (+20%); 241% beam, 195% fission (+50%); and 720% beam, 526% fission (+100%). Decreasing the percent variation of the smoothing parameter (nearing direct inversion), we find: 47% beam, 46% fission (-20%); 83% beam, 86% fission (-50%); and 100% beam, 99% fission (-99%). We find that an error of  $\pm 1\text{-}\sigma$  in the smoothing parameter results in a 2% error in the total number of neutron counts in the energy spectrum. A variation  $\leq 30\%$  in the total number of neutron counts corresponds to an error in the smoothing parameter within  $\pm 5\text{-}\sigma$  of the optimal value.

The image performance is judged by detector pairs viewing a point source from many viewing angles to get an unbiased, angle-independent measure of the spread in event circle intersections. With the data set from 38 separate viewing angles observing a point source at 3 m, the spread of the most intense part of the distribution (the four highest contours in Figure 6-27) is consistent with an ARM of  $\sim 5^\circ$ . With the location known, the prototype instrument demonstrates the ability to accurately identify source

locations, even in the limit where only one viewing angle is available and experimental symmetry is used. For a space-based instrument with limited mass and potentially only a small, two-cell instrument available for flight, source location is known and only directional information would be needed to reject background. A more efficient instrument outside the laboratory for terrestrial applications would result in the higher number of potential scattering paths and hence would produce an image width on par with the ARM width.

The work outlined in this thesis is intended as a baseline for double scatter neutron instrumentation of similar character. The prototype demonstrated excellent performance but the final instrument design will be driven by the intended application. As we have shown in Chapter 7, instruments based on the work done by FNIT have been designed and tested through both simulation and laboratory studies. These instruments demonstrate the ability to conduct studies based on FNIT-like principles. Future double scatter detectors with varied designs will need to address how to obtain efficient light collection, good energy resolution, and methods for determining spatial reconstruction with good resolution.

## REFERENCES

- Agostinelli, S., J. Allison, et al. 2003. "Geant4 – A Simulation Toolkit." *Nuclear Instruments and Methods in Physics Research Section A* 506 (3): 250–303.
- Allison, J., K. Amako, et al. 2006. "Geant4 Developments and Applications." *IEEE Transactions on Nuclear Science* 53 (1): 270–278.
- Amsler, C., M. Doser, et al. 2008. "The Review of Particle Physics." *Physics Letters* B667:1.
- Axford, W. I. 1981. "Acceleration of Cosmic Rays by Shock Waves." In: *Proceedings of the 17th International Cosmic Ray Conference, Paris*. 12: 155.
- Baba, M., Y. Nauchi, et al. 1999. "Characterization of a 40-90 MeV  ${}^7\text{Li}(p,n)$  neutron source at TIARA using a proton recoil telescope and a TOF method." *Nuclear Instruments and Methods in Physics Research Section A* 428 (2–3): 454–465.
- Barschall, H. H., and M. H. Kanner. 1940. "On the Angular Distribution of Fast Neutrons Scattered by Hydrogen, Deuterium and Helium." *Physical Review* 58 (7): 590–596.
- Barton, J. C. 1976. "Basic Physics and Statistics of Photomultipliers." *EMI Electronics Limited, Electronics Tube Division*.
- Bayanov, B., V. Belov, et al. 2006. "Neutron producing target for accelerator based neutron capture therapy." *Journal of Physics: Conference Series* 41 (1): 460–465.
- Beckurts, K. H. and K. Wirtz. 1964. *Neutron Physics*. New York: Springer.
- Bell, Z. 1981. "Tests on a digital neutron-gamma pulse shape discrimination with NE213." *Nuclear Instruments and Methods* 188: 105–109.
- Beringer, J. 2004. "(p,xn) Production Cross Sections: A Benchmark Study for the Validation of Hadronic Physics Simulations at LHC." *CERN-LCGAPP-2003-18*.
- Bethe, H. A. and J. Ashkin. 1953. "Passage of radiations through matter." In *Experimental Nuclear Physics* (ed. E. Segre). New York: John Wiley and Sons, Inc.

- Bethe, Hans A. and Philip Morrison. 1956. *Elementary Nuclear Theory*. 2nd ed. New York: John Wiley & Sons, Inc.
- Bevington, Philip R. and D. Keith Robinson. 2003. *Data Reduction and Error Analysis for the Physical Sciences*. Boston, MA: McGraw-Hill.
- Biermann, L., O. Haxel, et al. 1951. "Neutral cosmic radiation from the Sun." *Z. Naturforsch* 6a: 47.
- Birks, J. B. 1964. *The Theory and Practice of Scintillation Counting*. Oxford: Pergamon.
- Bramblett, R. L., R. I. Ewing, et al. 1960. "A new type of neutron spectrometer." *Nuclear Instruments and Methods* 9: 1–12.
- Brannen, E. and G. L. Olde. 1962. "The Response of Organic Scintillators to Electron Energy Deposited in Them." *Radiation Research* 16 (1): 1–6.
- Bravar, U., Bruillard, P. J., et al. 2006. "Design and Testing of a Position-Sensitive Plastic Scintillator Detector for Fast Neutron Imaging." *IEEE Transactions on Nuclear Science* 53 (6): 3894–3903.
- Bravar, U., Woolf, R. S., et al. 2009. "Calibration of the Fast Neutron Imaging Telescope (FNIT) Prototype Detector." *IEEE Transactions on Nuclear Science* 56 (5): 2947–2954.
- Brooks, F. D. and H. Klein. 2002. "Neutron Spectrometry—historical review and present status." *Nuclear Instruments and Methods in Physics Research Section A* 476 (1–2): 1–11.
- Brooks, F. D. and H. Klein. 2006. "Scintillation Detectors for Fast Neutrons." In: *Proceedings of the Conference FNDA2006, International Workshop on Fast Neutron Detectors*, University of Cape Town, South Africa, April 3–6, 2006.
- Brooks, F. D., R. W. Pringle, et al. 1958. "Pulse Shape Discrimination in a Plastic Scintillator." *IRE Transactions on Nuclear Science* 7 (2): 35–38.
- Carrington, R. C. 1859. "Description of a Singular Appearance seen in the Sun on September 1, 1859." *Monthly Notices of the Royal Astronomical Society* 20: 13–15.
- Castaneda, C. M. 2001. "Crocker Nuclear Laboratory (CNL) Radiation Effects Measurement and Test Facility." *2001 IEEE Radiation Effects Data Workshop*. 77–81. doi: 10.1109/REDW.2001.960454

- Cecil, R. A., B. D. Anderson, et al. 1979. "Improved predictions of neutron detection efficiency for hydrocarbon scintillators from 1 MeV to about 300 MeV." *Nuclear Instruments and Methods* 161 (3): 439–447.
- Chadwick, J. 1932. "The Existence of a Neutron." *Proceedings of the Royal Society, Series A* 136: 692–708.
- Chadwick, M. B., P. Oblozinsky, et al. 2006. "ENDF/B-VII.0: Next Generation Evaluated Nuclear Data Library for Nuclear Science and Technology." *Nuclear Data Sheets* 107: 2931–3060.
- Chao, Alex W. and Maury Tigner. 1999. *Handbook of Accelerator Physics and Engineering*. Singapore: World Scientific.
- Chu, W. T. 2005. "Ernest Orlando Lawrence (1901-1958), Cyclotron and Medicine." *Lawrence Berkeley National Laboratory* n.d.
- Chupp, E. L., H. Debrunner, et al. 1987. "Solar neutron emissivity during the large flare on 1982 June 3." *The Astrophysical Journal* 318 (July 15): 913–925.
- Chupp, E. L., D. J. Forrest, et al. 1973. "Solar Gamma Ray Lines observed during the Solar Activity of August 2 to August 11, 1972." *Nature* 241 (5388): 333–335.
- Chupp, E. L., D. J. Forrest, et al. 1982. "A direct observation of solar neutrons following the 0118 UT flare on 1980 June 21." *The Astrophysical Journal* 263 (Dec 15): L95–L99.
- Chupp, E. L. and J. M. Ryan. 2009. "High energy neutron and pion-decay gamma-ray emissions from solar flares." *Research in Astronomy and Astrophysics* 9 (1): 11–40.
- Cliver, E. W. 1996. "Solar flare gamma-ray emission and energetic particles in space." In: *High Energy Solar Physics*. AIP Conference Proceedings 374: 45–60.
- Craig, Ian J. D. and John C. Brown. 1986. *Inverse Problems in Astronomy: A Guide to Inversion Strategies for Remotely Sensed Data*. Bristol, England and Boston, MA: Adam Hilger, Ltd.
- Czirr, J. B., D. R. Nygren, et al. 1964. "Calibration and performance of a neutron time-of-flight detector." *Nuclear Instruments and Methods in Physics Research* 31 (2): 226–232.



- Daibog, E. I. and V. G. Stolpovskii. 1987. "Can we Detect Electrons from the Decay of Solar Neutrons?" *Soviet Astronomy Letters (TR:PISMA)* 13 (6): 458.
- deBoer, H., K. Bennett, et al. 1992. "Maximum likelihood method applied to COMPTEL source recognition and analysis." In: *Data Analysis in Astronomy IV*, edited by V. Di Gesú 59: 241–249. New York: Plenum Press.
- Debrunner, H., E. O. Flückiger, et al. 1983. "Comparison of the Energy Spectra and Pitch Angle Distributions for Solar Energetic Particles." In: *Proceedings of the 18th International Cosmic Ray Conference, Bangalore* 4: 144–147.
- Debrunner, H., J. A. Lockwood, et al. 1993. "Neutrons from the 15 June 1991 Solar Flare." In: *Proceedings of the 23rd International Cosmic Ray Conference, Calgary* 3: 115–118.
- Dennis, B. R. and R. A. Schwartz. 1989. "Solar flares: The impulsive phase." *Solar Physics* 121: 75–94.
- de Nolfo, G. A., S. Hunter, et al. 2009. "Neutron Imaging Camera." In: *IEEE Conference on Technologies for Homeland Security* 282–286 doi: 10.1109/THS.2009.5168047.
- Diehl, R. and U. Graser. 1981. "Energy calibration of organic scintillation detectors for gamma rays." *Nuclear Instruments and Methods in Physics Research* 186 (3): 665–668.
- Dröge, W., D. Ruffolo, et al. 1996. "Observation of Electrons from the Decay of Solar Flare Neutrons." *The Astrophysical Journal* 464 (June 10): L87–L90.
- Efimov, Y. E., G. E. Kocharov, et al. 1983. "On the solar neutrons observation on high mountain neutron monitor." In: *Proceedings of the 18th International Cosmic Ray Conference, Bangalore* 10: 276–278.
- Ellison, D. C. and R. Ramaty. 1985. "Shock acceleration of electrons and ions in solar flares." *The Astrophysical Journal* 298 (Nov 1): 400–408.
- Evans, R. D. 1955. *The Atomic Nucleus*. New York: McGraw-Hill.
- Evenson, P., P. Meyer, et al. 1983. "Protons from the decay of solar flare neutrons." *The Astrophysical Journal* 274 (Nov 15): 875–882.
- Feffer, P. T., R. P. Lin, et al. 1997. "Solar Energetic Ion and Electron Limits from HIREGS Observations." *Solar Physics* 171 (2): 419–445.

- Fermi, E. 1949. "On the Origin of the Cosmic Radiation." *Physical Review* 75 (8): 1169–1174.
- Fermi, Enrico. 1950. *Nuclear Physics*. Chicago: The University of Chicago Press.
- Fetter, S., V. A. Frolov, et al. 1990. "Detecting Nuclear Warheads." *Science & Global Security* 1: 225–302.
- Flaska, M. 2007. "Identification of shielded neutron sources with liquid scintillator BC-501A using a digital pulse shape discrimination method." *Nuclear Instruments and Methods in Physics Research Section A* 577 (3): 654–663.
- Foderaro, A. 1971. *The Elements of Neutron Interaction Theory*. Cambridge, MA: The MIT Press.
- Gedcke, D. A. and W. J. McDonald. 1968. "Design of the constant fraction of pulse height trigger for optimum time resolution." *Nuclear Instruments and Methods* 58 (2): 253–260.
- Glasko, V. B. 1986. *Inverse Problems of Mathematical Physics*. AIP Translation Series.
- Glässel, P., R. Schmid-Fabian, et al. 1989. "<sup>252</sup>Cf fission revisited – new insights into the fission process." *Nuclear Physics A* 502 (October 9): 315c–324c.
- Gleeson, L. J. and W. I. Axford. 1968. "Solar Modulation of Galactic Cosmic Rays." *The Astrophysical Journal* 154 (Dec): 1011–1026.
- Golub, G. H. and C. Reinsch. 1970. "Singular value decomposition and least squares solutions." *Numerische Mathematik* 14 (5): 403–420.
- Hadamard, J. 1923. *Lectures on Cauchy's Problem in Linear Partial Differential Equations*. New Haven, CT: Yale University Press.
- Hannah, I., S. Christe, et al. 2008. "RHESSI Microflare Statistics. II. X-ray Imaging, Spectroscopy, and Energy Distributions." *The Astrophysical Journal* 677 (April 10): 704–718.
- Hansen, P. C. 1989. "Regularization, GSVD, and truncated GSVD." *BIT Numerical Mathematics* 29: 491–504.
- Hansen, P. C. 1990. "The discrete picard condition for discrete ill-posed problems." *BIT Numerical Mathematics* 30: 658–672.

- Hansen, P. C. 1992. "Analysis of discrete ill-posed problems by means of the L-curve." *SIAM Review* 34 (4): 561–580.
- Hansen, Per Christian. 1998. *Rank-Deficient and Discrete Ill-Posed Problems: Numerical Aspects of Linear Inversion*. Philadelphia, PA: Society for Industrial and Applied Mathematics.
- Hansen, P. C. 2007. "Regularization Tools version 4.0 for Matlab 7.3." *Numerical Algorithms* 46: 189–194.
- Hansen, P. C. 2008. "Regularization Tools: A Matlab Package for Analysis and Solution of Discrete Ill-Posed Problems, Version 4.1 for Matlab 7.3." *Online*. Available: <http://www2.imm.dtu.dk/~pch/Regutools/RTv4manual.pdf>
- Harris, M. J., G. H. Share, et al. 1992. "Upper limit on the steady emission of the 2.223 MeV neutron capture  $\gamma$ -ray line from the Sun." *Solar Physics* 142 (1): 171–185.
- Hodgson, R. 1859. "On a curious Appearance seen in the Sun." *Monthly Notices of the Royal Astronomical Society* 20: 15–16.
- Horvath, A., K. Ieki, et al. 2000. "Comparison of two liquid scintillators used for neutron detection." *Nuclear Instruments and Methods in Physics Research Section A* 440 (1): 241–244.
- Hua, X. M., B. Kozlovsky, et al. 2002. "Angular and Energy-dependent Neutron Emission from Solar Flare Magnetic Loops." *The Astrophysical Journal Supplemental Series* 140: 563–579.
- Iguchi, T., N. Nakayamada, et al. 1994. "Neutron spectrometry using a  $^3\text{He}$  gas ionization chamber." *Nuclear Instruments and Methods in Physics Research in Section A* 353 (1–3): 152–155.
- Iucci, N., M. Parisi, et al. 1984. "Interplanetary disturbances during Forbush decreases." *Il Nuovo Cimento* 7C: 467.
- Jess, D., M. Mathioudakis, et al. 2009. "Alfvén Waves in the Lower Solar Atmosphere." *Science* 323 (5921): 1582–1585.
- The Johns Hopkins University Applied Physics Laboratory. 2008. "Feasible Mission Designs for Solar Probe Plus in 2015, 2016, 2017, or 2018." *Online*. Available: <http://solarprobe.jhuapl.edu/mission/docs/2015-2018missions.pdf>.

- Jungerman, J. A. and F. P. Brady. 1970. "A medium-energy neutron facility." *Nuclear Instruments and Methods in Physics Research* 89 (Dec 1): 167–172.
- Kahler, S. W. 1992. "Solar Flares and Coronal Mass Ejections." *Annual Review of Astronomy and Astrophysics* 30: 113–141.
- Kanbach, G., K. Pinkau, et al. 1981. "Model Calculations on Fast Solar Neutrons and the 2.2 MeV Line Emission from Solar Flares." In *Proceedings of the 17th International Cosmic Ray Conference, Paris* 10: 9.
- Kanbach, G., C. Reppin, et al. 1975. "Time History and Model Calculations of the 2.2 MeV Gamma Ray Line from the Flares of August, 1972." In: *Proceedings of the 14th International Cosmic Ray Conference, München* 5: 1644.
- Kluge, H. and K. Weise. 1982. "The Neutron Energy Spectrum of a  $^{241}\text{Am}$ -Be( $\alpha$ ,n) Source and Resulting Mean Fluence to Dose Equivalent Conversion Factors." *Radiation Protection Dosimetry* 2: 85.
- Knoll, G. F. 2000. *Radiation Detection and Measurement*, 3rd edition. John Wiley & Sons, Inc.
- Kocharov, L., H. Debrunner, et al. 1998. "Deduced spectrum of interacting protons accelerated after the impulsive phase of the 15 June 1991 solar flare." *Astronomy and Astrophysics* 340: 257–264.
- Kontar, E. P., M. Piana, et al. 2004. "Generalized Regularization Techniques with Constraints for the Analysis of Solar Bremsstrahlung X-ray Spectra." *Solar Physics* 225 (2): 293–309.
- Kouzes, R. T. 2009. "The  $^3\text{He}$  Supply Problem." *Pacific Northwest National Laboratory, PNNL-18388*.
- Kouzes, R. T., J. H. Ely, et al. 2008. "Skyshine interference with radiation detection systems." *IEEE Nuclear Science Symposium Conference Record* 1295–1260 doi: 10.1109/NSSMIC.2008.4774634.
- Kouzes, R. T., J. H. Ely, et al. 2008. "Cosmic-ray-induced ship-effect neutron measurements and implications for cargo scanning at borders." *Nuclear Instruments and Methods in Physics Research Section A* 587 (1): 89–100.
- Landi, G. 2003. "Properties of the center of gravity as an algorithm for position measurements: two-dimensional geometry." *Nuclear Instruments and Methods in Physics Research A* 497: 511–534.

- Leamon, R., W. Matthaeus, et al. 2000. "MHD-driven Kinetic Dissipation in the Solar Wind and Corona." *The Astrophysical Journal* 537 (2): 1054–1062.
- Lee, M. 1994. "Stochastic Fermi acceleration and solar cosmic rays." In: *High-Energy Solar Phenomena – A New Era of Spacecraft Measurements*. AIP Conference Proceedings 294: 134–142.
- Leo, W. 1994. *Techniques for Nuclear and Particle Physics Experiments: A How-to Approach*. 2nd rev. ed. Berlin: Springer-Verlag.
- Lin, R. P., R. A. Schwartz, et al. 1984. "Solar hard X-Ray microflares." *The Astrophysical Journal* 283 (Aug 1): 421–425.
- Lingenfelter, R. E. 1994. "Solar flare neutrons and gamma rays." In: *High-Energy Solar Phenomena – A New Era of Spacecraft Measurements*. AIP Conference Proceedings 294: 77–88.
- Lingenfelter, R. E., E. J. Flamm, et al. 1965a. "High Energy Solar Neutrons, I. Production in Flares." *Journal of Geophysical Research* 70: 4077–4086.
- Lingenfelter, R. E., E. J. Flamm, et al. 1965b. "High Energy Solar Neutrons, II. Flux at the Earth." *Journal of Geophysical Research* 70: 4087–4095.
- Lingenfelter, R. E. and R. Ramaty. 1967. "High-Energy Nuclear Reactions in Solar Flares." In: *High Energy Nuclear Reactions in Astrophysics*, ed. B. S. P. Shen. 99–158 New York: Benjamin Inc.
- Liskien, H. and A. Paulsen. 1975. "Neutron production cross sections and energies for the reactions  ${}^7\text{Li}(p,n){}^7\text{Be}$  and  ${}^7\text{Li}(p,n){}^7\text{Be}^*$ ." *Atomic Data and Nuclear Data Tables* 15: 57–84.
- Lockwood, J. A., H. Debrunner, et al. 1997. "The Relationship Between Solar Flare Gamma-Ray Emission and Neutron Production." *Solar Physics* 173: 151–176.
- Longair, M. S. 1992. *High Energy Astrophysics, Volume 1: Particles, Photons, and their Detection*. 2nd ed. Cambridge, UK: Cambridge University Press.
- Lucy, L. B. 1972. "An iterative technique for the rectification of observed distributions." *The Astronomical Journal* 79 (6): 745–754.
- Lynch, F. J. 1966. "Improved Timing with NaI(Tl)." *IEEE Transactions on Nuclear Science* 13 (3): 140–147.

- MacKinnon, A. and J. Ryan. 2010. "Quiet Sun Fast Neutron Measurements in Space." *In Preparation*.
- Mallik, P. C. V. 2009. *Diagnostics of Solar Flare Energetic Particles: Neglected Hard X-ray Processes and Neutron Astronomy in the Inner Heliosphere*. PhD diss., University of Glasgow.
- Mark, J. C. 1993. "Explosive Properties of Reactor-Grade Plutonium." *Science & Global Security* 4: 111–128.
- Martin, R. C., J. B. Knauer, et al. 1999. "Production, Distribution, and Applications of Californium-252 Neutron Sources." In: *IRRMA '99 4th Topical Meeting on Industrial Radiation and Radioisotope Measurement Applications*. Raleigh, NC. October 3–7.
- Mascarenhas, N. 2007. *in private communication*.
- McConnell, M. L. 2010. *in private communication*.
- McConnell, M. L., K. Bennett, et al. 1997. "A Search for MeV Gamma-Ray Emission from the Quiet-Time Sun." In: *Proceedings of the 25th International Cosmic Ray Conference, Durban* 1: 13.
- McKibben, R. B., J. J. Connell, et al. 2005. "Applications of a phoswich-based detector for fast (~1–10 MeV) solar neutrons for missions to the inner heliosphere." *Advances in Space Research* 36 (8): 1432–1438.
- McLane, Victoria, Charles L. Dunford, and Philip F. Rose. 1988. *Neutron Cross Sections, Volume 2: Neutron Cross Section Curves*. Boston, MA: Academic Press, Inc.
- Mesytec MDS–8 GmbH, Germany. n.d. "MDS–8: 8 Channel Spectroscopy Amplifier with Timing Filter Outputs." *Online Available*: <http://mesytec.com/datasheets/MDS-8.pdf>
- Mesytec MPD–4 GmbH, Germany. n.d. "MPD–4: 4 Channel Particle Discriminator Module for Liquid Scintillators." *Online Available*: <http://mesytec.com/datasheets/MPD-4.pdf>
- Monte Carlo N-Particle (MCNP). 2003. "MCNP – A General Purpose Monte Carlo N-Particle Transport Code, Version 5." *MCNPX-5 Monte Carlo Team, LA-UR-03-1987* Los Alamos National Laboratory, Los Alamos, New Mexico.

- Moon, S., G. M. Simnett, et al. 1976. "Upper limits to the quiet-time solar neutron flux from 10 to 100 MeV." *The Astrophysical Journal* 207 (July 15): 630–638.
- Morrison, P. 1958. "On gamma-ray astronomy." *Il Nuovo Cimento* 7 (6): 858–865.
- Moser, M. R., E. O. Flückiger, et al. 2005. "A fast neutron imaging telescope for inner heliosphere missions." *Advances in Space Research* 36 (8): 1399–1405.
- Moser, M. R., J. M. Ryan, et al. 2005b. "Atmospheric Neutron Measurements in the 10–170 MeV Range." In: *Proceedings of the 29th International Cosmic Ray Conference, Pune 2*: 421–424.
- Moser, M. R., J. M. Ryan, et al. 2006. "SONNE: A Telescope for Imaging Solar Neutrons Below 30 MeV in the Inner Heliosphere." In: *Proceedings for the 2nd Solar Orbiter Workshop SP-641*.
- Murphy, R. J., C. D. Dermer, et al. 1987. "High Energy Processes in Solar Flares." *The Astrophysical Journal Supplement Series* 63 (March): 721–748.
- Murphy, R. J., B. Kozlovsky, et al. 2007. "Using Gamma-Ray and Neutron Emission to Determine Solar Flare Accelerated Particle Spectra and Composition and the Conditions within the Flare Magnetic Loop." *The Astrophysical Journal Supplement Series* 168 (1): 167–194.
- Murphy, R. J., R. Ramaty, et al. 1991. "Solar abundances from gamma-ray spectroscopy: Comparisons with energetic particle, photospheric, and coronal abundances." *The Astrophysical Journal, Part 1* 371 (April 20): 793–803.
- Murphy, R. J., G. H. Share, et al. 1999. "Surprisingly Intense Neutron Emission from a Flare Behind the Limb of the Sun." *The Astrophysical Journal Letters* 510: 1011–1017.
- Murphy, R. J., G. H. Share, et al. 2003. "Physical Implications of RHESSI Neutron Capture-Line Measurements." *The Astrophysical Journal Letters* 595 (2): L93–L96.
- Murray, K. M., W. J. Stapor, et al. 1989. "Calibrated charged particle radiation system with precision dosimetric measurement and control." *Nuclear Instruments and Methods in Physics Research Section A* 281 (3): 616–621.
- Myers, W. L., C. A. Goulding, et al. 2005. "Photon and Neutron Active Interrogation of Highly Enriched Uranium." In: *International Conference on Nuclear Data for Science and Technology*. AIP Conference Proceedings 769: 1688–1692.

- Normand, S., B. Mouanda, et al. 2002. "Study of a new boron loaded plastic scintillator." *IEEE Transactions on Nuclear Science* 49 (2): 577–582.
- Parker, E. N. 1988. "Nanoflares and the solar X-ray corona." *The Astrophysical Journal* 330 (July 1): 474–479.
- Piana, M. 1994. "Inversion of bremsstrahlung spectra emitted by solar plasma." *Astronomy and Astrophysics* 288: 949–959.
- Pinchenot, G., S. Guldbakke, et al. 2002. "Characterisation of spherical recoil proton proportional counters used for neutron spectrometry." *Nuclear Instruments and Methods in Physics Research A* 476: 165–169.
- Pirard, B., R. S. Woolf, et al. 2009. "Test and simulation of a Fast Neutron Imaging Telescope." *Nuclear Instruments and Methods in Physics Research Section A* 60 (3): 406–414.
- Pokotilovski, Y. N. 2010. "Options for the Neutron Lifetime Measurements in Traps." *Physics of Atomic Nuclei* 73: 725.
- Povh, Bogdan, Klaus Rith, Christoph Scholz, and Frank Zetsche. 2004. *Particles and Nuclei: An Introduction to the Physical Concepts*, 4th ed. Berlin Heidelberg New York: Springer-Verlag.
- Prato, M., M. Piana, et al. 2006. "Regularized Reconstruction of the Differential Emission Measure from Solar Flare Hard X-ray Spectra." *Solar Physics* 237: 61–83.
- Priest, E. R. 1981. *Solar Flare Magnetohydrodynamics*. New York: Gordon and Breach Science Publishers, Inc.
- Ramaty, R. 1979. "Energetic Particles in Solar Flares." In: *Particle Acceleration Mechanisms in Astrophysics*, edited by: J Arons, C. Max, C. McKee. 56: 135 New York: AIP.
- Ramaty, R. and M. A. Forman. 1986. "Particle Acceleration in Solar Flares." In *Essays in Space Science*, edited by: R. Ramaty, T. L. Cline, and J. F. Ormes. NASA CP-2464: 47.
- Ramaty, R., B. Kozlovsky, et al. 1975. "Solar gamma rays." *Space Science Reviews* 18: 341–388.



- Ramaty, R., B. Kozlovsky, et al. 1979. "Nuclear gamma-rays from energetic particle interactions." *The Astrophysical Journal Supplement Series* 40: 487–526.
- Ramaty, R. and R. J. Murphy. 1987. "Nuclear processes and accelerated particles in solar flares." *Space Science Reviews* 45: 213–218.
- Ramaty, R., R. J. Murphy, et al. 1983. "Gamma-ray lines and neutrons from solar flares." *Solar Physics* 86: 395–408.
- Rank, G., J. Ryan, et al. 2001. "Extended gamma-ray emission of the solar flares in June 1991." *Astronomy and Astrophysics* 378: 1046–1066.
- Reames, D. V. 1990. "Acceleration of energetic particles by shock waves from large solar flares." *The Astrophysical Journal, Part 2 – Letters* 358 (Aug 1): L63–67.
- Reames, D. V., J. P. Meyer, et al. 1994. "Energetic-particle abundances in impulsive solar flare events." *The Astrophysical Journal Supplement Series* 90: 649–667.
- Richardson, W. H. 1972. "Bayesian-Based Iterative Method of Image Restoration." *Journal of the Optical Society of America* 62 (1): 55–59.
- Rinard, P. M. 1991. "Neutron Interactions with Matter." In: *Passive Nondestructive Assay of Nuclear Material*, Los Alamos Technical Report NUREG/CR-5550, LA-UR-90-732:357–377.
- Roelof, E. C. 1966. "Effect of the Interplanetary Magnetic Field on Solar Neutron-Decay Protons." *Journal of Geophysical Research* 71 (5): 1305–1317.
- Ruben, A., T. E. Hoagland, et al. 2007. "A new four channel pulse shape discriminator." *IEEE 2007 Nuclear Science Symposium Conference Record* N15-237: 681–684.
- Ruffolo, D. 1991. "Interplanetary transport of decay protons from solar flare neutrons." *The Astrophysical Journal* 382 (Dec 1): 688–698.
- Ryan, J. M. 2000. "Long-Duration Solar Gamma-Ray Flares." *Space Science Reviews* 93 (3–4): 581–610.
- Ryan, J. M., C. Bancroft, et al. 2010. "An Imaging Neutron Spectrometer." *IEEE Conference on Technologies for Homeland Security* Submitted.
- Ryan, J., K. Bennett, et al. 1993. "COMPTEL Measurements of Solar Flare Neutrons." *Advances in Space Research* 13 (9): 255.

- Ryan, J., D. Forrest, et al. 1994. "Neutron and Gamma-Ray Measurements of the Solar Flare of 1991 June 9." In: *High-Energy Solar Phenomena – A New Era of Spacecraft Measurements*. AIP Conference Proceedings 294: 89–93.
- Saint-Gobain Crystals. n.d. "BC-501/BC-501A/BC-519 Liquid Scintillators." *Online Available*: <http://www.detectors.saint-gobain.com>.
- Saxena, R. 1990. "Ground Level Atmospheric Neutron Flux Measurements in the 10–170 MeV Range." PhD. diss., University of New Hampshire.
- Schlickeiser, R., A. Campeanu, et al. 1993. "Stochastic particle acceleration at parallel astrophysical shock waves." *Astronomy and Astrophysics* 276: 614–624.
- Schönfelder, V., H. Aarts, et al. 1993. "Instrument description and performance of the Imaging Gamma-Ray Telescope COMPTEL aboard the Compton Gamma-Ray Observatory." *The Astrophysical Journal Supplement Series* 86 (2): 657–692.
- Serber, Robert. 1992. *The Los Alamos Primer: The First Lectures on How to Build an Atomic Bomb*. Berkeley and Los Angeles, CA: University of California Press.
- Share, G. H. and R. J. Murphy. 1995. "Gamma-Ray Measurements of Flare-to-Flare Variations in Ambient Solar Abundances." *The Astrophysical Journal* 452 (Oct 20): 933–943.
- Slaughter, D. R., M. R. Accatino, et al. 2003. "Detection of special nuclear material in cargo containers using neutron interrogation." *Lawrence Livermore National Laboratory UCRL-ID-155315*.
- Slaughter, D. R., M. R. Accatino, et al. 2007. "The nuclear car wash: A system to detect nuclear weapons in commercial cargo shipments." *Nuclear Instruments and Methods in Physics Research in Section A* 579: 349–352.
- Smith, A. B, P. R. Roberts, et al. 1957. "Spontaneous Fission Neutron Spectrum of Cf<sup>252</sup>." *Physical Review* 108 (2): 411–413.
- Solar Probe Science and Technology Definition Team. 2008. "Solar Probe+: Report of the Science and Technology Definition Team." *NASA/TM-2008-214161*. *Online Available*: <http://solarprobe.gsfc.nasa.gov/SolarProbe+Web.pdf>.
- Strijkmans, K. 2001. "The isochronous cyclotron: principles and recent Developments." *Computerized Medical Imaging and Graphics* 25 (2): 69–78.

- Strong, A. W., P. Cabeza-Orcel, et al. 1992. "Maximum entropy imaging and spectral deconvolution for COMPTEL." In: *Data Analysis in Astronomy IV*, edited by V Di Gesú. 59:251–260 New York: Plenum Press.
- Takeda, N., K. Kudo., et al. 1999. "A development of NRESPG Monte Carlo code for the calculation of neutron response function for gas counters." *Nuclear Instruments and Methods in Physics Research in Section A* 422 (1–3): 69–74.
- Taylor, C. J. 1951. "Response of Some Scintillation Crystals to Charged Particles." *Physical Review* 84: 1034–1043.
- Thompson, A. M., I. J. D. Craig. 1992. "Automatic strategies for astrophysical inverse problems." *Astronomy and Astrophysics* 262: 359–368.
- Tikhonov, A. N. 1963. "Solution of incorrectly formulated problems and the regularization method." *Soviet Math Dokl* 4: 1035–1038.
- Tikhonov, A. N., A. V. Goncharsky, 1995. *Numerical Methods for the Solution of Ill-Posed Problems*. Dordrecht, The Netherlands: Kluwer Academic.
- Toner, M. P., J. M. Ryan, et al. 2001. "Improved Analysis of COMPTEL Solar Neutron Data, with Application to the 15 June 1991 Flare." In: *Recent Insights into the Physics of the Sun and Heliosphere – Highlights from SOHO and Other Space Missions*. Proceedings of IAU, edited by Brekke, P. 203: 571.
- Turchin, V. F. 1967. "Solution of the Fredholm equation of the first kind in a statistical ensemble of smooth functions." *U.S.S.R. Computational Mathematics and Mathematical Physics* 7 (6): 79–96.
- Van Dijk, R. 1996. "Gamma-Ray Observations of X-ray binaries with COMPTEL. A study of black-hole candidates and 2CG 135+01." PhD diss., University of Amsterdam.
- Van Loan, C. F. 1976. "Generalizing the singular value decomposition." *SIAM Journal on Numerical Analysis* 13 (1): 76–83.
- Verbinski, V. V., W. R. Burns, et al. 1968. "Calibration of an organic scintillator for neutron spectrometry." *Nuclear Instruments and Methods* 65 (1): 8–25.
- Vilmer, N. and M. Maksimovic. 2001. "Ion acceleration in solar flares: low energy neutron measurements." In: *Solar Encounter. Proceedings of the First Solar Orbiter Workshop*, eds. B. Battrock 14–18 May 2001: 405–410.

- Wang, H. T. and R. Ramaty. 1974. "Neutron propagation and 2.2 MeV gamma-ray line production in the solar atmosphere." *Solar Physics* 36: 129–137.
- Watt, B. E. 1952. "Energy Spectrum of Neutrons Thermal Fission of  $U^{235}$ ." *Physical Review* 87 (6): 1037–1041.
- Williamson, J. F., J. F. Dempsey, et al. 1999. "Plastic scintillator response to low-energy photons." *Physics in Medicine and Biology* 44: 857–871.
- Winkler, C., K. Bennett, et al. 1993. "The gamma-ray burst of 3 May 1991 observed by COMPTEL on board GRO." *Astronomy and Astrophysics* 255 (1–2): L9–L12.
- Withbroe, G. L. and R. W. Noyes. 1977. "Mass and Energy Flow in the Solar Chromosphere and Corona." *Annual Review of Astronomy and Astrophysics* 15: 363–387.
- Woolf, R. S., P. F. Bloser, et al. 2009. "Imaging and Spectroscopy of Fission Neutron with the FNIT Experiment." *IEEE Conference on Technologies for Homeland Security* 274–281 doi: 10.1109/THS.2009.5168046.
- Woolf, R. S., J. M. Ryan, et al. 2009. "Advanced Characterization and Simulation of SONNE: a Fast Neutron Spectrometer for Solar Probe Plus." In: *Proceedings of SPIE – Solar Physics and Space Weather Instrumentation III*, ed. by Fineschi 7438: 19–30.
- Wu, M. W., T. C. Guung, et al. 1999. "Absolute neutron fluence measurements between 0.5 and 3 MeV and their intercomparisons." *Nuclear Instruments and Methods in Physics Research Section A* 422: 79–83.
- Young, C. A. 2001. "Solar Flare Gamma-Ray Spectroscopy with CRGO-COMPTEL." PhD diss., University of New Hampshire.
- Young, C. A., A. Connors, et al. 2001. "Bayesian Multiscale Deconvolution Applied to Gamma-ray Spectroscopy." In: *GAMMA 2001: Gamma-Ray Astrophysics 2001*. AIP Conference Proceedings 587: 701–705.